Technische Universität München

Physik-Department

Forschungs-Neutronenquelle
Heinz Maier-Leibnitz (FRM II)

A model system for transient calculations for research reactors with a compact core

Dissertation

Christian Reiter

January 2019

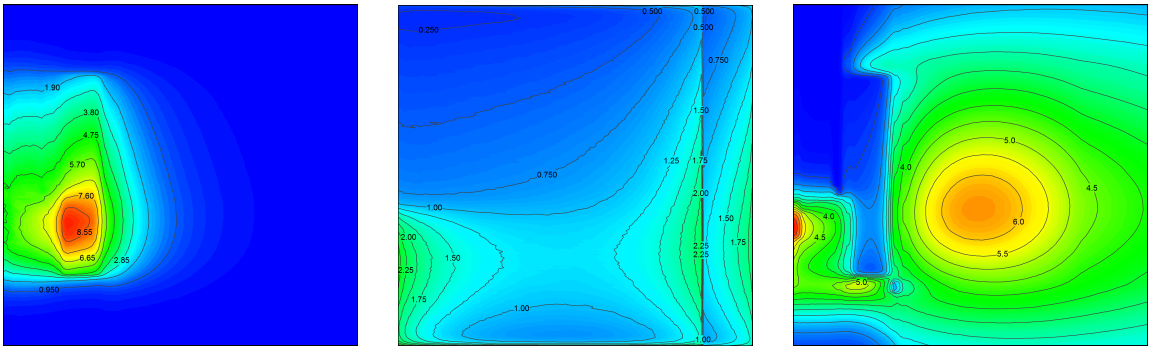

Prof. Dr. Winfried Petry, Lehrstuhl E13

TECHNISCHE UNIVERSITÄT MÜNCHEN

Physik Department

Lehrstuhl für Funktionelle Materialien (E13)
Forschungs-Neutronenquelle Heinz Maier-Leibnitz

A model system for transient calculations for research reactors with a compact core

Christian Reiter

Vollständiger Abdruck der von der Fakultät für Physik der Technischen Universität München zur Erlangung des akademischen Grades eines

Doktors der Naturwissenschaften (Dr. rer. nat.)

genehmigten Dissertation.

Vorsitzender:	Prof. Dr. Martin Zacharias
Prüfer der Dissertation:	1. Prof. Dr. Winfried Petry
	2. Prof. Dr. Rafael Macián-Juan

Die Dissertation wurde am 09.01.2019 bei der Technischen Universität München eingereicht und durch die Fakultät für Physik am 12.03.2019 angenommen.

Es ist schwieriger, eine vorgefasste Meinung zu zertrümmern als ein Atom.
Albert Einstein

Abstract

The Forschungs-Neutronenquelle Heinz Maier-Leibnitz (FRM II) actively supports international efforts for the development of a new high-density fuel to reduce the amount of highly enriched uranium in civilian circulation. Together with international partners and operators of other research reactors, a new high-density fuel based on uranium-molybdenum (UMo) alloys is being developed to replace the currently used fuels.
Because of the inevitable change of the core geometry and the different absorption characteristics of the new fuel, a reassessment of both the neutronic and thermal-hydraulical behavior of the FRM II is required. The present work focuses on the development of a complete code and model system with which coupled transient calculations for the FRM II can be carried out. For this the deterministic neutronic TORT-TD code and the thermo-hydraulic system code ATHLET have been selected.
Starting from the well-established full core MCNP6 model of the FRM II, a substitutional geometry has been designed and validated. For this substitutional geometry an appropriate Serpent 2 model was developed to provide the needed homogenized group cross sections required as input for TORT-TD. Finally, all results, especially reactivity and distribution of neutron fluxes and fission power, obtained from TORT-TD using the substitutional geometry were validated against the MCNP6 calculations.
A similar proceeding was chosen for the thermal-hydraulic calculations. After modeling the cooling circuits of the FRM II in ATHLET, the results were then validated using an already existing CFD core model based upon ANSYS-CFX that has been analyzed in depth recently.
Following the validation of the neutronic and thermal-hydraulic models, TORT-TD and ATHLET were used in coupled mode in order to carry out transient calculations. Three main scenarios have been investigated in detail: Uncontrolled insertion of reactivity, loss of coolant accident (LOCA) and running on emergency power. It could be shown that the results of these transient calculations matches with the results obtained by the general contractor Siemens during the licensing process. Afterwards, the same three transient calculations have been carried out using a possible core with a 50 % enriched dispersed UMo fuel. It turned out that the times for reaching the prescribed thresholds of the reactor safety system could be predicted well, and it could also be shown that the reactor safety system does not require a massive change if this possible fuel would be used.
Also presented in this thesis is a burnup study using an inbuilt capability of Serpent 2. The results obtained match well with those from former studies of both Breitkreutz and Röhrmoser. Only for very light isotopes like tritium, for example, significant deviations are to be noted.
To carry out this thesis, the comfortable user interface C^2 has been developed. This code provides all necessary tools for an easy set-up of new models with other possible fuel candidates, and it also allows the easy post-processing and evaluation of computed data.

Zusammenfassung

Die Forschungs-Neutronenquelle Heinz Maier-Leibnitz (FRM II) unterstützt aktiv die internationalen Bestrebungen für die Entwicklung eines neuen hochdichten Brennstoffes, um die Menge an hochangereichertem Uran im zivilen Kreislauf zu minimieren. Zusammen mit internationalen Partnern und Betreibern von anderen Forschungsreaktoren wird an einem solchen Brennstoff aus Uran-Molybdän (UMo) gearbeitet.
Durch die unumgängliche Veränderung der Kerngeometrie und der unterschiedlichen Absorption des neuen Brennstoffes ist eine Neubewertung der Neutronik sowie der Thermohydraulik des FRM II erforderlich. In dieser Arbeit wurde ein Modellsystem entwickelt, mit dem gekoppelte Transientenrechnungen für den FRM II durchgeführt werden können. Hierfür wurde das deterministische Neutronikprogramm TORT-TD und der Systemcode ATHLET verwendet.
Ausgehend von dem etablierten MCNP6 FRM II Modell wurde zunächst eine äquivalente Ersatzgeometrie entworfen und validiert. Für diese Ersatzgeometrie wurde ein entsprechendes Serpent 2 Modell entwickelt, um die für TORT-TD benötigten Wirkungsquerschnitte zu generieren. Abschließend wurden alle mit dem auf der Ersatzgeometrie beruhenden TORT-TD Modell erzielten Ergebnisse, insbesondere Reaktivität, die Verteilung von Neutronenflüssen und der Leistungsdeposition, anhand der MCNP6 Rechnungen validiert.
Ein ähnliches Vorgehen wurde für die Thermohydraulik gewählt. Zunächst wurde das Kühlungssystem des FRM II in ATHLET modelliert. Dieses Modell wurde dann mittels des CFD Programms ANSYS-CFX validiert.
Nach erfolgter Validierung der Neutronik als auch der Thermohydraulik wurden gekoppelte Transientenrechnungen durchgeführt und die drei wichtigsten Szenarien genauer untersucht: Eine unkontrollierte Reaktivitätszufuhr, ein Kühlmittelverlust (LOCA) und der Notstromfall. Es konnte gezeigt werden, dass die Ergebnisse mit denen, die seinerzeit der Generalunternehmer Siemens zur Inbetriebnahme durchgeführt hatte, übereinstimmen.
Nachfolgend wurde auf die gleiche Weise ein potentieller disperser UMo Kern mit 50 % Anreicherung untersucht. Dabei ergab sich, dass die Zeiten, die es braucht, bis das Schutzsystem den Reaktor abschaltet, den erwarteten Werten entspricht. Zudem konnte gezeigt werden, dass das Reaktorschutzsystem bei der Umstellung auf diesen Brennstoff nicht stark verändert werden müsste.
Diese Arbeit enthält zudem eine mittels Serpent 2 durchgeführte Abbrandstudie. Die dabei erzielten Ergebnisse stimmen gut mit denen aus den Studien von Breitkreutz and Röhrmoser überein. Lediglich bei den sehr leichten Isotopen, wie beispielsweise Tritium, ergeben sich signifikante Unterschiede.
Im Rahmen dieser Arbeit wurde die komfortable Benutzeroberfläche C^2 entwickelt. Dieses Programm stellt alle notwendigen Werkzeuge zur effektiven Erstellung neuer Modelle sowie zu einer bequemen Datenaufbereitung zur Verfügung.

Contents

CHAPTER 1

Introduction

1.1 The FRM II

The FRM II is the direct successor of Germany's first nuclear research reactor, the Forschungsreaktor München (FRM) "Atomei", that started operation in October 1957 and was decommissioned in July 2000 (see Figure 1.1). The FRM II is the only high flux research reactor which is operated by an university, the Technische Universität München (TUM). As one of the most modern research reactors in the world, the design of the current fuel element is the result of a consequent advancement of the fuel elements of the High Flux Isotope Reactor (HFIR) at the Oak Ridge National Laboratory (ORNL) and the High Flux Reactor (HFR) at the Institut Laue-Langevin (Institut Laue-Langevin). The core design of FRM II is optimized for beam tube experiments and for a high thermal neutron flux outside the fuel element. Therefore, it significantly differs from any common nuclear power reactor. With a thermal power of only 20 MW, an undisturbed maximum thermal neutron flux of $8.0 \cdot 10^{14}\,{}^{\mathrm{n}}/_{\mathrm{cm}^2\,\mathrm{s}}$ can be provided for 60 d continuous operational time. The FRM II provides the highest flux-to-power ratio worldwide.

Figure 1.1: *Scenic overview of the* FRM II *area with the characteristic dome of the "Atomei" on the right.*

1.1.1 Reactor Design

The FRM II is a light water cooled, light- and heavy water moderated and heavy water reflected research reactor. The heavy water is located in a separate tank outside the central channel in which the fuel element is situated. The tank contains numerous installations, e.g. a cold and a hot source, safety shut down rods, irradiation positions, etc. A CAD model of the core is

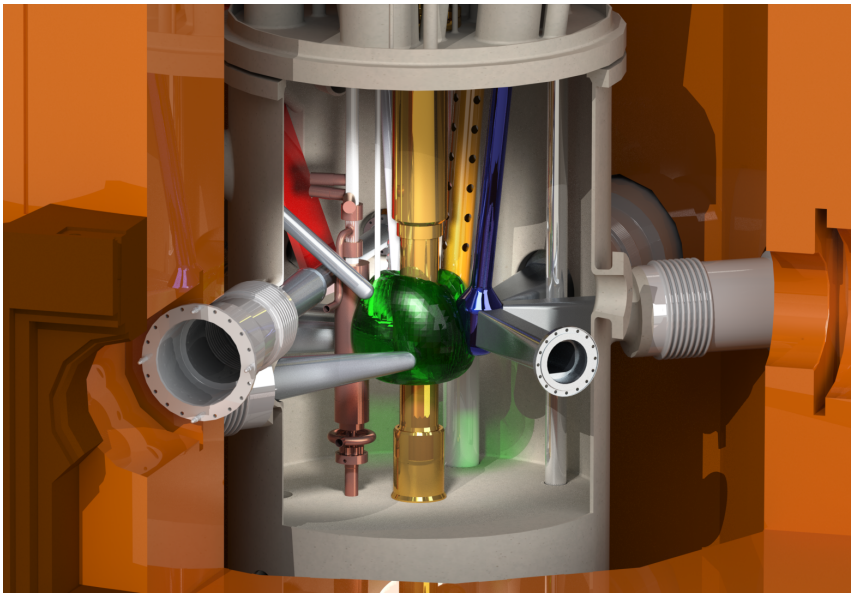

Figure 1.2: *CAD model of the reactor core. The heavy water moderator tank is shown along with the central channel in the middle (gold). Originating from the cold neutron source (blue) some beam tubes are also depicted. The converter plate for medical applications is shown in red. The thermal neutron cloud is shown in green.*

depicted in Figure 1.2, and a vertical cut through the FRM II reactor core is shown in Figure 1.3. The heavy water moderator tank can be found at the bottom of the reactor pool. Separated by a concrete wall and a door, the spent fuel element storage pool is situated next to the reactor pool. Both the reactor and storage pool are filled with deionized light water. The main cooling water feed tube, the so-called central channel runs through the center of the moderator tank. As a compact core reactor, FRM II has only one single fuel element, which is placed in the middle of the moderator tank inside the central channel. The fuel assembly consists of 113 involute shaped fuel plates. Currently, FRM II uses highly enriched uranium (HEU) with 93 % enrichment in the form of a U_3Si_2 compound dispersed in an Al-matrix. The complete uranium inventory of the core is 8.1 kg. More detailed information regarding the fuel element can be found in Chapter 6.1. To reduce the heat load near the heavy water tank that reflects a significant fraction of the neutrons back into the core, the uranium density is reduced from 3.0 $^{gU}/_{cm^3}$ in the inner region to 1.5 $^{gU}/_{cm^3}$ in the outer region of the fuel plate. The total height of the fuel zone is 70 cm. 2.2 mm thick cooling channels are located in-between the fuel plates. Due to the involute geometry of the cooling channels, this width remains constant throughout the whole core. 300 $^{kg}/_{s}$ of light water run through the central channel, whereas 274.5 kg go through FRM II's fuel element with a corresponding average flow speed of 15.91 $^{m}/_{s}$ [30]. Detailed information of the cooling system of FRM II can be found in Chapter 7.

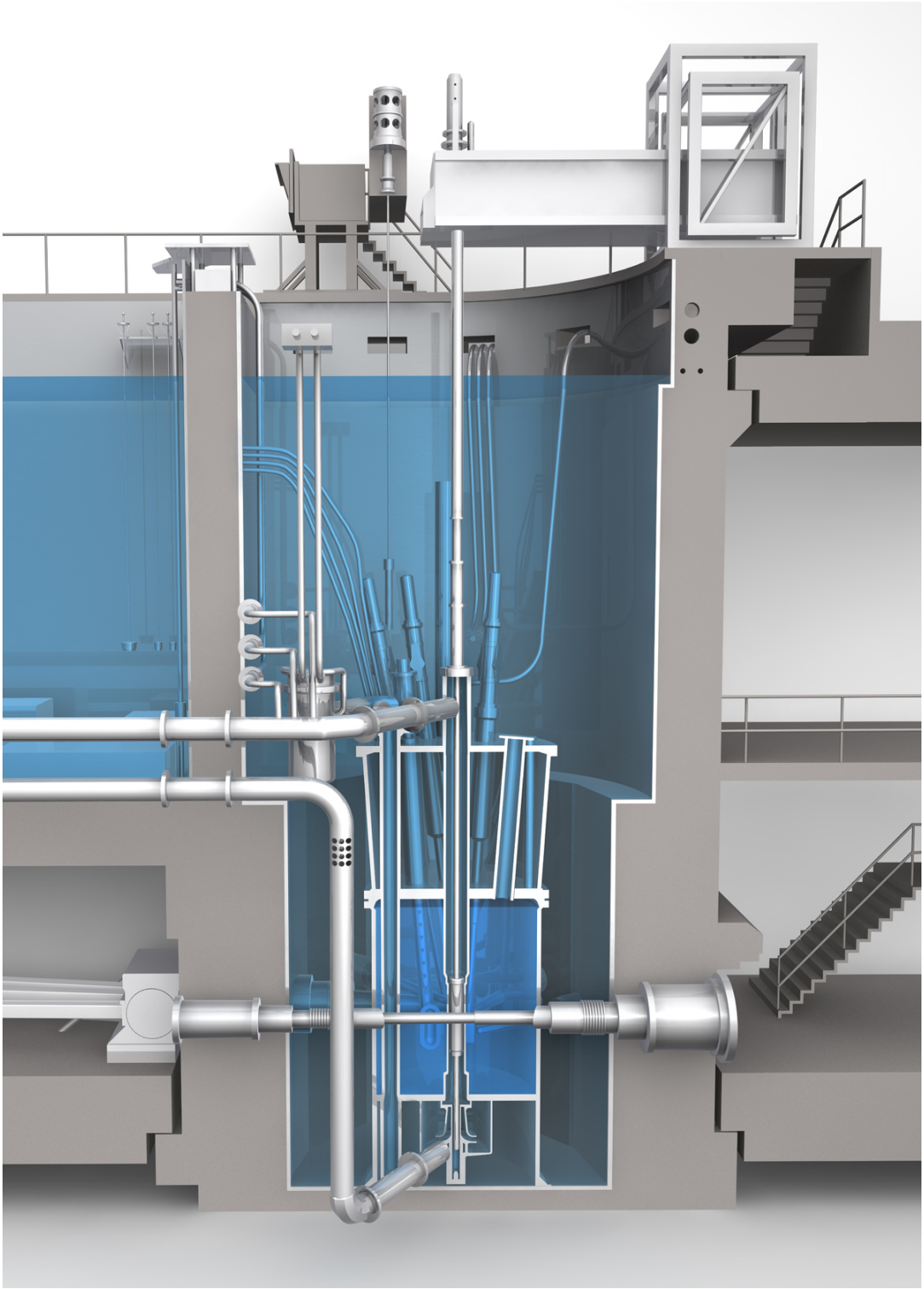

Figure 1.3: *Vertical cut through the reactor core. The heavy water moderator tank (dark blue) is situated within the reactor pool, which is filled with light water (light blue). The fuel element is located inside the central cooling channel. Also depicted are some core installations, like the control rod, emergency shutdown rods, the cold source the beam tube SR6.*

1.1.2 Kinetic and Dynamic Properties

In order to provide a better understanding of the challenges of the transient calculations within this thesis, some general facts on kinetic and dynamic properties will be outlined here. Particularly, the unique core characteristic of FRM II will be covered here.
The dynamic behavior of a reactor can be divided into three different time scales [16]:

1. The neutron flux drives phenomena on the short time scale ranging from microseconds to seconds, up to a few minutes in some rare cases.

2. The nuclear chain reaction leads to a build-up, burnup and decay of fission products. Some of these isotopes, especially ^{135}Xe and ^{149}Sm are strong neutron poisons. Theses processes happen on medium time scales between hours and a few days.

3. Long-term phenomena include the burnup as well as build-up of fissionable transuranium isotopes, and the burnup, build-up and decay of all other fission products. They evolve over days to years.

In FRM II, the moderation process which belongs to the first group, follows two different timescales, due to the different materials used: Light and heavy water. The number of collisions n needed to slow down a neutron from fast to thermal energy can be estimated with the mean logarithmic reduction of neutron energy per collision ξ:

$$n = \frac{1}{\xi} (\ln E_0 - \ln E_1) \tag{1.1}$$

Here, E_0 and E_1 are the energies of thermal and fast fission neutrons, respectively. Light water in average needs 18 collisions while heavy water needs 25 collisions. More detailed information on the timescale during transient scenarios will be given later on. Figure 1.4 shows schematically the steady-state neutron balance at Begin Of Life (BOL) in order to emphasize the peculiarities of FRM II's compact core concept. An energy of 0.625 eV was chosen as threshold for thermal neutrons. A decreasing arrow thickness symbolizes absorbed or lost neutrons due to leakage. Due to the very constraint dimensions, leakage plays a significant role for FRM II's neutron balance. 72.5 % of the fast fission neutrons initially escape the core into the heavy water moderation tank. Due to the smaller absorption cross section and the higher number of collisions needed (see Eq. 1.1), the neutrons inside the heavy water can diffuse for a rather long time before they may find their way back into the fuel element. Some of these neutrons may fly into a beam tube to an experiment, others will be scattered back to the fuel element as still fast or thermalized neutron. Part of the neutrons, which stay inside the core area are, i.e. absorbed inside the control rod and are therefore used to control the reactor.
During a transient event, the delay of neutrons due to the heavy water moderator plays a significant role. This becomes clearly visible by taking a look at the mean prompt neutron generation time Λ for the critical configuration. Λ gives information about the time between the birth of a neutron and the subsequent absorption inducing a fission event [16]. For BOL, [20] reports $\Lambda \approx 764\,\mu$s without any user installations in the moderator tank, and $\Lambda \approx 430\,\mu$s with user installations. For common light water moderated power reactors, the mean prompt neutron generation time is typically $10\,\mu$s [56], i.e. one order of magnitude smaller than for FRM II. One may consequently expect that FRM II's kinetics to be significantly slower in the prompt critical regime than those of common power reactors [16].

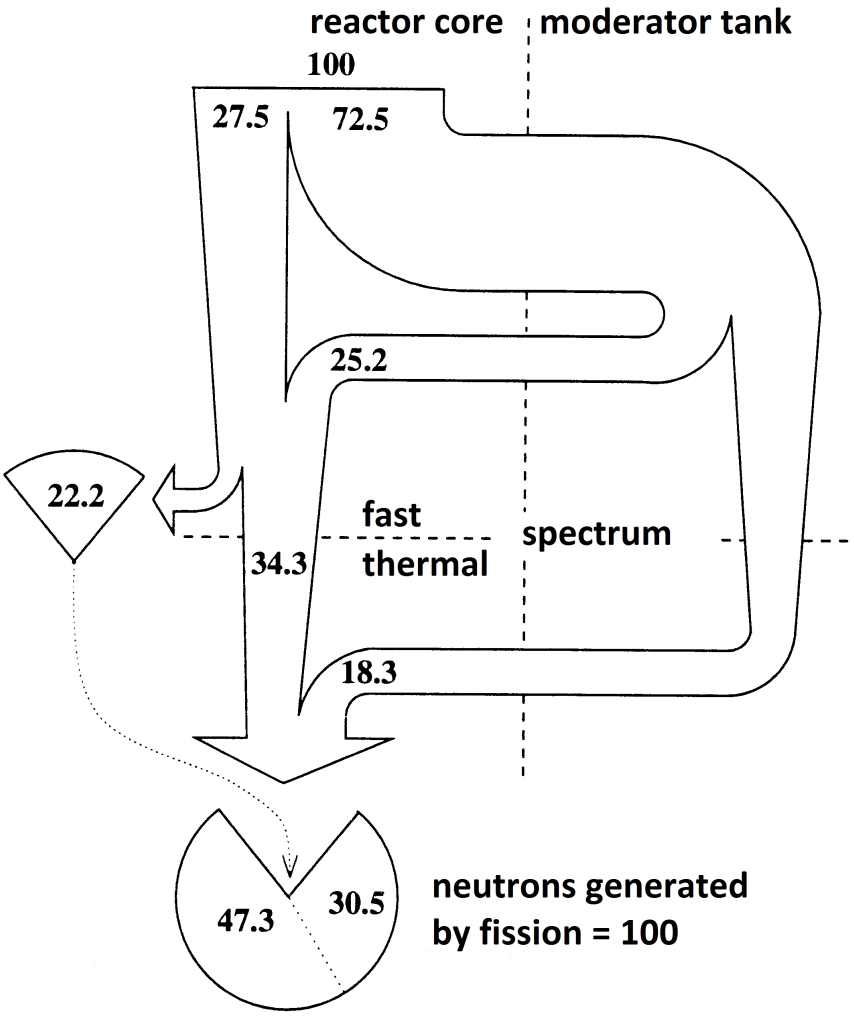

Figure 1.4: *Neutron balance at BOL without user installations in the moderator tank (adapted from [20]). From 100 starting fast fission neutrons* 72.5 % *fly into the heavy water moderation tank. The remaining* 27.5 % *stay within the light water inside the central channel.* 25.2 % *fast neutrons diffuse back from the heavy water to the fuel zone and are moderated within the light water coolant. Overall,* 77.8 % *are then used inside the fuel zone to cause fission.*

Another point, which influences the reactor during a transient is the change of temperature. This causes mainly two dominant feedback effects: On the one hand, the resonance absorption in the fuel (Doppler effect) is a function of the fuel temperature and on the other hand, the moderator and/or coolant density also changes. The FRM II is also special with regard to this point, because the change of the light water coolant density alters the delicate neutron balance of the core [16]. The coolant density has a direct impact to the number of neutrons which return to the core. With decreasing coolant density, the number of neutrons escaping the compact core increases. Since not all neutrons diffuse back to the core, this yields an additional leakage term in the neutron balance. In almost every transient scenario, the temperature of the light water moderator changes, but not the temperature of the heavy water. Therefore, the temperature of the heavy water moderator and other properties may be assumed as independent

from temperature changes of the fuel or light cooling water. These effects have to be taken into account for precise transient calculations. In this theses cross sections for different temperatures and densities are generated to be used in the deterministic calculations. More detailed information can be found in Chapter 2.2.3.4.

1.2 Conversion to lower enrichment

To support the global efforts to minimize the use of highly enriched uranium (HEU) in the civil cycle, FRM II is actively working towards the conversion of its fuel element to an uranium enrichment which is significantly lower than the current 93 %. In an international collaboration with other research reactor operators, a new high density fuel based on uranium-molybdenum (UMo) alloys is being developed to replace the currently used fuels which cannot provide a sufficiently high chemical Uranium density to compensate the lower enrichment. There are two forms of this fuel candidate available, a dispersed form with UMo-particles embedded in an aluminum matrix and a monolithic form.
In either case, only very slight changes of the dimensions of the fuel element are possible due to the very constraint geometry. Therefore, the following four general conditions for the conversion are:

- In all aspects, the new core has to be as save as the current one.
- The achievable cycle length must remain as it is today: 60 days at 20 MW.
- The neutron fluency provided to the users must only change marginally (i.e. $< 10\,\%$).
- Any conversion to lower enrichment has to be economically reasonable.

In the field of fuel conversion, much work has been done by TUM and its partners, on both the experimental and theoretical side. The interested reader may refer to [12, 73].

1.3 This work

Due to the changes to the core geometry as well as the different absorption behavior of the UMo alloys, a re-evaluation of both the neutronic and thermal-hydraulical behavior of the FRM II, in normal operation as well as in off-normal transients is required. While steady-state operation behavior has already been demonstrated to a large extent [10, 71, 72] and work is still ongoing, the present project focuses on the development of a complete code and model system for transient calculations for FRM II. The models developed within this thesis should be as accurate as possible and, as little unphysical assumptions as possible should be used. This thesis is also influenced by the thesis of C. Bogenberger [8] and M. Däubler [16], who both performed preliminary studies for transient and safety analysis for FRM II.
In a preliminary step, different codes were analyzed regarding their applicability to the very constraint conditions found within the compact core of FRM II. As the most promising solution, a coupling of the deterministic neutronic code TORT-TD (see Chapter 4.3) and the thermal-hydraulic system code ATHLET (see Chapter 5.2) was identified.
The starting point is the well-established full core MCNP6 model of FRM II [10, 71] (see Chapter 6.2). After a simplification of the model, an equivalent model in Serpent 2 was developed and validated against the results obtained with MCNP6 (see Chapter 6.3). With a fully functional

Serpent 2 model, the homogenized group cross sections, which are needed for TORT-TD, can be calculated. In the end of this process, all results, especially reactivity, flux and fission power distribution obtained from TORT-TD were validated against the MCNP6 calculations (see Chapter 6.4).

A similar proceeding was chosen for the thermal-hydraulic calculations. A CFD core model already exists for Ansys-Cfx steady state which has previously been analyzed in depth. After modeling the FRM II in ATHLET, the results were then validated using the Cfx results [10] (see Chapter 7).

Following the validation of the neutronic and thermal-hydraulic models, TORT-TD and ATHLET were used in coupled mode in order to calculate the respective transients (see Chapter 10). First, the results obtained by Siemens for transient calculations during the licensing process [79, 81, 82] were compared to the newly developed code/model system. As a final result, transients for promising UMo-fuel candidates are shown and discussed. All steps performed in this thesis are shown in the flowchart which is depicted in Figure 1.5.

During this work, the post-processing tool c^2 was developed (see Appendix D). c^2 provides all necessary tools for an easy set up of new models with other possible fuel candidates. In addition to this capabilities, c^2 can also be used for the evaluation of Serpent 2 burnup calculations.

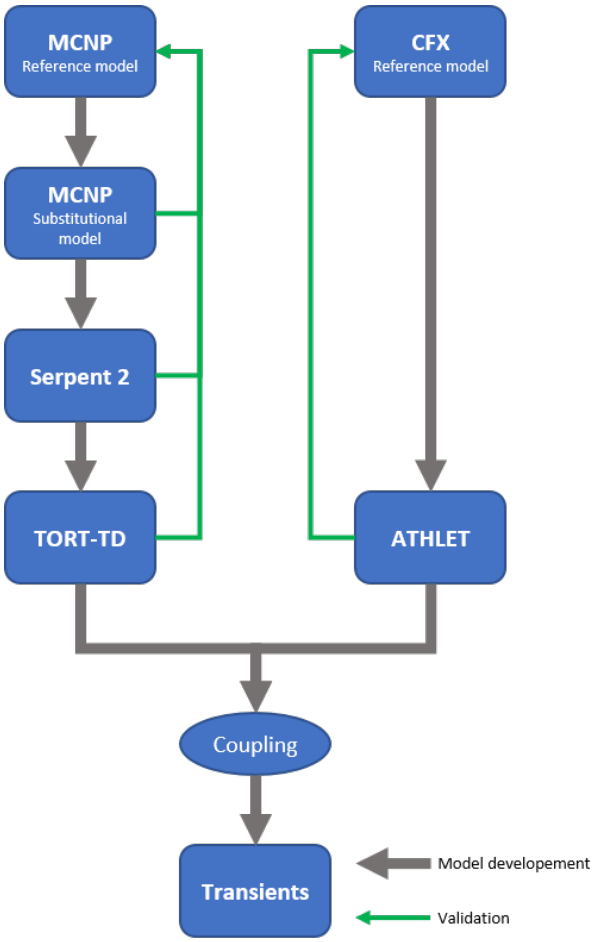

Figure 1.5: *Flowchart of this thesis.*

Part I

Theory

CHAPTER 2

Neutronics

2.1 Deterministic calculations

2.1.1 The Boltzmann equation for neutron transport

The following calculations performed with TORT-TD (see Chapter 4.3), the transients (see Chapter 10) and the derivation of the results, are based on the neutron transport theory, which will be conveyed in the following section based upon [24, 49]. Since, not every single detail can be covered, more detailed information on classic reactor physics can be found in coursebooks [23] or [85], for example. Since the general principle of neutron transport is similar to other transport problems, such as molecular movement in gases or liquids, or the drift of charged particles in a plasma, and since it is also based on conservation laws, neutron transport can be described by adjusting Boltzmann's description of the kinetic gas theory in the following points:

- Contrary to gas atoms, effusion of neutrons out of the considered volume element
- Neglection of exterior force fields, such as gravitation or electric field
- Neglection of Neutron-Neutron collisions [1]
- Consideration of collisions of neutrons with their host material, i.e. fissile material, moderator, cooling medium or structural material
- Consideration of inelastic scattering in addition to elastic scattering
- Consideration of absorption, which causes a decrease of the number of neutrons
- Consideration of fission, which increase the number of neutrons.

FRM IIs core, in particular the fuel element, control rod and heavy water moderation tank, has a cylindrical geometry. Therefore, the following calculations will be performed in cylindrical coordinates. The basic variable in neutron transport theory is the directional neutron flux $\Phi(\mathbf{r},E,\mathbf{\Omega},t)$, which is defined as

$$\Phi(\mathbf{r},E,\mathbf{\Omega},t) = v\, n(\mathbf{r},E,\mathbf{\Omega},t). \tag{2.1}$$

[1] very low neutron density: ca. $10^{10}\,\mathrm{cm}^{-3}$, sufficiently small cross sections

Here, $n(\mathbf{r},E,\mathbf{\Omega},t)\,dE\,d\mathbf{\Omega}\,dV$ is the number of neutrons in volume element dV at position $\mathbf{r}$ and time t, moving at speed $|\mathbf{v}| = v = \sqrt{\mathbf{v}\cdot\mathbf{v}}$ in directions inside the cone $d\mathbf{\Omega}$ around the angle $\mathbf{\Omega}$ with an energy in the range of $E + dE$. The angular current density $\mathbf{j}$ is derived from the neutron

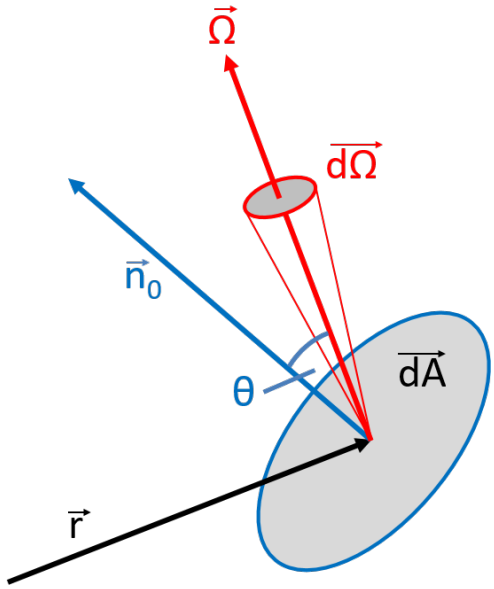

Figure 2.1: *Directional vectors describing an arbitrary neutron field originating from the surface element* $d\mathbf{q}$ *located at position* $\mathbf{r}$ *and traveling in direction* $\mathbf{\Omega}$. $\mathbf{n_0}$ *is the normal to* $\mathbf{dA}$.

flux as

$$\mathbf{j}(\mathbf{r},E,\mathbf{\Omega},t) = \mathbf{\Omega}\cdot\Phi(\mathbf{r},E,\mathbf{\Omega},t), \tag{2.2}$$

and provides information about the directional flow of the neutrons.
Integration of Equations (2.1) and (2.2) over the whole solid angle $\mathbf{\Omega}$, respectively, leads to the angular independent scalar neutron flux $\varphi(\mathbf{r},E,t)$ and neutron current density $\hat{\mathbf{j}}(\mathbf{r},E,t)$, viz.

$$\varphi(\mathbf{r},E,t) = \int_{\mathbf{\Omega}} \Phi(\mathbf{r},E,\mathbf{\Omega},t)\,d\mathbf{\Omega}, \tag{2.3}$$

$$\hat{\mathbf{j}}(\mathbf{r},E,t) = \int_{\mathbf{\Omega}} \mathbf{\Omega}\cdot\Phi(\mathbf{r},E,\mathbf{\Omega},t)\,d\mathbf{\Omega}. \tag{2.4}$$

Using the generalized volume element $\mathbf{dq}$ (see Figure 2.1)

$$d\mathbf{q} = dE\,d\mathbf{\Omega}\,dV, \tag{2.5}$$

the balance of the neutrons in $d\mathbf{q}$ can be written as

$$\frac{1}{v}\frac{\partial\Phi(\mathbf{r},E,\mathbf{\Omega},t)}{\partial t}\,d\mathbf{q} = G_{\text{tot}} - L_{\text{tot}}. \tag{2.6}$$

Here, G_{tot} and L_{tot} are the total gains and the total losses per time interval dt in d$\mathbf{q}$, respectively.

- Gain terms:
  On the one hand, neutrons with an energy in the intervall of $E' + dE'$ and inside a cone

$d\mathbf{\Omega}'$ around $\mathbf{\Omega}'$ can be scattered into the energy band in the range of $E + dE$ inside a cone $d\mathbf{\Omega}$ around $\mathbf{\Omega}$. This can be expressed as

$$G_{\mathrm{s}}(\mathbf{r},E,\mathbf{\Omega},t)\,d\mathbf{q} = d\mathbf{q}\int_{\mathrm{E}'=0}^{\infty}\int_{\mathbf{\Omega}'}\Sigma_{\mathrm{s}}(E',\mathbf{\Omega}'\rightarrow E,\mathbf{\Omega})\,\Phi(\mathbf{r},E',\mathbf{\Omega}',t)\,dE'\,d\mathbf{\Omega}'. \tag{2.7}$$

Hereby, $\Sigma_{\mathrm{s}}(E',\mathbf{\Omega}'\rightarrow E,\mathbf{\Omega})$ is the macroscopic scattering transfer cross section for the energy and the solid angle transfer. These cross sections highly depend on the geometry and defined energy group structure (see Chapter 2.1.2) and therefore, these transfer cross sections have to be calculated on a problem specific basis. In this thesis, the Monte Carlo code Serpent 2 will be used for the generation of the cross section libraries (see Chapter 4.2.1).

On the other hand, neutrons which are produced by fission are generally isotropically distributed over the whole solid angle. As most fissions are induced by thermal neutrons, it is assumed that the energy spectrum $\chi(E)$ of all fission neutrons is independent of the energy of the incident neutrons which triggered the fission. So the contribution of fission to the balance in the volume element $d\mathbf{q}$ can therefore be expressed as

$$G_{\mathrm{f}}(\mathbf{r},E,\mathbf{\Omega},t)\,d\mathbf{q} = \frac{d\mathbf{q}}{4\pi}\,\chi(E)\int_{\mathrm{E}'=0}^{\infty}\int_{\mathbf{\Omega}'}\nu(E')\Sigma_{\mathrm{f}}(E')\Phi(\mathbf{r},E',\mathbf{\Omega}')\,dE'\,d\mathbf{\Omega}'. \tag{2.8}$$

Whereas $\nu(E')$ is the number of neutrons which are emitted in average during one fission, and $\Sigma_{\mathrm{f}}(E')$ is the macroscopic fission cross section. Summing up Equations (2.7) and (2.8) gives the total gains

$$G_{\mathrm{tot}} = \left(G_{\mathrm{s}}(\mathbf{r},E,\mathbf{\Omega},t) + G_{\mathrm{f}}(\mathbf{r},E,\mathbf{\Omega},t)\right)d\mathbf{q}. \tag{2.9}$$

Photo- and delayed neutrons are are time-dependent gain terms which are not taken into account for this derivation. Comments on these phenomena can be found in Chapters 2.1.5.1 and 2.1.5.2. An additional external source, i.e. spontaneous neutron emitters like the start-up source ^{252}Cf, can be taken into account by an additional source term G_{ex} in Eq. (2.6).

- Loss terms:
  Some neutrons are lost due to effusion out of $d\mathbf{q}$, as

$$\begin{aligned} L_{\mathrm{e}}(\mathbf{r},E,\mathbf{\Omega},t)\,d\mathbf{q} &= \operatorname{div}\mathbf{j}(\mathbf{r},E,\mathbf{\Omega},t)\,d\mathbf{q} \\ &= \mathbf{\Omega}\cdot\nabla\Phi(\mathbf{r},E,\mathbf{\Omega})d\mathbf{q}. \end{aligned} \tag{2.10}$$

  Also, neutrons can be scattered out of the energy interval $E+dE$ and/or solid angle $\mathbf{\Omega}+d\mathbf{\Omega}$ (reverse process of Eq. (2.7) or are absorbed, which can be written as

$$L_{\mathrm{a}}(\mathbf{r},E,\mathbf{\Omega},t)\,d\mathbf{q} = \Big(\Sigma_{\mathrm{s}}(E) + \Sigma_{\mathrm{a}}(E)\Big)\,\Phi(\mathbf{r},E,\mathbf{\Omega},t)\,d\mathbf{q}. \tag{2.11}$$

  Here, Σ_{s} is the macroscopic cross section for scattering into another energy or solid angle interval and Σ_{a} is the macroscopic absorption cross section, which includes the macroscopic fission cross section Σ_{f}. Summing up Equations (2.10) and (2.11) yields the total losses

$$L_{\mathrm{tot}} = \left(L_{\mathrm{e}}(\mathbf{r},E,\mathbf{\Omega},t) + L_{\mathrm{a}}(\mathbf{r},E,\mathbf{\Omega},t)\right)d\mathbf{q}. \tag{2.12}$$

Inserting Equations (2.9) and (2.12) into Equation (2.6) leads to the Boltzmann equation for neutron transport:

$$\begin{aligned}\frac{1}{v}\frac{\partial \Phi(\mathbf{r},E,\mathbf{\Omega},t)}{\partial t} =& -\mathbf{\Omega}\cdot\nabla\Phi(\mathbf{r},E,\mathbf{\Omega},t) - \Big(\Sigma_\mathrm{s}(E)+\Sigma_\mathrm{a}(E)\Big)\,\Phi(\mathbf{r},E,\mathbf{\Omega},t)\\ &+\int_{\mathrm{E}'=0}^{\infty}\int_{\mathbf{\Omega}'}\Sigma_\mathrm{s}(E',\mathbf{\Omega}'\rightarrow E,\mathbf{\Omega})\,\Phi(\mathbf{r},E',\mathbf{\Omega}',t)\,dE'\,d\mathbf{\Omega}'\\ &+\frac{1}{4\,\pi}\,\chi(E)\int_{\mathrm{E}'=0}^{\infty}\int_{\mathbf{\Omega}'}\nu(E')\Sigma_\mathrm{f}(E')\Phi(\mathbf{r},E',\mathbf{\Omega}',t)\,dE'\,d\mathbf{\Omega}'\\ &+G_\mathrm{ex}.\end{aligned} \tag{2.13}$$

The solution of Equation (2.13) for a given geometry provides all important core key parameters. In reality, however, the geometries to be investigated are too complex to solve Equation (2.13) analytically. Hence, numerical methods have to be used. The code employed in this thesis, TORT-TD, uses the Discrete Ordinates Method and is described in Chapters 2.1.4, 2.1.5 and 4.3. Almost all such deterministic methods use a multi-group approach and discretize the full energy spectrum into a finite number of energy groups. The explicit definition of the group structure highly depends on the problem. In each group g of interest, steady state ($t_0 = \mathrm{const}$), effective temperature-dependent cross sections $\bar{\sigma}^\mathrm{i}_\mathrm{g}(\mathbf{r},T)$ for each nuclide and interaction i have to be calculated from existing evaluated nuclear data files, such as ENDF/B:

$$\bar{\sigma}^\mathrm{i}_\mathrm{g}(\mathbf{r},T) = \frac{\displaystyle\int_{\mathrm{E_g}}^{\mathrm{E_{g+1}}}\int_{\mathbf{\Omega}'}\sigma^\mathrm{i}(\mathbf{r},E,T)\,\Phi(\mathbf{r},E,\mathbf{\Omega},t_0)\,d\mathbf{\Omega}\,dE}{\displaystyle\int_{\mathrm{E_g}}^{\mathrm{E_{g+1}}}\int_{\mathbf{\Omega}'}\Phi(\mathbf{r},E,\mathbf{\Omega},t_0)\,d\mathbf{\Omega}\,dE}. \tag{2.14}$$

Usually, these effective multi-group cross sections are calculated using lattice physics codes like HELIOS2 [92], CASMO [68] or Monte Carlo codes like Serpent (see Chapter 4.2.1).
With a group structure in place, integration of Equation (2.13) leads to a coupled system of differential equations which is formally independent of energy. For group g and the steady state case this results in

$$\begin{aligned}-\mathbf{\Omega}\cdot\nabla\Phi_\mathrm{g}(\mathbf{r},\mathbf{\Omega}) - \Big(\Sigma_\mathrm{s}(g)+\Sigma_\mathrm{a}(g)\Big)\,\Phi_\mathrm{g}(\mathbf{r},\mathbf{\Omega}) +&\\ +\sum_{\mathrm{g}'}\int_{\mathbf{\Omega}'}\Sigma_\mathrm{s}(g',\mathbf{\Omega}'\rightarrow g,\mathbf{\Omega})\,\Phi_{\mathrm{g}'}(\mathbf{r},\mathbf{\Omega})\,d\mathbf{\Omega}' +&\\ +\frac{1}{4\,\pi}\,\chi_\mathrm{g}\sum_{\mathrm{g}'}\nu_{\mathrm{g}'}\Sigma_\mathrm{f}(g')\int_{\mathbf{\Omega}'}\Phi_{\mathrm{g}'}(\mathbf{r},\mathbf{\Omega})\,d\mathbf{\Omega}' &\\ +G_\mathrm{ex}=0,&\end{aligned} \tag{2.15}$$

where the following definitions have been used:

$$\Phi_\mathrm{g}(\mathbf{r},\mathbf{\Omega}) = \int_{\Delta\mathrm{E_g}}\Phi(\mathbf{r},E,\mathbf{\Omega})\,dE, \tag{2.16}$$

$$\Sigma_\mathrm{s}(g',\mathbf{\Omega}'\rightarrow g,\mathbf{\Omega})\,\Phi_{\mathrm{g}'}(\mathbf{r},\mathbf{\Omega}) = \int_{\Delta\mathrm{E}_{\mathrm{g}'}}\Phi(\mathbf{r},E',\mathbf{\Omega})\,dE'\int_{\Delta\mathrm{E_g}}\Sigma_\mathrm{s}(E',\mathbf{\Omega}'\rightarrow E,\mathbf{\Omega})\,dE. \tag{2.17}$$

2.1.2 The diffusion approximation

An important approximation to the Boltzmann transport equation for neutrons is the diffusion equation, which will be used later for performance enhancement where applicable (see Chapter 6.4.2). Similar to thermal diffusion, such relatively simple description has the great advantage of illustrating many of the important features of nuclear reactors. Moreover, the diffusion theory is sufficiently accurate to provide a quantitative understanding of many physics features of nuclear reactors. Following [24], the derivation of the steady state diffusion equation from the transport equation is as follows.
An expansion of the directional neutron flux $\Phi(\mathbf{r},E,\mathbf{\Omega})$ into spherical harmonics $Y_{\mathrm{lm}}(\theta,\phi)$ up to the first order (P_1 approximation) leads to

$$\begin{aligned}\Phi(\mathbf{r},E,\mathbf{\Omega}) &= \sum_{\mathrm{l}=0}^{\infty}\sum_{\mathrm{m}=-\mathrm{l}}^{\mathrm{l}} A_{\mathrm{lm}}Y_{\mathrm{lm}}(\theta,\phi) \\ &\approx A_{00}Y_{00} + A_{1,-1}Y_{1,-1} + A_{10}Y_{10} + A_{11}Y_{11}.\end{aligned} \tag{2.18}$$

Here, θ (see Fig. 2.1) and ϕ are the spherical angular coordinates. The time dependence of the directional neutron flux Φ has been disregarded because the steady state case, $\partial\Phi(\mathbf{r},E,\mathbf{\Omega},t)/\partial t = 0$, has been assumed. Exploiting the orthogonality and the normalization of the spherical harmonics, i.e.

$$\int_{\mathbf{\Omega}} Y^*_{\mathrm{l'm'}}(\theta,\phi)\, Y_{\mathrm{lm}}(\theta,\phi)\, d\mathbf{\Omega} = \delta_{\mathrm{ll'}}\delta_{\mathrm{mm'}}, \tag{2.19}$$

where the asterisk denotes the complex conjugate, the expansion coefficients A_{lm} in (2.18) are given by

$$A_{\mathrm{lm}} = \int_{\mathbf{\Omega}} Y^*_{\mathrm{lm}}(\theta,\phi)\, \Phi(\mathbf{r},E,\mathbf{\Omega})\, d\mathbf{\Omega}. \tag{2.20}$$

With $Y_{00} = 1/\sqrt{4\pi}$ and by means of Equation (2.20), the term $A_{00}Y_{00}$ in (2.18) can be expressed as:

$$A_{00}Y_{00} = \frac{1}{4\,\pi}\,\varphi(\mathbf{r},E), \tag{2.21}$$

with $\varphi(\mathbf{r},E)$ being the scalar neutron flux as defined in (2.3). Similarly, with the spherical harmonics

$$Y_{1,-1} = \frac{3}{8\,\pi}\sin\theta\exp(-i\phi),\; Y_{1,0} = \frac{3}{4\,\pi}\cos\theta,\; Y_{1,1} = -\frac{3}{8\,\pi}\sin\theta\exp(i\phi), \tag{2.22}$$

the remaining expansion terms in (2.18) can be calculated to obtain

$$A_{1,-1}Y_{1,-1} + A_{1,0}Y_{1,0} + A_{1,1}Y_{1,0} = \frac{3}{4\,\pi}\,\mathbf{\Omega}\cdot\hat{\mathbf{j}}(\mathbf{r},E), \tag{2.23}$$

with $\hat{\mathbf{j}}(\mathbf{r},E)$ being the neutron current density as defined in (2.1.1) [85]. By inserting Equations (2.21) and (2.23) into (2.18), the expansion of the directional neutron flux Φ can finally be written as

$$\Phi(\mathbf{r},E,\mathbf{\Omega}) = \frac{1}{4\,\pi}\,\varphi(\mathbf{r},E) + \frac{3}{4\,\pi}\,\mathbf{\Omega}\cdot\hat{\mathbf{j}}(\mathbf{r},E). \tag{2.24}$$

Treating the macroscopic translation cross section $\Sigma_{\mathrm{s}}(E',\mathbf{\Omega}' \to E,\mathbf{\Omega})$ (see Eq. (2.7)) in the same manner yields

$$\Sigma_{\mathrm{s}}(E',\mathbf{\Omega}' \to E,\mathbf{\Omega}) = \frac{1}{4\,\pi}\Sigma_{\mathrm{s},0}(E' \to E) + \frac{3}{4\,\pi}\Sigma_{\mathrm{s},1}(E' \to E)(\mathbf{\Omega}\cdot\mathbf{\Omega}'). \tag{2.25}$$

Inserting (2.24) and (2.25) into the transport equation (2.13) and performing two integrations first directly, and the other time after multiplication with $\mathbf{\Omega}$ over all directions, leads to the balancing equations of the P_1 approximation, viz.

$$\begin{aligned}\operatorname{div}\mathbf{j}(\mathbf{r},E) + \Sigma_{\mathrm{t}}(E)\,\Phi(\mathbf{r},E) = &\int_{\mathrm{E}'=0}^{\infty}\Sigma_{\mathrm{s},0}(E' \to E)\,\Phi(\mathbf{r},E')\,dE' + \\ &+\chi(E)\int_{\mathrm{E}'=0}^{\infty}\nu(E')\,\Sigma_{\mathrm{f}}(E')\,\Phi(\mathbf{r},E')\,dE',\end{aligned} \tag{2.26}$$

$$\frac{1}{3}\nabla\Phi(\mathbf{r},E) + \Sigma_{\mathrm{t}}\,\mathbf{j}(\mathbf{r},E) = \int_{\mathrm{E}'=0}^{\infty}\Sigma_{\mathrm{s},1}(E' \to E)\,\mathbf{j}(\mathbf{r},E')\,dE', \tag{2.27}$$

with $\Sigma_{\mathrm{t}} = \Sigma_{\mathrm{a}} + \Sigma_{\mathrm{s}}$.
Integration of Equations (2.26) and (2.27) over the g^{th} energy group ΔE_{g} leads to the following coupled, yet energy independent differential equations

$$\begin{aligned}\operatorname{div}\mathbf{j}(\mathbf{r}) + \Sigma_{\mathrm{t,g}}\,\varphi_{\mathrm{g}}(\mathbf{r}) = &\sum_{\mathrm{g}'}\Sigma_{\mathrm{s},0}(g' \to g)\,\varphi_{\mathrm{g}'}(\mathbf{r}) + \\ &+\chi_{\mathrm{g}}\sum_{\mathrm{g}'}\nu_{\mathrm{g}'}\Sigma_{\mathrm{f,g}'}\,\varphi_{\mathrm{g}'}(\mathbf{r}),\end{aligned} \tag{2.28}$$

$$\frac{1}{3}\nabla\varphi_{\mathrm{g}}(\mathbf{r}) + \Sigma_{\mathrm{t,g}}\,\mathbf{j}(\mathbf{r}) = \sum_{\mathrm{g}'}\Sigma_{\mathrm{s},1}(g' \to g)\,\mathbf{j}_{\mathrm{g}'}(\mathbf{r}). \tag{2.29}$$

Applying Fick's law on Equations (2.26) and (2.27), respectively, leads to

$$\mathbf{j}(\mathbf{r},E) = -D(\mathbf{r},E)\,\nabla\varphi(\mathbf{r},E), \tag{2.30}$$

and the stationary diffusion equation

$$\begin{aligned}\Big[\nabla\,D(\mathbf{r},E)\,\nabla - \Sigma_{\mathrm{t}}(\mathbf{r},E)\Big]\Phi(\mathbf{r},E) + Q(\mathbf{r},E) + \\ +\sum_{\mathrm{m}}\frac{1}{1-\alpha^{\mathrm{m}}}\int_{\mathrm{E}}^{\mathrm{E}/\alpha^{\mathrm{m}}}\frac{dE'}{E'}\,\Sigma_{\mathrm{n}}^{\mathrm{m}}(\mathbf{r},E')\,\Phi(\mathbf{r},E') = 0,\end{aligned} \tag{2.31}$$

whereas $D(\mathbf{r},E)$, with

$$D(\mathbf{r},E) = \frac{1}{3\ (\Sigma_\mathrm{t}(E) - \bar{\mu_0}\,\Sigma_\mathrm{s}(E))} \tag{2.32}$$

is the diffusion constant for given energy E, local total cross section Σ_t, scattering cross section Σ_s and average cosine of the scattering angle $\bar{\mu_0}$.

$$\alpha^\mathrm{m} = \left(\frac{A-1}{A+1}\right)^2 \tag{2.33}$$

is the general scattering parameter, A is the mass number of the scattering isotope, m is the energy group index and all source terms are lumped together in $Q(\mathbf{r},E)$.
In the case of only one energy group, the diffusion equation (2.31) can be simplified to read

$$D(\mathbf{r})\,\Delta\,\Phi(\mathbf{r}) - \Sigma_\mathrm{a}\,\Phi(\mathbf{r}) + \nu\,\Sigma_\mathrm{f}\,\Phi(\mathbf{r}) = 0. \tag{2.34}$$

Here, Σ_a and Σ_f is the macroscopic absorption and fission cross section, respectively.

2.1.3 Important terminologies

In this section, some important terminologies which are used often in the following will be explained.

Multiplication factor
The Boltzmann equation for neutron transport (2.13) does neither provide direct information about the extent to which the system is critical nor whether it is subcritical or supercritical. Therefore, the Boltzmann equation (2.13) is re-formulated as an eigenvalue problem by assuming that ν, the average number of neutrons per fission can be adjusted to obtain a time-independent solution [37]. In terms of the multiplication factor k, which is an eigenvalue, this solution can be characterized by means of three cases, viz.:

$$k \begin{cases} > 1 & \text{supercritical} \\ = 1 & \text{critical} \\ < 1 & \text{subcritical} \end{cases}$$

A more heuristic approach to the multiplication factor k has been given by Fermi:

$$k = \epsilon \cdot p \cdot f \cdot \eta \cdot P_\mathrm{NL}. \tag{2.35}$$

Here the individual factors have the following meaning:

Fast fission ϵ
Some fissions are caused by the fission of nonfissile fuel nuclides by fast neutrons. The fast fission factor can be defined as [85]:

$$\epsilon = \frac{\text{total fission neutron production rate}}{\text{fission neutron production rate in fissile nuclides}} \tag{2.36}$$

Resonance escape probability p
: The probability that a neutron is not captured during the slowing down process is referred to as the resonance escape probability p [85].

Neutron utilization f
: The fraction of the absorbed neutrons which are absorbed in the fissile nuclides is denoted with f [85].

Number of fission neutrons per neutron absorbed in fuel η
: η is given by the capture-to-fission ratio multiplied with the average number of neutrons released per fission [85].

Nonleakage probability P_{NL}
: P_{NL} is defined as the probability that a fast or thermal neutron does not leave the system [85]. The larger the dimensions of the systems are, the higher is P_{NL}.

Reactivity
: The reactivity gives the amount of how much the multiplication factors differs from 1. The reactivity is therefore used to describe time-dependent scenarios [24].

Reactor period
: The reactor period is the time required for reactor power to change by a factor of e [1].

A detailed discussion of this terminology can be found in Stacey [85].

2.1.4 Numerical methods

As already mentioned, the Boltzmann transport equation (2.13) is an integro-differential equation which cannot be solved in a straightforward manner. Only for special cases and with certain assumptions analytical solutions exist. Therefore, in most cases numerical methods have to be used to solve realistic nuclear systems/reactors.

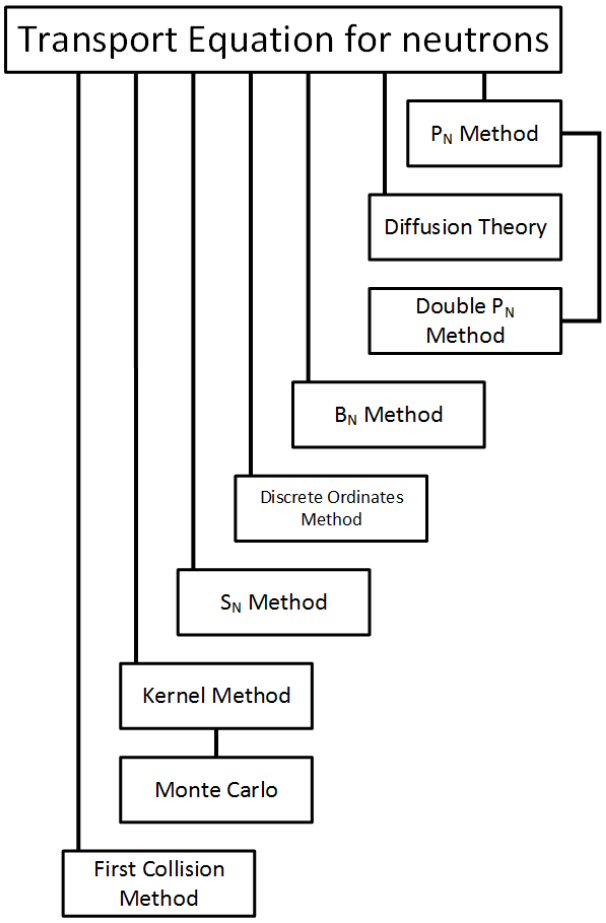

Figure 2.2: *Different numerical methods for solving the Boltzmann transport equation for neutrons. Also the dependencies of each method is depicted.*

Figure 2.2 gives an overview of available methods for solving the transport equation for neutrons. For more detailed information about the different methods, the reader is referred to the numerous course books on that topic, in particular [17]. Here, the general ideas of the most important approaches will be reviewed: the Spherical Harmonics Method (P_N), the diffusion approximation and the Discrete Ordinates Method (S_N). In Chapter 4.3 the ascertained implementation of the Discrete Ordinates Method in TORT-TD will be detailled.

- Spherical Harmonics Method (P_N):
  In this method the angular dependency of the angular neutron flux is expanded in a set of orthogonal polynomials. In general, spherical harmonics are used and the expansion is terminated after N terms. For a spatially one dimensional problem, Legendre polynomials are used (see Chapter 2.1.2). Historically, finite differences have been used for spatial discretization, but were replaced by finite elements, variational nodal and integral methods. This leads to large sets of sparse matrix equations which have to be solved by iterative methods. These methods are hardly paralliziable and therefore less efficient on modern parallel computer architectures [4].

Even though, each equation is rotationally symmetric and, therefore, free of any numerical "ray effects". These effects are numerical artifacts manifesting as "rays" whereas in between those "rays" the results are not meaningful. The number of equations to be solved for expansion order N scales with $(N+1)^2$.

There are some reactor simulation codes using the Spherical Harmonics Method, e.g. ERANOS [21, 63, 69], but today, simplified angular approximations based on the spherical harmonics method, namely the SP_N method, play an increasing role [16]. For some preliminary considerations on this thesis' topic in connection with FRM II, the SP_3 approximation was used in the thesis of Däubler [16].

- Diffusion Approximation:
  The diffusion approximation is related to the P_1 expansion (see Spherical Harmonics Method) and is the most-widely used method. A detailed mathematical description can be found in Chapter 2.1.2. There are different codes which use finite differences, finite elements as well as nodal methods to discretize the spatial variables. In case of finite difference methods, the accuracy of the results highly depends on the structure of the calculation mesh used. If the mesh spacing is smaller than the smallest group diffusion length, the results may be acceptably accurate. This restriction normally results in a large number of mesh cells needed and hence, leads to a correspondingly high computational load [16].

  Codes based upon nodal methods are widely used in full reactor core calculations and are the main computational engine in any reactor simulator code. The numerical methods used there are designed to allow very coarse meshes in order to reduce the computational load drastically. Hence, these codes are specialized to deal with the geometrical configurations of power reactors in mind and, hence, makes them unsuitable for simulating compact research reactors like the FRM II [16, 55].

- Discrete Ordinates Method (S_N):
  The discrete ordinates method is based upon the "discrete S_N method" reported by Carlson and Bell in 1958 [15]. In this method, the multi-group Boltzmann transport equation for neutrons (2.15) is evaluated over a specific set of discrete directions, and the integral is approximated by a weighted sum over the directional results. Once again, a set of algebraic equations is obtained, which is solved by a combination of recursion and iterative procedures [67].

  The method can be very well adapted to any computing machinery, can conserve particles without any fixups and is readily extendable to multiple space dimensions and anisotropic scattering treatments. The accuracy of this method can easily be improved by adding more directions, and the computational load increases only linearly with the number of discrete directions [67]. TORT-TD, the deterministic neutronics codes used in this thesis, resorts to this method, and the specific implementation is shown in Chapter 4.3.

2.1.5 Nuclear Reactor Dynamics and Space-Time Neutron Kinetics

The understanding of the time-dependent behavior of the neutron population in a nuclear system during any change of operational conditions is very important. Specifically, it is of utmost importance to ensure that the response of the nuclear system during a transient is still manageable by the reactor infrastructure, regardless if the transient is planned, unplanned or even an abnormal condition drift [85].

After the disintegration of a nucleus, the possible emission of fission neutrons can happen promptly or delayed. The response of the promptly emitted neutrons can be considered to be without delay (10^{-14} s). However, unless the nuclear system is supercritical on prompt neutrons only, the small fraction β of delayed neutrons slows down the increase of the neutron population to the timescale of the delayed neutron precursor decay time, i.e. seconds [85]. Only because of the presence of the delayed neutrons, there is sufficient time to take corrective control measures. In the case of a supercrititcal system on prompt neutrons, only intrinsic negative feedback mechanisms can compensate the runaway of the neutron population. In general, the system specific feedback mechanisms can have a positive, enhancing or negative, decelerating effect on the nuclear chain reaction. Hence, the knowledge of these mechanisms is also of very high importance, e.g., the cooling void coefficient is highly negative in a Pressurized Water Reactor (PWR) or Boiling Water Reactor (BWR), but positive in the Russian High Power Channel-type Reactor (RBMK) design. In the following chapter reactor dynamics phenomena and reactivity feedback coefficients will be discussed.

2.1.5.1 Delayed Neutrons

As already mentioned above, the reactor dynamics are primarily driven by the characteristics of the delayed neutrons emitted from fission products. Thereby, the yield of delayed neutrons ν_d strongly depends upon the fissioning isotope q and the energy of the incident neutron that caused fission. The total fraction of delayed neutrons is $\beta = \nu_\mathrm{d}/\nu$, with ν being the total number of neutrons emitted during fission.
In a real nuclear system there are normally several fissionable isotopes, such as ^{235}U, ^{238}U, ^{239}Pu, ^{240}Pu,.... In the actual reactor designs mainly uranium oxide fuel and sometimes MOX fuel is used. For modern fast reactor designs also fuel with minor actinides will be licensed. Within the international conversion framework UMo is investigated as possible fuel candidate for high power research reactors. In practical applications the delayed neutrons are divided into several effective time-groups n. Each group i, $i = 1,...,n$, can be characterized by a decay constant λ_i and a relative yield β_i/β. Since delayed neutrons have a different effectiveness in producing a subsequent fission event than the prompt ones, and their energy distribution differs as well, an importance function $\Phi^+(\mathbf{r},E)$ can be defined. This function considers the probability that a neutron introduced at position $\mathbf{r}$ with energy E will result in a fission. As described in [85], a relative importance $I^\mathrm{q}_\mathrm{d,i}$ and $I^\mathrm{q}_\mathrm{d,i,p}$ of delayed neutrons in group i emitted with energy distribution $\chi^\mathrm{q}_\mathrm{d,i}(E)$ and prompt neutrons from the fission of isotope q emitted with energy distribution $\chi^\mathrm{q}_\mathrm{p}(E)$ can be written as

$$I^\mathrm{q}_\mathrm{d,i} = \int dV \int_{\mathrm{E}=0}^{\infty} \chi^\mathrm{q}_\mathrm{d,i}(E)\, \Phi^+(\mathbf{r},E)\, dE \int_{\mathrm{E}'=0}^{\infty} \nu\, \sigma^\mathrm{q}_\mathrm{f}(E')\, N_\mathrm{q}(\mathbf{r})\, \Phi(\mathbf{r},E')\, dE', \tag{2.37}$$

$$I^\mathrm{q}_\mathrm{p} = \int dV \int_{\mathrm{E}=0}^{\infty} \chi^\mathrm{q}_\mathrm{p}(E)\, \Phi^+(\mathbf{r},E)\, dE \int_{\mathrm{E}'=0}^{\infty} \nu\, \sigma^\mathrm{q}_\mathrm{f}(E')\, N_\mathrm{q}(\mathbf{r})\, \Phi(\mathbf{r},E')\, dE'. \tag{2.38}$$

With Equations (2.37) and (2.38) a relative effective delayed neutron yield of group i for the fissionable isotope q can be defined as $I^\mathrm{q}_\mathrm{d,i}\,\beta^\mathrm{q}_\mathrm{i}$, where $\beta^\mathrm{q}_\mathrm{i}$ is the group i delayed neutron yield of fissionable isotope q. Assuming a mixture of fissionable isotopes then leads to an effective group i delayed neutron fraction for isotope q of

$$\overline{\gamma_\mathrm{i}\,\beta^\mathrm{q}_\mathrm{i}} = \frac{I^\mathrm{q}_\mathrm{d,i}\,\beta^\mathrm{q}_\mathrm{i}}{\sum_\mathrm{q}\left[I^\mathrm{q}_\mathrm{p}\,(1-\sum_{i=1}^{\mathrm{n}}) + \sum_{i=1}^{\mathrm{n}} I^\mathrm{q}_\mathrm{d,i}\,\beta^\mathrm{q}_\mathrm{i}\right]}. \tag{2.39}$$

The effectiveness of delayed neutron group i of fissionable isotope q in a specific admixture of fissionable isotopes and reactor geometry is then $\gamma_{\mathrm{i}}^{\mathrm{q}} = \overline{\gamma_{\mathrm{i}}\,\beta_{\mathrm{i}}^{\mathrm{q}}}/\beta_{\mathrm{i}}^{\mathrm{q}}$ [85].

2.1.5.2 Photoneutrons

Because of the limited energy of most of the emitted gamma rays, which are emitted during the β-decay of the fission fragments, they usually can only induce a (γ,n) reaction in nuclei where the neutron binding energy does not exceed 6 MeV. There are four relevant nuclei with sufficiently low neutron binding energy E_{n}: ^{2}D ($E_{\mathrm{n}} = 2.2\,\mathrm{MeV}$), ^{9}Be ($E_{\mathrm{n}} = 1.7\,\mathrm{MeV}$), ^{6}Li ($E_{\mathrm{n}} = 5.4\,\mathrm{MeV}$) and ^{13}C ($E_{\mathrm{n}} = 4.9\,\mathrm{MeV}$). Because of the core design of FRM II (see Chapter 6.1), only ^{2}D and ^{9}Be have to be considered in the calculations. These delayed photoneutrons influence the generation of decay heat as well as the reactor dynamics, even though the change in the effective delayed neutron yield is comparably small [16]. Since the β-decay of fission products is generally much slower than the direct neutron decay, the photoneutron precursor decay constants are much smaller as compared to the delayed neutrons described in Chapter 2.1.5.1 [85]. Hence, additional precursor families and equations have to be introduced, whereas the source term in the precursor evolution equations includes the angular photon flux. A detailed discussion of the precursor groups for FRM II can be found in [19]. It has to be noted that some of the photoneutrons are emitted from very long-living fission products and therefore, lead to a noticeable neutron background after reactor shutdown [33].

2.1.5.3 Flux Tilts and delayed neutron hold back

During a transient, flux tilts and delayed neutron hold back have a significant impact upon the state of a reactor.
A deviation of the neutron flux distribution shape from the normal flux distribution is called a flux tilt. This phenomenon can lead to difficult and challenging situations during reactor operation. A tilt will not occur instantaneously, but rather will gradually build in over time. The prompt neutrons respond instantaneously to a change of reactor conditions, but the delayed neutron source only gradually changes from the initial fundamental mode distribution into the asymptotic distribution [85]. This effect is called delayed neutron hold back.
So far, the time dependency of the Boltzmann transport equation for neutrons (2.13) has not been taken into account. It would be preferable to integrate the time-dependent equations in a straightforward manner. Since these are stiff differential equations, implicit time integration methods should be applied due to stability reasons. The stiffness of the equations is due to the largely different time scales of prompt and delayed neutrons.
For a better understanding of the influence of changing fluxes and the hold back caused by delayed neutrons, a short introduction to the related theory will be given here. For a detailed discussion one may refer to [85]. To describe such phenomena, a step-like local perturbation in the material composition of an initially critical reactor is considered. Then the initial critical reactor can be described by a multi-group diffusion theory approach similar to Equation (2.31), and can therefore be written as

$$(-\nabla\, D_{\mathrm{g}}(\mathbf{r},t)\,\nabla + \Sigma_{\mathrm{t}}^{\mathrm{g}}(\mathbf{r},E,t))\;\Phi_{\mathrm{g}}(\mathbf{r},t) - \sum_{\mathrm{g}'=1}^{\mathrm{G}} \Sigma_{\mathrm{s}}(g' \to g)\,\Phi_{\mathrm{g}'}(\mathbf{r},t) = \chi_{\mathrm{g}} \sum_{\mathrm{g}'=1}^{\mathrm{G}} \nu\,\Sigma_{\mathrm{f}}^{\mathrm{g}'}\,\Phi_{\mathrm{g}'}(\mathbf{r},t), \quad (2.40)$$

where g is the energy group and G the maximum number of groups. Equation (2.40) can be written in operator notation as

$$A_0\,\Phi_0 = M_0\,\Phi_0, \tag{2.41}$$

where the zero subscript is used to indicate the initial critical state, A is the destruction operator and M is the fission operator. A spatially nonuniform change in material properties can be written as perturbation ΔA and ΔM respectively, of these operators which then lead to new operators $A = A_0 + \Delta A$ and $M = M_0 + \Delta M$ for the perturbed system. Simplified to one single delayed neutron precursor group C, the neutron kinetics can then be described by

$$0 = \Big(- A + (1-\beta)\,M\Big)\Phi + \lambda C, \tag{2.42}$$

$$\dot{C} = \beta\,M\,\Phi - \lambda C, \tag{2.43}$$

whereas $\beta \approx 0.0075$ is the fraction of delayed neutrons and $\lambda \approx 0.08\,{}^1\!/_{\mathrm{s}}$ is the corresponding decay constant for a neutron emission. Expanding about the initial critical distribution, linearizing (i.e. ignoring quadratic terms in $\Delta M\,\Delta\Phi$,etc.), Laplace transforming or equivalently assuming an exponential time dependence $e^{-s\,t}$ and combining the two equations results in an equation for the time dependence (assuming of the neutron flux $\Delta\Phi$ in the frequency domain [85]):

$$0 = \left[-A_0 + \left(1 - \frac{s\,\beta}{s+\lambda}\right)\,M_0\right]\Delta\tilde{\Phi}(\mathbf{r},E,s) + \frac{1}{s}\left[-\Delta A + \left(1 - \frac{s\,\beta}{s+\lambda}\right)\Delta M\right]\Phi_0. \tag{2.44}$$

Now the time dependent flux can be expanded by

$$\Delta\Phi(\mathbf{r},E,t) = \sum_{\mathrm{n}=0} a_{\mathrm{n}}(t)\,\Psi_{\mathrm{n}}(\mathbf{r},E), \tag{2.45}$$

where Ψ_{n} are the spatial eigenfunctions of the initial critical reactor that satisfy

$$A_0\Psi_{\mathrm{n}} = \frac{1}{k_{\mathrm{n}}}M_0\Psi_{\mathrm{n}}, \tag{2.46}$$

where k_{n} is the mth-mode eigenvalue. With the orthogonality property

$$\langle\Psi^*_{\mathrm{m}},M_0\Psi_{\mathrm{n}}\rangle = \delta_{\mathrm{mn}} \tag{2.47}$$

the relationship

$$\langle\Psi^*_{\mathrm{m}},A_0\Psi_{\mathrm{n}}\rangle = \frac{1}{k_{\mathrm{n}}}\langle\Psi^*_{\mathrm{m}},M_0\Psi_{\mathrm{n}}\rangle \tag{2.48}$$

can be established, where $\langle X\,X\rangle$ indicates integration over space and summation over groups [85]. Inserting the expansion (2.45) in Equation (2.44), multiplying with the corresponding adjoint eigenfunction Ψ^*_{n}, integrating over space, summing over the energy groups used, and performing an inverse Laplace transformation leads to:

$$\begin{aligned} a_{\mathrm{m}}(t) =& \frac{\rho_{\mathrm{m}}\,k_{\mathrm{m}}}{1-k_{\mathrm{m}}}\left\{1 - \frac{\beta\,k_{\mathrm{m}}}{1-(1-\beta)k_{\mathrm{m}}}\exp\left[\frac{-\lambda\,(1-k_{\mathrm{m}})\,t}{1-(1-\beta)\,k_{\mathrm{m}}}\right]\right\} \\ & - \frac{\beta\,k_{\mathrm{m}}\,\langle\Psi^*_{\mathrm{m}},\,\Delta M\Phi_0\rangle}{[1-(1-\beta)\,k_{\mathrm{m}}]\,\langle\Psi^*_{\mathrm{m}},\,M_0\Psi_{\mathrm{m}}\rangle}\exp\left[\frac{-\lambda\,(1-k_{\mathrm{m}})\,t}{1-(1-\beta)\,k_{\mathrm{m}}}\right], \end{aligned} \tag{2.49}$$

where

$$\rho_{\mathrm{m}} = \frac{\langle \Psi_{\mathrm{m}}^{*}, (-\Delta A + \Delta M)\Phi_0 \rangle}{\langle \Psi_{\mathrm{m}}^{*}, M_0 \Psi_{\mathrm{m}} \rangle} \tag{2.50}$$

is the mth-mode reactivity [85]. For a nonuniform perturbation with $\rho_{\mathrm{m}} \neq 0$ higher harmonic eigenfunctions are introduced into the flux distribution, which becomes after the transient terms in Eq. (2.49) have died out

$$\Phi(\mathbf{r},\infty) = [1 + a_0(\infty)]\Phi_0(\mathbf{r}) + \sum_{\mathrm{n}=1} \frac{\rho_{\mathrm{n}}\, k_{\mathrm{n}}}{1 - k_{\mathrm{n}}}\, \Psi_{\mathrm{n}}(\mathbf{r}). \tag{2.51}$$

The most important parameter models, which solve the time dependent model, are the Point Kinetics (PK), the Quasi-Static (QS) and the Improved Quasi-Static (IQS) models. Here, only the one-energy group diffusion approximation will be discussed, but all methods also exist in multi-group diffusion and transport forms, which are also used by TORT-TD.
For the PK model two basic approximations have to be made:

1. The neutron flux $\Phi(\mathbf{r},E,\mathbf{\Omega},t)$ is separable in a shape function $\Psi(\mathbf{r},E,\mathbf{\Omega})$ and an amplitude function $T(t)$ [85]:

   $$\Phi(\mathbf{r},E,\mathbf{\Omega},t) = \Psi(\mathbf{r},E,\mathbf{\Omega})\, T(t)$$

2. The spatial flux distribution is a steady-state one, i.e. the shape function $\Psi(\mathbf{r},E,\mathbf{\Omega},t_0)$ does not change with time [16].

With these assumptions, the linear Boltzmann transport equation turns into a system of $n+1$ stiff ordinary differential equations, where n is the number of delayed neutron precursor families [4]:

$$\frac{dT}{dt} = \frac{\rho(t) - \beta(t)}{\Lambda(t)}\, T(t) + \sum_{\mathrm{i}=1}^{\mathrm{n}} \lambda_{\mathrm{i}}\, C_{\mathrm{i}}(t), \tag{2.52}$$

$$\frac{dC_{\mathrm{i}}}{dt} = -\lambda_{\mathrm{i}}\, C_{\mathrm{i}}(t) + \frac{\beta_{\mathrm{i}(t)}}{\Lambda(t)}\, T(t), \tag{2.53}$$

where $\rho(t)$ is the reactivity, $\Lambda(t)$ is the mean prompt neutron generation time and β_{i} are the effective delayed neutron fractions given by the initial shape function Ψ_0. Eq. (2.52) and (2.53) show the time dependent evolution of the delayed neutron precursor groups and the amplitude function depending upon the important parameters. In the quasi-static method, the PK equations are used for the flux amplitude, but the flux shape function is recomputed at each time step t_{n} [85]. The IQS explicitly takes into account the time dependence and is the main method found in production reactor simulator codes today [16].

2.2 Monte Carlo

Due to the increasing computational power available, a totally different approach from deterministic codes came into focus: The Monte Carlo (MC) method. In contrast to deterministic methods, MC reactor codes do not solve the Boltzmann equation (see Eq. 2.13). Even though often entitled as “method of last resort”, with the increasing CPU power, the MC method allows very powerful codes, like MCNP6 or Serpent 2, to calculate complex-formed reactor cores and, moreover, they

can even deal with modern concepts like fast reactors or fusion plasmas [52]. Figure 2.3 shows the

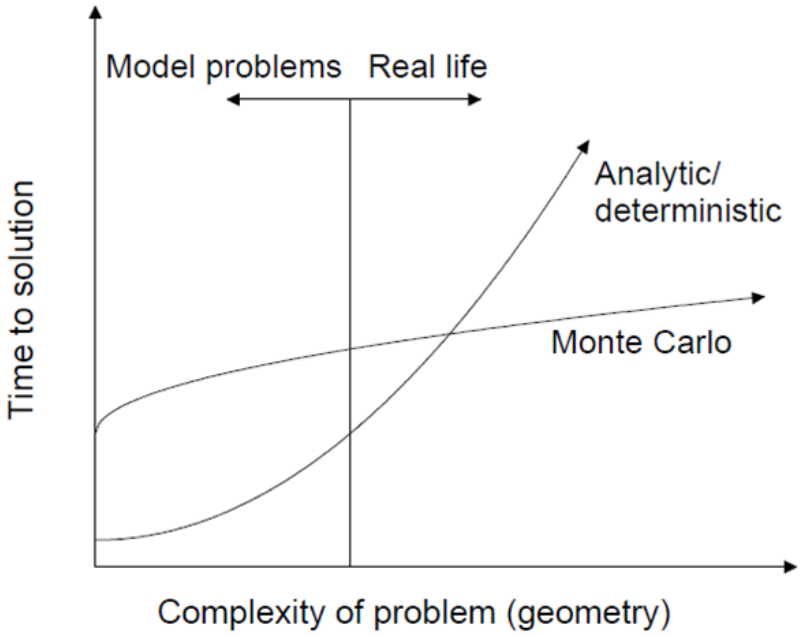

Figure 2.3: *Comparison of MC and analytic/deterministic methods in terms of the time needed to solve a problem of a given complexity [11].*

advantage of the MC method when simulating realistic systems. Whereas deterministic methods can solve model problems rather fast, real life problems have to be simplified or transferred to substitutional models in order to be solvable within acceptable computational time. Also, the parallelization of a deterministic calculation is not straightforward and so a lot of effort has to be put into that topic [4].
MC codes uses a totally different approach to obtain their results and simulate histories of particle motion through a predefined geometry. But because of the central limit theorem the MC simulation will converge to reality within the limits of statistics. The solution therefore does not provide the full phase-space information, but specific parts need to be selected prior to the actual computation. Thereby, several aspects of their averaged behavior, which are called tallies, are tracked. To describe a real life problem adequately, the number of trials needed is usually quite large. Due to the direct approach MC codes are much easier to parallelize. Hence, with the rapid growth of computational power MC can solve complex problems without simplifications and faster as deterministic codes.
In the following, the deterministic and MC approach for neutron transport is described in detail. If an equation is formulated, which derives the probability density of particles in phase space, an integral form of the transport equation results [94]. Therefore, a deterministic approach and the MC method basically solve the same equation, but written in different forms: The integro-differential form for the deterministic method and the integral form for MC.
In general, the life of a particle is tracked more or less from “birth” to “death”. During the MC calculation, the simulated particles are transported between different events, such as scattering, absorption or fission (see Figure 2.4). The type of event is selected by random numbers in the range from 0 to 1, based on the physics and transport data governing the processes and materials

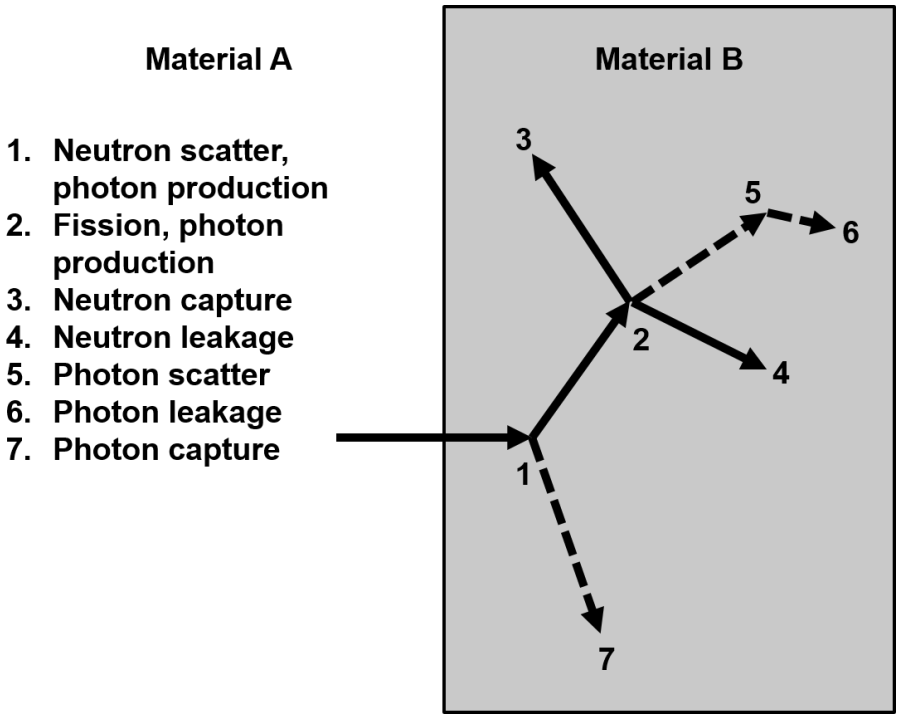

Figure 2.4: *Exemplary history of one particle simulated with MC. Each number represents a possible interaction, which is defined with corresponding cross sections.*

involved. The more particle histories are followed, both the neutron and photon distributions become better known [94]. Because these events are separated in space and time, no averaging approximations in space, energy or time are necessary [94]. Due to the event based calculation, for meaningful results a detailed representation of all physical aspects in the nuclear data is important.
In this work, the MC codes MCNP6 [59], developed at Los Alamos National Laboratory, and Serpent 2 [52], developed at Technical Research Center of Finland (VTT), are used, respectively.

2.2.1 Nomenclature of Monte Carlo codes

Some basic terms, which are needed to understand the principle of operation of MC Codes will be introduced in the following Section.

Cell

A geometry unit which consists of two- or three dimensional regions. A cell is defined with a set of $\longrightarrow$ surfaces and can have a nearly arbitrary shape. Cells are filled with a single $\longrightarrow$ material or a $\longrightarrow$ universe. Multiple cells can be combined in one universe.

Cell-Importance

A $\longrightarrow$ cell can have a weight assigned. This weight is called importance and specifies how important a specific cell is considered to be. In combination with variance reduction techniques, it can be used to turn attention on specific parts of the geometry.

Cycle
: A cycle is the simulation of a user defined number of ⟶ histories. It has to be distinguished between inactive and active cycles. Inactive cycles are used to generate an adequate source distribution and therefore do not contribute to the final results. In active cycles the desired events are tracked and memorized (⟶ Tally).

Detector
: ⟶ Tally

History
: Fate of a particle, from "birth" to "death". If ⟶ variance reduction techniques are available in the MC Code, one history can include several particles (⟶ Track)

Material
: Definition of a material used in the model. Mass or atomic density, thermal scattering libraries and optional features have to be specified, too, and are bound to a material.

Mesh
: A (un-)structured mesh or grid is a tessellation of the Euclidean space. In a regular mesh, every single mesh cell is distinctly defined by indices, whereas unstructured grids don't have a fixed topology. In MC Codes a mesh can be used to set up superimposed ⟶ tallies (independent from the ⟶ cell based geometry).

Mesh tally
: A ⟶ tally, that is independent of the ⟶ cell-geometry, i.e. superimposed, is called "mesh tally".

Surface
: Elementary or derived surfaces exist, e.g. planes, spheres or cylinders. They are used to define ⟶ cells or are used for ⟶ tallies

Tally
: A tally is a virtual detector. In a tally, information about specific reactions for distinct regions (⟶ surface, ⟶ cell, ⟶ material) are stored. Serpent 2 calls a tally a ⟶ detector [49].

Track
: Path of one fraction of a particle. If particles aren't split into subitems (⟶ variance reduction), a track is equivalent to the ⟶ history [10].

Universe
: In a universe, several ⟶ cells or other ⟶ universes are collected. Using universes, the model geometry can be separated into several logical levels which are all constructed independently. In MCNP6, universes can be used optionally to collect logical parts; if no universe is provided the ⟶ cell is automatically part of the base universe 0. But in Serpent 2 every ⟶ cell needs a containing universe.

Variance Reduction
: Even with growing computational power, a "dumb" direct computational approach is prohibitively expensive and therefore variance reduction techniques have to be resorted to. The goal of every technique available is to "guide" the neutrons to the area of interest.

While the Serpent 2 version used here did not have this capability, MCNP6 implements several different methods. Here, the following most important are presented:

Particle Splitting: If a particle moves from a $\longrightarrow$cell with importance ω_a into another cell with importance ω_b, the particle is split into $\omega_\mathrm{b}/\omega_\mathrm{a}$ particles[2], if $\omega_\mathrm{b} > \omega_\mathrm{a}$. Then the original weight is multiplied with the inverse fraction and transferred to the new particles. This technique is normally used to model important parts of a geometry well.

Russian Roulette: This is the counterpart to particle splitting, meaning that $\omega_\mathrm{b} < \omega_\mathrm{a}$. Here, a particle is killed with a probability $1 - \omega_\mathrm{b}/\omega_\mathrm{a}$. If a particle is not killed its weight is adjusted with $\omega_\mathrm{a}/\omega_\mathrm{b}$. Russian Roulette is typically used to model regions of small relevance.

Exponential Transform: This method puts a preferred direction to a particle by lowering cross sections in that direction and raising it in other ones. Then a virtual cross section Σ_t^* can be defined:

$$\Sigma_\mathrm{t}^* = \Sigma_\mathrm{t}\,(1 - p\,\cos\theta). \tag{2.54}$$

Here, geometrical parts are treated unequally, which has to be balanced by adjusting the particle weight W by

$$W' = \frac{\Sigma_\mathrm{t}\,e^{-\Sigma_\mathrm{t}\,s}}{\Sigma_\mathrm{t}^*\,e^{-\Sigma_\mathrm{t}^*\,s}}\,W, \tag{2.55}$$

with s being the distance to the next collision.

Weight Windows: In weight windows, three limits can be set for particles weights: W_u as upper limit, W_l as lower limit and W_s as the survival weight. If a particle's weight exceeds the upper limit, it is split ($\longrightarrow$Particle Splitting) and if its weight falls below the lower limit, Russian Roulette is played. If the particle survives, its weight is set to the survival weight.

Forced Collisions: If the user is interested in collisions, he can enforce collisions in certain cells. Then the particle is split in one that collided and in an uncollided one. Also the corresponding weights have to be adjusted to $W_\mathrm{c} = W\,[1 - \exp(-\Sigma_\mathrm{t}\,d)]$ for the collided one and $W_\mathrm{u} = W\,\exp(-\Sigma_\mathrm{t}\,d)$ for the uncollided one, where d is the distance from the particle's position to the border of the cell in flight direction.

A decent compilation of the available variance reduction techniques can be found in [10].

With these general terms, the treatment of interaction physics and cross sections in MC codes will be explained next.

2.2.2 Interactions

In order to describe complex physical behavior, a MC code does not solve complex mathematical equations; rather it resorts to using random numbers to reproduce real physics. In this chapter, only a short overview of the needed models will be given to familiarize the reader with the MC concept, based on the MCNP6 documentation [59]. Detailed information on MC simulations can be found, for example, in [26, 45, 75].

[2] If this fraction is not an integer, the following splitting and reweighting will be done in a probabilistic way

2.2.2.1 Interaction Probability

First, the probability of an interaction for a tracked particle has to be determined. Let a particle move in the direction $\mathbf{v}/v$ with speed $v = \sqrt{\mathbf{v} \cdot \mathbf{v}}$; then the probability p of an interaction for that particular particle between l and $l + dl$ is given by

$$p(l)\, dl = e^{-\Sigma_T\, l}\, \Sigma_T\, dl, \tag{2.56}$$

whereas Σ_T is the macroscopic total cross section of the material the particle moves in. Given a set of uniformly distributed random numbers $0 \leq \kappa < 1$, κ decides whether an interaction takes place ($\kappa \leq p$) or not ($\kappa > p$):

$$\kappa = \int_0^l e^{-\Sigma_T\, s}\, \Sigma_T\, ds = 1 - e^{-\Sigma_T\, l}. \tag{2.57}$$

It directly follows that

$$l = -\frac{1}{\Sigma_T} \ln(1 - \kappa). \tag{2.58}$$

Because $1 - \kappa$ is distributed in the same manner as κ, and hence can by replaced by κ, the expression for the interaction distance l is obtained,

$$l = -\frac{1}{\Sigma_T} \ln \kappa. \tag{2.59}$$

2.2.2.2 Choice of Interaction

Next, the type of interaction has to be determined. Multiple ways of interaction and corresponding cross sections are available and the most prominent examples are shown in the following.

Σ_T: Total cross section: $\Sigma_\mathrm{s} + \Sigma_\mathrm{a} + \Sigma_\mathrm{f}$

Σ_n: Elastic scattering cross section

$\Sigma_{\mathrm{n}'}$: Nonelastic neutron cross section

Σ_s: Total scattering cross section: $(\Sigma_n + \Sigma_{n'})$

Σ_f: Fission cross section

Σ_a: Absorption cross section (including fission): $\Sigma_\mathrm{a} + \Sigma_\mathrm{f} + \Sigma_\gamma + \Sigma_\mathrm{2n} + \Sigma_\alpha + \Sigma_\mathrm{p} + ...$

Σ_2n: Cross section for production of two neutrons: (n,2n)

Σ_α: Cross section for production of an alpha particle: (n,α)

Σ_p: Cross section for production of a proton: (n,p)

Σ_γ: Cross section for emission of a γ ray: (n,γ)

The choice of the performed interaction must again be modeled by a random number. If there are n different nuclides forming the cell's material in which the interaction does occur, and if $0 \leq \kappa < 1$ is a uniformly distributed random number, then the jth interaction is chosen if

$$\sum_{i=1}^{j-1} \Sigma_{T,i} < \kappa \sum_{i=1}^{n} \Sigma_{T,i} \leq \sum_{i=1}^{j} \Sigma_{T,i}, \tag{2.60}$$

whereas $\Sigma_{T,i}$ is the macroscopic total cross section of nuclide i.

2.2.3 Cross sections

There are certain conditions where the cross sections discussed above cannot be taken directly from a library, but rather have to be adjusted [10]. In the following, possible adjustments for the scattering and absorption cross sections, the treatment of unresolved resonances and temperature changes will be discussed.

2.2.3.1 Scattering Cross Sections

For a collision between a thermal neutron and an atom, the thermal motion of the atom has to be taken into account, especially for neutrons with energies below 4 eV for hydrogen, and even higher energies for other light elements. In addition, the presence of nearby atoms, chemical bindings and the crystal structure play an important role for low-energy scattering processes. This behavior can be accounted for by using the so called Free Gas Model or preferably, if available, the $S(\alpha,\beta)$ thermal scattering laws [5, 94].

Free Gas Model

A neutron with velocity v passes atoms having a thermal velocity v'. A Maxwell distribution $p(v')$ can be assumed for the velocity distribution of the atoms, which can be written as

$$p(v') = \frac{4}{\sqrt{\pi}} \beta^3 \, v'^2 \, e^{-(\beta \, v')^2}, \tag{2.61}$$

with

$$\beta = \sqrt{\frac{A \, M_n}{2 \, k_\mathrm{B} \, T}},$$

whereas A is the mass number, M_n the molar mass, T the temperature of the scattering nuclide, and k_B the Boltzmann constant. With the distribution (2.61), an effective scattering cross section $\sigma_{\mathrm{s,eff}}$ is calculated by

$$\sigma_{\mathrm{s,eff}}(E) = \frac{1}{v} \iint \sigma_\mathrm{s}(v_\mathrm{r}) \, v_\mathrm{r} \, p(v') \, dv' \frac{d\cos\theta}{2}. \tag{2.62}$$

Here, θ is the scattering angle between the neutron and its interaction partner and $v_r = \sqrt{v^2 + v'^2 + 2\,v\,v'\,\cos\theta}$ is the corresponding relative velocity. Equation (2.62) implies that the probability distribution for a target velocity v' and $\cos\theta$ is given by

$$p(v',\omega) = \frac{1}{2} \, p(v') \, \frac{v_\mathrm{r}}{v'} \, \frac{\sigma_\mathrm{s}(v_\mathrm{r})}{\sigma_{\mathrm{s,eff}}(E)}. \tag{2.63}$$

Calculating the probability distribution (2.63) is extremely memory and time consuming, therefore a simplified method needs to be applied. It can be assumed that the variation of σ_s with the target velocity can be ignored. On the one hand, for light nuclei σ_s is slowly varying with velocity and, on the other hand for heavy nuclei, for which σ_s can vary rapidly near resonances, the moderation effect is small [94]. This leads to

$$p(v',\omega) \propto \frac{\sqrt{v^2 + v'^2 + 2\,v\,v'\,\cos\omega}}{v + v'} \left(v'^3\, e^{-(\beta\,v')^2} + v\,v'^2 \right). \tag{2.64}$$

Now a velocity v' for MC calculation can be selected as follows [10]:

- A uniformly distributed random number $0 \leq \kappa < 1$ is generated
- With $y = (v'\,\beta)^2$ and $y' = v'\,\beta$, a velocity is sampled from

$$p'(v') = \begin{cases} y\,e^{-y} & \kappa < \left(1 + \frac{\sqrt{\pi}\,\beta\,v'}{2}\right)^{-1} \\ \frac{4}{\sqrt{\pi}}\,y'^2\,e^{-y'^2} & \text{otherwise} \end{cases} \tag{2.65}$$

- An angle is chosen from $-1 \leq \cos\theta \leq 1$ using a second random number
- The result is accepted with a probability

$$p'' = \frac{\sqrt{v^2 + v'^2 + 2\,v\,v'\,\cos\omega}}{v + v'}. \tag{2.66}$$

  If not, the calculation is repeated.

$S(\alpha,\beta)$ Thermal Scattering Laws

The $S(\alpha,\beta)$ thermal scattering Laws account for chemical bindings, crystal structure and aggregate state. The use of these $S(\alpha,\beta)$ libraries is important in problems where incoherent inelastic scattering occurs or where neutrons are scattered on light particles. If there is $S(\alpha,\beta)$ data available, then this is the method of choice. Most libraries provide data up to an energy of 4 eV. There are two procedures provided, viz. inelastic scattering ($\sigma_{n'}$) with correlated energy-angle-distribution and elastic scattering (σ_n) without influencing the energy of the scattered neutron with an angular treatment derived from lattice parameters [10].
Now a cross section $\sigma(E,E',\cos\theta)$ can be formulated by applying the equation for incoherent inelastic scattering:

$$\sigma(E,E',\cos\theta) = \frac{\sigma(T=0)}{2\,k_b\,T}\sqrt{\frac{E'}{E}}\,\exp\left(-\frac{\beta}{2}\right)\,S(\alpha,\beta), \tag{2.67}$$

whereas E is the energy of the incoming, E' the energy of the outgoing neutron and θ the scattering angle and where α and β are reduced values for momentum and energy transfer, respectively:

$$\alpha = \frac{E' + E - 2\sqrt{E\,E'}\,\cos\theta}{A\,k_b\,T}, \tag{2.68}$$

$$\beta = \frac{E' - E}{k_b\,T}. \tag{2.69}$$

Here, A stands for the mass number of the scattering nuclide.
In the case of inelastic scattering, the secondary energies are represented by a set of equally probable final energies, along with a set of angular data for each initial and final energy [94]. Then the selection of a final energy E' given an initial energy E can be calculated from the distribution

$$p(E'|E_\mathrm{i} < \xi < E_{\mathrm{i}+1}) = \frac{1}{N} \sum_{\mathrm{j}=1}^{\mathrm{N}} \delta \left[E' - \rho\, E_{\mathrm{i,j}} - (1-\rho)\, E_{\mathrm{i}+1,\mathrm{j}} \right], \tag{2.70}$$

where E_i and $E_{\mathrm{i}+1}$ are adjacent elements on the initial energy grid, $E_{\mathrm{i,j}}$ is the j^{th} discrete end energy for the corresponding starting energy E_i, N is the number of equiprobable end energies and

$$\rho = \frac{E_{\mathrm{i}+1} - E}{E_{\mathrm{i}+1} - E_\mathrm{i}} \tag{2.71}$$

is a selected starting energy in the interval $E_\mathrm{i} < E < E_{\mathrm{i}+1}$. Then a set of ν associated scattering angles $\mu = \cos\theta$ can be assigned to each transition and with a probability of $1/\nu$ an angle $\mu_{\mathrm{i,j,k}}$ is selected and the final scattering angle μ can be calculated:

$$\mu = \rho\, \mu_{\mathrm{i,j,k}} + (1-\rho) \mu_{\mathrm{i}+1,\mathrm{j,k}}. \tag{2.72}$$

The method described above is applied in the case of an incoherent approximation. Otherwise, for the case of a coherent derivation, a set of parameters D_k that is based on Bragg energies E_k is used. These Bragg energies are typically derived from lattice parameters, and the scattering angle μ is given by

$$\mu = 1 - 2\,\frac{E_\mathrm{k}}{E}, \tag{2.73}$$

whereas $E_\mathrm{k} < E < E_{\mathrm{k}+1}$ and $D_\mathrm{i}/D_\mathrm{k}$ is the probability of scattering from the i^{th} Bragg edge. The elastic scattering treatment is applied with a probability of $\sigma_\mathrm{n}/(\sigma_\mathrm{n} + \sigma_{\mathrm{n}'})$.

2.2.3.2 Absorption

A MC Code can deal with absorption in two ways: analogue or implicit. For the analogue case, in every interaction the particle is just killed with a probability of $\sigma_\mathrm{a}/\sigma_\mathrm{t}$ and the particle tracking is stopped. In the implicit case the tracking continues, but the particle weight is lowered to

$$W_{\mathrm{n}'} = \left(1 - \frac{\sigma_\mathrm{a}}{\sigma_\mathrm{t}}\right) W_\mathrm{n}. \tag{2.74}$$

If the new calculated weight $W_{\mathrm{n}'}$ falls below the lower weight limit (see Chapter 2.2.1, Variance Reduction), Russian Roulette is played, resulting altogether in fewer particles with larger weight. The implicit absorption can also be applied along a flight path. For a detailed explanation one may refer to [94]. This is then done continuously along the flight path of a particle and so the scatter distance l' rather than the interaction distance is sampled (see Eq. 2.59):

$$l' = -\frac{1}{\Sigma_\mathrm{s}} \ln(1-\kappa), \tag{2.75}$$

where κ is again a uniformly distributed random number in the range from 0 to 1. Because of the expected absorption along the flight path, the particle weight at the scattering point has to be reduced to

$$W' = W\, e^{-\Sigma_a\, l'}. \tag{2.76}$$

2.2.3.3 Unresolved Resonances

The continuous cross sections are smooth functions of energy in certain regions, whereas resonances are fine, sharp, dense, and are especially for higher energies often not resolved during the measurement of the cross sections. Furthermore, the smoothly-varying cross sections may hide resonance self-shielding effects. So in these regions of unresolved resonances, i.e. in the energy range $10\,\text{keV} < E < 149.03\,\text{keV}$ for ^{238}U (the energy interval depends on the isotope), probability tables are employed. This technique produces tables of the cross sections for a given number of energies, and then a chosen value is applied to the reaction of the tracked neutron. In [54] the general impact of this method is discussed, and in most cases the impact is negligibly small.
In anticipation of Chapter 6.3, Serpent 2 allows a detailed study of the impact of the unresolved resonances. This internal treatment must be explicitly turned on by the user. A detailed model of FRM II has been set up and the effective multiplication factor has been calculated with and without the internal treatment of unresolved resonances. It turned out that effective multiplication factors from both calculations, agree within one standard deviation. However, to make the results presented in this thesis as most accurate as possible, the unresolved resonances were need to be taken into account for further calculations.

2.2.3.4 Temperature Adjustments

Tabluated cross sections are usually measured at one specific temperature. Techniques exist for an on-the-fly temperature adjustment of these cross sections. The goal of all such techniques is the adaption of the effective cross section during the MC calculation. Based on [90] only a short overview over the available methods will be given here. The interested reader is refered to [90].

Interpolation between data for different temperatures:

The most straightforward way to deal with the temperature dependency of the cross sections, is the interpolation between existing cross section data for different temperatures. The accuracy of this method highly depends on the interpolation scheme and the spacing of available temperatures. Principally, there are two possibilities to interpolate the data: The so called stochastic mixing/pseudo material approach and the direct interpolation.

In the pseudo material approach there is no real interpolation carried out, rather the cross section at the new temperature is calculated by defining the material composition as mixture of nuclides at different temperatures, for which the cross section data is available.

Using the direct interpolation for the supposed supporting points $\sigma(E,T_1)$ and $\sigma(E,T_2)$, different methods can be used to calculate the effective cross section for a temperature T' ($T_1 \leq T' \leq T_2$). The "log-log" method, as shown in Equation (2.77), turned out to be the best fitting approach [87]:

$$\ln(\sigma(E,T')) = \ln(\sigma(E,T_1)) + \Big[\ln\Big(\sigma(E,T_2)\Big) - \ln\Big(\sigma(E,T_1)\Big)\Big]\,\frac{\ln(T') - \ln(T_1)}{\ln(T_2) - \ln(T_1)}. \tag{2.77}$$

The accuracy of this linear interpolation scheme highly depends on the temperature intervals between the two supporting points involved. Even with small intervals of 28 K the challenging case of ^{238}U can barely be covered within a 0.1 % accuracy [90]. In any case, the computer memory consumption is rather tremendous. Method employed in [10] due toe lack of better options in MCNPX.

Direct Doppler-broadening with Solbrig's kernel:

A method, which only requires the cross section data for one temperature, is the on-the-fly Doppler-broadening with Solbrig's kernel [84], which can be expressed in terms of the neutron velocity:

$$\sigma(v,T') = \frac{\gamma}{v^2\sqrt{\pi}} \int_0^\infty v'^2\,\sigma(v')\left(e^{-\gamma^2\,(v-v')^2} - e^{-\gamma^2\,(v+v')^2}\right) dv', \tag{2.78}$$

where

$$\gamma(T,A) = \sqrt{\frac{A\,M}{2\,k_\mathrm{B}\,T}} \tag{2.79}$$

is a function of the mass number A, the molare mass M and the temperature T. In [18] and [95] this method is studied in detail and is used as reference solution. However, even with the high accuracy and less supporting points needed, this method leads to a substantially slow down of the calculations and is, therefore, not often being used.

Target Motion Sampling (TMS) temperature treatment technique:

Target Motion Sampling (TMS) is a stochastic on-the-fly temperature treatment method, which samples the thermal motion of target nuclides at each collision site. The reaction probability is calculated by using cross sections at a temperature below that of the material [90]. This method is exclusively implemented in Serpent 2 and, therefore, the discussion here is based on facts specific to Serpent 2. Most effort on this method was put in the dissertation of Viitanen [90]. Actually, this method does not provide Doppler broadend cross sections. Moreover, the path lengths are sampled based on the variation of the total cross section, which is caused by the thermal motion. With a Maxwell distribution, which would also be used in the free gas theory, the influence of the thermal motion can be modeled very detailed. Additionally, this method is less memory consuming compared to the other methods already described before. As a unique feature, TMS is capable of modeling geometry regions with inhomogeneous temperature profiles [90]. TMS is the method which will be used to generate the interpolated cross sections for transient calculations in Section 4.2.1.

CHAPTER 3

Thermo-Hydraulics

3.1 Basic Considerations

The models used in this thesis for transient calculations will be compared with results obtained by classical calculation schemes which are based upon the numerical solution of the Navier Stokes Equations (see Chapter 5.1). Classical schemes are used, for example, by the program NBK, developed by Anton Röhrmoser and discussed in detail in [19, 70]. In this method dimensionless numbers derived from similitude theory are used in combination with a variety of correlations. A short overview of these relations and quantities will be given in the following section.

3.1.1 Calculation of basic Quantities and Ratios

Hydraulic Diameter:

The hydraulic diameter, d_{h}, is a geometrical parameter of a pipe with a non-circular cross section and is equivalent to an effective length representing the cross section of the wetted pipe. The hydraulic diameter relations, developed for circular-shaped pipes can even be applied to complex-shaped pipes. The hydraulic diameter is defined as follows,

$$d_{\mathrm{h}} = 4\,\frac{A}{U}, \tag{3.1}$$

whereas A is the traversed area and U is the wetted perimeter of the cross section. For a circular-shaped and non-wetted pipe the hydraulic diameter is simply the geometrical diameter of the pipe. With the arc length of the fuel plate of 69.4 mm, a channel width of 2.2 mm and a passed through are per cooling channel of 131.7 mm^2, for FRM's compact core a hydraulic diameter of 4.26 mm is calculated and is used in the later described ATHLET model (see Chapter 7).

Reynolds Number:

The ratio of the inertial force to the viscous force is called the Reynolds number, Re. It is a dimensionless number which gives an information of the flow behavior. The Reynolds number is generally considered the most important dimensionless parameter in the field of fluid mechanics. For low Reynolds numbers the flow tends to be dominated by a laminar flow. For a steady laminar flow, the velocity at a point remains constant with time, while

in a turbulent flow the velocity trace indicates random fluctuations of the instantaneous velocity time mean velocity.

Moreover, the turbulent behavior of geometrically related bodies is identical for equal Reynolds numbers. With increasing Reynolds number, the flow becomes turbulent and is dominated by inertial forces, which tend to produce a chaotic flow pattern with vortices and flow instabilities. The equation of the Reynolds number is given by

$$\mathrm{Re} = \frac{v\, d_\mathrm{h}}{\nu}, \tag{3.2}$$

whereas v is the velocity of the fluid, d_h is the characteristic parameter of the pipe, here the hydraulic diameter, and ν is the kinematic viscosity of the fluid. The viscosity ν highly depends on the temperature of the fluid. With the hydraulic diameter d_h as calculated above and an average velocity of 15.91 $\mathrm{m/s}$ of the cooling fluid, a Reynolds number of roughly 10^5 can be calculated for FRM II. This defines a turbulent flow, because the calculated value is well above the critical value $\mathrm{Re_c} \approx 2300$, which defines the transition from a laminar to a turbulent flow in a technical pipe [10].

Prandtl Number:

The Prandtl number, Pr, is defined as the ratio of the kinematic viscosity, ν, to the thermal diffusivity, α:

$$\mathrm{Pr} = \frac{\nu}{\alpha}. \tag{3.3}$$

This dimensionless ratio, which is primarily a function of temperature, indicates the relative ease of momentum and energy transport in flow systems. The Prandtl number can also be interpreted as the ratio between convective and conductive heat transfer. For FRM II, a Prandtl number of $\mathrm{Pr} \approx 4.56$ results for the current operating conditions at a temperature of 37 °C.

Nusselt Number:

The Nusselt number, Nu, is a dimensionless parameter coming from the heat conduction similitude theory and describes the convective heat transfer between a solid surface and a streaming liquid. The Nusselt number is defined as the intensity ratio of the actual convective heat transfer to a theoretical pure thermal conduction through a static fluid layer with thickness d. It is, therefore, defined as:

$$\mathrm{Nu} = \frac{h\, d}{\kappa}, \tag{3.4}$$

whereas h is the convective heat transfer coefficient and κ is the thermal conductivity of the fluid. Unlike the thermal conductivity κ, the heat transfer coefficient h is not an intrinsic property of the fluid, but rather depends strongly on the circumstances in which the convective heat transfer occurs, e.g. on the properties of the fluid, the geometry and the flow regime. The flow conditions, and here especially the thickness of the viscous and thermal boundary layers as well as the turbulent flow conditions determine the effectiveness of the convective heat transfer. As a result, by the formation of a non-linear temperature profile the temperature gradient in the boundary layers steepens to make the heat transfer coefficient significantly larger than the thermal conductivity.

In [28] Gnielinski presented the relation between the Nusselt, Prandtl and Reynolds number for turbulent flows in rectangular channels, viz.

$$\mathrm{Nu}_0 = \frac{\frac{\xi}{8}\,(\mathrm{Re} - 1000)\,\mathrm{Pr}}{1 + 12.7\sqrt{\frac{\xi}{8}}\left(\mathrm{Pr}^{2/3} - 1\right)}\,K_{\mathrm{Pr}}. \tag{3.5}$$

Here, the symbol ξ denotes the friction factor for sleek tubes calculated from the relationship

$$\xi = (1.82\,\log \mathrm{Re} - 1.64)^{-2}, \tag{3.6}$$

and

$$K_{\mathrm{Pr}} = \left(\frac{\mathrm{Pr_F}}{\mathrm{Pr_S}}\right)^{0.11} \tag{3.7}$$

is a correction factor for the temperature profile near the surface with $\mathrm{Pr_F}$ and $\mathrm{Pr_S}$ being the Prandtl number of the liquid at the mean (bulk) temperature T_{F} and the surface temperature T_{S}, respectively. Equation (3.5) is valid over a range of $10^4 < \mathrm{Re} < 5 \cdot 10^6$ and $0.5 < \mathrm{Pr} < 2000$. However, the Nusselt number Nu_0 calculated from Equation (3.5) has to be corrected for the friction at the pipe walls to get the Nusselt number Nu. This can be achieved by applying the empirical relation

$$\mathrm{Nu} = \mathrm{Nu}_0\, f_{\mathrm{k}} \left(\frac{\zeta_{\mathrm{r}}}{\zeta_{\mathrm{g}}}\right)^{0.68\cdot\mathrm{Pr}^{0.215}}. \tag{3.8}$$

Here, f_{k} is a correction factor for the shape of the tube, and ζ_{g} and ζ_{r} are the frictions for a sleek and a rough-textured tube, respectively. The friction for a sleek tube, ζ_{g}, can be calculated in a two-step procedure. First, the friction $\zeta_{\mathrm{g,0}}$ is calculated from

$$\frac{1}{\sqrt{\zeta_{\mathrm{g,0}}}} = 2\,\log \frac{\mathrm{Re}^*\sqrt{\zeta_{\mathrm{g,0}}}}{2.51} \tag{3.9}$$

[91], where Re^* is the modified Reynolds number defined as

$$\mathrm{Re}^* = \frac{v_{\mathrm{avg}}\,D}{\nu}, \tag{3.10}$$

where v_{avg} is the average velocity over the cross section in the tube, D is the diameter of the tube, and ν is the kinematic viscosity. The friction $\zeta_{\mathrm{g,0}}$ is given implicitly by Equation (3.9). This equation does not take into account both the wall heating and the temperature dependence of the viscosity. More corrections have to be applied to get

$$\zeta_{\mathrm{g}} = \frac{1}{6}\,\zeta_{\mathrm{g,0}}\left(7 - \frac{\mu_{\mathrm{F}}}{\mu_{\mathrm{W}}}\right), \tag{3.11}$$

in the second step [61]. Here, μ_{F} and μ_{W} are the dynamic viscosities of the fluid at the mean temperature, T_{F}, and at the temperature of the tube wall, T_{W}, respectively. The dynamic viscosity is the product of the kinematic viscosity ν and the density ρ of the fluid, i.e. $\mu = \nu\rho$.

The friction for a rough-textured tube, ζ_r, is also calculated in a two-step procedure. First, the friction $\zeta_{\mathrm{r},0}$ is calculated from a formula given by Colebrook and White[1], viz.

$$\frac{1}{\sqrt{\zeta_{\mathrm{r},0}}} = -2\,\log\left(\frac{\epsilon}{3.71} + \frac{2.51}{\mathrm{Re}\,\sqrt{\zeta_{\mathrm{r},0}}}\right). \tag{3.12}$$

Here, ϵ is the relative roughness which is given by

$$\epsilon = \frac{\vartheta}{d_\mathrm{h}}, \tag{3.13}$$

where ϑ is the absolute roughness and d_h is the hydraulic diameter of the pipe. For new, smooth, pultruded metal tubes an absolute roughness of 0.0013 to 0.0015 can be assumed. Comparable seamless steel tubes have an absolute roughness of 0.02 to 0.16. The friction $\zeta_{\mathrm{r},0}$ resulting from Equation (3.12) does not take into account the heating of the pipe walls. Therefore, in the second step the friction ζ_r is calculated from

$$\zeta_\mathrm{r} = \zeta_{\mathrm{r},0}\left(\frac{\mu_\mathrm{F}}{\mu_\mathrm{W}}\right)^{0.182+800/(\mathrm{Re}+18000)} \tag{3.14}$$

[36], with μ_F and μ_W being given above in the context of Equation (3.11).

3.2 Fluid Mechanics

In the following section, a general introduction to the basics of fluid mechanics will be given. The fundamental equations of fluid mechanics are the *Navier Stokes Equations*, corresponding to the conservation of momentum, the *Mass Equation*, corresponding to conservation of mass and the *Energy Equation* which describes the conservation of energy.

3.2.1 Navier Stokes Equations

The following derivation of the *Navier Stokes Equations* is based upon [44]. Starting from *Euler's Equation*,

$$\frac{\partial \mathbf{v}}{\partial t} + (\mathbf{v}\cdot\boldsymbol{\nabla})\,\mathbf{v} = -\frac{1}{\rho}\,\boldsymbol{\nabla}\,p, \tag{3.15}$$

where $\mathbf{v}$ is the velocity, ρ the density, p the pressure, and $\boldsymbol{\nabla}$ the Nabla operator, the equations describing the motion of a viscous fluid can be derived. Equation (3.15) is one of the fundamental equations of hydrodynamics, and has been first obtained by the mathematician L. Euler in 1755. By introducing the momentum flux density tensor Π_ik, the ith component of which is the amount

[1] In [30] another formula had been used, viz.

$$\zeta_{\mathrm{r},0} = 0.0055\left(1 + \sqrt[3]{20000\,\epsilon + \frac{10^6}{\mathrm{Re}}}\right).$$

For FRM II working conditions, the deviation between this equation and Eq. (3.12) is about 1.5 %.

of the ith component of the momentum flowing in unit time through unit area perpendicular to the x_k-axis, Equation (3.15) can be rewritten as:

$$\frac{\partial}{\partial t}\left(\rho\, v_\mathrm{i}\right) = -\frac{\partial \Pi_\mathrm{ik}}{\partial x_\mathrm{k}}. \tag{3.16}$$

It is to be noted that Π_ik only represents a completely reversible transfer of momentum simply due to mechanical particle transport and to the pressure forces acting in the fluid, because processes of energy dissipation are not taken into account. In a viscous fluid, there is also an irreversible transfer of momentum caused by internal friction. In this case, the viscous stress tensor σ'_ik has to be included in the description of the momentum flux. As a result, the momentum flux density tensor has to be written as:

$$\Pi_\mathrm{ik} = p\,\delta_\mathrm{ik} + \rho\, v_\mathrm{i}\, v_\mathrm{k} - \sigma'_\mathrm{ik} = -\sigma_\mathrm{ik} + \rho\, v_\mathrm{i}\, v_\mathrm{k}, \tag{3.17}$$

with

$$\sigma_\mathrm{ik} = -p\,\delta_\mathrm{ik} + \sigma'_\mathrm{ik} \tag{3.18}$$

being the so-called stress tensor. The general form of the viscous stress tensor σ'_ik can be derived on the following considerations:

- Processes caused by internal friction only occur when different fluid parts move with different velocities. There is a relative motion between these various parts of the fluid. Hence, σ'_ik depends on the spatial derivatives of the velocity. If the velocity gradients are small, the momentum transfer only depends on the first derivatives of the velocity. So, σ'_ik may be supposed to be a linear function of the derivatives $\partial v_\mathrm{i}/\partial x_\mathrm{k}$. Every term in σ'_ik must depend on $\partial v_\mathrm{i}/\partial x_\mathrm{k}$ because σ'_ik has to vanish for $\mathbf{v} = \text{const}$.
- The viscous stress tensor must also vanish for uniformly rotating liquids, since it is clear that in such a motion no internal friction does occur in the fluid. With angular speed $\mathbf{\Omega}$, the resulting velocity is equal to $\mathbf{\Omega} \times \mathbf{r}$. This means that sums like

  $$\frac{\partial v_\mathrm{i}}{\partial x_\mathrm{k}} + \frac{\partial v_\mathrm{k}}{\partial x_\mathrm{i}}$$

  are linear combinations of the derivatives $\partial v_\mathrm{i}/\partial x_\mathrm{k}$ and therefore vanish when $\mathbf{v} = \mathbf{\Omega} \times \mathbf{r}$. Hence, σ'_ik must contain just these symmetrical combinations of those derivatives.

The most general tensor satisfying the above mentioned conditions, can be written as:

$$\sigma'_\mathrm{ik} = \eta\left(\frac{\partial v_\mathrm{i}}{\partial x_\mathrm{k}} + \frac{\partial v_\mathrm{k}}{\partial x_\mathrm{i}} - \frac{2}{3}\,\delta_\mathrm{ik}\,\frac{\partial v_\mathrm{l}}{\partial x_\mathrm{l}}\right) + \zeta\,\delta_\mathrm{ik}\,\frac{\partial v_\mathrm{l}}{\partial x_\mathrm{l}}. \tag{3.19}$$

Here, the coefficients η and ζ are called the coefficients of viscosity, and ζ often is called the second viscosity. Both parameters are independent of the velocity and are positive throughout. Now, the equations of motion of a viscous fluid can be obtained by simply adding the expressions $\partial\sigma'_\mathrm{ik}/\partial x_\mathrm{k}$ to the right-hand side of Euler's equation (3.16) [44]. This results in

$$\rho\left(\frac{\partial v_\mathrm{i}}{\partial t} + v_\mathrm{k}\,\frac{\partial v_\mathrm{i}}{\partial x_\mathrm{k}}\right) = -\frac{\partial p}{\partial x_\mathrm{i}} + \frac{\partial}{\partial x_\mathrm{k}}\left[\eta\left(\frac{\partial v_\mathrm{i}}{\partial x_\mathrm{k}} + \frac{\partial v_\mathrm{k}}{\partial x_\mathrm{i}} - \frac{2}{3}\,\delta_\mathrm{ik}\,\frac{\partial v_\mathrm{l}}{\partial x_\mathrm{l}}\right)\right] + \frac{\partial}{\partial x_\mathrm{k}}\left(\zeta\,\frac{\partial v_\mathrm{l}}{\partial x_\mathrm{l}}\right). \tag{3.20}$$

Equation (3.20) is the most general form of the equation of motion of viscous fluids. In general, both η and ζ depend on the pressure p and the temperature T. However, in the vast majority of cases the viscosity coefficients do not change noticeably in the fluid and, therefore, can be assumed as constant. Then, Equation (3.20) is in vector form:

$$\rho \left[\frac{\partial \mathbf{v}}{\partial t} + (\mathbf{v} \cdot \boldsymbol{\nabla}) \, \mathbf{v} \right] = -\boldsymbol{\nabla} \, p + \eta \, \Delta \, \mathbf{v} + \left(\zeta + \frac{1}{3} \, \eta \right) \, \boldsymbol{\nabla} \, (\operatorname{div} \mathbf{v}), \tag{3.21}$$

where Δ denotes the Laplace operator. Equation (3.21) is commonly known as the *Navier Stokes Equation*. If an incompressible fluid is assumed, $\operatorname{div} \mathbf{v} = 0$ and Equation (3.21) can be simplified to read

$$\frac{\partial \mathbf{v}}{\partial t} + (\mathbf{v} \cdot \boldsymbol{\nabla}) \, \mathbf{v} = -\frac{1}{\rho} \, \boldsymbol{\nabla} \, p + \frac{\eta}{\rho} \, \Delta \, \mathbf{v}. \tag{3.22}$$

3.2.2 Mass Equation

In order to derive the mass equation, the mass conservation in a (finite) volume V is considered. The surface of this volume is denoted as S with the outward pointing normal unit vector at each location on the surface denoted as $\mathbf{n}$, and the differential surface element denoted as dS. If mass is conserved in V, the variation of the mass in the volume must be entirely due to the in- or outflow of mass through V:

$$\frac{\partial}{\partial t} \int_V \rho \, \mathrm{dV} = - \int \rho \, \mathbf{v} \cdot \, \mathbf{n} \, \mathrm{dS}, \tag{3.23}$$

whereas $\mathbf{v}$ is the flow velocity, and ρ is the density of the fluid. Using the Gauß divergence theorem, this can be recasted to read

$$\int_V \left[\frac{\partial \rho}{\partial t} + \boldsymbol{\nabla} \cdot (\rho \, \mathbf{v}) \right] \mathrm{dV} = 0. \tag{3.24}$$

Since this equation must hold for any chosen volume V, the integrand must vanish, i.e.

$$\frac{\partial \rho}{\partial t} + \boldsymbol{\nabla} \cdot (\rho \, \mathbf{v}) = 0. \tag{3.25}$$

This is the differential equation for conservation of mass.

3.2.3 Energy Equation

In order to derive the energy conservation equation, a volume V is considered that is fixed in space and through which a fluid is flowing. The energy $\rho \, E \, \mathrm{dV}$ inside a volume element dV in V is given by the sum of the internal energy $\rho \, e \, \mathrm{dV}$ and the kinetic energy $(\rho \, |\mathbf{v}|^2 / 2) \, \mathrm{dV}$ of the fluid, i.e.

$$\rho \, E \, \mathrm{dV} = \rho \, e \, \mathrm{dV} + \frac{1}{2} \, \rho \, |\mathbf{v}|^2 \, \mathrm{dV}. \tag{3.26}$$

Here, ρ is the density, E the energy per unit mass, e the internal energy per unit mass, and $\mathbf{v}$ the flow velocity of the fluid. With Equation (3.26), the overall energy E_{tot} inside the volume V is given by

$$E_{\text{tot}} = \int_V \rho\, E \,\mathrm{dV}. \tag{3.27}$$

Because both kinetic energy and internal energy may be entering the volume V by convective transport, E_{tot} is a function of time. Using Reynolds transport theorem [91], the change of E_{tot} with time can be expressed as

$$\frac{\mathrm{d}}{\mathrm{dt}} \int_V \rho\, E \,\mathrm{dV} = \int_V \frac{\partial(\rho\, E)}{\partial t} \,\mathrm{dV} + \int_S \rho\, E\, \mathbf{v} \cdot \mathbf{n} \,\mathrm{dS}, \tag{3.28}$$

where $\mathbf{n}$ is the outward pointing normal unit vector at each surface element dS of the surface S bounding volume V.
The energy E_{tot} within volume V may also change with time by heat entering and leaving V by heat conduction, and by a heat source inside V. Describing heat conduction by Fourier's law, which states that the heat flux by conduction is proportional to the temperature gradient [7], the overall change of heat with time, $\dot{\mathrm{Q}}$, within volume V is given by

$$\dot{Q} = \int_V \rho\, q \,\mathrm{dV} - \int_S \kappa\, \mathbf{n} \cdot \boldsymbol{\nabla}\, T \,\mathrm{dS}, \tag{3.29}$$

where q is the strength of the heating source measured in power per unit mass, κ is the thermal conductivity, and T is temperature.
Finally, work may also be done on the fluid inside volume V by the stresses as well as by virtue of external forces, such as gravity. This work done per unit time, $\dot{\mathrm{W}}$, is given by

$$\dot{W} = \int_V \rho\, \mathbf{g} \cdot \mathbf{v} \,\mathrm{dV} + \int_S \mathbf{v} \cdot (\boldsymbol{\sigma} \cdot \mathbf{n}) \,\mathrm{dS}, \tag{3.30}$$

where $\mathbf{g}$ is the vector of gravitational acceleration, and $\boldsymbol{\sigma} = (\sigma_{\mathrm{ik}})$ is the stress tensor, as defined in Equation (3.18), which includes both pressure forces and viscous forces.
According to the first law of thermodynamics the rate of change of the total energy E_{tot} must equal the sum of rate of energy addition by heat transfer, $\dot{\mathrm{Q}}$, and by work transfer, $\dot{\mathrm{W}}$. With Equation (3.28) this results in

$$\int_V \frac{\partial(\rho\, E)}{\partial t} \,\mathrm{dV} + \int_S \rho\, E\, \mathbf{v} \cdot \mathbf{n} \,\mathrm{dS} = \dot{Q} + \dot{W}. \tag{3.31}$$

Inserting Equations (3.29) and (3.30) into Equation (3.31), and applying the Gauß divergence theorem leads to

$$\int_V \left[\frac{\partial(\rho\, E)}{\partial t} + \boldsymbol{\nabla} \cdot (\rho\, E\, \mathbf{v}) - \rho\, q + \boldsymbol{\nabla} \cdot (\kappa\, \boldsymbol{\nabla}\, T) - \rho\, \mathbf{g} \cdot \mathbf{v} - \boldsymbol{\nabla} \cdot (\boldsymbol{\sigma} \cdot \mathbf{v}) \right] \mathrm{dV} = 0. \tag{3.32}$$

Because this equation must hold for any chosen volume V, the integrand must vanish, i.e.

$$\frac{\partial(\rho\, E)}{\partial t} + \boldsymbol{\nabla} \cdot (\rho\, E\, \mathbf{v}) - \rho\, q + \boldsymbol{\nabla} \cdot (\kappa\, \boldsymbol{\nabla}\, T) - \rho\, \mathbf{g} \cdot \mathbf{v} - \boldsymbol{\nabla} \cdot (\boldsymbol{\sigma} \cdot \mathbf{v}) = 0. \tag{3.33}$$

This is the equation of energy conservation.

3.3 Heat Conduction in Solids

Heat transfer by conduction is the flow of thermal energy within solids and non-flowing fluids, driven by temperature differences. According to the second law of thermodynamics, energy is transferred from high-temperature regions to low-temperature regions due to a thermal diffusion process. Mathematically, this is described by the diffusion equation:

$$\frac{\partial T}{\partial t} = \boldsymbol{\nabla} \left(\alpha \, \boldsymbol{\nabla} T \right) + S. \tag{3.34}$$

Here, T is temperature, S is a general source term, and α is the thermal diffusivity,

$$\alpha = \frac{\kappa}{c_\mathrm{p} \, \rho}, \tag{3.35}$$

where κ is the thermal conductivity, c_p is the specific heat capacity, and ρ is the density. The source term S can be treated as a general temperature source,

$$S = \frac{Q}{c_\mathrm{p} \, \rho}, \tag{3.36}$$

where Q is the strength of the heat source measured in power per unit volume.
Physically, Equation (3.34) expresses the conservation of heat per unit volume over an infinitesimally small volume lying in the interior of the flow domain. In the stationary case, i.e. $\partial T / \partial t = 0$, and for $\alpha = \text{const}$. Equation (3.34) takes the form of a Poisson equation, viz.

$$\Delta T = -\frac{Q}{\kappa}. \tag{3.37}$$

Part II

Explanation of Codes used

CHAPTER 4

Neutronics Codes used

4.1 MCNP6

MCNP6 is a general-purpose Monte Carlo N-Particle (MCNP) code that has been developed at Los Alamos National Laboratory (LANL), with version one being released in 1977. It goes straight back to the original Monte Carlo work performed by John von Neumann and others at LANL [14]. As a MC code, MCNP6 uses the methods and terms described in Chapter 2.2. Through continuous development the current version six is capable of calculating MC transport for neutrons, photons and electrons for nearly any shaped geometry. By using pointwise cross section libraries like Evaluated Nuclear Data File (ENDF/B), every reaction available in a particular cross section library can be tallied (see Section 2.2.1). MCNP6 is very well validated and has found wide-spread application. There is a lot of literature about MCNP6, in particular about its validation, and the reader may refer to [13, 29, 94].
For FRM II there are very well-established full-core MCNP6 models, mainly developed by Dr. Anton Röhrmoser and extensively used in [10]. Also, MCNP6 is readily available, has a huge user community, and is constantly improved and updated. This gives a solid basis for all further developments in this thesis and provides a reference against which all models developed here have to be validated.

4.2 Serpent 2

As MCNP6, Serpent 2 is also a MC reactor code. The first version of Serpent has been written as part of the doctoral thesis of Leppänen [49]. Starting from there, Serpent 1 and finally Serpent 2 have been developed at VTT. Serpent 2 is a multi-purpose three-dimensional continuous-energy MC particle transport code which is still further developed at VTT. Because of the more modern methods implemented, the powerful capability to generate multi-group cross sections for the whole full-core model, the active user community, and the easy access to the developer, Serpent 2 was chosen as tool to provide the needed cross section data for further deterministic transient calculations.
As a rather "young" code, the description of the required input desk is much more flexible than is the case for MCNP6. Also, Serpent 2 provides more comfortable easements. The basic geometry description in Serpent 2 is similar to other MC codes and, therefore, allows nearly any two- or three-dimensional fuel or reactor configuration. As already described in Chapter 2.2.1, a geometry modeled with Serpent 2 consists of homogeneous material cells defined by surfaces.

Contrary to MCNP6, the particle transport in Serpent 2 not only relies on classical surface-tracking, but also uses the so-called *Woodcock delta-tracking* method [93]. This approach has proven efficient for all geometries for which the neutron mean-free-path is large compared to the assembly dimensions. The traditional delta-tracking method is subject to certain efficiency problems related to localized heavy absorbers, which in Serpent 2 are avoided by switching to surface-tracking when necessary [50].
As MCNP6, Serpent 2 also provides a well proven burnup calculation capability, which is entirely based on built-in calculation routines. Increasing progress has been achieved in coupled multi-physics simulations and variance reduction techniques. As a result, today Serpent 2 can be internally coupled to built-in solvers for fuel behavior and thermal hydraulics, and externally via the universal multi-physics interface [89]. For validation purposes each Serpent 2 update is checked by comparison to results obtained from MCNP6 by running a standard set of assembly calculations problems. Even though Serpent 2 has a growing user base and new features are constantly added, the documentation is not as detailed as it is for MCNP6.

4.2.1 Calculation of multi-group cross sections with Serpent 2

One of the main purposes of the development of Serpent 2 was the idea to comfortably generate multi-group cross sections. Hence, the Serpent 2 input desk and also the output is highly optimized for that purpose. Even though MCNP6 also has such capabilities Serpent 2 performs better and more comfortable in generating multi-group cross sections. The capability to calculate multi-group cross sections was already implemented in the very first version of Serpent 1, as developed in [49]. During the generation of the homogenized group constants, the integral reaction rate balance has to be preserved. With that assumption the homogenized cross section for group g and reaction i (absorption, fission, etc...), $\Sigma_{\mathrm{i,g}}$ is given by

$$\Sigma_{\mathrm{i,g}} = \frac{\int_{\mathrm{V}} \int_{\mathrm{E_g}}^{\mathrm{E_{g-1}}} \Sigma_{\mathrm{i}}(\mathbf{r},E)\, \Phi(\mathbf{r},E)\, \mathrm{d}V \mathrm{d}E}{\int_{\mathrm{V}} \int_{\mathrm{E_g}}^{\mathrm{E_{g-1}}} \Phi(\mathbf{r},E)\, \mathrm{d}V \mathrm{d}E}, \tag{4.1}$$

whereas V is the volume of the mesh/lattice cell, E is the energy, E_{g} is the energy threshold of energy group g, $\Sigma_{\mathrm{i}}(\mathbf{r},E)$ is the local cross section related to interaction i, and $\Phi(\mathbf{r},E)$ is the corresponding neutron flux. Equations similar to Equation (4.1) can also be written for the homogenization of other interaction parameters [49]. Both methods, the standard and Cumulative Migration Method (CMM), how Serpent 2 calculates the diffusion coefficients are described in [51] and [53], respectively.
In contrast to cross sections of reactions which are listed in databases, as all multi-group cross sections, the calculation of group-transfer cross sections, $\Sigma_{\mathrm{s,g'\to g}}$, highly depends on the predefined group structure. Hence, a group-transfer probability $P_{\mathrm{g'\to g}}$ is calculated first, viz.

$$P_{\mathrm{g'\to g}} = \frac{\int_{\mathrm{V}} \int_{\mathrm{E_g}}^{\mathrm{E_{g-1}}} \int_{\mathrm{E_{g'}}}^{\mathrm{E_{g'-1}}} \Sigma_{\mathrm{s}}(\mathbf{r},E' \to E)\, \Phi(\mathbf{r},E')\, \mathrm{d}V \mathrm{d}E \mathrm{d}E'}{\int_{\mathrm{V}} \int_{\mathrm{E_{g'}}}^{\mathrm{E_{g'-1}}} \Sigma_{\mathrm{s}}(\mathbf{r},E')\, \Phi(\mathbf{r},E')\, \mathrm{d}V \mathrm{d}E'}, \tag{4.2}$$

where $\Sigma_s(\mathbf{r},E' \rightarrow E)$ is the group transfer cross section. This can be easily done by a MC code by simply counting the neutrons being scattered from group g' to g. Then, together with Equation (4.2) and the corresponding total scattering cross sections $\Sigma_{s,g'}$ for the energy group g', the group-transfer cross section $\Sigma_{s,g'\rightarrow g}$ can be calculated by using:

$$\Sigma_{s,g'\rightarrow g} = P_{g'\rightarrow g}\,\Sigma_{s,g'}. \tag{4.3}$$

In order to get reliable results for the transient calculations, cross sections for the whole anticipated temperature range of fuel, moderator, coolant and structural materials have to be provided. The method used in Serpent 2 has already been described in Chapter 2.2.3.4. In this thesis transient scenarios are only simulated until the reactor safety system safely shuts down the reactor, so the temperature range which has to be covered is limited. With CFX the temperature of the cladding T_c and both fuel zones (T_{f1} for the high uranium density zone, T_{f2} for the high uranium density zone) in respect to the cooling water temperature T_w have been determined at nominal power.

$$T_c = T_w + 17.0\,^\circ\mathrm{C} \tag{4.4}$$
$$T_{f1} = T_w + 23.1\,^\circ\mathrm{C} \tag{4.5}$$
$$T_{f2} = T_w + 19.2\,^\circ\mathrm{C} \tag{4.6}$$

These temperature differences are assumed to be constant over the whole relevant temperature range. Then, cross sections can be calculated starting from room temperature to 110 °C in 10 °C steps. Because steady-state calculations provide only a rough estimation of the thermal-hydraulical conditions during reactivity transients, a detailed study on this will have to be done in a future work.
The cross sections as calculated with Serpent 2 are then parametrized and tabulated in cross section libraries readable for TORT-TD, using the self-developed post processing tool C^2 (see Appendix D). Serpent 2 also provides grouped data for diffusion constants, the prompt fission spectrum, inverse neutron velocity, delayed neutron fraction and delayed neutron decay constant.

4.3 TORT-TD

TORT-TD is a time-dependent three dimensional multi-group discrete ordinates neutron transport code developed at the Gesellschaft für Anlagen- und Reaktorsicherheit gGmbH (GRS) [78]. It is based on the DOORS steady-state neutron transport code TORT [66] developed at the ORNL which solves the steady-state and time-dependent multi-group transport equation with an arbitrary number of prompt and delayed neutron precursor groups in both Cartesian and cylindrical (r-ϑ-z) geometry. Very detailed information about TORT is given in [67].
TORT-TD calculates the flux or fluency through a two- or three-dimensional geometry by solving the Boltzmann transport equation for neutrons (see Eq. 2.15). Thereby, TORT-TD uses the method of discrete ordinates (see Chapter 2.1.4) to treat the directional variable and the weighted difference, nodal, or characteristic method to treat spatial variables [67]. Building weighted sums over the directional results delivers integral quantities such as the scalar neutron flux.
In order to achieve unconditional numerical stability in transient calculations, a fully implicit time discretization scheme is used in TORT-TD. Scattering anisotropy is treated in terms of a P_l Legendre scattering cross section expansion. In order to reduce spatial homogenization errors at the level of pin cells, the Generalized Equivalence Theory (GET) has been implemented in TORT-TD in terms of pin cell discontinuity factors [76]. TORT-TD has also been extended

to account for time-dependent anisotropically distributed external sources [77], a feature that becomes relevant in order to model subcritical systems driven by external neutron sources. For treating thermal-hydraulic feedback, TORT-TD has been coupled with the GRS system code ATHLET [3]. By implementing steady-state and transient Iodine-Xenon equations, TORT-TD has been prepared for the simulation of operational transients.
In [16] TORT-TD was ranked second as best available neutronics code for transient calculations. Significant improvements in the coupling of TORT-TD and ATHLET, and the easy access to the code developer at the GRS on the campus put the coupled code system TORT-TD/ATHLET in front of TRACE/PARCS [22, 88].

CHAPTER 5

Thermohydraulic Codes used

5.1 CFX

A proceeding similar to the neutronics was chosen for the thermal-hydraulic calculations. A well-proven CFD core model already exists for ANSYS-CFX which has previously been analyzed in depth for steady state conditions. ANSYS-CFX is a well proven, commercial software package for simulating three-dimensional flow networks. Heat transfer is also included in the numerical calculations. After modeling the FRM II in ATHLET, the results will then be validated using the CFX results [10]. In the following part, the implementation of the numerical fluid dynamics will be presented.

5.1.1 Implementation in CFX

Because most real-life applications cannot be described by analytical solutions of the Navier Stokes Equations, numerical methods have to be applied. Hereby, the basic equations are transformed to algebraic approximations which then are solved numerically.

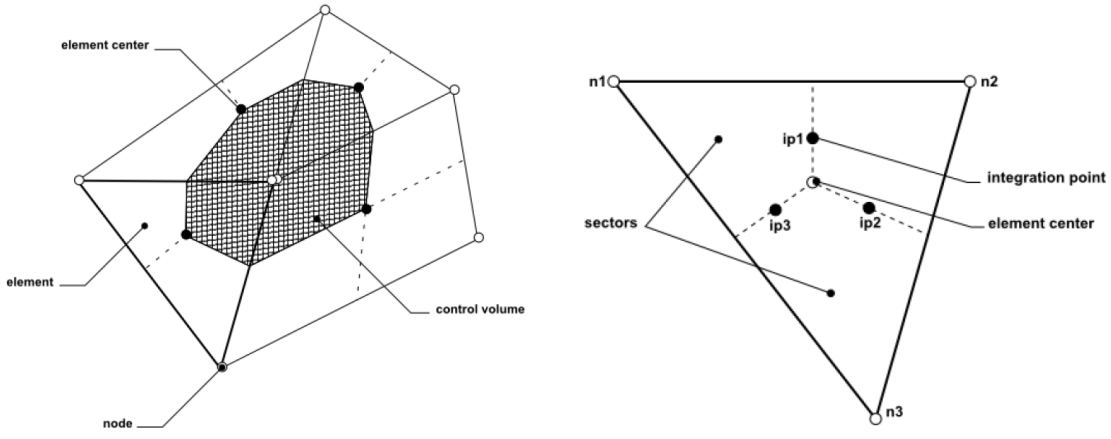

(a) Typical two-dimensional mesh

(b) Sketch of a mesh element

Figure 5.1: *The left panel (a) shows a sketch of a typical two-dimensional mesh. Around the mesh nodes a control volume is constructed. In the right panel (b) a sketch of a mesh element is shown.*

The basis of the Ansys-Cfx code system is an element-based Finite-Volume Method in which a body is discretized by finite volumes. Figure 5.1(a) shows a typical two-dimensional mesh with nodes, control volume and mesh element. Each element includes the relevant quantities such as energy, mass and momentum. For these quantities the conservation equations (see Chapter 3.2) are integrated over a so-called control volume, which is defined as the volume spanned by the centers of surrounding elements. Applying the Gauß divergence theorem and treating the time derivatives separately of the volume integrals, which is possible because the control volumes are not deformed with time, leads to a system of the conservation equations consisting of volume and surface integrals. Hereby, the volume integrals represent source terms, while the surface integrals represent the summation of the fluxes.
Figure 5.1(b) illustrates a single mesh element which consists of mesh points (n_1, n_2, n_3), integration points (ip_1, ip_2, ip_3) and sectors. These sectors are defined to deal with the discretization of the volume integrals and allocate the result to the corresponding control volume. For the discretization of the surface integrals the integration points (IP), which are located at the center of each surface segment, are used. The result of each integration point is then accumulated to the adjacent control volumes. This method ensures that the surface integrals are locally conservative.

5.1.1.1 Shape functions

As already mentioned above, the solution for the relevant quantities are stored at the mesh nodes. For the evaluation of many terms, an approximation of the stored quantities at the integration points is required. Hence, Ansys-Cfx uses finite-element shape functions that describe the variation of a variable X:

$$X = \sum_{\mathrm{i} \in \mathrm{Nodes}} N_\mathrm{i}\, x_\mathrm{i}, \tag{5.1}$$

where x_i is the value stored at the mesh node i, and N_i is the shape function of the node. The shape functions are tri-linear and are also used for geometric calculations, as Equation (5.1) also holds for the coordinates. An overview of these functions and their form depending upon the shape of the volume element can be found in [2].

5.1.1.2 Control Volume gradients

Using the Gauß divergence theorem the control volume gradients of a variable X at the nodes can be calculated as:

$$\boldsymbol{\nabla} X = \frac{1}{V} \sum_{\mathrm{i} \in \mathrm{IP}} (X\, \mathbf{n})_{\mathrm{IP_i}}. \tag{5.2}$$

Hereby, $\mathbf{n}$ is the outward pointing surface vector at the integration point $\mathrm{IP_i}$. The variable X is evaluated at IP.

5.1.1.3 Diffusion terms

The spatial derivatives for all diffusion terms can also be calculated using shape functions:

$$\left.\frac{\partial X}{\partial x}\right|_{\mathrm{IP}} = \sum_{\mathrm{i} \in \mathrm{Nodes}} \left.\frac{\partial N_\mathrm{i}}{\partial x}\right|_{\mathrm{IP}} x_\mathrm{i}. \tag{5.3}$$

In this way spatial derivatives in diffusion terms are evaluated.

5.1.1.4 Pressure gradient and Mass flows

In the momentum equations the surface integral of the pressure gradients has to be evaluated by using the following equation:

$$P_{\mathrm{IP}} = \sum_{\mathrm{i} \in \mathrm{Nodes}} N_{\mathrm{i}} \left(s_{\mathrm{IP}}, t_{\mathrm{IP}}, u_{\mathrm{IP}} \right) P_{\mathrm{i}}. \tag{5.4}$$

Furthermore, the mass flow through a control volume is discretized and leads to a pressure-velocity coupling that contains the effects of compressibility. More detailed information regarding the discretization of the mass flow and the coupling of pressure and velocity can be found in [2].

5.1.1.5 Coupled System of equations

Applying the above-described Finite-Volume Method to all elements in the domain, a linear set of equations arises. For a mesh point i this can be written in the form

$$\sum_{n_{\mathrm{i}} \in \mathrm{Neighbors\ of\ i}} a^{\mathrm{i}}_{n_{\mathrm{i}}} x^{\mathrm{i}}_{n_{\mathrm{i}}} = b_{\mathrm{i}}. \tag{5.5}$$

While for scalar equations, such as enthalpy, a_{i}, b_{i} and x_{i} are plain numbers, for the coupled 3D mass-momentum equations they are matrices and vectors.

5.1.1.6 Solution Strategy

In contrast to non-coupled or segregated solvers, in ANSYS-CFX a coupled solver is implemented. It solves the hydrodynamic equations as a single system and computes a fully implicit discretization of the equations. This approach has multiple advantages over non-coupled or segregated solvers, e.g. robustness, generality, efficiency and simplicity. The drawback is the excessive need of memory to store all the quantities. For steady-state problems, the time-dependent equations are solved as a kind of 'acceleration' to guide the approximate solutions in a physically based manner to a steady-state solution ("false timestepping"). Therefore, good initial values have to be specified to limit the time needed for the solution.

5.1.1.7 General Solution

Figure 5.2 shows a simplified flowchart of the CFX solver. Only actually used capabilities are shown in this chart. Two numerically intensive operations are required for each set of field equations for each time step: The coefficient generation where the non-linear equations are linearized and assembled into the solution matrix, and the equation solution itself. The outer iteration is controlled by the (false) time step. The inner linearization operations are performed only once per outer iteration in steady state analysis and multiple times per time step in transient analysis.

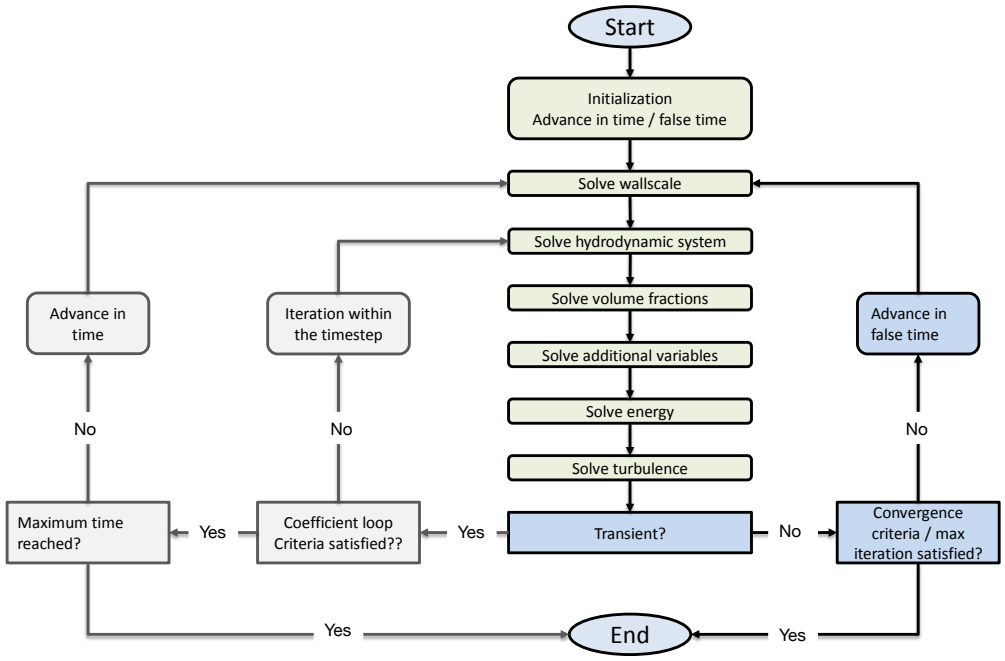

Figure 5.2: *Simplified flowchart of the general solution process with naming conventions, taken from [2] and [10]. The outer iteration is arranged by the (false) time step. Since in this thesis only steady-state calculations are performed with* CFX*, the outer transient iteration (left) is marked in gray shades. Therefore, the inner linearization is performed only once per time step.*

Linear Equation solution The CFX solver uses the *Incomplete Lower Upper* factorization technique (ILU) to iteratively solve the discretized system of linearized equations. The system of discrete equations can formally be written as

$$\mathbb{A} \cdot \boldsymbol{X} = \mathbf{b}, \tag{5.6}$$

with the coefficient matrix $\mathbb{A}$ and the solution vector $\boldsymbol{X}$. The approximate solution $\boldsymbol{X}_\mathrm{n}$ at the nth iteration step is to be improved by $\boldsymbol{X}'$ yielding

$$\boldsymbol{X}_{\mathrm{n}+1} = \boldsymbol{X}_\mathrm{n} + \boldsymbol{X}', \tag{5.7}$$

where the correction $\boldsymbol{X}'$ is a solution of

$$\mathbb{A} \cdot \boldsymbol{X}' = \mathbf{r}_\mathrm{n}, \tag{5.8}$$

where $\mathbf{r}_\mathrm{n}$ is the residual as calculated by

$$\mathbf{r}_\mathrm{n} = \mathbf{b} - \mathbb{A} \cdot \boldsymbol{X}_\mathrm{n}. \tag{5.9}$$

Inherently, the performance of ILU-Solvers decreases rapidly with an increasing number of mesh elements and large element aspect ratio.

The Algebraic Multigrid Method The CFX solver is a so-called *multigrid solver*. This means that early iterations are performed on a fine grid that is progressively coarsened in later iterations. Finally, the results are transferred back from the coarsest mesh to the original fine mesh. This technique enhances the convergence behavior of matrix inversions and offers a significant advantage in the treatment of discretization errors. In principle, iterative solvers are efficient only at reducing errors with a wavelength of the order of the mesh spacing. The coarsening of the mesh within the Multigrid Method leads to an increase of the mesh spacing and, therefore, to a reduction of errors with larger wavelengths.
The coarsening of the mesh is handled in CFX by a so-called Algebraic Multigrid Method. A schematic draw of this method is shown here in Figure 5.3. This method enables the usage of only one fine mesh of the geometry. Coarser meshes are generated by creating a system of discrete equations by summing the fine mesh equations. A key advantage of the Algebraic Multigrid Method is the reduction of time consumption. The non-linear equations need to be discretized only once for the finest mesh and can be passed then to the virtual coarser ones.

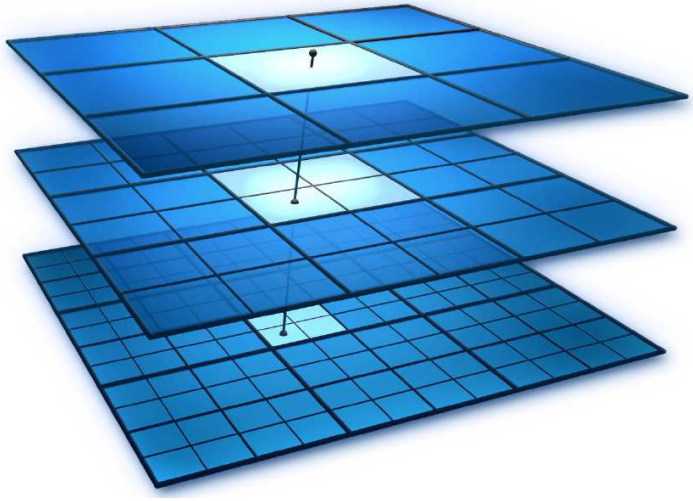

Figure 5.3: *Schematic drawing of the idea behind the Algebraic Multigrid Method, taken from [10]. Early iterations are performed on a fine mesh, later iterations on coarser virtual meshes. This way, errors with longer wavelength on the order of the domain size can be treated in a less time consuming manner.*

In ANSYS-CFX a particular version of the Algebraic Multigrid Method is implemented, viz. a so-called *Additive Correction*. This approach takes advantage of the Finite-Volume Method implemented in CFX. The discrete conservation equations are representative of the balance of conserved quantities over a control volume which, therefore, can be merged to create larger ones while coarsening the mesh. In doing so, the error components at longer wavelength are reduced significantly.

5.2 ATHLET

The thermal-hydraulic computer code ATHLET (Analysis of THermal-hydraulics of LEaks and Transients) is being developed by the GRS for the analysis of operational conditions, abnormal transients and all kinds of leaks and breaks in nuclear power plants. The aim of the code development is to cover the whole spectrum of design basis and beyond design basis accidents

for PWRs, BWRs, SMRs and future Gen IV reactors with one single code [27]. In this thesis, an adapted model for the primary circuit and reactor control system of the FRM II has been developed and was used for the coupled transient calculations (see Chapter 10).

5.2.1 The Finite-Volume Approach in ATHLET

In the following section, the numerical methods used by ATHLET (Analysis of THermal-hydraulics of LEaks and Transients) will be presented briefly. For detailed information one may refer to [3]. In ATHLET a thermal-hydraulic system is represented by a modular network technique. Therewith, the system configuration is simulated by connecting basic Thermo-Fluiddynamic Objects (TFOs) which include control volumes and junctions. The control volumes are spatial entities where mass and energy are distributed homogeneously. The junctions are volumeless, contain neither mass nor energy, and establish connections between the centers of the control volumes where mass and energy are transported. This approach leads to a finite-volume staggered grid, where the junction centers are displaced by half a control volume length from the control volume centers, as is shown in Figure 5.4. The control volumes/junctions are the smallest modelling units. Their characteristic length determines both the computational speed and accuracy.

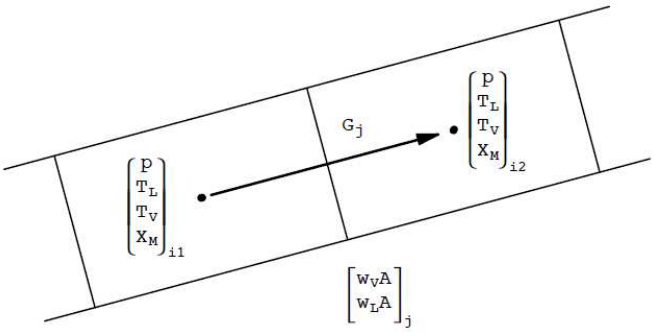

Figure 5.4: *Staggered grid as used in ATHLET showing control volumes i_1 and i_2 with connecting junction j, taken from [3]. The solution variables are the pressure p, the liquid temperature T_L, the vapor temperature T_V, and the mass quality x_M (see Eq. 5.10) within the control volumes, as well as the velocities w_L and w_V for the liquid and the vapor, respectively, for the junction. A is the total flow area.*

The control volumes are used as the integration domains for the spatial integration of the mass and energy conservation equations, whereas the junctions are the integration domains for the spatial integration of the momentum balances. This spatial integration leads to quantities related to both the control volumes and junctions, which represent the local physical state in a spatially averaged mode, and which are time dependent only.
The time integration of the thermo-fluiddynamic model is performed with the general purpose ODE-solver FEBE (Forward-Euler, Backward-Euler). FEBE provides the solution of an initial value problem for a large system of Ordinary Differential Equations (ODEs) of first order. The main features of FEBE include:

- By means of the implicit Euler method the basic solution of the ODE system is calculated at discrete sub-points of the basic time step interval.

- Using the basic solution as supporting points, solutions of different orders of consistency are calculated by means of local polynomial extrapolation. By comparison of these solutions, the local discretization error is quantified.
- The system of ODEs is split into two subsystems, the first being integrated explicitly (forward), the second implicitly (backward).

In ATHLET each thermo-fluiddynamic object provides a subset of the entire ODE system, which is integrated simultaneously by FEBE. Because the resulting system of ODEs is of the stiff type, the fully implicit option in FEBE is used throughout.
The use of the implicit Euler scheme requires the calculation of the Jacobian matrix. In ATHLET applications, the Jacobian is a sparse band matrix, i.e. most of its elements outside the diagonal band are equal to zero. Independently of the problem size, the bandwidth is around 30 elements. To gain efficiency and high computational speed in calculating the Jacobian matrix and solving the linear systems associated with Euler's method, the sparse matrix package FTRIX is applied which exploits the sparseness of the Jacobian matrix for its calculation by numerical differentiation and the solution of the resulting system of linear equations.
In FEBE, a rigorous error control is performed on the basis of an extrapolation technique. According to the error bound specified by the user, the time step size and the order of the method (> 2) are adequately determined for every integration step.

5.2.2 The 5-Equation Model

ATHLET supports two different models to describe a hydraulical system: The 5- and 6-Equation Model. In this thesis, the 5-Equation Model as described in [3], is used in order to consider the relative velocity between phases. This model solves the mass and energy balances in the control volumes separately for the liquid and vapor phase and calculates the mixture momentum balance at the junctions. It accounts for thermal and mechanical non-equilibrium and includes a mixture level tracking capability. In the derivation of the differential equations two assumptions have been made:

- Changes in the geometry of flow channels and structures are neglected.
- In the energy balance equations, both the potential energy contribution and the dissipation energy is neglected.

The differential equations include the following solution variables:

Mass quality $\boldsymbol{x_{\mathrm{M}}}$*:*

$$\frac{\mathrm{d}x_{\mathrm{M}}}{\mathrm{dt}} = \frac{m_{\mathrm{L}} \dfrac{\mathrm{d}m_{\mathrm{V}}}{\mathrm{dt}} - m_{\mathrm{V}} \dfrac{\mathrm{d}m_{\mathrm{L}}}{\mathrm{dt}}}{\left(m_{\mathrm{L}} + m_{\mathrm{V}}\right)^2}, \tag{5.10}$$

where x_{M} is the mass quality, m_{L} is the mass of the liquid and m_{V} is the vapor mass.

Liquid temperature $\boldsymbol{T_{\mathrm{L}}}$*:*

$$\frac{\mathrm{d}T_{\mathrm{L}}}{\mathrm{dt}} = \frac{1}{c_{\mathrm{p,L}}} \frac{E_{\mathrm{L}}}{m_{\mathrm{L}}} + \frac{1}{c_{\mathrm{p,L}}} \left(\nu_{\mathrm{L}} - \left. \frac{\partial h_{\mathrm{L}}}{\partial p} \right|_{T_{\mathrm{L}}} \right) \frac{\mathrm{dp}}{\mathrm{dt}}, \tag{5.11}$$

where T_L is the liquid temperature, $c_\mathrm{p,L}$ is the heat capacity of the liquid at constant pressure, E_L is the total energy of the liquid, ν_L is the viscosity of the liquid, h_L is the enthalpy of the liquid, and p is the pressure of the liquid.

Vapor temperature $\boldsymbol{T_\mathrm{V}}$:

$$\frac{\mathrm{d}T_\mathrm{V}}{\mathrm{dt}} = \frac{1}{c_\mathrm{p,V}} \frac{E_\mathrm{V}}{m_\mathrm{V}} + \frac{1}{c_\mathrm{p,V}} \left(\nu_\mathrm{V} - \left. \frac{\partial h_\mathrm{V}}{\partial p} \right|_{T_\mathrm{V}} \right) \frac{\mathrm{dp}}{\mathrm{dt}}, \tag{5.12}$$

where T_V is the vapor temperature, $c_\mathrm{p,V}$ is the heat capacity of the vapor phase at constant pressure, E_V is the total energy of the vapor, ν_V is the viscosity of the vapor, h_V is the enthalpy of the vapor, and p is the pressure of the vapor.

Pressure $\boldsymbol{p}$:

$$\frac{\mathrm{d}p}{\mathrm{dt}} = -\frac{\dfrac{\mathrm{d}m_\mathrm{V}}{\mathrm{dt}} \nu_\mathrm{V} + m_\mathrm{V} \left. \dfrac{\partial \nu_\mathrm{V}}{\partial T_\mathrm{V}} \right|_p \dfrac{\mathrm{d}T_\mathrm{V}}{\mathrm{dt}} + \dfrac{\mathrm{d}m_\mathrm{L}}{\mathrm{dt}} \nu_\mathrm{L} + m_\mathrm{L} \left. \dfrac{\partial \nu_\mathrm{L}}{\partial T_\mathrm{L}} \right|_p \dfrac{\mathrm{d}T_\mathrm{L}}{\mathrm{dt}}}{m_\mathrm{V} \left. \dfrac{\partial \nu_\mathrm{V}}{\partial p} \right|_{T_\mathrm{V}} + m_\mathrm{L} \left. \dfrac{\partial \nu_\mathrm{L}}{\partial p} \right|_{T_\mathrm{L}}}, \tag{5.13}$$

where m_V is the mass of the vapor, m_L is the mass of the liquid, ν_V is the viscosity of the vapor, ν_L is the viscosity of the liquid, and the temporal derivatives of T_V and T_L are given by Equations (5.12) and (5.11), respectively.

Mixture mass flow rate $\boldsymbol{G}$:

$$\frac{\mathrm{d}G}{\mathrm{dt}} = \frac{1}{Z} \left(p(i_2) - p(i_1) + \Delta p_\mathrm{MF} + \Delta p_\mathrm{WR} + \Delta p_\mathrm{grav} + \Delta p_\mathrm{fric} + \Delta p_\mathrm{æ} + \Delta p_\mathrm{I} \right), \tag{5.14}$$

where $p(i_1)$ and $p(i_2)$ is the pressure in the control volumes i_1 and i_2, respectively, and Z is given by

$$Z = \int \frac{\mathrm{d}s}{A}, \tag{5.15}$$

with A being the flow area and $\mathrm{d}s$ is an infinitesimal length. For the fairly complicated calculation of the momentum flux term Δp_MF, the relative velocity term Δp_WR, the elevation term Δp_grav, the friction term Δp_fric, the density derivative term $\Delta p_\mathrm{æ}$, and the source term Δp_I the reader is referred to [3].

Average fluid velocity $\boldsymbol{w_\mathrm{i}}$:

The average fluid velocity, w_i, in control volume i is calculated as a function of the inlet and outlet mass flow rates, G_in and G_out, assuming that the flows are homogeneous:

$$\frac{\mathrm{d}w_\mathrm{i}}{\mathrm{dt}} = \frac{1}{2\, A_\mathrm{i}\, \rho_\mathrm{m}} \left[\frac{\mathrm{d}G_\mathrm{in}}{\mathrm{dt}} + \frac{\mathrm{d}G_\mathrm{out}}{\mathrm{dt}} - \frac{G_\mathrm{in} + G_\mathrm{out}}{m_\mathrm{L} + m_\mathrm{V}} \left(\frac{\mathrm{d}m_\mathrm{L}}{\mathrm{dt}} + \frac{\mathrm{d}m_\mathrm{V}}{\mathrm{dt}} \right) \right]. \tag{5.16}$$

Here, A_i is the flow area, and

$$\rho_\mathrm{m} = \alpha\,\rho_\mathrm{V} + (1-\alpha)\,\rho_\mathrm{L} \tag{5.17}$$

is the weighted average of the vapor and liquid densities ρ_V and ρ_L, with the weighting factor α being defined as

$$\alpha = \frac{m_\mathrm{V}\nu_\mathrm{V}}{m_\mathrm{V}\nu_\mathrm{V} + m_\mathrm{L}\nu_\mathrm{L}}, \tag{5.18}$$

where m_V is the mass of the vapor, m_L is the mass of the liquid, ν_V is the viscosity of the vapor, and ν_L is the viscosity of the liquid.

Part III

Explanation of Models used

CHAPTER 6

Development of the Neutronics Models used

A well-mapped computational model, which can be used for the neutronic simulations, must represent all important parameters of the real core of FRM II. As a basis for such a model, the well-established full core MCNP6 model of FRM II called OISM can be taken, in which the involute shaped fuel plates are approximated by parabolas and hyperbolas [60]. For the calculations reported in this Chapter the design of the fuel zone was adapted, and both the required mesh tallies and the general MCNP6 run parameters have been set up in the needed way.
However, neither Serpent 2 nor TORT-TD are able to handle this kind of geometry [46, 67]. Therefore a simplified MCNP6 model was developed which is suitable for use with both Serpent 2 and TORT-TD hereafter. After its validation this simplified substitutional model has been translated into a geometrically equivalent Serpent 2 model. With the fully functional and validated Serpent 2 model, the homogenized group cross sections needed for TORT-TD can then be calculated (see Chapter 4.2.1). At the end of this process, multiplication factor, fission power distribution and neutron fluxes obtained from TORT-TD, will be validated against the MCNP6 calculations. For all MC calculations ENDF/B-VII.1 cross sections have been used.

6.1 The neutronics of FRM II's fuel element

FRM II is a research reactor with a very compact core designed for beam tube experiments. The very compact design leads to a high brilliance B, which is defined as follows:

$$B = \frac{\Delta N}{t\, A\, \Delta\Omega\, \frac{\Delta\lambda}{\lambda}}, \tag{6.1}$$

where ΔN is the number of neutrons within a certain wavelength band $\Delta\lambda/\lambda$ per time t, per area A and per solid angle $\Delta\Omega$. This very high brilliance is unique world wide and enables measurements of very high precision. To achieve a high brilliance some special reactor design features have been implemented which will be described in detail in the following.
FRM II is a light water cooled and heavy water reflected reactor. Inside a separated tank outside the central channel the heavy water is situated and contains numerous installations, e.g. a cold and a hot source, safety shutdown rods, irradiation positions, etc.. However, all these installations are not explicitly modeled but are rather realized by using a "smeared" heavy water material composition. As a compact core reactor, FRM II has only a single fuel element consisting of 113 involute shaped fuel plates (cf. Figure 6.1) with an evolute radius of 64.025 mm. With

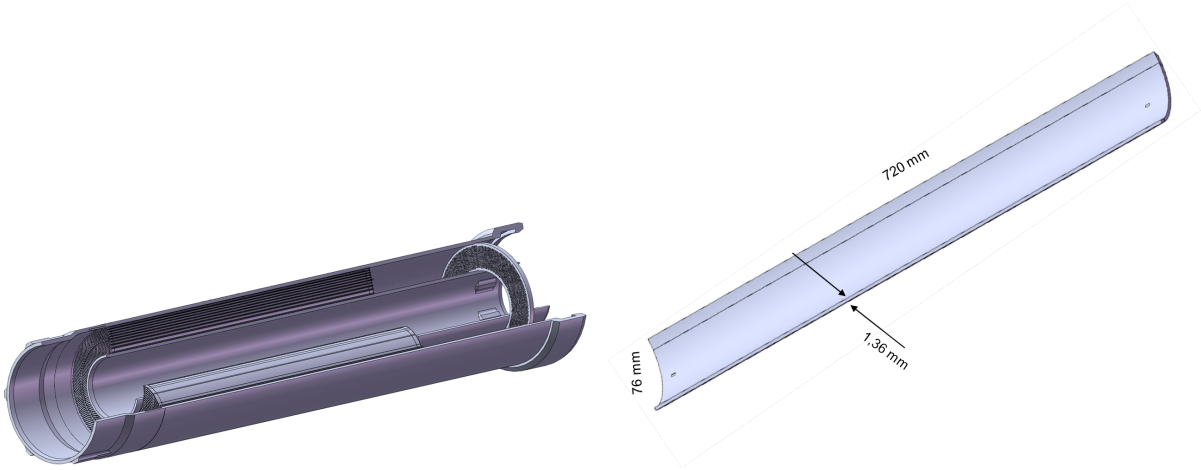

(a) CAD model of the fuel element of FRM II

(b) CAD model of one representative fuel plate

Figure 6.1: *The left panel (a) shows a CAD model of a fuel element of FRM II. The sieve, fuel plates and the tube for the control rod can be clearly seen. In the right panel (b) a CAD model with dimensions of a representative fuel plate is shown.*

such uniquely shaped plates, the spacing of the cooling channels is independent of the radius. This provides an excellent cooling capability over the whole active core volume. The fuel plates themselves are fixed with $AlMg_2$-holdings between cylindrical ducts with radii of 65 mm and 114.5 mm, respectively. One plate consists of two layers of cladding, each 0.38 mm thick, and a 0.60 mm fuel layer. Currently, FRM II uses highly enriched uranium with 93 % enrichment in the form of an U_3Si_2 compound dispersed in an Al-matrix. To reduce the heat load near the heavy water tank, the uranium density is reduced from $3.0\,\mathrm{gU/cm^3}$ in the inner region to $1.5\,\mathrm{gU/cm^3}$ in the outer region. Especially at the bottom of the outer region of the fuel zone, the heat load needs to be even more reduced. Therefore a boron absorber ring is installed in that part of the fuel element. The total height of the fuel zone is 70 cm, and there are 2.2 mm wide cooling channels located in-between the fuel plates. The single control rod consists of a hafnium absorber to suppress the neutron flux and, a beryllium follower (cf. Figure 6.2). Inside the follower the neutron flux is increased leading to an increase of cycle time. The impact of the beryllium follower upon the reactor operation is described in more detail in Chapter 9.4. The control rod also has decidedly built-in cooling channels to remove the heat deposited in it due to the γ- and n-radiation. In the unlikely event of a failure of the control rod, five emergency shutdown rods are placed inside the moderator tank to ensure a safe shutdown at all times. During normal operation all of these are fully withdrawn. In the neutronics models used in this thesis, these rods are not explicitly modeled. Their tubing, as other core installations are realized in "smeared" heavy water.

For the following calculations the position of the border between the hafnium absorber and the beryllium reflector is situated at -6.92 cm from core mid-plane where, i.e. a fresh U_3Si_2 fuel element becomes critical. The Evaluated Nuclear Data File (ENDF/B) Version 7 was used for cross section data. With a total of 10^6 simulated particles per cycle, 25 inactive cycles and 150

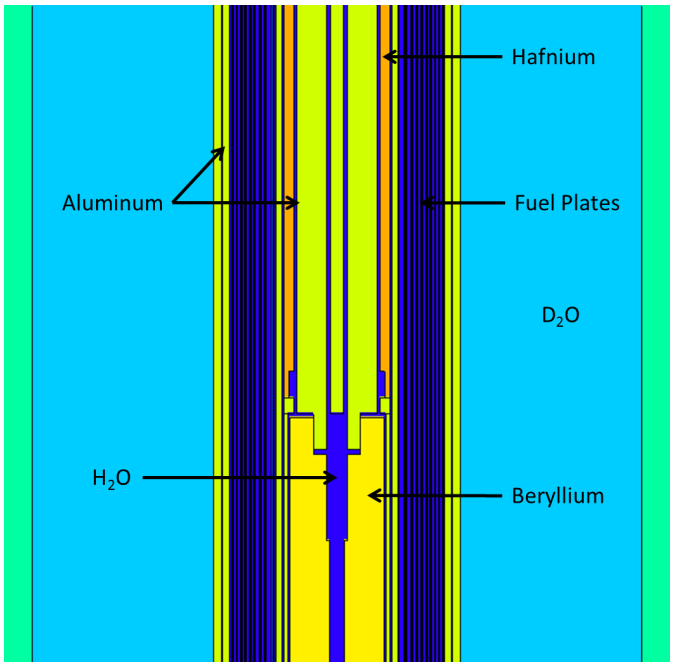

Figure 6.2: *MCNP6 model of the control rod. Different colors represent different materials; orange stands for the hafnium absorber, yellow represents the beryllium follower and green stands for aluminum. Also shown are the fuel plates and the heavy water.*

active cycles (see 2.2.1), this full core MCNP6 model OISM leads to an effective multiplication factor k_{evolv} of

$$k_{\text{evolv}} = 0.99772 \pm 0.00009. \tag{6.2}$$

Adjusting the model until a multiplication factor of exact equals 1 is not necessary because this value is close enough and furthermore due to the MC approach not possible. Also, the model comparison in the following has been performed with the same geometry. Therefore, a multiplication factor very close to 1 is sufficient.
For the validation of the substitutional geometries as described in Section 6.2, the detailed knowledge of the power deposition in the fuel plates of the current core is necessary as well. Therefore, a cylindrical mesh tally TMESH of type 3 [59] was used, which covers the whole fuel area. The origin of this cylindrical coordinate system (r, θ, z) is located at the intersection of the core-midplane and the symmetry axis of the fuel element, with the z-axis being identical to the symmetry axis. The TMESH is constructed from with several radial areas, whereat the number of equidistant meshcells follows the expected curvature of the power deposition:

- From $r = 6.75\,\text{cm}$ to $7.5\,\text{cm}$: 10 meshcells
- From $r = 7.5\,\text{cm}$ to $10.0\,\text{cm}$: 20 meshcells
- From $r = 10.0\,\text{cm}$ to $10.54\,\text{cm}$: 10 meshcells
- From $r = 10.54\,\text{cm}$ to $10.55\,\text{cm}$: 1 meshcell
- From $r = 10.55\,\text{cm}$ to $10.56\,\text{cm}$: 1 meshcell

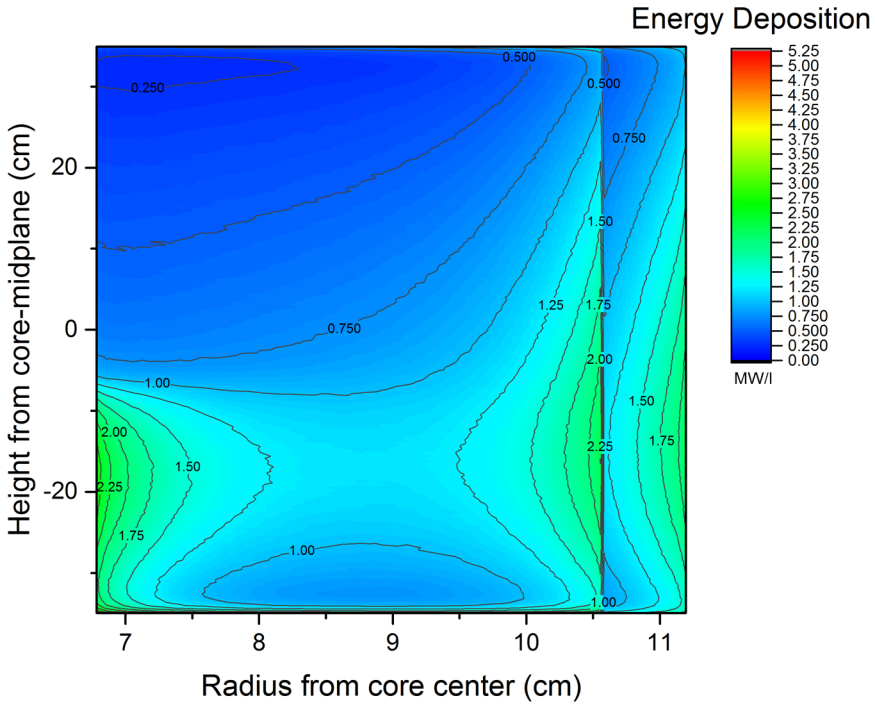

Figure 6.3: *Power deposition in* MW/l *at BOL in one representative fuel plate of the current fuel element as calculated with MCNP6.*

- From $r = 10.56\,\text{cm}$ to $11.15\,\text{cm}$: 12 meshcells
- From $r = 11.15\,\text{cm}$ to $11.18\,\text{cm}$: 1 meshcell
- From $r = 11.18\,\text{cm}$ to $11.19\,\text{cm}$: 1 meshcell
- From $r = 11.19\,\text{cm}$ to $11.20\,\text{cm}$: 1 meshcell

In z-direction one mesh tally cell covers one fuel assembly, consisting of the cooling water channel, cladding and fuel. The results obtained from MCNP6 are averaged throughout over θ in the range from 0 to 2π. Figure 6.3 shows the power deposition for one representative fuel plate. The maximum is located at the lower left side where the beryllium follower has an increasing effect. At the right, near the heavy water moderator, the power density is again increased. As expected, the hafnium absorber at the top left side decreases the deposited power because of the flux suppression. Also the sharp decrease in the uranium density can be clearly seen as the sharp decrease in power deposition at a radius of 10.56 cm.
For the transient calculations the thermal neutron flux inside the core and specifically near the shutdown rods is very important to estimate their effectiveness during a reactor shutdown maneuver. Since the FRM II is a research reactor optimized for beam tube experiments, the thermal flux in the region of the beam tubes is also of interest to the installed experiments. To calculate both the thermal and fast neutron flux, a mesh tally TMESH of type 1 [59] was used in MCNP6 with the following radial subdivision:

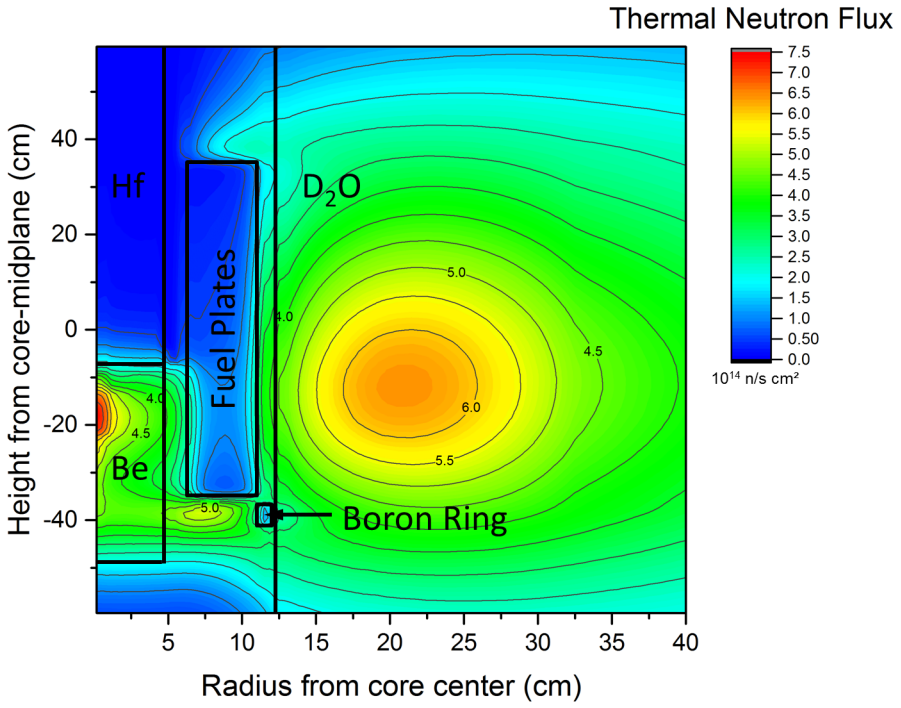

Figure 6.4: *Thermal neutron flux in* $10^{14}\,\mathrm{n/cm^2s}$ *of the current fuel element at BOL as calculated with MCNP6. The core installations are realized in "smeared" heavy water. To illustrate the core layout, the control rod, fuel zone, boron ring and the heavy water reflector tank are sketched. The absolute maximum of the thermal neutron flux is located inside the beryllium follower. However, the maximum usable for experiments is located within the heavy water moderator tank.*

1. From $r = 0.0\,\mathrm{cm}$ to $20.0\,\mathrm{cm}$: 60 meshcells
2. From $r = 20.0\,\mathrm{cm}$ to $50.0\,\mathrm{cm}$: 30 meshcells
3. From $r = 50.0\,\mathrm{cm}$ to $100.0\,\mathrm{cm}$: 25 meshcells
4. From $r = 100.0\,\mathrm{cm}$ to $200.0\,\mathrm{cm}$: 20 meshcells

In z-direction in the range from $z = -60.0\,\mathrm{cm}$ to $60.0\,\mathrm{cm}$, the geometry is divided into 120 equidistant subcells. The core installations were realized by using a "smeared" heavy water material composition. Figure 6.4 shows the steady-state thermal neutron flux distribution of the core in the FRM II, azimuthally averaged, and calculated with MCNP6 for the time of the reactor start with a fresh fuel element. The thermal neutron flux has been calculated in the energy interval from 0 eV to 0.625 eV. As a result, the absolute flux maximum of $7.4 \cdot 10^{14}\,\mathrm{n/cm^2s}$ is located inside the Beryllium follower, whereas the maximum available thermal neutron flux usable for experiments, $6.4 \cdot 10^{14}\,\mathrm{n/cm^2s}$, is located inside the heavy water moderator tank (cf. Figure 6.4). The intended flux depression caused by the installed boron ring is also clearly visible in Figure 6.4.
For transient calculations, the knowledge of the evolution of the fast neutron flux is important, too, because it highly influences the reactor dynamics. Figure 6.5 shows the azimuthally averaged

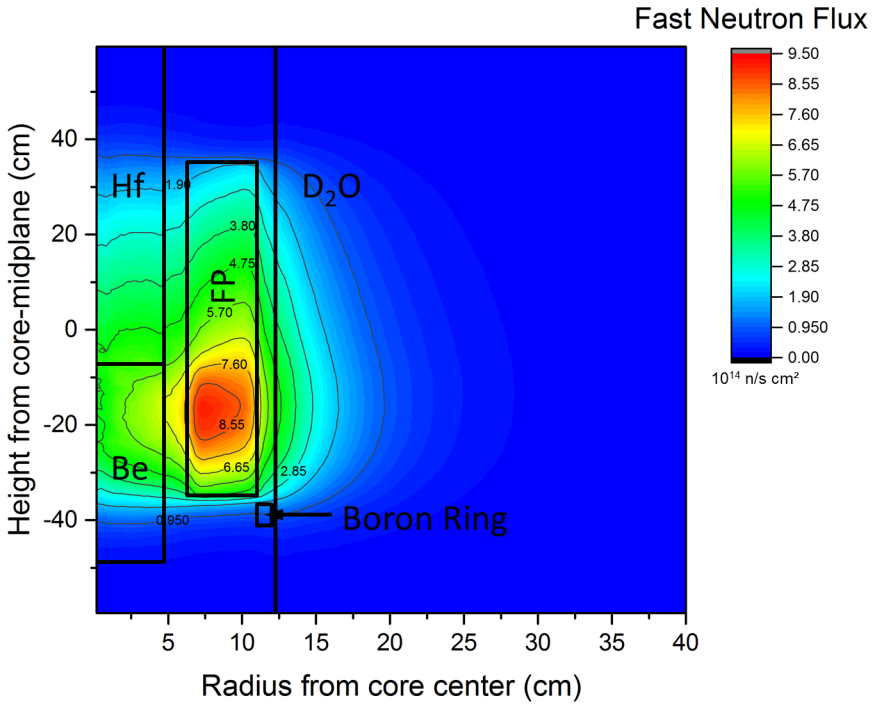

Figure 6.5: *Fast neutron flux in* $10^{14}\,\mathrm{n/cm^2s}$ *of the current fuel element at BOL as calculated with MCNP6. As in Figure 6.4, the core installations are realized in "'smeared"' heavy water, and the core layout is sketched. The highest fast neutron flux is located in the lower fuel zone, where most fissions occur due to the control rod position of* $-6.92\,\mathrm{cm}$ *from core midplane.*

steady state fast neutron flux for the actual fuel element, calculated with MCNP6 in the energy interval from 0.1 MeV to 20 MeV. It can be clearly seen that the maximal fast neutron flux of about $9.0 \cdot 10^{14}\,\mathrm{n/cm^2s}$ is situated in the range from $z = -25\,\mathrm{cm}$ to $-10\,\mathrm{cm}$ of the fuel plates near the beryllium follower.
These values for multiplication factor, power distribution, thermal and fast neutron flux are used as references in the following.

6.2 Substitutional Geometry

The main goal of a substitutional geometry is to simplify the geometry while at the same time preserving of the key core parameters, especially the multiplication factor of the fresh core, the fission power distribution and the thermal and fast neutron flux. Also certain key core characteristics, in particular the total fissile core inventory, the uranium density jump, the boron ring and the control rod design (see section 6.1) should be well reproduced. The more similar the substitutional model is compared to the original involute shaped fuel plates, the more valuable is the new model. Röhrmoser already developed several MCNP models with a substitution of the involute shaped fuel plates: One with concentric tubes and one vertical stack model [72]. The

advantages and drawback of these two options together with a fully homogenized fuel zone and the insertion of two homogenized, reduced fuel plates will be discussed below.
As criteria for a suitable substitutional geometry, the following conditions have to be fulfilled:

- Best possible consistency with the original geometry.
- Matching of the multiplication factors within their uncertainty margins.
- Matching of the power deposition within ±5 %. In unimportant or small areas, relative deviations up to 7.5 % are acceptable.
- Matching thermal and fast neutron fluxes within ±5 %.

Out of the models to be discussed in the following, the best fitting model will be chosen based upon a decision matrix regarding the above defined conditions (see chapter 6.2.5).

6.2.1 Concentric tubes model (CTM)

In this model, the original core geometry is replaced by concentric tubes. This has the advantage that the original core geometry is fully rebuilt in z–direction, but in r–direction this substitution is only a rough estimate as compared to the involute shaped fuel plates. The core installations are again implicitly taken into account using a "smeared" heavy water material composition. One option to set up a neutronically equivalent model is the preservation of at least of the

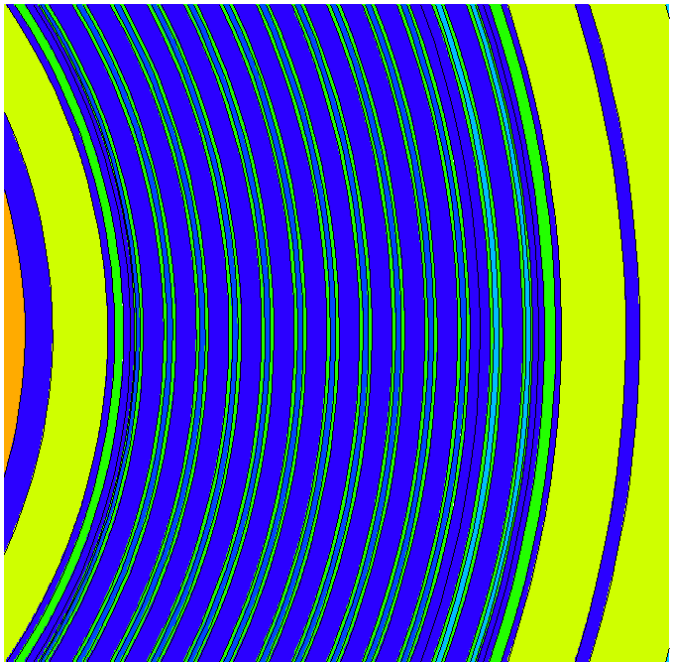

Figure 6.6: *Topview of the MCNP6 concentric tube model. The fuel plates are realized as concentric tubes, whereas the two outer tubes have a reduced uranium density of* $1.5\,\mathrm{g/cm^3}$ *and are emphasized with a lighter blue. The remaining core layout stays the same.*

total fissile core inventory. Also, the original plate dimensions must not be changed. Therefore, the width of the cooling channels between two tubes stays at 2.2 mm and one tube consists of two times 0.38 mm cladding and of 0.6 mm fuel. As a compromise between these two described

conditions a total of 13 concentric tubes replace the involute shaped fuel plates, whereas the midmost and most outer tube must have reduced dimensions in order to fit in the prescribed active core volume. Figure 6.6 shows the topview of the concentric tubes model. To represent the density jump, the fuel in the outer two tubes has a reduced uranium density of $1.5\,\mathrm{g/cm^3}$.

Multiplication factor For a fresh core, with a control position of $-6.92\,\mathrm{cm}$ from core midplane (see chapter 6.1) and with a neutron population of 10^6, 150 active and 25 inactive cycles, MCNP6 calculates an effective multiplication factor k_{tube} of

$$k_{\mathrm{tube}} = 0.99711 \pm 0.00009, \tag{6.3}$$

which differs significantly with more than $3-\sigma$ from the value given in (6.2).

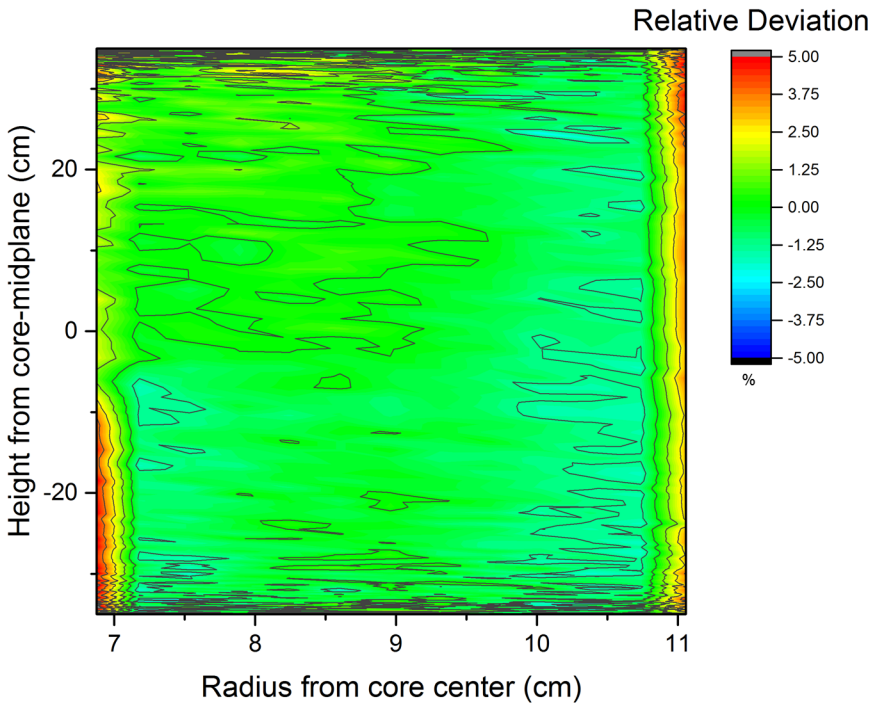

Figure 6.7: *Relative deviation in % between the power deposition between the original involute shaped fuel plates (OISM, see Figure 6.3) and the tube of the concentric tube model (CTM) in the sense of "CTM − OISM" at BOL.*

Power deposition Figure 6.7 shows the deviation in percent of the power deposition as calculated with the CTM from that of the OISM. To compare both models, the used mesh tally TMESH of type 3 was set up in such that each cell contains the same amount of fuel, cooling water and cladding. Otherwise the results of both models cannot be compared directly. Near the heavy water moderator tank and the beryllium follower, the CTM overestimates the power deposition by up to 5 %. Because of the rather coarse mesh in radial direction of the CTM due to the inherent

geometry, an investigation of the deviation with higher spatial distribution is not possible. For the remaining geometry the power distribution matches within ±2 %.

Thermal and fast neutron flux distribution Figure 6.8(a) shows the deviation of the thermal flux as calculated with the CTM from that of the OISM (see Figure 6.4). The thermal flux in the heavy water moderation tank matches within ±1 %. In the near outer region of the fuel zone, the thermal flux calculated for the CTM is 2.5 % lower than the involute model (see Chapter 6.2.4). This effect will be discussed in detail in Chapter 6.2.4. Within the fuel zone itself and the beryllium follower, the thermal flux is in good agreement. Due to the absorbing effect of hafnium for thermal neutrons (see Figure A.1), inside the hafnium absorber of the control rod the neutron statistic in MCNP6 is very poor. This effect leads to highly varying deviations in the thermal fluxes of the two models.
Over the whole geometry the fast neutron flux matches within ±1 %. Only at the border to the heavy water moderator tank, the deviation rises to 1.5 % − 2.5 %. With increasing distance from the fuel element the fast neutron flux decreases (see Figure 6.5) due to moderation. With decreasing fast neutron flux, the statistics uncertainties rises. This leads to the increasing deviations at the top and bottom of Figure 6.8(b). Longer calculation times or coarser meshes would fix this, however there is no particular interest for that regarding the goals of this work.

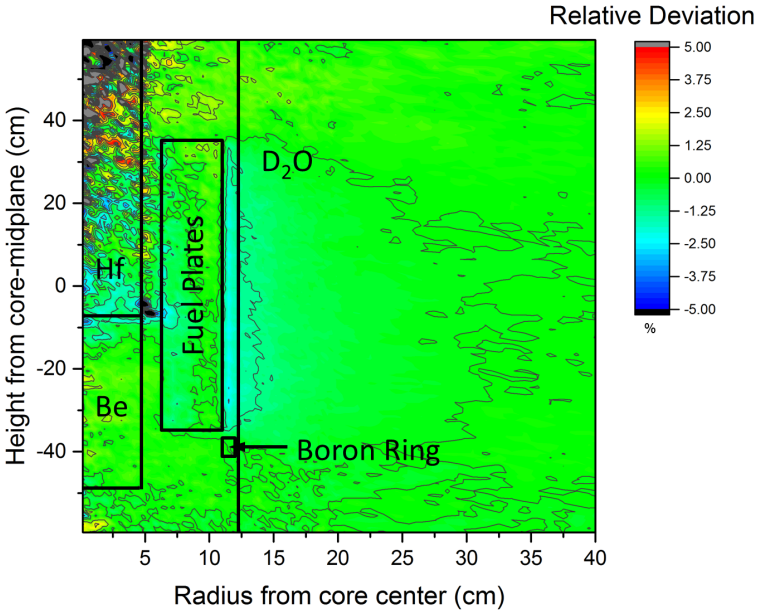

(a) Comparison of the thermal neutron flux

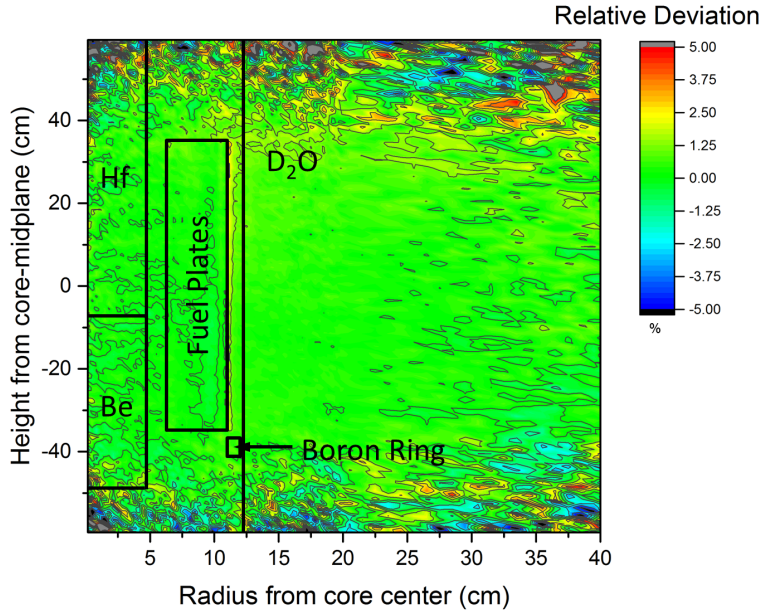

(b) Comparison of fast neutron flux

Figure 6.8: *The top panel (a) shows the relative deviation in % between the thermal neutron flux of the original involute shaped fuel plates (OISM, see Figure 6.4) and the concentric tube model (CTM) in the sense of "CTM − OISM" at BOL. The bottom panel (b) shows the corresponding relative deviation in % between the fast neutron flux.*

6.2.2 Homogenized fuel zone model (MMFZ)

In the deterministic TORT-TD calculations (see Chapter 6.4) the fine structure of the fuel zone (fuel plates, cladding, cooling channels) cannot be modeled explicitly due to excessive size of the resulting calculation grid. Homogenized, material mixing cross sections will be used for the fuel zone. This model verifies that the cross sections have to be calculated by the best substitutional model possible in order to achieve correct results using TORT-TD.
In this model, the materials in the $AlMg_2$-holding zone as well as in both fuel zones with high and low uranium density, respectively, were unweighted mixed in MCNP6. Only material mixtures taking into account the total masses in every area and not flux averaged materials (see Section 6.4) were built. Hence, the total mass of fissile material, the density step and the general core design are preserved.

Multiplication Factor For a material mixture in the fuel zone with 10^6 neutron histories per cycle, 25 inactive and 150 active cycles MCNP6 calculates an effective multiplication factor k_{mix} of

$$k_{\text{mix}} = 1.02994 \pm 0.00009 \tag{6.4}$$

which is unacceptably different from the value obtained with the original involute fuel plates model (see eq. (6.2)). The multiplication factor of a complete homogenized reactor is always smaller than it is for a heterogeneous one. It is to be noted that the just partial homogenization of the core used for this model leads to an increase of the multiplication factor k_{eff} although k_{eff} should get smaller when mixing the core layout. This effect is explainable by the only partial mixing, while the clear separation of the heavy water moderation tank persists.

Power deposition When mixing the cooling water, cladding and fuel, the fast neutrons cannot tunnel via the aluminum into the heavy water but are rather causing more fast fission inside the fuel zone. Especially at the top of the fuel zone the mixed model overestimates the power deposition by about 10 %. As shown in Figure 6.9, however, the power deposition is decreased between 3 % and 10 % in the area with a lower uranium density and also near the beryllium follower. In the middle of the fuel element the power deposition matches within ±2 %. With smaller distance from the low uranium density zone the deviation of the power deposition increases systematically from about 2.5 % to 5 % up to the already described maximum of 10 % at the top of the fuel zone.

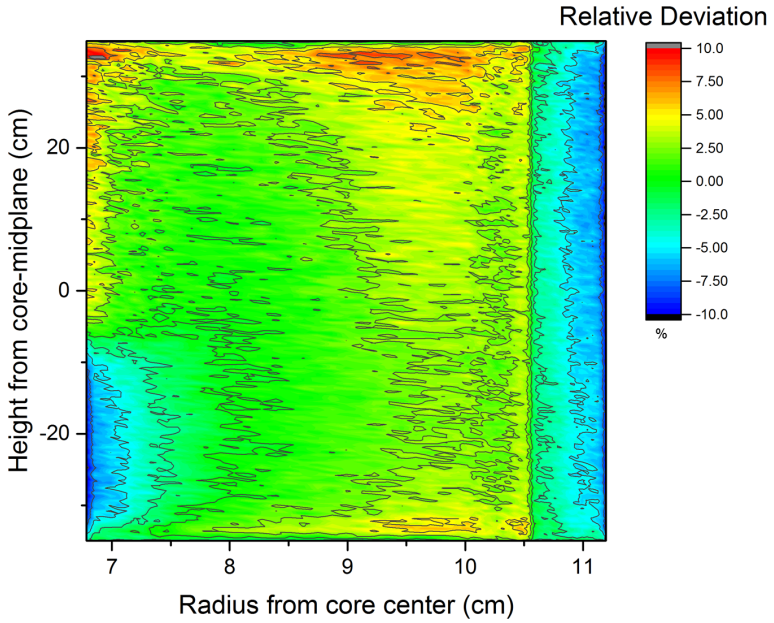

Figure 6.9: *Relative deviation in % of the power deposition at BOL between one original involute shaped fuel plate (OISM, see Figure 6.3) and the corresponding part of a homogenized fuel zone (MMFZ) in the sense of "MMFZ − OISM", as calculated with MCNP6. At the top of the fuel zone this substitutional model overestimates the power deposition by* 10 %*, but at the right and left edge the power deposition is underestimated by* 10 %*.*

Thermal and fast neutron flux distribution With homogenizing the fuel zone the moderation inside the fuel element is increased, e.g. due to less self shielding. This results in an increasing multiplication factor (see eq. (6.2) and (6.4)). With more neutrons absorbed inside the fuel zone, the neutron flux inside the moderation tank decreases. As shown in Figure 6.10(a) for the thermal and in Figure 6.10(b) for the fast neutron flux, the neutron flux is drastically suppressed in the MMFZ. The thermal flux inside the fuel plates is depressed by about 7.5 % to 15 % and near the beryllium follower up to 20 %. Also at the right side of the fuel zone the flux depression increases up to more than 15 %. Inside the heavy water moderation tank and near the fuel element the flux is 10 % smaller than expected. The deviation between the two models decreases with further distance to the fuel zone. A similar behavior is shown for the fast neutron flux. For the whole geometry the fast flux is between 1 % and 5.5 % systematically lower as compared to the original model.

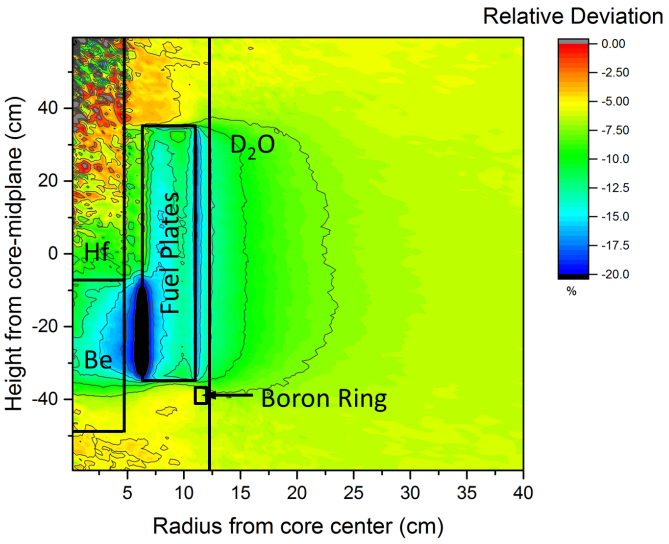

(a) Comparison of the thermal neutron flux

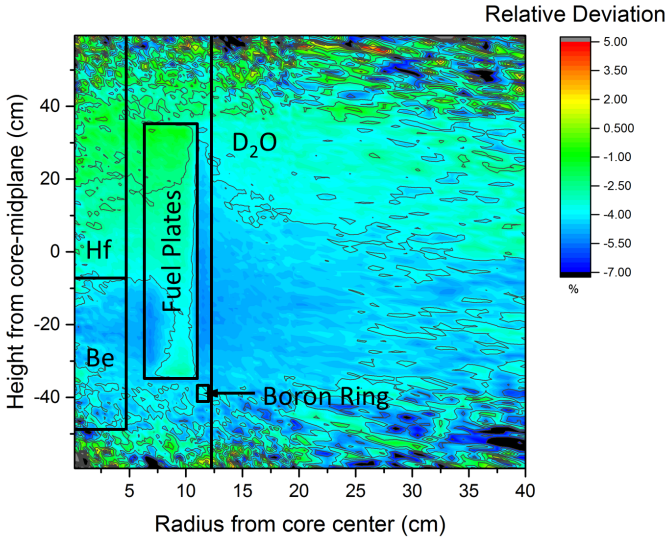

(b) Comparison of the fast neutron flux

Figure 6.10: *The top panel (a) shows the relative deviation in % of the thermal neutron flux at BOL between the original involute shaped fuel plates (OISM, see Figure 6.5) and the model with mixed materials (MMFZ) in the sense of "MMFZ − OISM", as calculated with MCNP6. Unweighted homogenization of materials leads to a massive underestimation of the thermal flux, especially in the fuel zone near the beryllium follower. The bottom panel (b) is the same as the top panel (a), but shows the relative deviation of the fast neutron flux. The fast neutron flux is systemically underestimated between 3 % to 5 % for the heavy water moderator tank and the beryllium follower. For the remaining zones the deviations fluctuate between +0.5 % and −2.5 %.*

6.2.3 Vertical stack model VSM

In the vertical stack model (VSM) virtual fuel, cladding and water discs are placed in the active core volume. In contrast to the concentric tubes model, the stacked design particularly allows for high resolution in the vertical direction of the power deposition profile, and it also reproduces the vertical distribution of the power deposition correctly, even near the density step. These discs preserve the general assembly of the original core layout: a cooling channel, two layers of cladding and a fuel layer. In the vertical stack model, the core installations are also implemented as "smeared" heavy water. In order to preserve the total fissile inventory of FRM II's core 192.62 stacked virtual discs are needed and have to be placed in the active core volume. Three different possibilities of placing the non-complete disc have been investigated: Either one 62 % disc in the core mid-plane (variant 1), two homogenized discs (variant 2), and rather explicit modeled discs scaled to 31 % of the original dimension placed at the top and bottom of the fuel zone (variant 3).

6.2.3.1 Variant 1: Insertion of one reduced fuel disc in the core mid-plane (VSM1)

Here, one explicit modeled disc, scaled to 62 % of the original height, is inserted in the core mid-plane (see Figure 6.11).

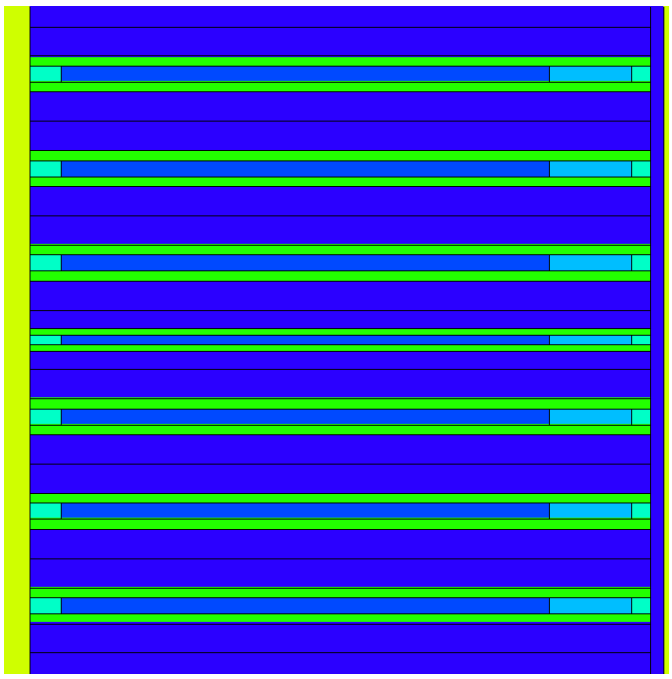

Figure 6.11: *Side view of the MCNP6 vertical stack model with inserted reduced fuel plate in the core midplane. The original involute shaped fuel plates are realized as "virtual discs", with the aluminum holdings and the two fuel zones with different uranium densities. In the core midplane a reduced fuel plate is inserted to preserve the total uranium core inventory. The remaining core layout stays the same.*

Multiplication factor With the control rod at a position of −6.92 cm from core midplane (see chapter 6.1), 10^6 neutrons per cycle, 150 active and 25 inactive cycles MCNP6 calculates for this model variant an effective multiplication factor $k_{\text{stack,mid}}$ of

$$k_{\text{stack,mid}} = 0.99775 \pm 0.00007 \tag{6.5}$$

which matches the value of the involute model Original model with involute shaped fuel plates (OISM) (Equation (6.2)) within the uncertainty margin.

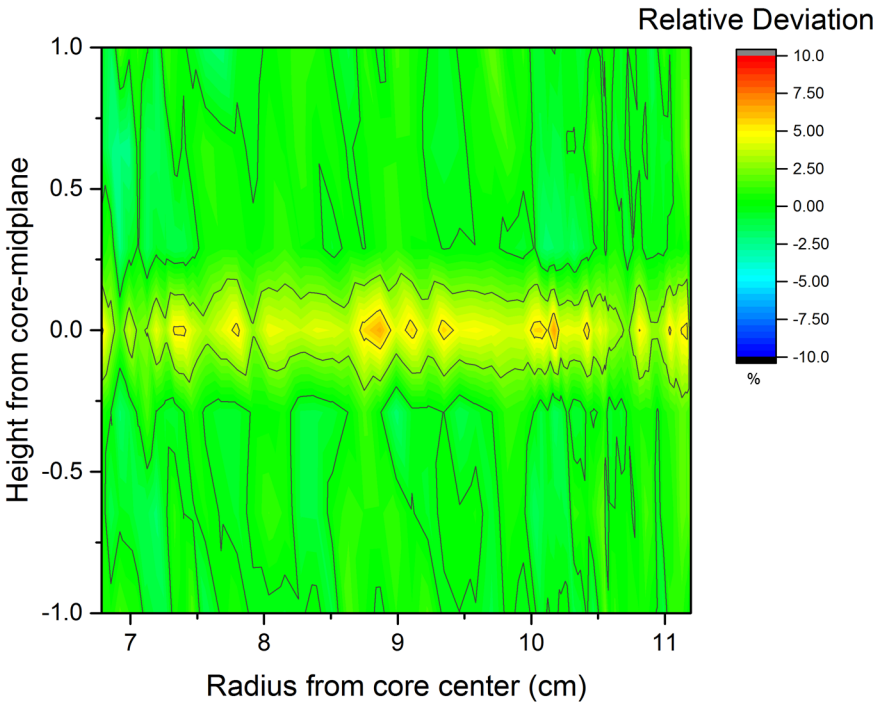

Figure 6.12: *Relative deviation in % of the power deposition at BOL around the core midplane between one representative involute shaped fuel plate (OISM, see Figure 6.3) and the corresponding part of the vertical stack model with a reduced "virtual disc" inserted in the core midplane (VSM1) in the sense of "VSM1 − OISM", as calculated with MCNP6. In the area of the reduced fuel plate, the vertical stack model overestimates the power deposition by 5 % to 7 %. For the rest both models deliver matching results within ±2 %.*

Power deposition A scaled fuel disc in core mid-plane leads to a local overestimation of the power deposition, as shown in Figure 6.12: The power deposition is 7.5 % too high compared to the original involute shaped fuel plates. This violates one of the criteria defined in chapter 6.2, because such a deviation would cause incorrect results for the subsequently calculated transients. As already stated, the models developed within this thesis should use as little unphysical approximations as possible. By adjusting the uranium density the power deposition can be tuned within certain limits given by the manufacturing tolerances. According to the specification of FRM II's fuel element it is possible to make local adjustments of the uranium density within

certain areas [80]. This gives the possibility to adjust the reduced disc without making unphysical approximations. In the specification of the current fuel element three areas for the uranium

Table 6.1: *Specification for the allowed uranium distribution for the current U_3Si_2-fuel element. For the middle section of the fuel zone the allowed deviation of the uranium distribution is far more strict than for both the top and bottom zone.*

Zone C (top)	Uranium density 3 g/cm³	+12% to −100%
	Uranium density 1.5 g/cm³	+15% to −100%
Zone B (mid)	Uranium density 3 g/cm³	±12%
	Uranium density 1.5 g/cm³	+15% to −20%
Zone A (bottom)	Uranium density 3 g/cm³	+12% to −100%
	Uranium density 1.5 g/cm³	+15% to −100%

distribution are defined [83]: Zone A from −35 cm to −33.65 cm, zone B from −33.65 cm to 33.4 cm and zone C from 33.4 cm to 35 cm. In each area the uranium density can vary within certain limits (see Table 6.1). In both the top and bottom zone, the limits for the uranium density are much more generous than in the middle of the fuel element. Within the limits given in Table 6.1, the uranium density in the reduced disc can be lowered, but it must be lowered by the same percentage due to consistency reasons for both the 3 g/cm³ and the 1.5 g/cm³ zone. Different changes of the uranium density for both zones are considered to be arbitrary and thus not realistic. To compensate the power over-estimation from Figure 6.5, the uranium density was lowered by 9 % in the middle disc. Adjustments like this have to consider the tolerance of

Table 6.2: *In the second row the allowed ^{235}U mass according to [83] is shown. The other three rows show the calculated ^{235}U masses for the three investigated substitutional models where the uranium density was locally reduced.*

Specification/Model	^{235}U mass g
Specification of fuel element	7539± 74
One explicit fuel plate (core midplane)	7531
Two homogenized fuel plate (top/bottom)	7526
Two explicit fuel plate (top/bottom)	7526

uranium density and the ^{235}U–mass as well. Table 6.2 gives the total ^{235}U–mass and its tolerance in one fuel element as 7539 ± 74 g [83] and the calculated ^{235}U–mass used to set up the different variants of the VSM, where the uranium density was locally reduced. With reducing the uranium density by 9 % the ^{235}U–mass is still within the thresholds. As shown in Figure 6.13 and as expected, the lower uranium density leads to a decreased power deposition in the core mid-plane. For the 1.5 g/cm³ zone, MCNP6 calculates deviations of ±2 %, but in the zone with an uranium density of 3 g/cm³ the deviations rise to 6 %. This shows that with the same adjustment of the uranium density matching results for the whole zone around the reduced fuel disc are barely achievable. Moreover, in the core mid-plane such large deviations are hardly acceptable.

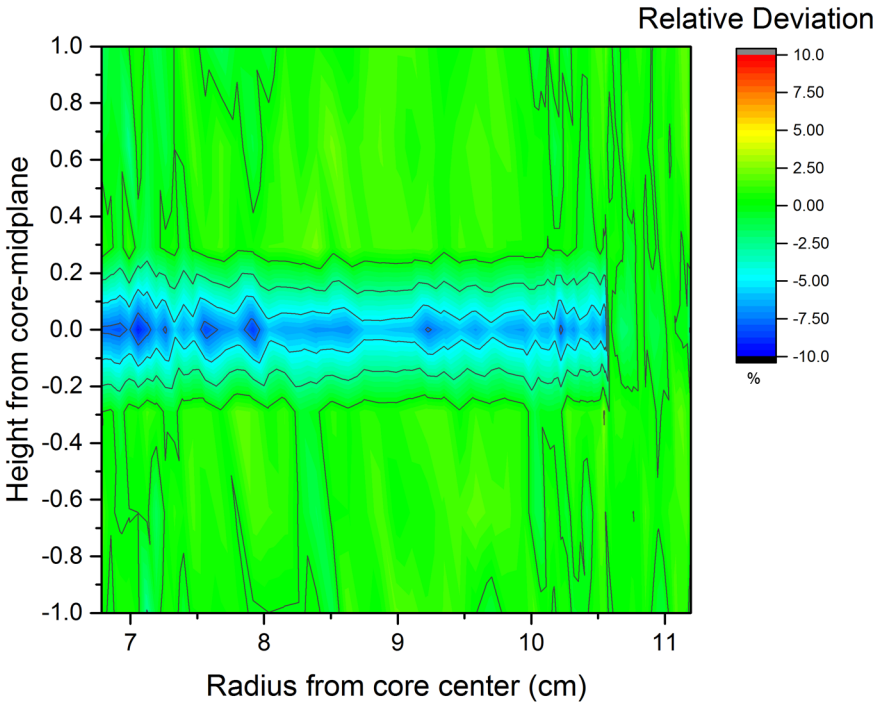

Figure 6.13: *Deviation in % of the power deposition at BOL between one representative involute shaped fuel plate (OISM, see Figure 6.3) and the corresponding part of the vertical stack model with a reduced "virtual disc" inserted in the core midplane (VSM1) after adjustment of the uranium density in the sense of "VSM1 − OISM", as calculated with MCNP6. In the zone with an original uranium density of* $1.5\,\mathrm{g/cm^3}$ *the calculated power depositions match within* $\pm 2.5\,\%$*, but for the high-density zone the power deposition is now underestimated between* $5\,\%$ *and* $7\,\%$*.*

Thermal and fast neutron flux distribution As Figure 6.14(a) shows, the thermal neutron fluxes match within $\pm 1.5\,\%$ for the whole core, except in the hafnium absorber and at the top and the transition zone between of the fuel element and the heavy water moderator tank (see Chapter 6.2.4). As mentioned before, inside the hafnium absorber the neutron statistic is very poor which leads to higher but negligible deviations in that particular area. Furthermore, the deviations at the top and outside of the fuel plates in direction to the moderator tank increase to $\pm 3\,\%$. Figure 6.14(b) shows matching fast neutron fluxes for the whole geometry.

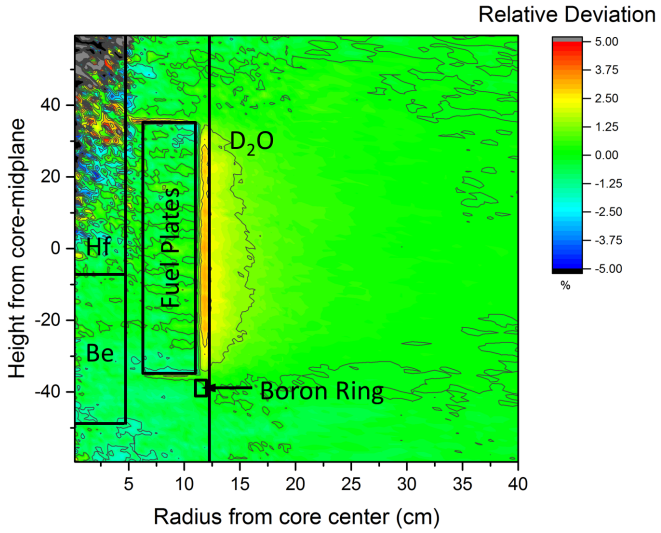

(a) Comparison of thermal neutron flux

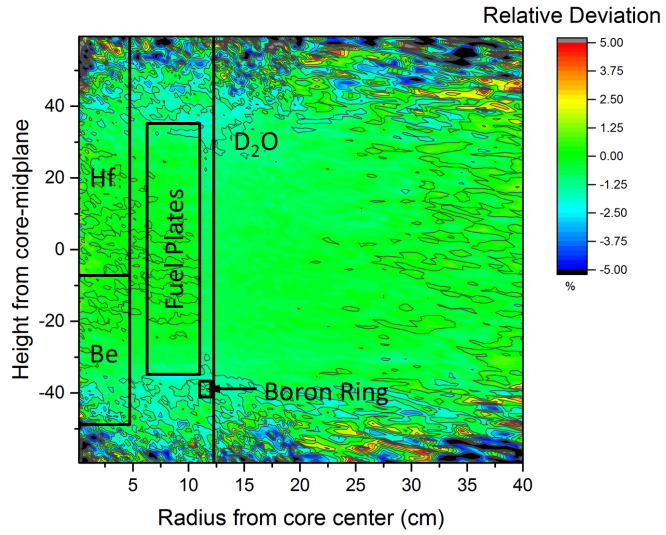

(b) Comparison of fast neutron flux

Figure 6.14: *The top panel (a) shows the relative deviation in % of the thermal neutron flux at BOL between the original involute shaped fuel plates (see Figure 6.3) and the vertical stack model with a reduced "virtual disc" inserted in the core midplane (VSM1) in the sense of "VSM1 − OISM". For most of the geometry both fluxes match within ±1 %, except between the outer edge of the fuel zone and the heavy water moderation tank, where the thermal neutron flux is overestimated by ±2.5 % to ±3 %. Near the hafnium absorber the deviations are increased in a statistically manner due to the poor statistics in MCNP6. The bottom panel (b) shows the corresponding relative deviation in % of the fast neutron flux. For most of the geometry both fluxes match within ±1 %. At the very top and bottom zones the neutron statistics get poorer, so the deviations are statistical artifacts.*

6.2.3.2 Variant 2: Insertion of two mixed, reduced fuel discs (VSM2m)

In this varaint of the VSM, two reduced discs with homogenized material, i.e. mashed fuel and cladding are inserted at both the top and bottom of the active fuel zone. Each disc is scaled to 31 % of the original height (see Figure 6.15).

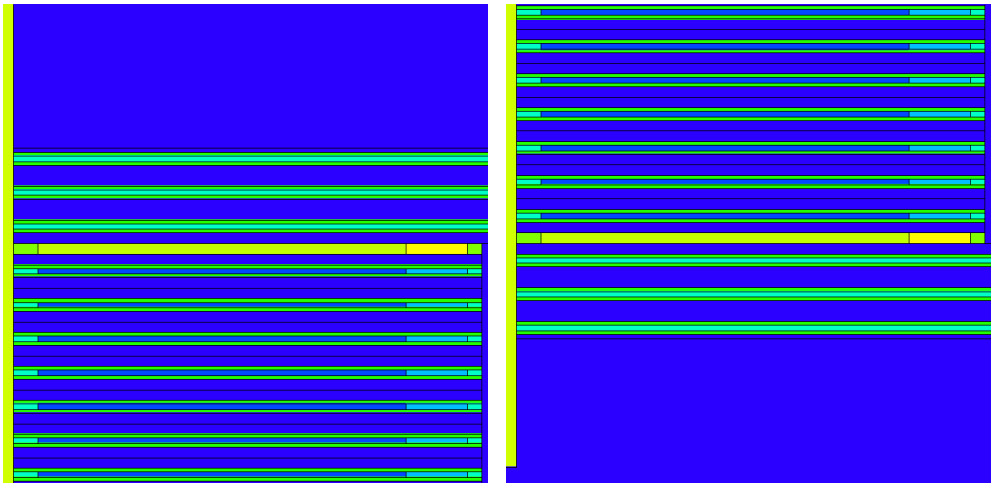

(a) Top section (b) Bottom section

Figure 6.15: *In the left panel (a) the top section of the vertical stack model is shown, where one mixed, reduced fuel plate is inserted. It can be seen, that the aluminum holdings and both zones containing fuel are separately mixed. In the right panel (b) the bottom section, modeled with the equivalent method, is depicted.*

The local power deposition changes as depicted in Figure 6.16 compared to the original model with involute shaped fuel plates. In the original model, neutrons diffusing from the water above and below the active zone back to the fuel zone see a clearly separated mixture of cooling water, cladding and fuel. In the model discussed here, neutrons diffusing back from the moderator see a solid disc of homogenized cladding, fuel and water. This gives rise to a local increase of the power deposition.

Adjustments This is depicted in the top panels of Figure 6.16 which show the relative deviation of the power deposition at the top and bottom of the fuel zone, respectively, as compared to the original model. At the top of the fuel zone, the insertion of a reduced and homogenized fuel disc leads to an overestimation of the power deposition by more than 10 % for the 3 g/cm^3 zone and by 6 % for the 1.5 g/cm^3 zone. At the bottom of the fuel zone, a similar behavior is to be observed. Here, the power deposition is overestimated by more than 10 % in the 3 g/cm^3 zone and by 8 % in the 1.5 g/cm^3 zone.
To make the model discussed here suitable for further calculations, the two reduced plates had to be adjusted appropriately (see Chapter 6.2.3.1). To match the power deposition, the uranium density of the two reduced discs has slightly been reduced to 2.656 g/cm^3 in the former 3 g/cm^3 area, and to 1.317 g/cm^3 in the original 1.5 g/cm^3 area, respectively. This equals to a 12 % decrease for both the 3 g/cm^3 and 1.5 g/cm^3 zone. These adjustments are well within the technical specification of a FRM IIs fuel element (see Table 6.1). As is shown in Table 6.2, the total ^{235}U mass is also within the specification.

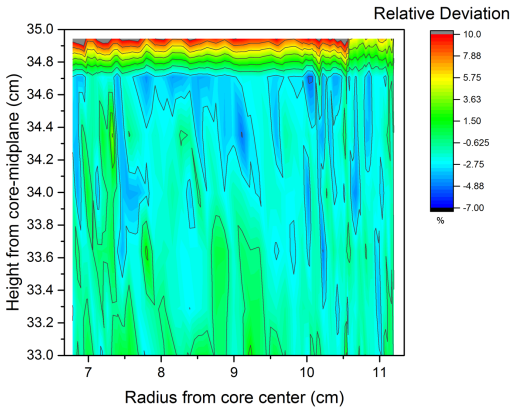

(a) Top section without adaption

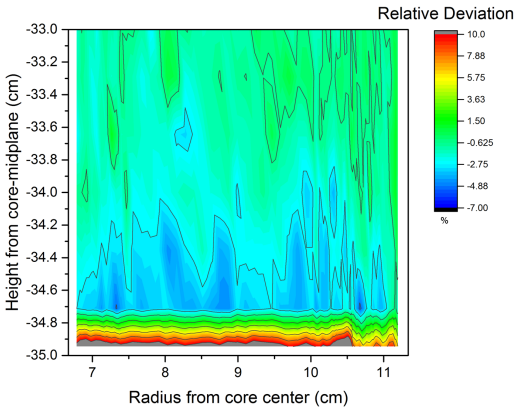

(b) Bottom section without adaption

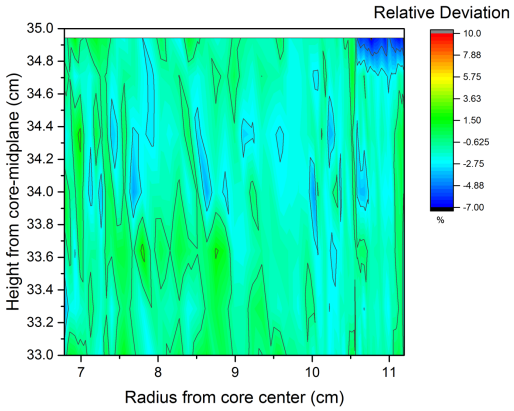

(c) Top section with adaption

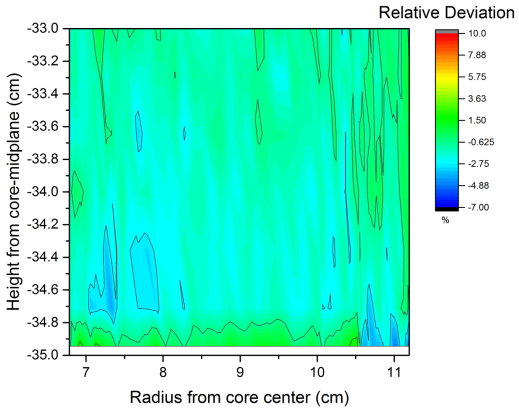

(d) Bottom section with adaption

Figure 6.16: *The top panels (a) and (b) show the relative deviation in % between the power deposition at BOL of the original involute shaped fuel plates (OISM, see Figure 6.3) and the vertical stack model with mixed, reduced "virtual disc" inserted at the top (a) and bottom (b) of the fuel zone (VSM2m) in the sense of "VSM2m − OISM". At the top the VSM2m overestimates the power deposition by 7 % to 10 %, whereas at the bottom the power deposition is overestimated by more than 10 %. Both bottom panels show the same comparison of both models after the adjustments of the uranium density. Here, the calculated power depositions match within ±5 %.*

Multiplication factor For a fresh core and with a neutron population of 10^6, 150 active and 25 inactive cycles MCNP6 calculates an effective multiplication factor $k_{\text{stack,mix}}$ of

$$k_{\text{stack,mix}} = 0.99760 \pm 0.00009 \tag{6.6}$$

for this model which is in agreement within the uncertainties with the multiplication factor obtained from the original model (see Eq. (6.2)).

Adjusted power deposition In the bottom panels of Figure 6.16 the impact of the adjustments of the uranium density on the local power deposition is shown. The power deposition matches within ±3.5 % in the 3 g/cm³ zone. For the outer zone with lower uranium density, the power deposition is now 5 % lower at the top and 3 % lower at the bottom of the fuel zone. This allows a more meaningful comparison of the VSM1 variant with the OISM.

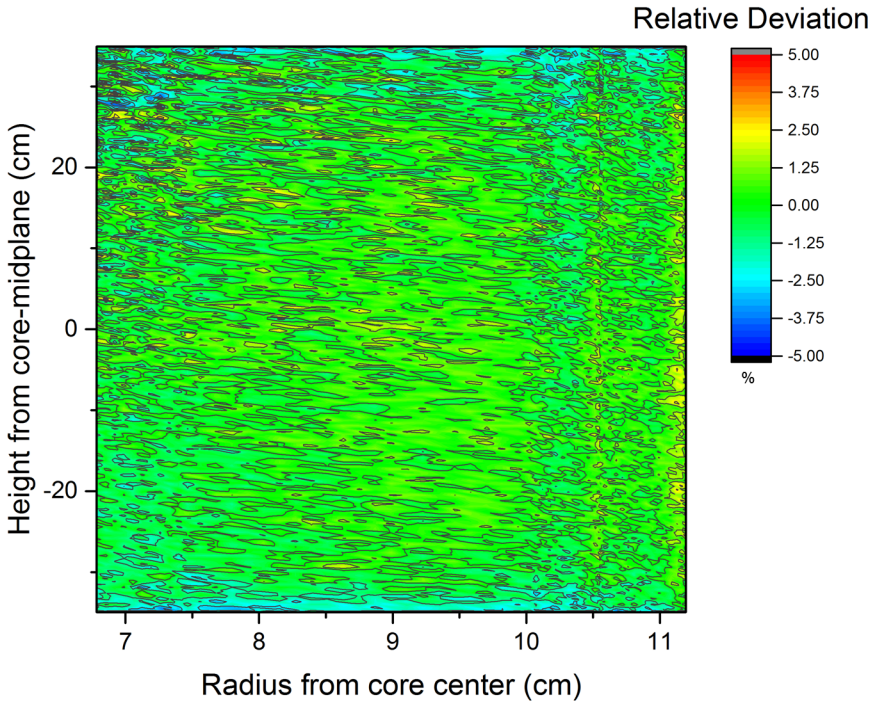

Figure 6.17: *Relative deviation in % of the power deposition at BOL between the original involute shaped fuel plates (OISM, see Figure 6.3) and the vertical stack model with mixed, reduced discs (VSM2m) in the sense of "VSM2m − OISM". For the whole geometry the calculated power deposition matches within ±2.5 %. A detailed comparison at the top and bottom of the fuel zone is depicted in the bottom panels of Figure 6.16.*

Figure 6.17 shows the full view relative deviation in percent of the power deposition of the two models. Except for the deviations that were already discussed and shown in the bottom panel of Figure 6.16, the power deposition matches within ±2.5 % for the rest of the fuel zone.

Thermal and fast neutron flux distribution Figure 6.18(a) shows the relative deviation in percent of the thermal neutron flux. In the area where the beam tubes are situated, the thermal neutron flux matches within ±2 %. Close to the fuel zone and in the heavy water moderator tank, the deviations increase to 3 % (see Chapter 6.2.4). As in all comparisons of the thermal neutron flux before, due to the strong absorbing characteristics of the hafnium absorber (see Figure A.1) the thermal neutron flux is rather small. As a result the deviations increase statistically in that particular area.
The fast neutron flux (see Figure 6.18(b)) matches within ±1.5 %. Only at the edges where the fast neutron flux decreases to a magnitude of $10^{12}\,\mathrm{n/cm^2s}$ (see Figure 6.5), the deviations increase due to statistical issues. Because this area is not crucial for transients, this model could serve as feasible substitutional geometry. The final evaluation of all possible models is based on a grading system and is shown in Chapter 6.2.5.

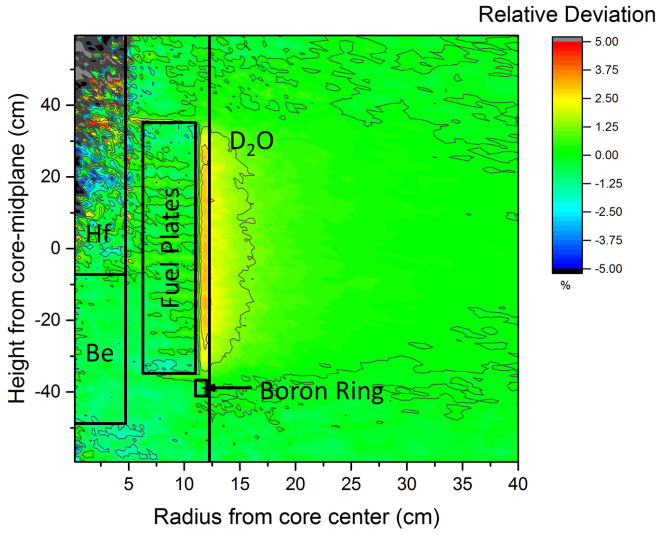

(a) Comparison of thermal neutron flux

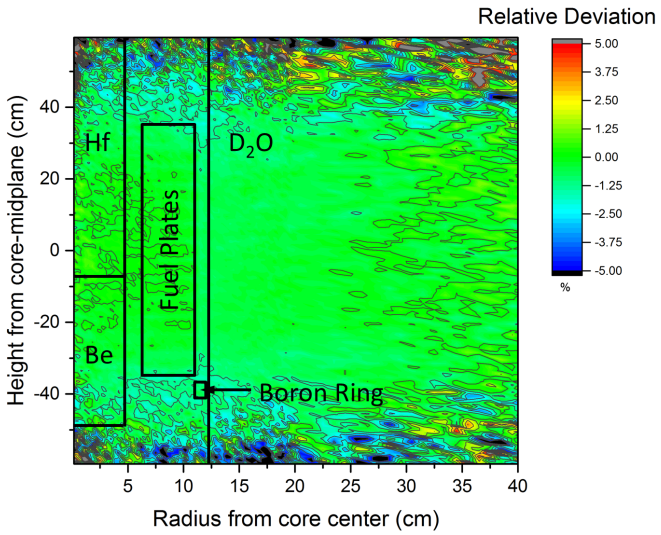

(b) Comparison of fast neutron flux

Figure 6.18: *The top panel (a) shows the relative deviation in % of the thermal neutron flux at BOL between the original involute shaped fuel plates (OISM, see Figure 6.3) and the the vertical stack model with inserted homogenized, reduced fuel plates (VSM2m) in the sense of "VSM2m − OISM". The thermal neutron fluxes match within ±2 %. Except in the fuel zone and the heavy water moderator tank where the deviations are increased to 3 %. The hafnium absorber increases the deviations artificially due to the poor neutron statistics in MCNP6. The bottom panel (b) shows the corresponding relative deviation in % of the fast neutron flux. For the fast neutron flux, both models deliver matching results within ±1.5 %. Only at the edges the deviation artificially increases due to poor neutron statistics.*

6.2.3.3 Variant 3: Two reduced fuel plates (VSM2)

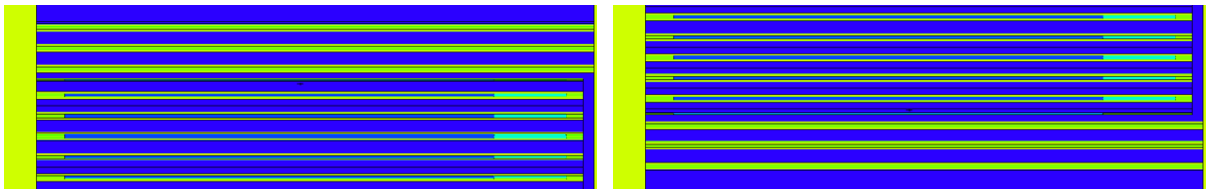

(a) Top section (b) Bottom section

Figure 6.19: *The left panel (a) shows the top section of the vertical stack model where an explicitly modeled, reduced fuel disc (VSM2) is inserted. The right panel (b) shows the equivalent bottom section.*

In this variant, instead of discs with homogenized material, two scaled (31 %) but explicitly modeled discs are inserted at the top and bottom of the fuel zone (see Figure 6.19). As already described in Chapter 6.2.3.2, in order to obtain matching power depositions at the top and bottom of the fuel zone, adjustments of the uranium density of these reduced plates are necessary. Hence, the uranium densities of these two reduced discs are again slightly lowered to 2.656 g/cm³ in the original 3 g/cm³ area and to 1.317 g/cm³ in the original 1.5 g/cm³ area, respectively. This 12 % decrease of uranium density is well within the bounds for the allowed uranium density given in Table 6.1.

Muliplication factor A control rod position of −6.92 cm from core mid-plane, 10^6 particles per cycle, 25 inactive and 150 active cycles this modified vertical stack model delivers an effective multiplication factor $k_{\text{stack,tb}}$ of

$$k_{\text{stack,tb}} = 0.99772 \pm 0.00009, \tag{6.7}$$

which is in perfect agreement with the multiplication factor obtained from the original model (see eq. 6.2).

Power deposition To calculate the power deposition a mesh tally TMESH type 3 which covers the fuel zone was used in MCNP6. Figure 6.20 shows the relative deviation in % of the calculated power deposition. In Figure 6.21 detailed views of the edges of the fuel zone are shown (Figure 6.21(a) top, Figure 6.21(b) bottom). Except for the top and bottom corner of the low uranium density zone, the calculated power deposition of both models matches within ±1.25 %. At the top outer corner of the zone with lower uranium density, the deviations are increased between 5 % and 7.5 %. A similar behavior is observable at the bottom right corner, where the deviations are increased to 5 %. For consistency, the uranium density was lowered by the same percentage for both uranium density zones, even though both zones would need a different treatment. The adjustments made are within the fabrication tolerances (Chapter 6.2).

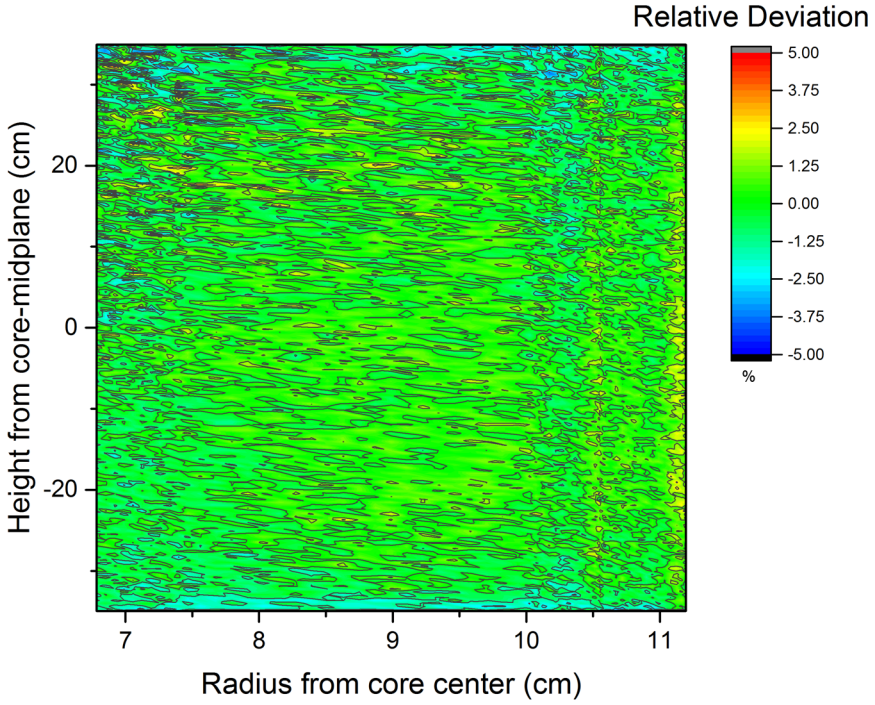

Figure 6.20: *Relative deviation in % of the power deposition at BOL between the original involute shaped fuel plates (OISM, see Figure 6.3) and the vertical stack model with explicitly modeled, reduced fuel discs in the sense of "VSM2 – OISM". Both models deliver matching results within* $\pm 1.25\,\%$.

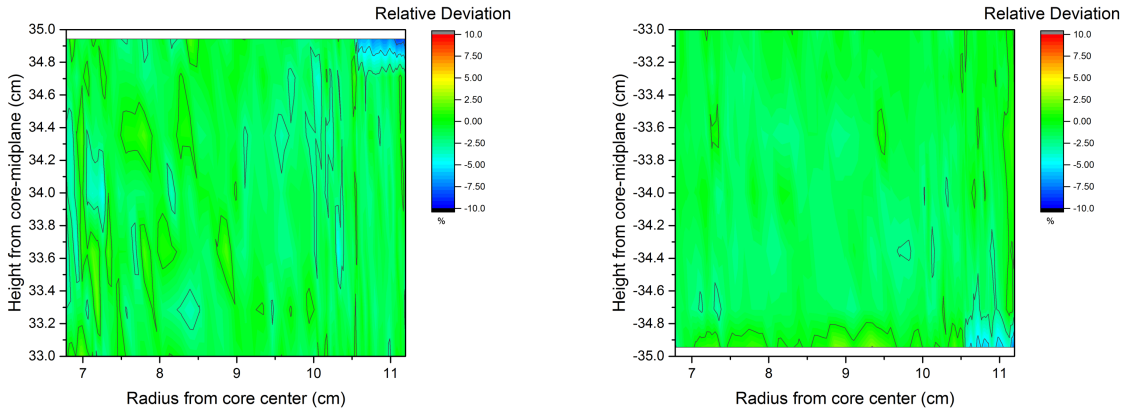

(a) Top section

(b) Bottom section

Figure 6.21: *In the left panel (a) the comparison of the power deposition at BOL in the top section of the fuel zone is shown. For the zone with an original uranium density of* $3\,\mathrm{g/cm^3}$ *the results match within* $\pm 1.25\,\%$*. Only at the top right corner, in the zone with originally* $1.5\,\mathrm{gU/cm^3}$*, the deviation increases to a maximum of* $7.5\,\%$*. In the right panel (b) the equivalent results for the bottom selection are depicted. For the high uranium density zone the results match within* $\pm 1.25\,\%$ *and for the low uranium density zone the results match within* $5\,\%$*.*

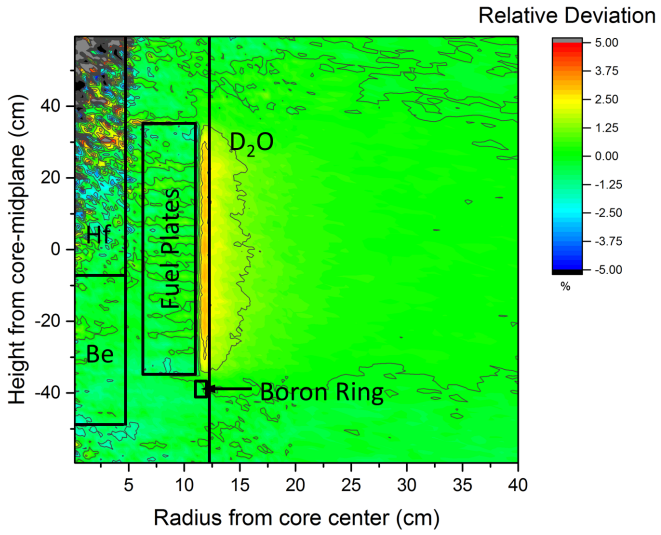

(a) Comparison of thermal neutron flux

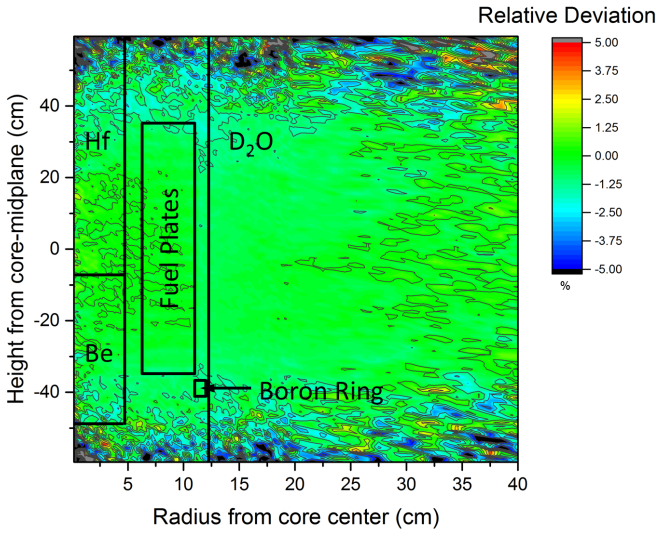

(b) Comparison of fast neutron flux

Figure 6.22: *The top panel (a) shows the relative deviation in % of the thermal neutron flux at BOL between the original involute shaped fuel plates (OISM, see Figure 6.3) and the vertical stack model with inserted homogenized, reduced fuel plates (VSM2) in the sense of "VSM2 − OISM". The thermal neutron fluxes match within ±1 %. Between the fuel zone and the heavy water moderator tank the deviation increases to 3 %, and in the hafnium absorber the deviations are artificially increased due to the poor neutron statistics in MCNP6. The bottom panel (b) shows the corresponding relative deviation in % of the fast neutron flux. For the fast neutron flux, both models deliver matching results within ±1 %. Just at the edges the deviation increases due to poor neutron statistics in MCNP6.*

Thermal and fast neutron flux distribution To calculate the thermal and fast neutron flux distribution a mesh tally TMESH type 1 with corresponding energy intervals were used. Figure 6.22(a) shows the deviation of the thermal neutron flux of both models. In the small water gap between the fuel element and the heavy water tank, the vertical stack model overestimates the thermal flux between 2.5 % and 3 % (see Chapter 6.2.4). Inside the hafnium absorber the already described statistical problems lead to an increase of the fluctuations. For the remaining geometry, both calculated fluxes match within 1 %.
The deviation of the fast neutron flux for both models is shown in Figure 6.22(b). Disregarding the high statistical uncertainties at the outer zones caused by increasing moderation, the fast neutron fluxes match perfectly within ±1 %.

6.2.4 Thermal neutron flux between the fuel zone and the heavy water moderator tank

During the discussion of the concentric tube model (CTM) and the different variants of the vertical stack model (VSM1, VSM2m, VSM2), it has been shown that in the small gap between the fuel zone and the heavy water moderator tank there is a small, but systematical deviation of the thermal neutron flux (see Figures 6.8(a), 6.14(a), 6.18(a), 6.22(a)). This effect is caused by the different material composition that the neutrons see when diffusing back from the heavy water into the fuel zone. The CTM and the VSM model, represent the extreme cases:

- The tubes in the CTM are parallel to the outer tubing of the fuel element, so the neutrons first see pure light water. This leads to the observed underestimation of the thermal flux there.
- Contrary to that, the virtual discs of the VSM are perpendicular to the outer tubing, so the neutrons see a mixture of water, aluminum and blank fuel. Because of the perpendicular connection, an overestimated thermal neutron flux is observed.

As depicted in Figure 6.23 the original involute shaped fuel plates are something between these two approximations, and so is the corresponding thermal neutron flux.

6.2.5 Choice of substitutional geometry

A grading system has been used in order to identify the best fitting model for use in further steps. In this approach, the multiplication factor, the power deposition, the thermal and the fast neutron flux of all models are compared and rated. To map the importance of each parameter, for each model i a rating factor β_i is introduced which is based on the difference of the multiplication factor $k_\mathrm{eff,i}$ from the reference value k_evolv (see Chapter 6.1), and on the average deviation and their corresponding standard deviation for the power deposition ($\iota_\mathrm{power,i}, \sigma_\mathrm{power,i}$), the thermal neutron flux ($\iota_\mathrm{therm,i}$,$\sigma_\mathrm{therm,i}$) and the fast neutron flux ($\iota_\mathrm{fast,i}, \sigma_\mathrm{fast,i}$). The input factors, i.e. average deviation and the corresponding standard deviation were calculated with C^2 (see Appendix D.8). In order to take the weight of each parameter properly into account, β_i is defined as follows:

$$\begin{aligned}\beta_\mathrm{i} = \frac{1}{16}(&4 \cdot \exp|k_\mathrm{eff,i} - k_\mathrm{evolv}| + 3 \cdot \exp|\iota_\mathrm{power,i}| + 3 \cdot \exp|\sigma_\mathrm{power,i}| + \\ &+ 2 \cdot \exp|\iota_\mathrm{therm,i}| + 2 \cdot \exp|\sigma_\mathrm{therm,i}| + 1 \cdot \exp|\iota_\mathrm{fast,i}| + 1 \cdot \exp|\sigma_\mathrm{fast,i}|).\end{aligned} \tag{6.8}$$

The weights of the individual parameters were chosen in an ad hoc manner. The exponential functions were introduced to make β_i better distinguishable. According to Eq. 6.8 an ideal model would yield $\beta_\mathrm{i} = 1$. Hence, the model with β_i closest to 1 is chosen.

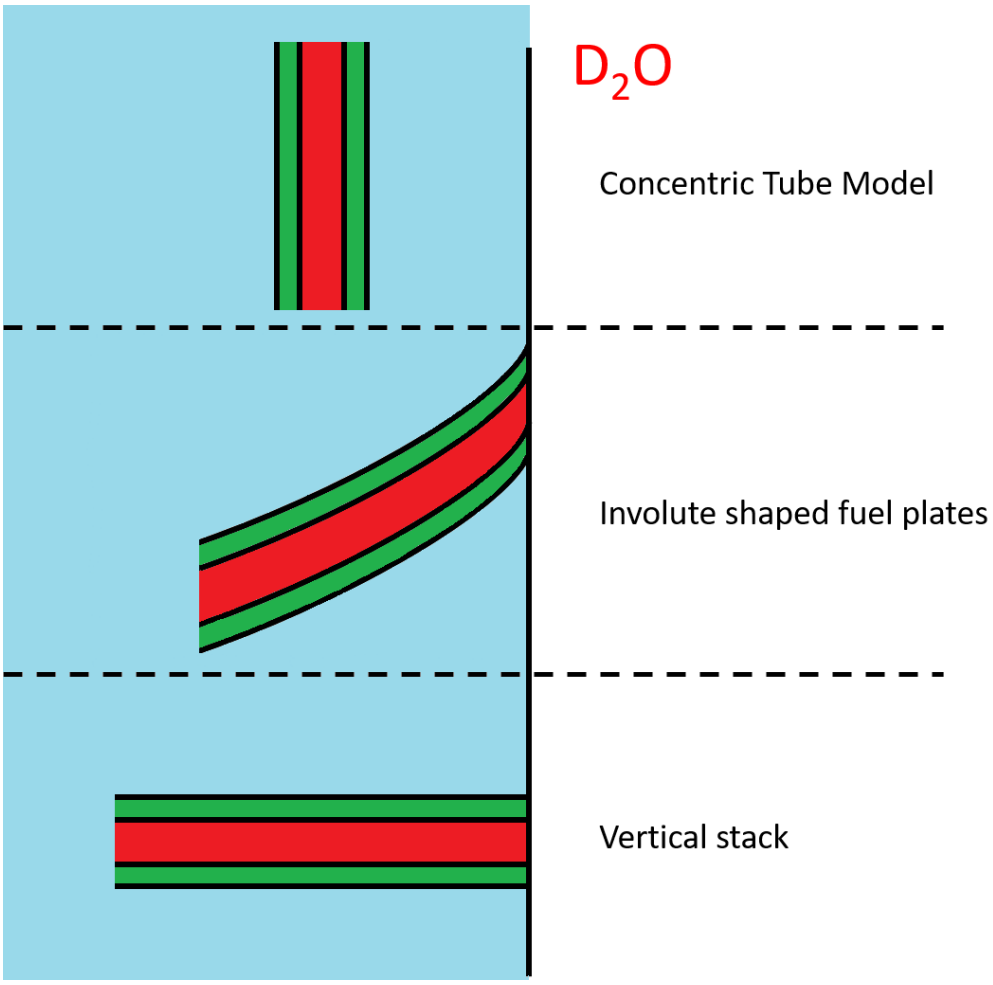

Figure 6.23: *Different shapes of the fuel plates depending upon the model used. One fuel plate with cladding and fuel is situated inside cooling water (left) and the transition to the heavy water moderation tank (right) is depicted. At the top a part of the concentric tubes model is shown, the middle picture shows the actual situation with the involute shaped fuel plates and at the bottom the vertical stack model is depicted from the side.*

As depicted in Table 6.3, the vertical stack model with two reduced, explicit modeled fuel discs at the top and bottom of the fuel zone (VSM2) (see chapter 6.2.3.3) is the best possible option, and will be thus used for the following steps. Its multiplication factor matches perfectly with the reference model OISM, the average deviation of the power deposition is almost zero with a small standard deviation, compared to the other models. Regarding the fast flux distribution only the Concentric tubes model (CTM) performs better, but for the thermal neutron flux this model performs best with a deviation of nearly zero and the smallest corresponding standard deviation.

Table 6.3: *Grading factor β_i for each investigated model. Also the corresponding average deviation and the standard deviation of the power deposition ($\iota_{\mathrm{power,i}}, \sigma_{\mathrm{power,i}}$), thermal ($\iota_{\mathrm{therm,i}}, \sigma_{\mathrm{therm,i}}$) and fast neutron flux ($\iota_{\mathrm{fast,i}}, \sigma_{\mathrm{fast,i}}$) as calculated with* C^2 *is given.*

Model #	**Model name**	$\mathbf{k}_{\mathrm{eff,i}}$	**Deviation power deposition** ($\iota_{\mathrm{power,i}} \pm \sigma_{\mathrm{power,i}}$)	**Deviation thermal flux** ($\iota_{\mathrm{therm,i}} \pm \sigma_{\mathrm{therm,i}}$)	**Deviation fast flux** ($\iota_{\mathrm{fast,i}} \pm \sigma_{\mathrm{fast,i}}$)	**Grading factor** β_i
1	CTM	0.99711	0.0283 ± 1.303	-0.448 ± 0.643	0.374 ± 0.361	2.174
2	MMFZ	1.02994	-0.397 ± 3.866	-11.264 ± 3.384	-4.076 ± 0.675	9765.086
3	VSM1	0.99775	-0.147 ± 1.020	0.323 ± 0.797	-0.619 ± 0.445	2.079
4	VSM2m	0.99760	-0.155 ± 0.943	0.311 ± 0.809	-0.597 ± 0.410	2.037
5	VSM2	0.99772	-0.144 ± 0.947	0.313 ± 0.775	-0.597 ± 0.392	2.026

6.3 Serpent 2 model

6.3.1 Comparison of the core key parameters

Based on the final choice of the modified vertical stack model (VSM2) (see chapter 6.2.3.3 and 6.2.5), the geometrically equivalent Serpent 2 model has been created. In order to use the Serpent 2 model for the calculation of multi-group cross sections, prompt fission spectra, inverse velocities, delay neutron fractions and delay neutron decay constants, respectively, it is validated by comparison of the resulting core key parameters with the MCNP6 model using involute shaped fuel plates. Because at the time the calculations were performed, Serpent 2 has been much more demanding in terms of computer memory than MCNP6, the calculations could only be performed with 50000 neutron histories per cycle. In order to reduce the resulting statistical error, the number of cycles had to be increased correspondingly. No variance reduction techniques as discussed in Chapter 2.2.1 were available in Serpent 2.

Table 6.4: *Multiplication factors obtained with MCNP6 and Serpent 2 using a total of 50000 neutron histories per cycle, 50 inactive and 250 active cycles.*

Code	Multiplication Factor
MCNP6	0.99794 ± 0.00029
Serpent 2	0.99832 ± 0.00031

Multiplication factor A comparative calculation with MCNP6 and Serpent 2 employing 50000 neutron histories, 50 inactive and 250 active cycles yielded the multiplication factors shown in Table 6.4. Both results match within their uncertainties and also match with the MCNP6 result calculated with more neutron histories (see Eq. (6.2)).

Power deposition Serpent 2 version 2.1.23 was not able to calculate the power distribution in the same way as MCNP6 [47], therefore only a comparison of the fission rate is possible using a mesh tally FMESH of type 4 with the same geometry like the FMESH used for the calculation of the power distribution (see Chapter 6.1). In Serpent 2, this FMESH has been substituted by 27 detectors with the same geometrical subdivisions. To compare the results from both codes, the results from Serpent 2 need to be post-processed, i.e. the cell volume need to be normalized, and the data from the individual meshes needs to be stitched together. Figure 6.24 shows the relative deviation of the calculated fission rates between MCNP6 and Serpent 2. For the whole geometry both codes deliver matching results within the statistical uncertainties. Near the hafnium absorber, where the fission density is fairly low (see Figure 6.3) and around the density jump, these fluctuations are increased. Figures 6.25(a) and 6.25(b) show a more detailed comparison of the fission densities at the borders of the fuel zone. At the bottom of the fuel plates, the fission rates match perfectly. Just at the very top, where the power deposition and hence the fission rate is decreased (see Figure 6.3), the deviations increase.

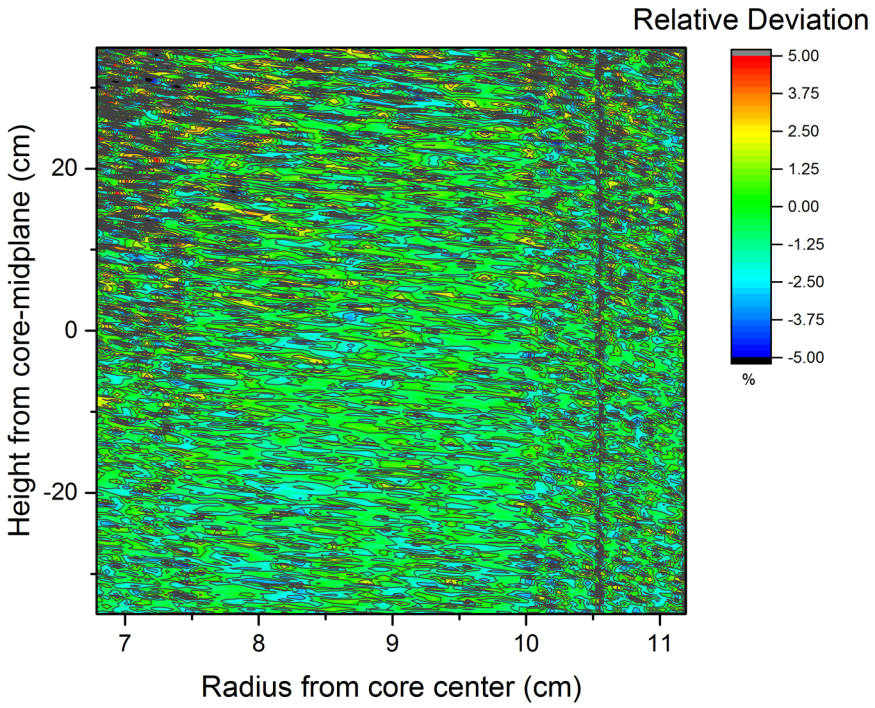

Figure 6.24: *Relative Deviation in % of the fission rate between MCNP6 and Serpent 2 in the sense of "Serpent 2 − MCNP6". The results are matching within statistical fluctuations. At a radius of* 10.56 cm *the influence of the density jump is visible.*

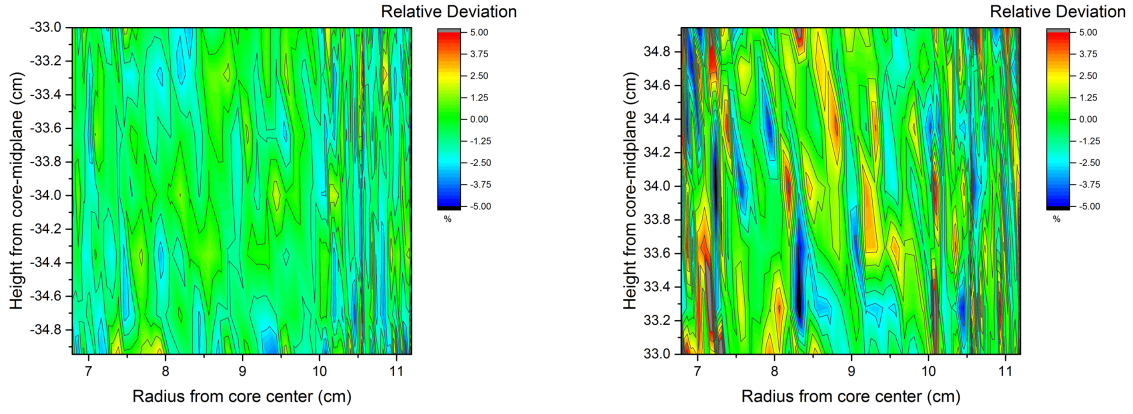

(a) Bottom section

(b) Top section

Figure 6.25: *In the left panel (a) the comparison of the fission rate of the top section of the fuel zone is shown. Both calculated fission rates match within statistical fluctuations in the rage of* ±5 %. *In the right panel (b) the equivalent results for the bottom section is depicted. Here, the deviations fluctuate between* ±2.5 %.

Thermal and fast neutron flux distribution In Serpent 2, four meshes were used in order to obtain the same mesh geometry as used in MCNP6. The first Serpent 2 mesh covers the area from $r = 0\,\text{cm}$ to $r = 20\,\text{cm}$ with a radial resolution of 0.3 cm, the second mesh covers $r = 20\,\text{cm}$ to $r = 50\,\text{cm}$ with a radial resolution of 1 cm, the third mesh covers $r = 50\,\text{cm}$ to $r = 100\,\text{cm}$ with a radial resolution of 2 cm, and the fourth mesh covers $r = 100\,\text{cm}$ to $r = 200\,\text{cm}$ with a radial resolution of 5 cm. As before for the fission rate, the data need to be post-processed in the same way.

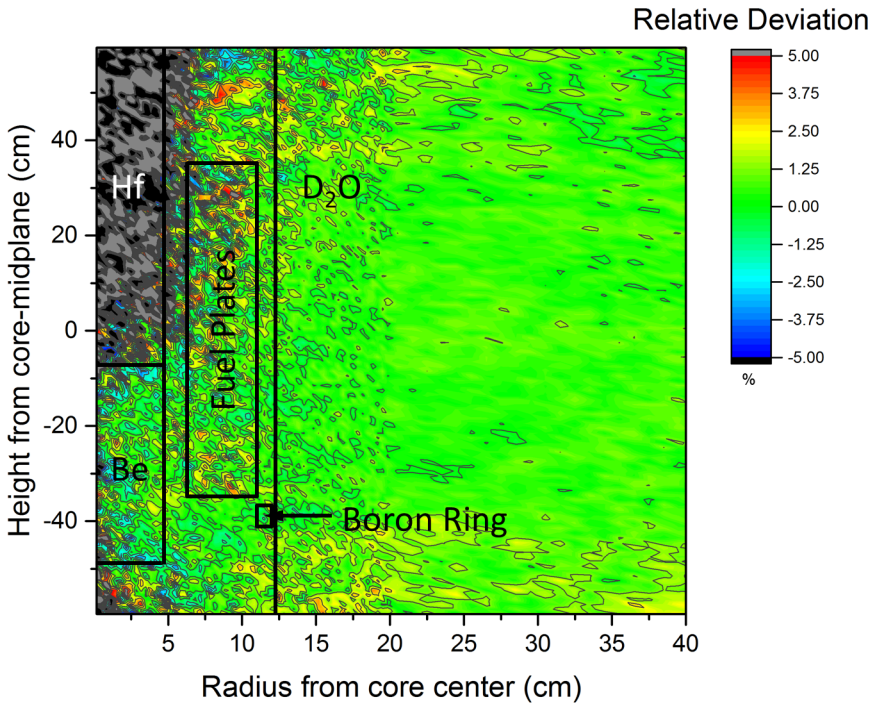

Figure 6.26: *Relative deviation in % of the thermal neutron fluxes, as calculated with MCNP6 and Serpent 2 in the sense of "Serpent 2 − MCNP6". Both fluxes match well within 2 %, except inside the hafnium absorber, where the deviations are increased artificially because of poor neutron statistics for both codes.*

In the fuel plates and in the region directly inside the heavy water moderator tank, where the emergency shutdown rods are installed, both codes deliver the same results for the thermal neutron flux distribution within statistical uncertainties. In the upper inner region, where the Hafnium–Absorber of the control rod is situated, there are strong statistical fluctuations, as shown in Figure 6.26. It is obvious that the absorber suppresses the neutron flux in this region, and with the settings used in MCNP6 and Serpent 2, respectively, the neutron statistics are too poor to allow for a meaningful comparison at such high resolution.
Inside the fuel plates the fast neutron fluxes match within statistical fluctuations of ±2 %, as shown in Figure 6.26. Near the fuel zone, inside the heavy water moderation tank, both fluxes also match well. The greater the distance from the fuel plates, the higher are the fluctuations due to the increasingly lower neutron statistics.

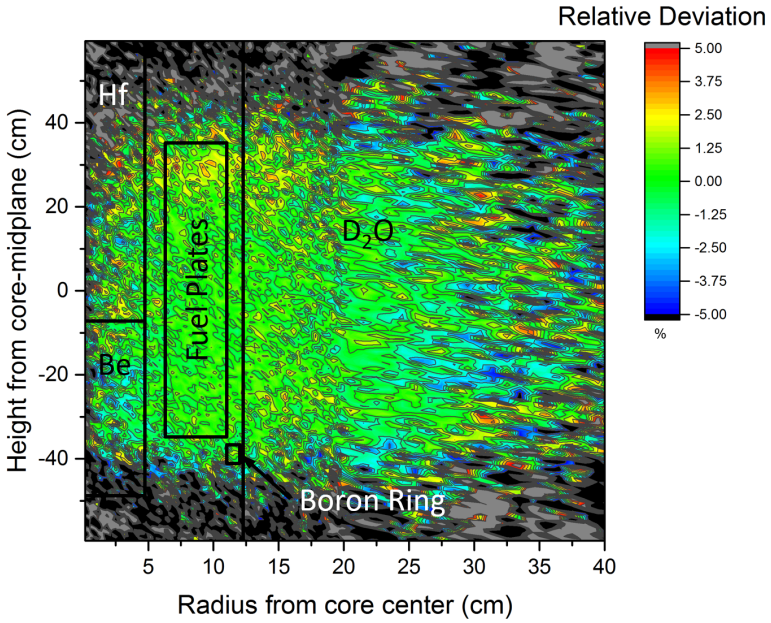

Figure 6.27: *Relative deviation in % of the fast neutron fluxes as calculated with MCNP6 and Serpent 2 in the sense of "Serpent 2 − MCNP6". Both fluxes match well within 2 %. With increasing distance to the fuel zone, the deviations increase due to increasing moderation and the higher statistical uncertainties in the calculated fast neutron flux.*

Validation Given the matching results for the multiplication factor, fission rate, thermal and fast neutron flux, respectively, the Serpent 2 model is considered to be sufficiently validated and adequate to calculate multi-group cross sections.

6.3.2 Calculation of the multi-group cross sections

6.3.2.1 General approach

The method implemented in Serpent 2 to calculate homogenized multi-group cross sections in each defined universe (see 2.2.1) is described in Chapter 4.2. To study the study the deterministic code TORT-TD later on several models will have to be created. Therefore, a maximum in flexibility should have to be achieved. Because Serpent 2 only can calculate multi-group cross sections within one universe, the model is created in the way that every single cell (see 2.2.1) is defined in one corresponding universe. In Figure 6.28 the basic idea of this concept is depicted.

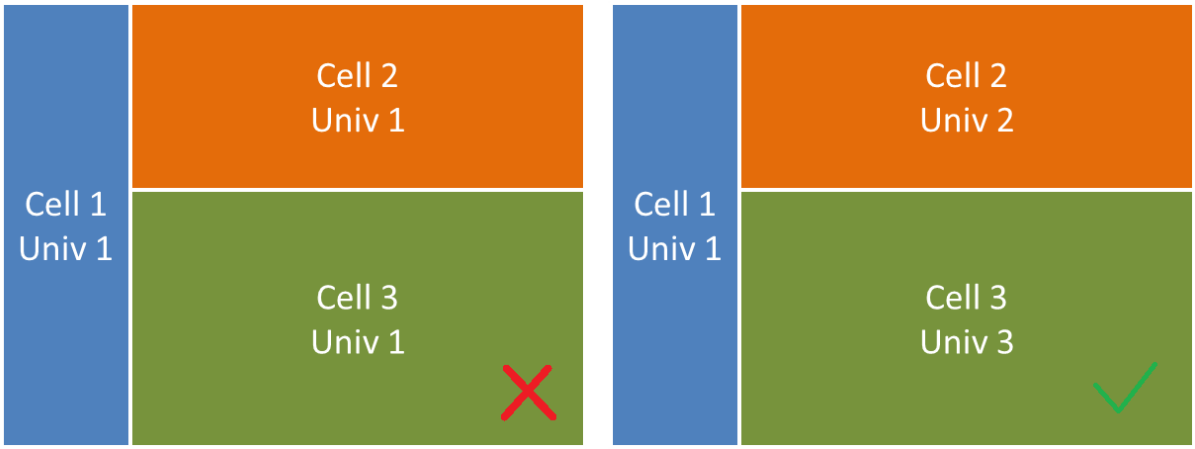

(a) Inflexible Option (b) Flexible Option

Figure 6.28: *In the left panel (a) the inflexible option for the cell definition is shown. Multiple cells (1 to 3) are combined in just one universe 1. In the right panel (b) the more flexible option is depicted. Here, for each cell one corresponding universe is defined.*

As it has been done regularly in MCNP6 before, multiple cells were combined in one universe, as it is shown in Figure 6.28(a), where the three cells 1 to 3 are combined into one universe 1. In contrast, in the here chosen approach each universe contains only one cell (see Figure 6.28(b)). With this approach cross sections for every single part of the reactor can be calculated quite fast. In order to obtain sufficiently small statistical uncertainties of the multi-group cross sections, the calculations were performed with version 2.1.25 of Serpent 2 on a linux cluster with 56 threads, employing 200000 neutron histories, 50 inactive, and 500 active cycles within a typical wall clock time of 2 h.

6.3.2.2 Handling of universes with poor neutron statistics

With the method described in Section 6.3.2.1, five zones in the reactor suffer from poor neutron statistics: three aluminum parts at both ends of the control rod, the helium above the heavy water fill level, and the hafnium control rod. Both the aluminum and hafnium zones are made of materials with small scattering and absorption cross sections and, moreover, these zones are far away from the high-flux regions. In the hafnium control rod, due to the strong absorbing character, there are just a few low energy groups with poor neutron statistics. Because of this, some important parameters, like the total cross section, the diffusion constant or the delayed

neutron parameters, cannot be calculated with the needed precision. Even though these zones and groups are claimed physically rather unimportant for the overall behavior of the reactor, numeric artifacts will appear that lead to unphysical results and even prevent convergence in TORT-TD.
To improve neutron statistics in these cells, the neutron flux, divided into 30 energy groups (see Table 6.7) to cover the whole energy range, is determined with a MCNP6 tally of type 4. Table A.1 shows the relative neutron flux in dependence of the corresponding energy range. The neutron fluxes in the remaining cells can be found in the Appendix E.
Each of the five problematic zones was rebuilt in a Serpent 2 model, whereas all cells representing the hafnium control rod are modeled explicitly. Together with the relative fluxes given in Table A.1, the external source mode [46] was used. This mode does not require a self-sustaining fission reactor. In this mode neutrons from a defined source are just sent through the geometry but all other features like calculating cross sections are fully functional. This way it is possible to calculate accurate multi-group cross sections as well as the remaining nuclear data needed as input for TORT-TD.

6.3.3 Geometrical division in critical areas

For spatially extended zones with steep gradients of the neutron flux, the above described method has to be adjusted. Serpent 2 calculates the averaged flux-weighted cross section for one universe (see chapter 4.2). If the spatial variation within one energy group is not negligible small, Serpent 2 would calculate unphysical results. So when there is a steep, non-linear flux gradient within one universe, the outcoming averaged cross sections are not fully correct. To achieve more accurate results the universe is divided into several smaller universes depending upon geometry and flux gradient. In the FRM II core model three zones are treated in this way: the beryllium reflector, the hafnium absorber and the heavy water moderator tank (see Figure 6.4). Figure 6.29 shows the finer subdivision of the beryllium reflector (Fig. 6.29(a)) and the hafnium absorber (Fig. 6.29(b)). The applied changes to the heavy water moderator tank are shown in Figure A.1 in the appendix. In total, the beryllium zone is divided into 17 additional universes, hafnium into 7, and in the heavy water moderator tank 78 additional universes have been introduced.

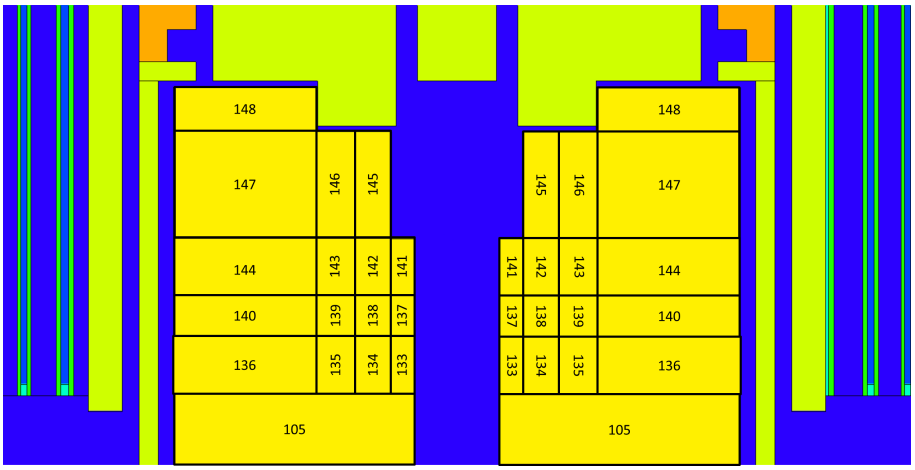

(a) Subdivision of Beryllium

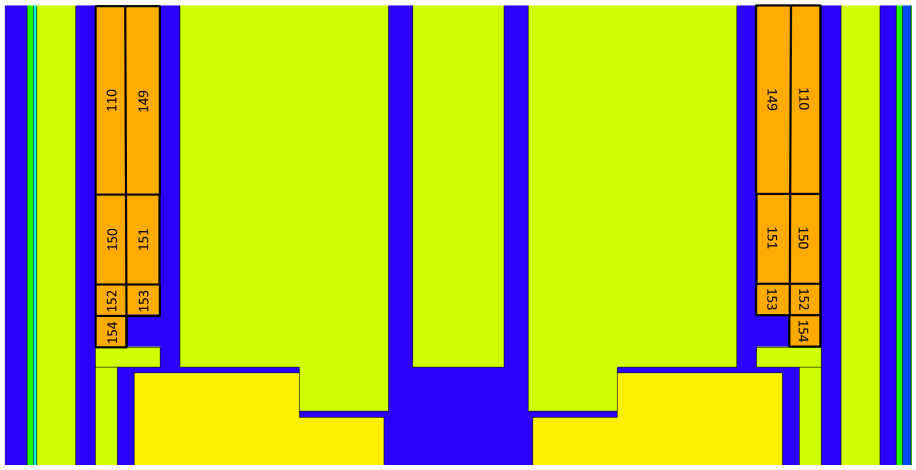

(b) Subdivision of Hafnium

Figure 6.29: *Due to the large flux gradients within both the beryllium follower and the hafnium absorber, these parts need a finer subdivision in order to calculate correct cross sections. The top panel (a) shows the detailed model for the beryllium follower, whereas in the bottom panel (b) the hafnium absorber is depicted.*

6.4 TORT-TD model

In the the next step, the vertical stack model (VSM2) is translated into an r-φ-z–mesh for use in TORT-TD. The meshing in the TORT-TD-geometry is aligned to the material borders of the real geometry. On top of that, the distance of neighboring nodes strongly depends on the total cross section of the material. To achieve numerically reliable results, the distance of two nodes has always to be significantly smaller than the neutron mean free path in the corresponding material.
With the self-developed post processing tool C^2 (see Appendix D), the TORT-TD mesh nodes are automatically created from the corresponding cross sections (see Chapter 6.3.2.1). In order to be employed for transient calculations, TORT-TD has to preserve all important reactor

key parameters (cf. Chapter 6.3). For the initial validation calculations, to account also scattering to higher energy groups cross sections to the first Legendre order have been used (see Chapter 2.1.1, 4.2, 6.4.2.3), a quadrature order of 8 has been employed, and a detailed mesh which could also cover asymmetric cases has been set up in TORT-TD: 451520 cells with 340 nodes in r-direction, 4 nodes in φ-direction and 332 nodes in z-direction. Several azimuthal segments would be needed if core installations, especially the cold source would have to be modeled explicitly.

6.4.1 TORT-TD ($S8$) calculation

As mentioned above the first validation calculations as well as the proof of the capability of TORT-TD to reproduce FRM II's core behavior have been performed with the most suitable and most precise approach:

- Cross sections to the first Legendre order including 30 energy groups.
- Quadrature order S8, because the discrete-ordinate method is known to possibly cause numerical artifacts, like such "rays", if the chosen quadrature order is too small [16, 65][1].
- 451520 mesh cells with 340 nodes in r-direction, 332 nodes in z-direction and an angular division of 90°.

As for the Serpent 2 model, TORT-TD has to reproduce the important key core parameters multiplication factor, power deposition distribution and neutron fluxes. The multiplication factor serves as a primary criterion for the quality of the model.

6.4.1.1 Multiplication Factor

Table 6.5 shows a comparison of the multiplication factors calculated with MCNP6, Serpent 2 and TORT-TD. Here, the value MCNP6 $_{\text{ref}}$ calculated with 10^6 neutron histories per cycle, 150 active and 25 inactive cycles serves as the most precise reference value available (see Eq. 6.2). The multiplication factor calculated with TORT-TD matches sufficiently well with both the MCNP6 reference value (see Eq. 6.2) and the Serpent 2 value (see Table 6.4).

Table 6.5: *Multiplication factors obtained with MCNP6 and Serpent 2 in comparison to the multiplication factor calculated with TORT-TD using* 30 *energy groups,* $S8$ *and cross sections to the first Legendre order. The most precise reference value (see Eq. 6.2) is shown in the row labeled MCNP6* $_{\text{ref}}$*. The value for Serpent 2 is taken from Table 6.4.*

Code	Multiplication Factor
MCNP6 $_{\text{ref}}$	0.99772 ± 0.00009
Serpent 2	0.99832 ± 0.00031
TORT-TD (S8)	0.99792

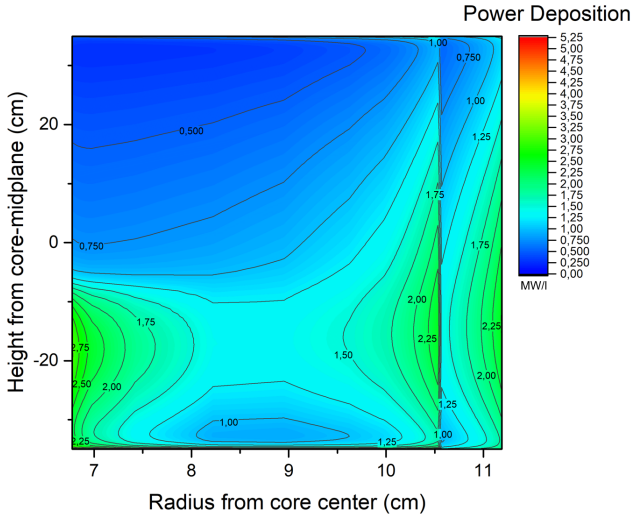

(a) Absolute TORT-TD ($S8$) power deposition without correction

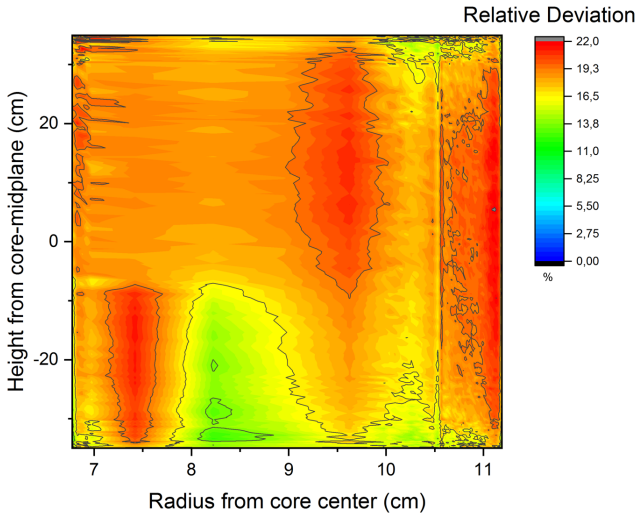

(b) TORT-TD ($S8$) relative comparison of power deposition without correction

Figure 6.30: *The top panel (a) shows the absolute power deposition as calculated with TORT-TD (S8). The distribution of the power deposition in one exemplary fuel plate is reproduced very well. Both the density jump at* 10.56 cm *and the influence of the hafnium absorber at the left side is clearly visible. The bottom panel (b) shows the relative deviation in* % *of the power deposition as calculated with TORT-TD (S8) and MCNP6, respectively, in the sense of "*$TORT - MCNP6$*". The results show a well matching trend but the result obtained by TORT-TD is systematically shifted by roughly* 18 %*.*

6.4.1.2 Power deposition distribution

In Figure 6.30(a) the absolute power deposition distribution in one exemplary fuel plate is depicted. The general shape is reproduced very well, and both the density jump at 10.56 cm from the core center and the influence of the hafnium absorber at the right side are clearly visible. Also, the absolute maximum is still located at the lower left fuel zone near the beryllium follower, and the power deposition increases near the heavy water moderation tank.
In order to compare the TORT-TD ($S8$) model described above with the MCNP6 reference calculation, a mesh tally TMESH type 3 covering the fuel zone has been set up in MCNP6 using the same mesh structure as the calculation grid employed in TORT-TD ($S8$). The lower panel of Figure 6.30 shows the relative deviation of the power deposition of TORT-TD and MCNP6 in %. As can be seen, the power deposition, as calculated with TORT-TD ($S8$) is systematically shifted upwards by roughly 18 %. TORT-TD does not transport secondary particles, like γs, but rather calculates a distribution of the power deposition only in cells where the macroscopic fission cross section is greater than zero, and then normalizes the distribution to the predefined power prescribed by the user. Hence, no power is calculated outside of the fuel zone, in contrast to MCNP6 where significant power is deposited outside of the fuel. The employed mesh tally TMESH tpye 3 sums up the deposited energies by using heating numbers. For neutrons, the heating number at a certain energy $H(E)$ is calculated using:

$$H(E) = E - \sum_{\mathrm{i}} p_{\mathrm{i}} \left[\bar{E}_{\mathrm{i,out}}(E) - Q_{\mathrm{i}} + \bar{E}_{\mathrm{i},\gamma}(E) \right], \tag{6.9}$$

where $p_{\mathrm{i}} = \sigma_{\mathrm{i}}(E)/\sigma_{\mathrm{T}}(E)$ is the probability for reaction i to take place, $\bar{E}_{\mathrm{i,out}}(E)$ the average exciting neutron energy for reaction i at neutron incident energy E, Q_{i} the Q-value of the reaction and $\bar{E}_{\mathrm{i},\gamma}$ the average exiting gamma energy [10, 59]. Then the tallied heating H is

$$H = \frac{n}{m} \int\int\int\int dE\, dt\, dV\, d\mathbf{\Omega}\, \sigma_{\mathrm{t}} \cdot H(E) \cdot \Phi(\mathbf{r},\mathbf{\Omega},E,t). \tag{6.10}$$

The observed deviation of the power deposition has to be independent of the used mesh as long as the mesh is dense enough and a small variation in the number of cells does not effect the result. As a check, the power deposition of both codes are compared whereas two different meshes have been used: The above described rather fine mesh which is supposed to be dense enough and a mesh covering the whole fuel zone with just one cell. As shown in Table 6.6, the

Table 6.6: *Averaged deviation of the power deposition, as calculated with MCNP6 and TORT-TD, respectively, in the sense of "$TORT - MCNP6$". In the first row the result for the coarse mesh with only one cell is shown. The second row shows the deviation averaged over all cells of the fine mesh.*

Average deviation coarse mesh [%]	1.181
Average deviation fine mesh[%]	1.179

deviations obtained from both meshes matches perfectly and so the observed systematical shift is mesh independent. Therefore, every value calculated with TORT-TD can be translated into the more realistic power density distribution of MCNP6 by dividing it by a correction factor of $\zeta = 1.179$, as given in the second row of Table 6.6. With that correction applied, the corrected

[1] Due to the excessive computational expense, TORT-TD would not be suitable for transient calculations if S16 or more is required.

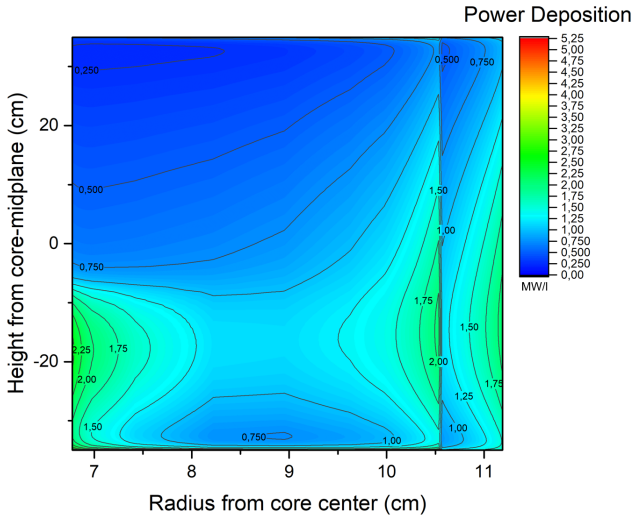

(a) Absolute TORT-TD ($S8$) power deposition with correction

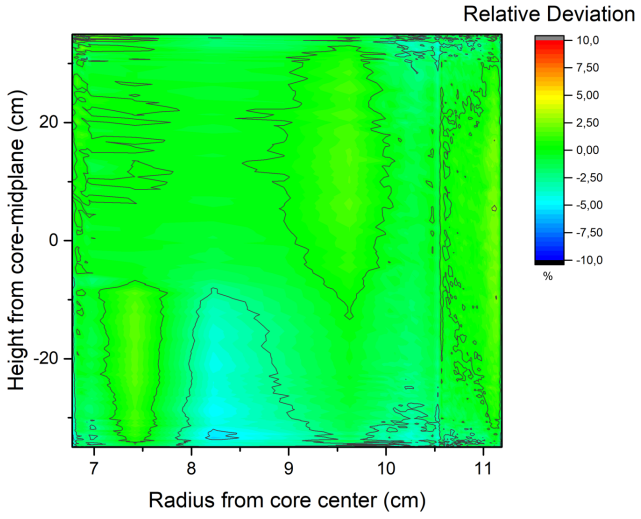

(b) TORT-TD ($S8$) comparison of power deposition with correction

Figure 6.31: *The top panel (a) shows the absolute power deposition after the correction has been applied. The bottom panel (b) shows the relative deviation of both codes after the applied correction.*

relative deviation of the power deposition of MCNP6 and TORT-TD is depicted in the right panel of Figure 6.31. Now the power deposition matches well within ±2.5 %. Especially around the density jump no increased deviations are observable. Just at the mid-bottom, where the absolute power deposition is rather low, the deviations rise to ±3 %. The corrected absolute power deposition distribution is shown in the left panel of Figure 6.31.

6.4.1.3 Neutron flux distribution

Table 6.7: *Lower boundaries of the used* 30 *energy groups in MeV.*

Group 1	**Group 2**	**Group 3**	**Group 4**	**Group 5**	**Group 6**
4.00	3.00	1.85	1.353	9.00E-1	1.00E-1
Group 7	**Group 8**	**Group 9**	**Group 10**	**Group 11**	**Group 12**
3.00E-3	1.00E-4	3.00E-5	1.00E-5	3.00E-6	1.77E-6
Group 13	**Group 14**	**Group 15**	**Group 16**	**Group 17**	**Group 18**
1.00E-6	0.625E-6	0.5125E-6	0.40E-6	3.375E-7	0.275E-6
Group 19	**Group 20**	**Group 21**	**Group 22**	**Group 23**	**Group 24**
0.15E-6	1.00E-7	5.00E-8	3.00E-8	1.00E-8	6.50E-9
Group 25	**Group 26**	**Group 27**	**Group 28**	**Group 29**	**Group 30**
3.00E-9	2.50E-9	2.00E-9	1.00E-9	1.00E-10	0

Since deterministic calculations use energy groups (Table 6.7), several groups have to be summed up for comparison of the results with previous MC calculations where $\Phi_{\mathrm{th}}(E < 0.625\,\mathrm{eV})$ was calculated in one group. Alternatively 30 mesh tallies of TMESH type 1 with the same group/energy structure as the TORT-TD calculation can be used in the MCNP6 model. To compare the thermal neutron flux distribution (see Figure 6.4) the single fluxes from TORT-TD of the energy groups up to an energy of 0.625 eV (see Table 6.9) are summed up. For the fast neutron flux distribution, the energy groups with an energy greater than 0.1 MeV (see Table 6.9) are summed up. For the comparison of single energy groups the alternative approach has been used.

Thermal neutron flux distribution The left panel of Figure 6.32 shows the thermal neutron flux distribution calculated with TORT-TD. TORT-TD reproduces the shape of the thermal neutron flux distribution (see Figure 6.4) that has been calculated with MCNP6: The absolute maximum is located in the beryllium follower of the control rod, a second maximum is located in the heavy water moderator tank and is usable for the installed beam tube experiments, the hafnium depresses the thermal neutron flux and even the influence of the installed boron ring is clearly visible. Also, the fast neutron flux distribution is reproduced accurately, as depicted in the right panel of Figure 6.32. With the control rod position at −6.92 cm, the maximum is located in the lower half of the fuel zone.
Figure 6.33 shows the relative deviation of the thermal neutron flux distribution between MCNP6 and TORT-TD. The results for the neutron fluxes calculated with both codes match well within ±2 % for almost the whole geometry. Within the boron ring and the hafnium absorber the

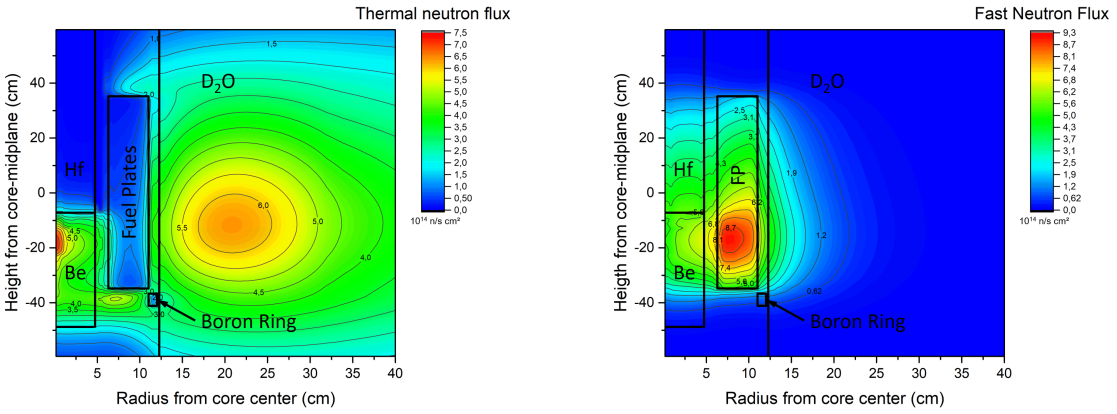

(a) Thermal neutron flux

(b) Fast neutron flux

Figure 6.32: *The left panel (a) shows the thermal neutron flux distribution as calculated with TORT-TD (S8). Because the deterministic calculation uses energy groups, the thermal neutron flux is the sum of all energy groups up to* $0.625 \cdot 10^{-6}$ MeV*. TORT-TD reproduces the FRM II thermal flux distribution very well; the maximum thermal flux usable is situated inside the heavy water moderation tank, the absolute maximum is located inside the beryllium follower and the installed hafnium depresses the thermal neutron flux. Also the boron ring is clearly visible. In the right panel (b) the fast neutron flux distribution is depicted. Energy groups greater than* 0.1 MeV *have been summed up. Again TORT-TD reproduces the fast flux distribution of FRM II very well.*

deviations rise to more than ±10 %. This is mainly due to the very strong flux gradient in the rather small dimensions of both the boron and the hafnium structure and the limited number of nodes within the materials. However, a very strong suppression of the thermal neutron flux inside the boron ring and hafnium absorber is clearly visible for both codes (see Figures 6.4, 6.32(a)), so a higher relative deviation there is of no consequences. In particular, during transients these larger deviations will be without effect, especially because of the very well matching multiplication factors (see Table 6.5) and power deposition distribution (see Figure 6.31(b)). At the very top of Figure 6.33 the relative deviations also rises to more than 10 %. This is caused by the numerical method used by TORT-TD which leads to a systematical underestimation of the thermal neutron flux in areas with a low absolute neutron flux.

Fast neutron flux distribution The fast neutron fluxes are compared in Figure 6.32(b). It can be seen that TORT-TD ($S8$) and MCNP6 deliver matching results within ±2 % for the fuel zone, the heavy water moderation tank and also for the boron ring. Starting from the edges of the fuel zone "ray effects" [16, 65] can be adumbrated. These "rays" lead to increasing deviations below and above the fuel zone. But nevertheless, due to increasing moderation and, therefore, decreased fast neutron flux, these areas are of minor interest only. These deviations do not affect the influence of the emergency shutdown rods, which are not modeled here, since they would fall into the area where the fast neutron flux distribution matches within ±2 %.

Group-wise fluxes Significant deviations of the neutron fluxes in some of the energy groups are present, even though the summed fluxes in the thermal and fast range match well. Figure 6.35

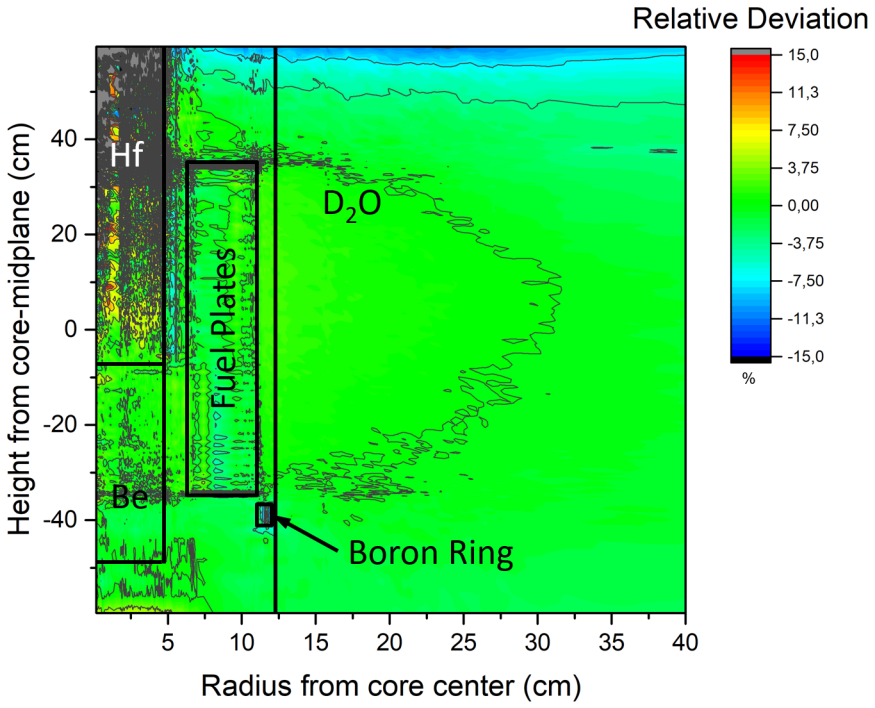

Figure 6.33: *Relative deviation in % of the thermal neutron flux between MCNP6 and TORT-TD (S8) in the sense of "TORT − MCNP6". To compare the thermal neutron flux (see Figure 6.4), the single fluxes of the energy groups up to an energy of* 0.625 eV *(see Table 6.9) are summed up. For the heavy water moderation tank, the beryllium follower and the fuel zone both codes deliver matching results within* ±2 %*. Inside the hafnium absorber TORT-TD systematically overestimates the thermal neutron flux by more than* 10 %*. Also inside the installed boron ring the deviations are increased.*

depicts the neutron flux of four selected energy groups ranging from fast to cold energies. The remaining groups are shown in the Appendix C.

- In Figure 6.35(a) the fastest energy group from 4 MeV to 20 MeV (see Table 6.9) is depicted. The known "ray effects" are clearly distinct for this energy group. However, both codes deliver well matching results for the important parts "between" these "rays".
- For the thermal energy groups from 0.40 eV to 0.5125 eV (see Figure 6.35(b)) and from 0.05 eV to 0.1 eV (see Figure 6.35(c)), TORT-TD and MCNP6 deliver very well matching results for almost the whole core. Only inside the hafnium absorber the deviations between the two codes increase, and only in the group starting from 0.40 eV eased "rays" starting at the corners of the fuel zone are visible.
- For some cold and ultra cold neutron energy groups, the neutron flux distributions deviate rather strongly, as shown for the group from 1.00 meV to 2.00 meV in Figure 6.35(d). Here, the results of both codes deviate systematically between 20 % and 38 %. Only inside the beryllium follower the deviations decrease to 12 %. In general, however, the influence

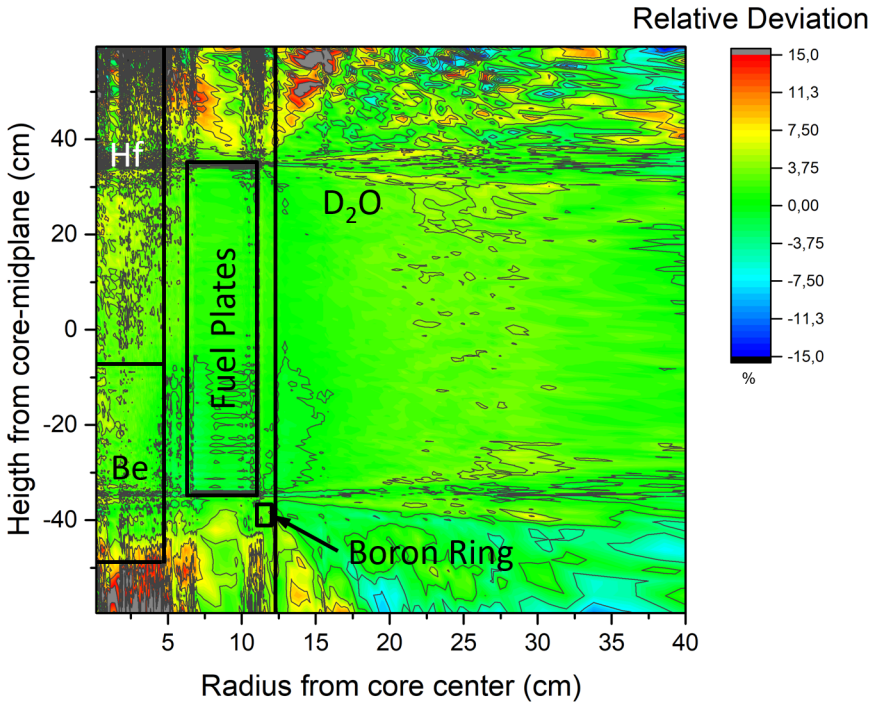

Figure 6.34: *Relative deviation in % of the fast neutron flux between MCNP6 and TORT-TD (S8) in the sense of "TORT − MCNP6". To compare the fast neutron flux (see Figure 6.4), the single fluxes of all energy groups greater than* 0.1 MeV *(see Table 6.9) are summed up. For the fuel zone the heavy water moderation tank, the hafnium absorber and the beryllium follower the deviations are within* ±2 %*. Some light "ray effects", starting at the edges of the fuel zone are visible which causes deviations* ±10 % *in some small areas above the fuel zone inside the heavy water moderation tank.*

of these groups on both the total thermal or fast neutron flux and the later calculated transients is negligibly small, first, due to the small energy range of the groups and, second, due to the generally small total neutron flux in those groups and their influence on the core behavior.

In summary, this very detailed model for deterministic calculations match very well with Monte Carlo calculations, and is thus able to reproduce the rather constraint conditions of FRM II's core.

6.4.1.4 Modeling of the control rod

The control rod defined in TORT-TD is part of the input desk and has to be assigned to a specific r-φ-z-coordinate of the calculation mesh used. At a given simulation time, this rod is then being moved through the geometry with specified velocity and acceleration. During the movement TORT-TD performs a flux-volume-averaging if the control rod is between two mesh cells with different materials. To deal with the movement of control rods, two cross sections have

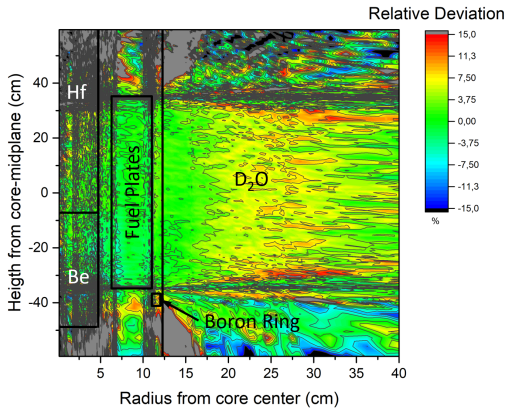

(a) Neutron Flux of energy group 1

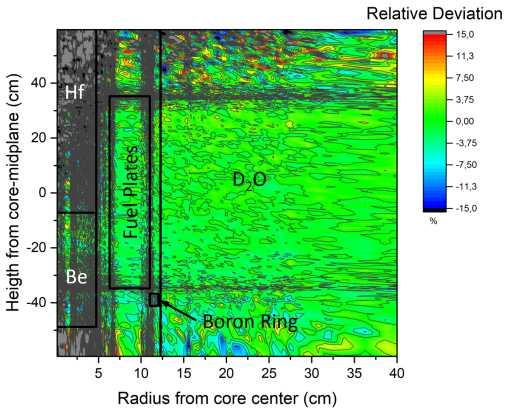

(b) Neutron Flux of energy group 16

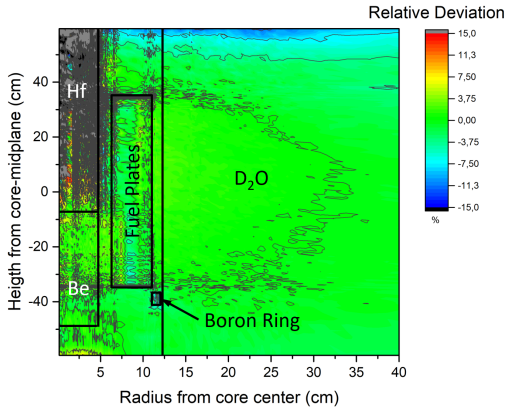

(c) Neutron Flux of energy group 21

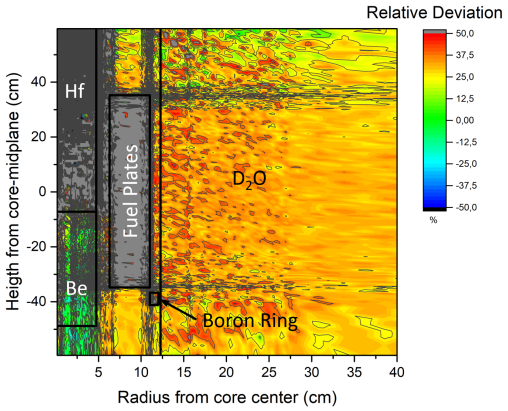

(d) Neutron Flux of energy group 28

Figure 6.35: *In the top left panel (a) the relative deviation in % of the neutron flux of the fastest energy group from* 4 MeV *to* 20 MeV *between MCNP6 and TORT-TD (S8), in the sense of "TORT − MCNP6", is depicted. "Ray effects" starting at the edges of the fuel zone are visible, but for the relevant area inside the heavy water moderation tank, both codes deliver matching results within* ±5 %*. Inside and near those "rays" the deviations are increased to more than* ±10 %*. The top right panel (b) shows a thermal energy group between* 0.4 eV *and* 0.5125 eV*. Here, the results of both codes are within* ±3.5 %*. But again "rays" starting at the edges of the fuel zone are visible. Inside the hafnium absorber the deviations are systematically increased to more than* 15 %*. The bottom left panel (c) depicts the neutron flux of the thermal energy group between* 0.05 MeV *and* 0.1 eV*. Here the calculated neutron fluxes matches within* ±3.5 % *for the heavy water moderation tank, the beryllium follower and the fuel zone. Again only inside the hafnium absorber are the deviations increased to more than* 10 %*. In the bottom right panel (d) the neutron flux of a cold energy group between* 1 meV *and* 2 meV *is shown. The neutron flux is systematically overestimated by ca.* 40 − 50 %*. Inside the fuel zone these deviations are even more than that. Inside the hafnium absorber, the neutron flux is underestimated by more than* 50 %*.*

to provided for every mesh node of the calculation grid: One for the controlled case which is used if this node is part of a control rod and one for the uncontrolled case which is used otherwise. The FRM II's control rod is structurally complex and is extended over several mesh cells in the TORT-TD model. Hence, in total 103 control rods have to be defined in TORT-TD to reproduce the exact geometry. Figure 6.36 depicts the r-z-mesh structure, which has to be translated to

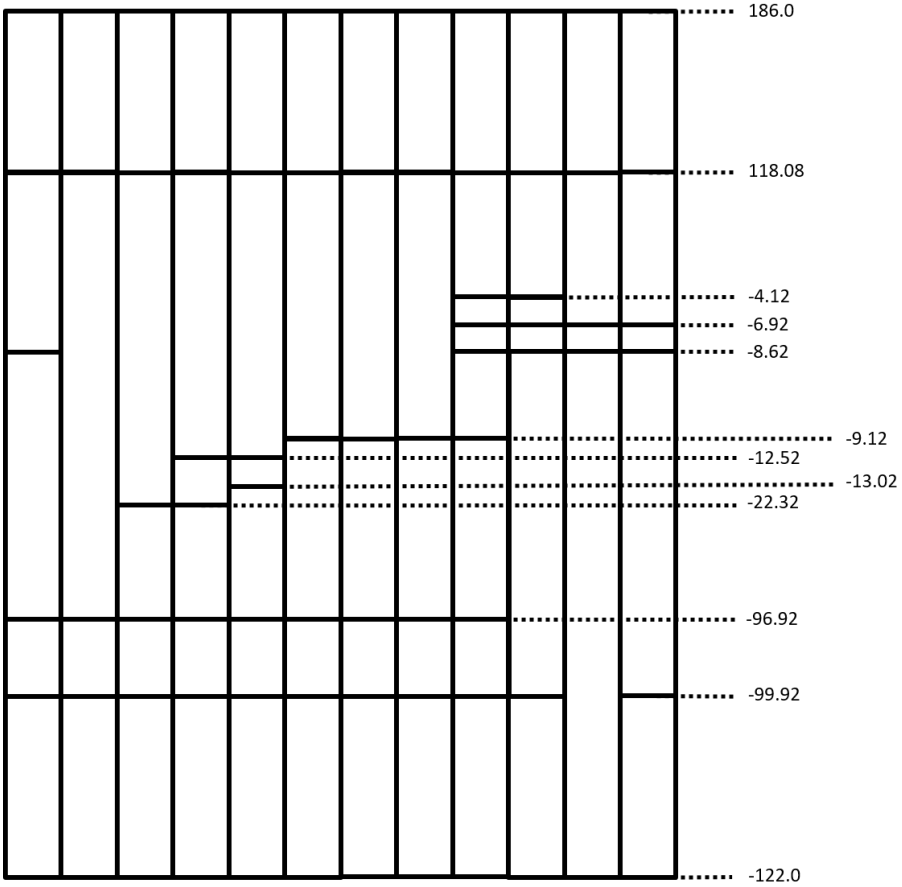

Figure 6.36: *Simplified r-z-mesh structure with major axial coordinates of all control rods modeled in TORT-TD.*

several single control rods in TORT-TD. During a transient simulation, all 103 control rods have to be moved simultaneously and in the very same manner. To generate the needed input automatically, the input for C^2 can be modified such that a complete TORT-TD input with control rods and adjusted definition of the cross section can be produced (see Figure A.6). With all 103 control rods defined, a steady state validation calculation has been performed and both models to proof the correct definition of the control rods and the input generated with C^2. Both models, with and without defined control rods, deliver perfectly matching results.

6.4.2 Performance optimization

TORT-TD is not parallelized, so the calculations run on a single CPU core and are fairly time consuming. Hence, it is desirable to apply measures to reduce the computational burden of TORT-TD ($S8$). As most important and most effective key step a possible reduction of the

quadrature order is highly desirable. Besides a reduction of the quadrature order other possible optimization measurements also include:

- Reduction of the quadrature order to $S4$.
- Reduction of the energy groups used.
- Reduction of the Legendre order of the cross sections used.
- Reduction of the azimuthal order.
- Lifting the convergence criteria.
- Optimization of the calculation grid.
- Partial usage of the diffusion approximation.

Calculations using these approaches and combinations thereof have been tested by comparing the multiplication factor and the needed calculation time. The final choice of the model is based upon a comparison using a weighting factor (see Chapter 6.12).

6.4.2.1 TORT-TD ($S4$) calculation

In the previous chapter it has been shown that TORT-TD ($S8$) is generally capable of dealing with the constraint conditions of FRM II's reactor core. But with nearly 68 h of CPU time needed just for the steady-state calculations, this is not a suitable approach for transient calculations which usually need many time steps. This means that the TORT-TD ($S8$) model (see Chapter 6.4.1) has to be simplified whereas the main parameters for the core behavior have to be preserved. As a first step, the quadrature order used is reduced from $S8$ to $S4$, and the computational mesh is pinched to 438240 mesh cells with 330 nodes in r-direction, 332 in z-direction and an angular division of 90°. The energy groups were kept at the same 30 group structure as for $S8$. With only 30 h of computational time needed for the steady state calculation, the TORT-TD ($S4$) model is more than twice as fast as TORT-TD ($S8$). In the following subsections the key core parameters are compared in order to asses the viability of this model for transient calculations for FRM II.

Table 6.8: *Multiplication factors obtained with MCNP6 and Serpent 2 in comparison to the multiplication factor calculated with TORT-TD using* 30 *energy groups,* $S8$ *and cross sections to the first Legendre order. The most precise reference value (see Eq. 6.2) is shown in the row labeled MCNP6* $_{\text{ref}}$*. The value for Serpent 2 is taken from Table 6.4.*

Code	Multiplication Factor
MCNP6 $_{\text{ref}}$	0.99772 ± 0.00009
Serpent 2	0.99832 ± 0.00031
TORT-TD (S8)	0.99792
TORT-TD (S4)	0.99988

Multiplication Factor By reducing the order of quadrature the multiplication factor increases by 1.96 ‰ compared to TORT-TD ($S8$). It is outside of the statistical uncertainties of the multiplication factors as calculated with MCNP6 and Serpent 2.
As already mentioned, the multiplication factor as calculated with TORT-TD ($S8$) matches with the corresponding value from MCNP6 and Serpent 2. Reducing the quadrature order to $S4$ is equals a reactivity increase of 0.30 \$, when taking an effective delayed neutron fraction of $\beta = 0.0065$. Compared to the excess reactivity of a fresh fuel element this difference is comparably small and as a positive side effect the multiplication factor from TORT-TD ($S4$) is closer to 1, so that the renormalization factor needed for the zero transient (see Chapter 10) is not getting too big. Therefore, an impact for transients is not expected, especially for well matching power deposition (see Chapter 6.4.2.1) and neutron flux distributions (see Chapter 6.4.2.1).
To get a better feeling how such a difference of the multiplication factor influences the reactor, the impact on the cycle time is a vivid description. This deviation of TORT-TD ($S4$) and MCNP6 equals roughly two days of operation [9]. However, taking into account that a radial shift of the density jump to the maximum value that is allowed by the specification of FRM II's fuel element would lead to nearly four days of operation time [6], the here observed deviation between TORT-TD ($S4$) and MCNP6 is still within acceptable limits.

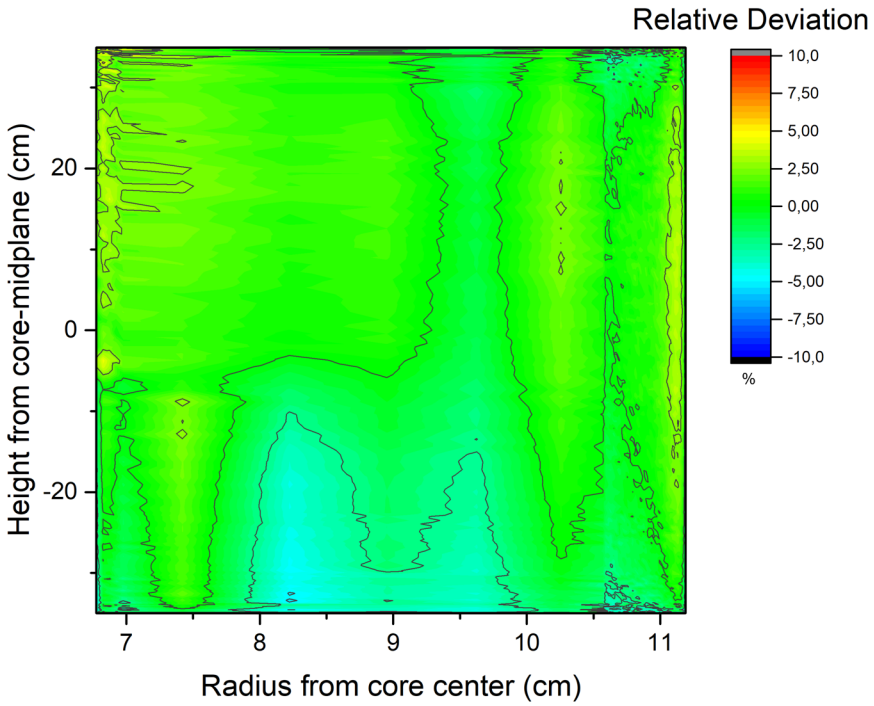

Figure 6.37: *Relative deviation in % of the power deposition after the applied correction (see Chapter 6.4.1.2) as calculated with TORT-TD (S4) and MCNP6, respectively, in the sense of "TORT − MCNP6". The results show a well matching trend for the whole fuel plate.*

Power deposition distribution Both the TORT-TD ($S4$) and MCNP6 calculation have been evaluated using c^2 (see Appendix D.7, D.6). The distribution calculated by TORT-TD ($S4$)

has been corrected in the same way as the TORT-TD ($S8$) calculation (see Chapter 6.4.1.2). As for TORT-TD ($S8$), the calculated deviation of the power deposition distribution between TORT-TD ($S4$) and MCNP6 is within $\pm 2\,\%$, as is shown in Figure 6.37. Only at the inner and outer border and at the bottom mid-part the deviations are slightly higher ($\pm 3\,\%$).

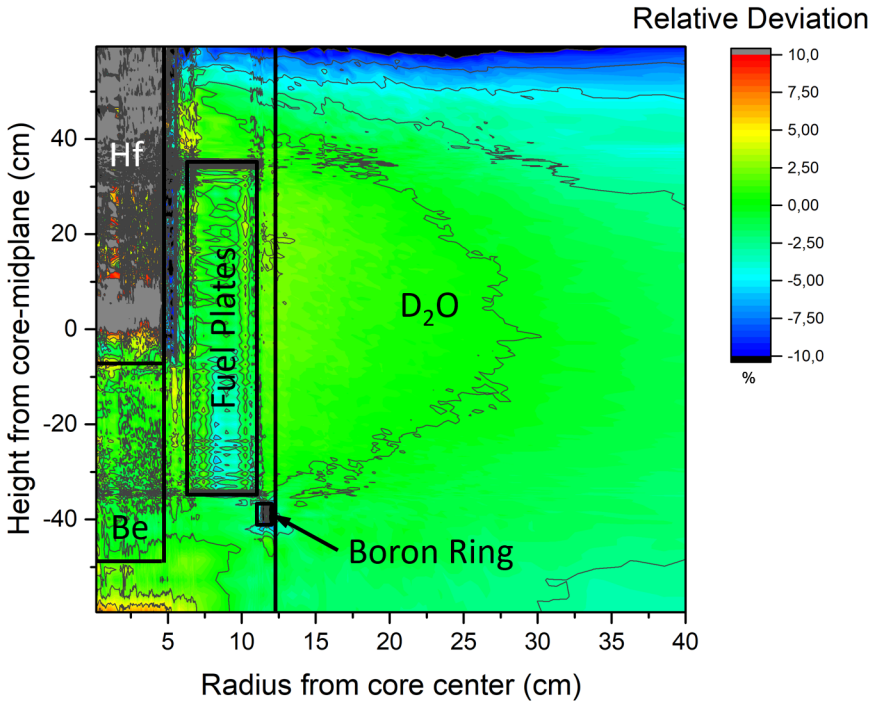

Figure 6.38: *Relative deviation in % of the thermal neutron flux between MCNP6 and TORT-TD ($S4$) in the sense of "TORT − MCNP6". To compare the thermal neutron flux (see Figure 6.4), the single fluxes of the energy groups up to an energy of* 0.625 V *(see Table 6.9) are summed up. For the heavy water moderation tank, the beryllium follower and the fuel zone both codes deliver matching results within* $\pm 2\,\%$*. Inside the hafnium absorber TORT-TD systematically overestimates the thermal neutron flux by more than* 10 %*. Also inside the installed boron ring the deviations are increased. Also, above* 45 cm *the deviations are increased to more than* $-10\,\%$*.*

Thermal neutron flux distribution Figure 6.38 shows the relative deviation of the thermal neutron flux distribution between MCNP6 and TORT-TD ($S4$). The results are very similar to those of the TORT-TD ($S8$) calculation.

Fast neutron flux distribution The fast neutron fluxes are compared in Figure 6.39. Here, the influence of the number of discrete ordinates used (see Chapter 2.1.4) becomes visible. Starting from the edges of the fuel zone, "rays" are much more pronounced. Inside these rays both codes again deliver well matching results within $\pm 2\,\%$. "Outside" of theses rays the deviations rise significantly above $\pm 10\,\%$, in comparison to TORT-TD ($S8$). Nevertheless, both codes deliver well matching results for the important parts inside these "rays".

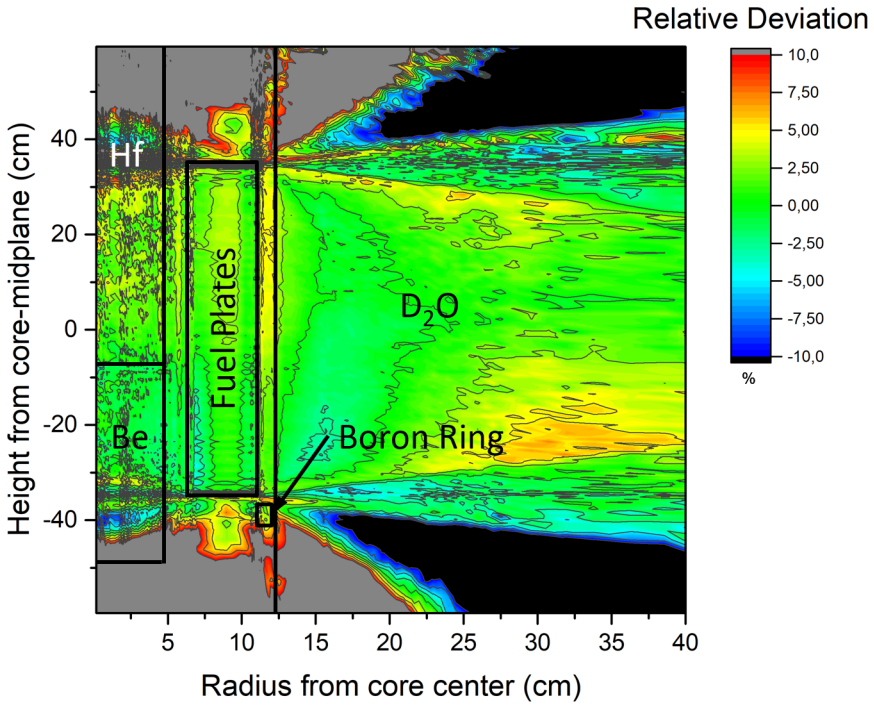

Figure 6.39: *Relative deviation in % of the fast neutron flux between MCNP6 and TORT-TD (S4) in the sense of "TORT − MCNP6". To compare the fast neutron flux (see Figure 6.4), the single fluxes of all energy groups larger than* 0.1 MeV *(see Table 6.9) are summed up. For the fuel zone the heavy water moderation tank, the hafnium absorber and the beryllium follower the deviations are mostly within* ±2 %*. Because of visible numerical "ray effects", starting at the edges of the fuel zone, the deviations outside these "rays" are increased to more than* ±10 %*.*

The results obtained with TORT-TD ($S4$) match sufficiently well the key parameters of FRM II's core.

6.4.2.2 Influence of the number of energy groups

Due to the inherent property of the numerical method employed (see Chapter 2.1.4) the computational expense rises with the number of energy groups used. In contrast, calculations with more groups deliver information about the neutron flux with higher energy resolution and a better matching multiplication factor compared to MC calculations. Calculations with 12, 20 and 30 energy groups have been performed for this parametric analysis study. The usage of more than 30 groups is prohibited because of the computational expense. Table 6.9 shows the energy group structure used for this study.
Table 6.10 illustrates the influence of the number of energy groups upon the multiplication factor. A clear trend is visible: With increasing number of energy groups, the deviation from the Monte Carlo calculations decreases. For reactivity transients the most important issues are matching

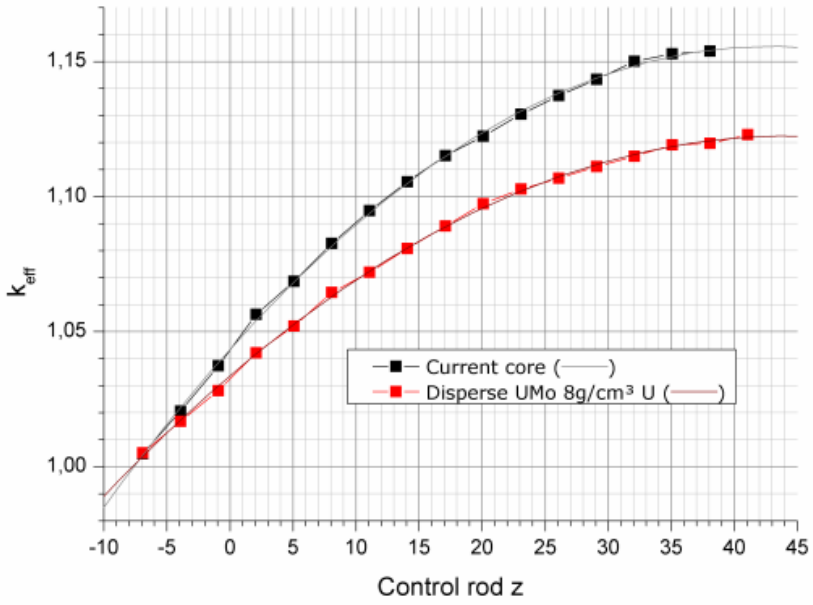

Figure 6.40: *Reactivity worth of* FRM II*'s control rod for the current fuel and a possible dispersed UMo fuel candidate (taken from [10]).*

kinetic core parameters. A too large deviation of the multiplication factor from the reference calculation would cause a mismatch of the reactivity worth of the control rod (Figure 6.40). A mismatching multiplication factor would lead to a different control rod position and, therefore, affect the kinetic core behavior. In order to represent the real core, an artificial correction would have to be applied in such a case. Taking the multiplication factors given in Table 6.10, 30 energy groups are suitable for further transient calculations to achieve the highest precision possible. Probably 20 energy groups would also be sufficient, but to proof this a more detailed study would be needed which involves actual transient calculations. The accuracy of calculations performed with 12 energy groups only is not suffcient and, therefore, further calculations have been discarded.
A study on the required number of energy groups has also been performed in [58]. However, due to the different approach of both modeling FRM II's core and of generating the multi-group cross sections, different positions of the control rod and different code versions, the values of

Table 6.9: *Energy group patterns for* 12, 20 *and* 30 *energy group calculations.*

Lower group border	Number of energy groups		
	12	**20**	**30**
4.00			1
3.00	1	1	2
1.85	2	2	3
1.353			4
9.00e-1	3	3	5
1.00e-1	4	4	6
3.00e-3	5	5	7
1.00e-4	6	6	8
3.00e-5	7	7	9
1.00e-5	8	8	10
3.00e-6	9	9	11
1.77e-6		10	12
1.00e-6		11	13
0.625e-6	10	12	14
5.125e-7			15
0.40e-6		13	16
3.375e-7			17
0.275e-6		14	18
0.15e-6		15	19
1.00e-7			20
5.00e-8		16	21
3.00e-8			22
1.00e-8	11	17	23
6.50e-9			24
3.00e-9		18	25
2.50e-9			26
2.00e-9		19	27
1.00e-9			28
1.00e-10			29
0.00	12	20	30

Table 6.10: *Influence of the number of energy groups upon the multiplication factor calculated with TORT-TD using* 12, 20 *and* 30 *energy groups, respectively.*

Number of energy groups	12	20	30
Multiplication Factor	1.01324	1.00278	0.999877
Absolute difference to reference (Eq. 6.2)	0.01552	0.00506	0.00216
Relative difference in ‰ to reference (Eq. 6.2)	15.56	5.07	2.16
Time for steady state convergence in h	6.83	10.70	30.20
Saving of time in % compared to 30 energy groups	77.4	64.6	-

the multiplication factor obtained in [58] are hardly comparable with the results obtained here. Anyway, both studies show the same trend, namely that with increasing number of energy groups the results obtained from the deterministic code match better with the Monte Carlo results.

6.4.2.3 Influence of the cross sections Legendre order

In general the scattering cross sections are expanded in Legendre basis functions (see Chapter 2.1.1). While the zeroth order describes the total probability for scattering, the subsequent orders describe the angular distribution of the particles emerging from that scattering event, expanded in Legendre basis functions. This improved description of the scattering processes leads to a more accurate description of the neutronical behavior of the core, which is bought with more computational time. For TORT-TD this information is given in the NEMTAB format which is used for the definition of the cross sections.
It has to be clarified if the zeroth or first order of the Legendre expansion is needed. Higher order expansions are computationally too expensive. Therefore, two TORT-TD ($S4$) calculations have been performed on the grid described above using 30 energy groups (see Chapter 6.4.2.2) in order to quantify the deviation of the multiplication factor caused by the order of the Legendre expansion.

Table 6.11: *Influence of the cross sections Legendre order on the multiplication factor calculated with TORT-TD (*$S4$*).*

Legendre Order	0	1
Multiplication Factor	1.09985	0.999877

The obtained multiplication factors are shown in Table 6.11. The comparison of these values with the reference value (see Eq. 6.2) shows, that scattering cross sections of the zeroth order are not sufficient. Hence, the first Legendre order has to be used.

6.4.2.4 Optimization of the calculation grid

Reducing the azimuthal segments The first comparative calculations have been performed using four azimuthal segments. These azimuthal segments would be needed in the case that the core installations, especially the cold source, and their caused feedback, were explicitly modeled. Because no core installations are explicitly modeled for the calculations performed within this

thesis, no information is lost if just one segment is modeled. The reduction of the azimuthal order leads to a multiplication factor of $k_{\mathrm{ra}} = 0.999765$. The required computational time is 560 min. This means a time reduction of 69.1 %, while the multiplication factors differ by 0.05 ‰ only. Because the core installations will be modeled in a further work, the number of azimuthal segments can be reduced for the calculations performed within this thesis.

Mesh sensitivity The mesh used for the TORT-TD calculations can have an influence on the resulting neutron fluxes. In order to identify areas where the computational grid has a strong impact to the result, a theoretical method has to be applied to increase the influence. One option to do so is by weighting the flux of each group with a factor of $1/v_i$, whereas v_i is the neutron velocity corresponding to the central energy of the group, strong and systematic deviations for the whole geometry would have to appear, when the computation mesh would cause problems. The comparison of the weighted flux, shows areas with exaggerated differences and areas with

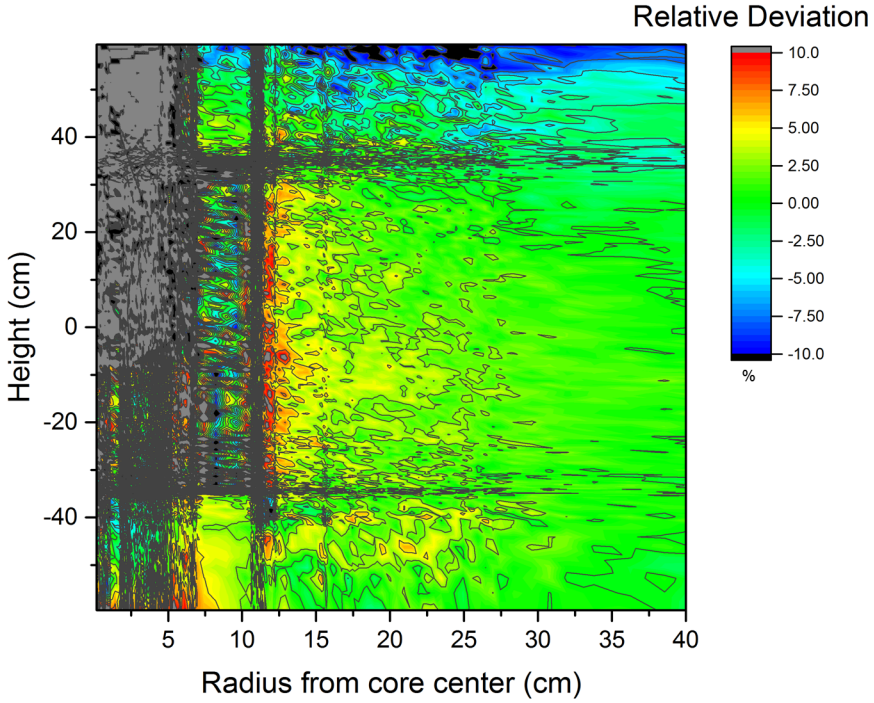

Figure 6.41: *Relative deviation in % of the sum of all energy groups up to* 0.625 eV*, as calculated with MCNP6 and TORT-TD in the sense of "TORT − MCNP6". Every energy group has been weighted with* $1/v$*. Here,* v *is neutron velocity corresponding to the central energy of the group. By applying such weighting factor the systematical differences caused by the mesh used are highlighted. For the heavy moderation tank no excessive deviation can be observed. In the fuel zone some regions with systematical relative deviations larger than* 10 %*, can be identified. Due to the strong depression of the thermal flux inside the hafnium absorber, no meaningful conclusions can be drawn for that particular area.*

sufficient mesh node density. With that information the calculation mesh can be suitably adopted, and the node density is increased in areas with large differences while it can be decreased in well

matching areas. Hence, in the optimized mesh, the number of radial nodes can be decreased from 333 to 275 nodes. Already the optimization of the radial computational grid decreases the computational time needed by 18.7 %. The multiplication factor of $k_{\mathrm{og}} = 1.001440$ is about 1.6 ‰ higher than the TORT-TD ($S4$) reference value. Because some regions in the fuel zone with systematic relative deviations have been identified, an adjusted computational grid avoids such deviations and will be therefore used for further calculations.

6.4.2.5 Lifting the convergence criteria

In order to save somputational time, the pointwise flux convergence criteria [67] can be increased from $5 \cdot 10^{-6}$ to 10^{-5}. Using the lifted numerical convergence criteria a multiplication factor of $k_{\mathrm{cc}} = 1.001520$ results. The required CPU time is 1806 min. This means a time saving of just 0.3 %. The deviation of the multiplication factor is with 0.08 ‰ comparably small. Lifting the convergence criteria does not lead to a significant decrease of the computational time needed, but increases the uncertainty of the result. Therefore, a more loose criteria will not be taken into account later on.

6.4.2.6 Usage of the diffusion approximation

The usage of the diffusion approximation is expected to deliver the highest saving of computational time (see Chapter 2.1.2). For a full switch from transport theory to diffusion approximation, the computational expanse decreases by about 66.3 %. But with a deviation of 3.81 %, the multiplication factor of $k_{\mathrm{d}} = 0.960862$ is not acceptable.
The most advanced possibility is the partial usage of the diffusion approximation. In that mode TORT-TD uses the diffusion equation (see Chapter 2.1.2) until one of the following conditions is true:

- A number of convergence cycles which has to be provided by the user
- The convergence of the calculation is sufficiently well (see Chapter 4.3).

Both parameters have to be preset in the input file. By using this mode the time saving of 64.2 % is almost as high as before, but the deviation of the resulting multiplication factor of $k_{\mathrm{sd}} = 0.999899$ decreases to 1.6 ‰. The time saving provided by this method is almost as high as for the reduction of azimuthal segments. With a very small impact on the multiplication factor, this method is very desirable to be used for the transient calculations.

6.4.2.7 Grading System

For the comparison of the various approaches listed in Section 6.4.2 a grading factor α has been introduced, which comparess each multiplication factor $k_{\mathrm{Tort,i}}$ and computational time $t_{\mathrm{Tort,i}}$ with the TORT-TD ($S4$) reference calculation ($k_{\mathrm{Tort,ref}}$, $t_{\mathrm{Tort,ref}}$) (see Table. 6.8), i.e.

$$\alpha = \frac{|k_{\mathrm{Tort,ref}} - k_{\mathrm{Tort,i}}|}{k_{\mathrm{Tort,ref}}} \cdot \left| 1 - \frac{|t_{\mathrm{Tort,ref}} - t_{\mathrm{Tort,i}}|}{t_{\mathrm{Tort,ref}}} \right|. \tag{6.11}$$

Hence, α is defined such that a small α indicates higher accuracy and smaller deviations of the model i from the original model. In Table 6.12, the different approaches along with their corresponding grading factor are shown. Accordingly, the reduction of the azimuthal

segmentation, usage of an optimized grid and the partial diffusion approximation results in the best performance-optimized model.

Table 6.12: *Grading factors α for six models. In the first column the model number is given including the TORT-TD (S4) reference calculation in the second row. In the second column the number of azimuthal segments is listed. Columns three through five show, respectively, if an optimized grid was used, if the convergence criterion was increased or if a partial diffusion approximation was applied. The last column shows the calculated grading factor α of each model, the lower the better.*

Model Nr.	**#Azimuth**	**opt. Grid**	**Convergence**	**Diffusion**	k_{eff}	**CPU time** [min]	α
Ref	4				0.999877	1812.0	-
1	1	x		x	0.999828	329.1	$8.90 \cdot 10^{-6}$
2	1			x	0.999800	649.2	$2.76 \cdot 10^{-5}$
3	4	x			1.001440	1472.5	$0.13 \cdot 10^{-2}$
4	4		x		1.001520	1806.5	$0.17 \cdot 10^{-2}$
5	4			x	0.999899	1386.7	$1.68 \cdot 10^{-5}$
6	1				0.999765	560.2	$3.46 \cdot 10^{-5}$

6.4.2.8 Optimized model

This model TORT-TD ($S4M$) results in a relative deviation of only 0.05 ‰ in the multiplication factor from the TORT-TD ($S4$) reference calculation and reduces the computational time by 81.8 %. The absolute power deposition distribution of the performance-enhanced TORT-TD ($S4M$) model is shown in Figure 6.42(a). As the TORT-TD ($S8$) calculation, this model reproduces the reference MCNP6 calculation very well. Between this enhanced TORT-TD ($S4M$) model and the MCNP6 reference result (see Figure 6.42(b)), no deviations larger than 5 % can be found. Around the density jump and at both edges of the fuel zone the deviations are well within ±2.5 %.
Also, the absolute thermal neutron flux distribution is well reproduced with the TORT-TD ($S4M$) model (see Figure 6.43(a)). In the detailed comparison with MCNP6 (see Figure 6.43(b)), there is almost no difference of the non-enhanced TORT-TD ($S4$) model and the enhanced $S4M$ (see Figure 6.38). As the non-enhanced model, the thermal neutron fluxes match within 2 % for all areas of interest. Inside the hafnium absorber and the boron ring this TORT-TD model also overestimates the thermal neutron flux.
Finally, the general shape of the fast neutron flux distribution is well reproduced, too. Because of the quadrature order of 4 this model also shows the numerical "ray" artifacts which have already been described in Chapter 6.4.2.1. The general behavior is very similar to the non-enhanced $S4$ calculation, i.e. matching of the fast neutron fluxes within ±2 % for all relevant areas inside these "rays".
Since all of the key core parameters match sufficiently well and the computational time has been reduced drastically, the coupled transient calculations will be performed with the enhanced TORT-TD ($S4M$) model exclusively.

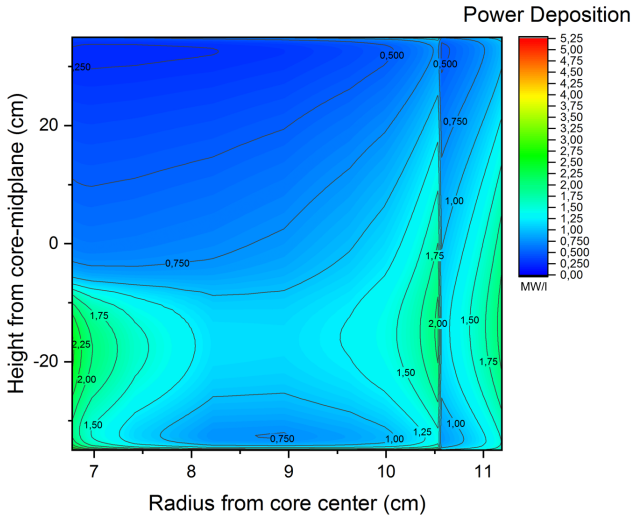

(a) Absolute TORT-TD *S4M* power deposition with correction

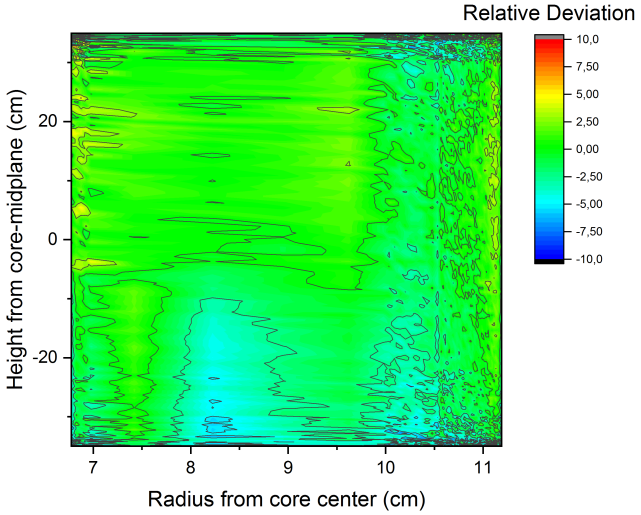

(b) TORT-TD *S4M* comparison of power deposition with correction

Figure 6.42: *The top panel (a) shows the absolute power deposition with correction (see Chapter 6.4.1.2) as calculated with the performance enhanced TORT-TD (S4M) model. The shape of the power deposition in one exemplary fuel plate is reproduced very well. Both the density jump at* 10.56 cm *and the influence of the hafnium absorber at the left side are clearly visible. In the bottom panel (b) the relative deviation in % of the power deposition as calculated with TORT-TD (S4M) and MCNP6, respectively, in the sense of "TORT − MCNP6" is depicted. The results show a well matching trend within* ±2 %*. In the middle lower part of the fuel plate the deviations between both codes rises to* ±3 %*.*

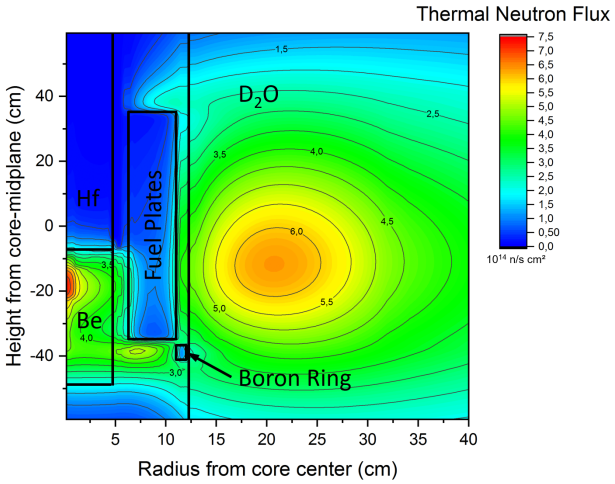

(a) Thermal neutron flux distribution calculated with TORT-TD (S4M)

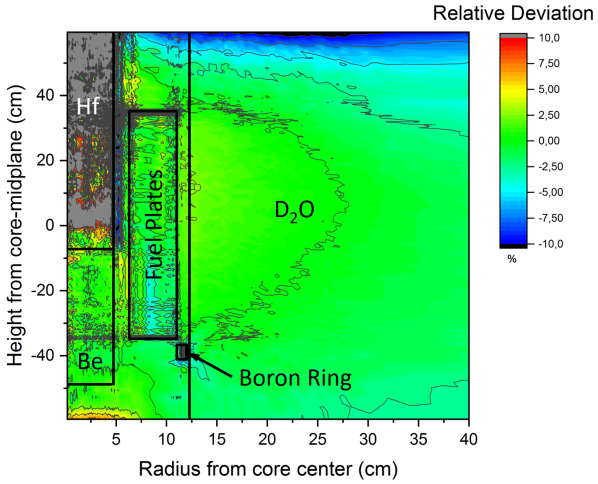

(b) Comparison of thermal neutron flux calculated between MCNP6 and TORT-TD (*S4M*)

Figure 6.43: *The top panel (a) show the thermal neutron flux distribution as calculated with TORT-TD (S4M). Again all energy groups up to* 0.625 eV *(see Table 6.9) were summed up. TORT-TD reproduces the FRM II thermal flux distribution very well; the maximum thermal flux usable is situated inside the heavy water moderation tank, the absolute maximum is located inside the beryllium follower and the installed hafnium depresses the thermal neutron flux. Also the boron ring is clearly visible. The bottom panel (b) shows the relative deviation in % of the thermal neutron flux between MCNP6 and TORT-TD (S4M) in the sense of "TORT − MCNP6". For the heavy water moderation tank, the beryllium follower and the fuel zone both codes deliver matching results within* ±2 %. *Inside the hafnium absorber TORT-TD (S4M) systematically overestimates the thermal neutron flux by more than* 10 %. *Also inside the installed boron ring the deviations are increased. Above* 45 cm *TORT-TD (S4M) underestimates the fast neutron flux by more than* −10 %.

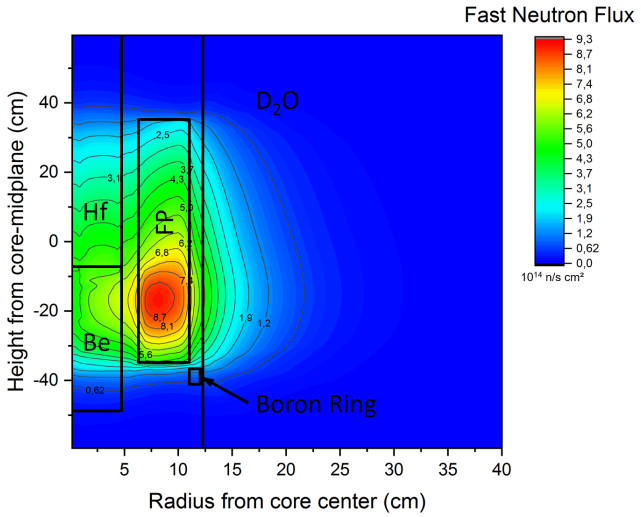

(a) Fast neutron flux distribution calculated with TORT-TD (S4M)

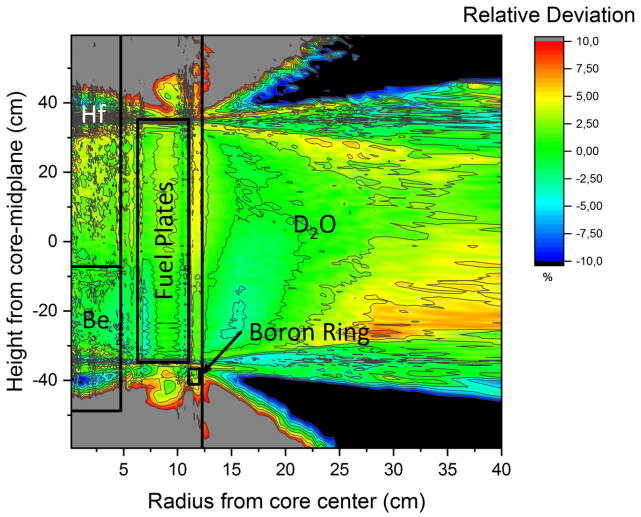

(b) Comparison of fast neutron flux calculated between MCNP6 and TORT-TD (*S4M*)

Figure 6.44: *In the top panel (a) the fast neutron flux distribution is depicted. Energy groups above* 0.1 MeV *have been summed up (see Table 6.9). TORT-TD (S4M) reproduces the fast flux distribution of* FRM II *very well. In the bottom panel (b) the relative deviation in % of the fast neutron flux between MCNP6 and TORT-TD (S4M) in the sense of "(TORT−MCNP6)/MCNP6" is depicted. For the fuel zone the heavy water moderation tank, the hafnium absorber and the beryllium follower the deviations are within ±2 %. Because of visible numerical "ray effects", starting at the edges of the fuel zone, the deviations outside these "rays" are increased to more than ±10 %.*

CHAPTER 7

Development of the Thermal-Hydraulic Models used

As for the neutronics, a well-mapped model for thermal-hydraulical calculations must represent all important parameters of the real core. Some transient scenarios, like Loss of coolant accident (LOCA) affect the full primary cooling circuit. Therefore, the primary cooling circuit including all the tubing, the main cooling pumps and heat exchangers must be modeled in ATHLET as well.
For the fuel element itself, highly detailed, steady state calculations have been performed within [10] using CFX. These results will serve as reference for the ATHLET calculations.

7.1 The thermal-hydraulical conditions in FRM II's core

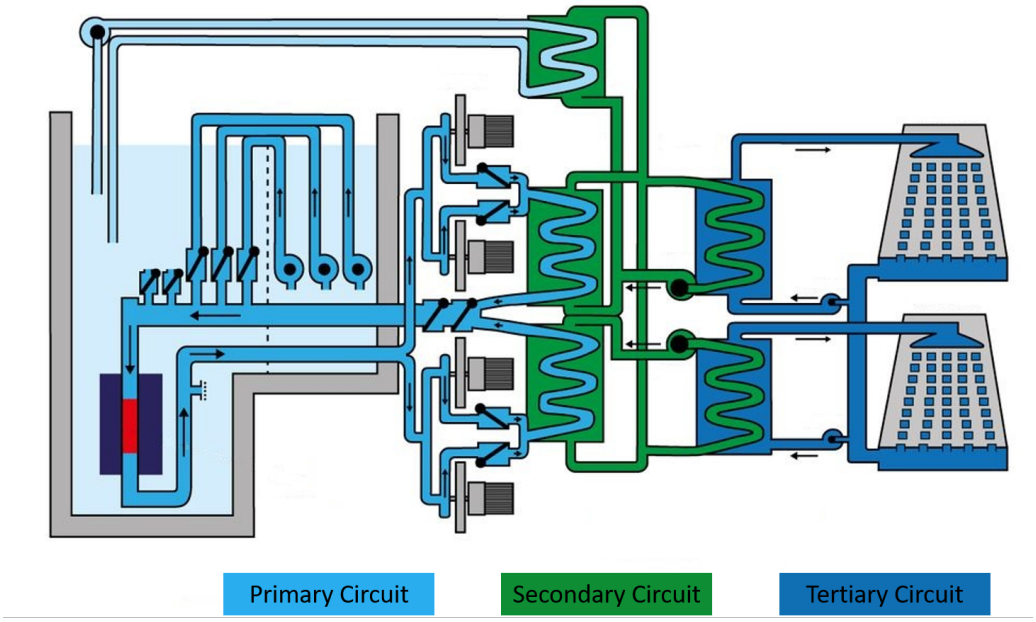

Figure 7.1: *Overview of* FRM II *'s three cooling circuits. Besides the four main cooling pumps, the three emergency pumps are also depicted. The heat is transported via heat exchangers between the circuits. The final heat sink are two cell coolers within the tertiary circuit.*

In Figure 7.1 a simplified diagram of the general cooling system of the reactor is depicted. In total, FRM II has three separate cooling circuits which use light water as a cooling medium. The central channel with the fuel element is part of the primary circuit and is fed by four main cooling pumps. The primary circuit is connected to the secondary by two heat exchangers. Directly connected to the primary circuit above the central channel are three emergency cooling pumps which also use light water from the pool to ensure the cooling of the core. In addition to the main heat exchangers in the primary loop, the reactor pool is also cooled by a separate heat exchanger, connected to the secondary circuit. Two cell coolers serve as a heat sink for the tertiary circuit. Both, the secondary and tertiary circuit are not modeled explicitly in the thermal-hydraulic ATHLET model but are represented by effective characteristics of the primary heat exchangers.
In total, 300 $^{kg}/_{s}$ of primary coolant flow through the central channel, whereof 274.5 $^{kg}/_{s}$ are guided through the fuel element itself (see Figure 7.2(b)). The remaining is used for the cooling of other parts like the control rod. A built-in sieve is installed at the top of the fuel element in order to protect the fuel assembly, especially from a blockage of cooling channels (see Figure 7.2(a)). The average flow speed of the cooling water between the fuel plates is 15.91 $^{m}/_{s}$ [30]. The 2.2 mm thick cooling channels are embedded in-between the fuel plates. Because of the involute shape of the fuel plates, the width of these channels is constant throughout the whole core. The cooling water enters the active zone with a temperature of 37 $^{\circ}C$ and is heated by about 16 $^{\circ}C$ [30]. Over the fuel plates a measured pressure drop of 5.13 bar is reported in [30]. A detailed study of the steady state pressure conditions in three dimensions has been performed within [10].

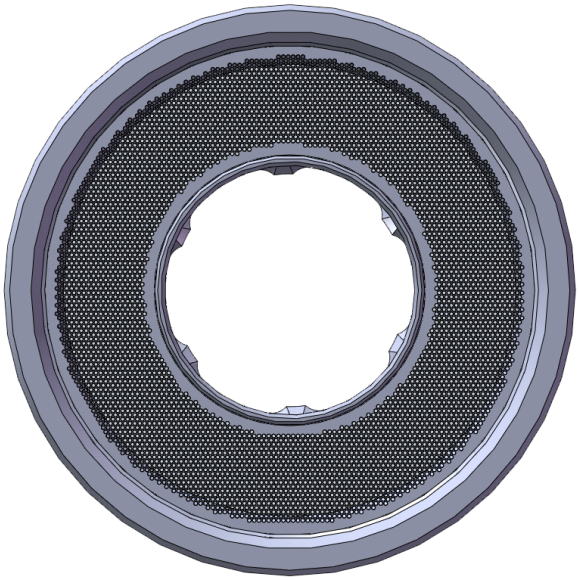

(a) Top view fuel element

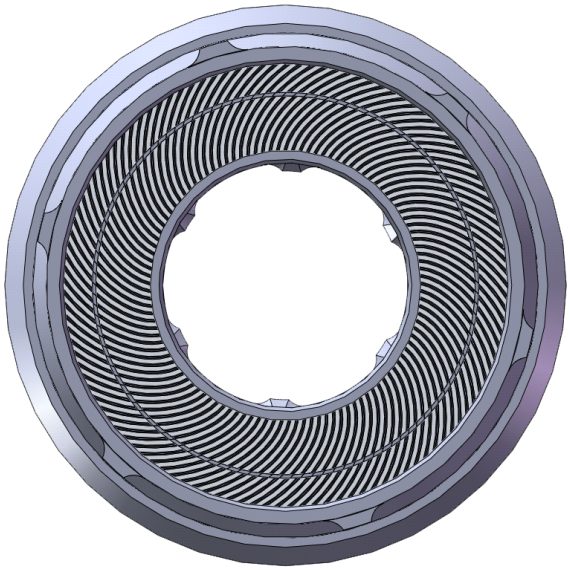

(b) Bottom view fuel element

Figure 7.2: *The top panel (a) shows the top view of a CAD model of a fuel element of* FRM II. *The sieve and the tube for the control rod can be clearly seen. In the bottom panel (b) a bottom view of the CAD model with all fuel plates is depicted.*

7.2 ATHLET model

7.2.1 Core model

Based on an FRM II-ATHLET model developed by A. Pöpperl [62], an improved ATHLET input desk has been created using the information of the thermal-hydraulical conditions in the

core of FRM II. In [62], the core is represented by an inlet which distributes the cooling water in four heated core channels and an un-cooled bypass. To take the power distribution profile of

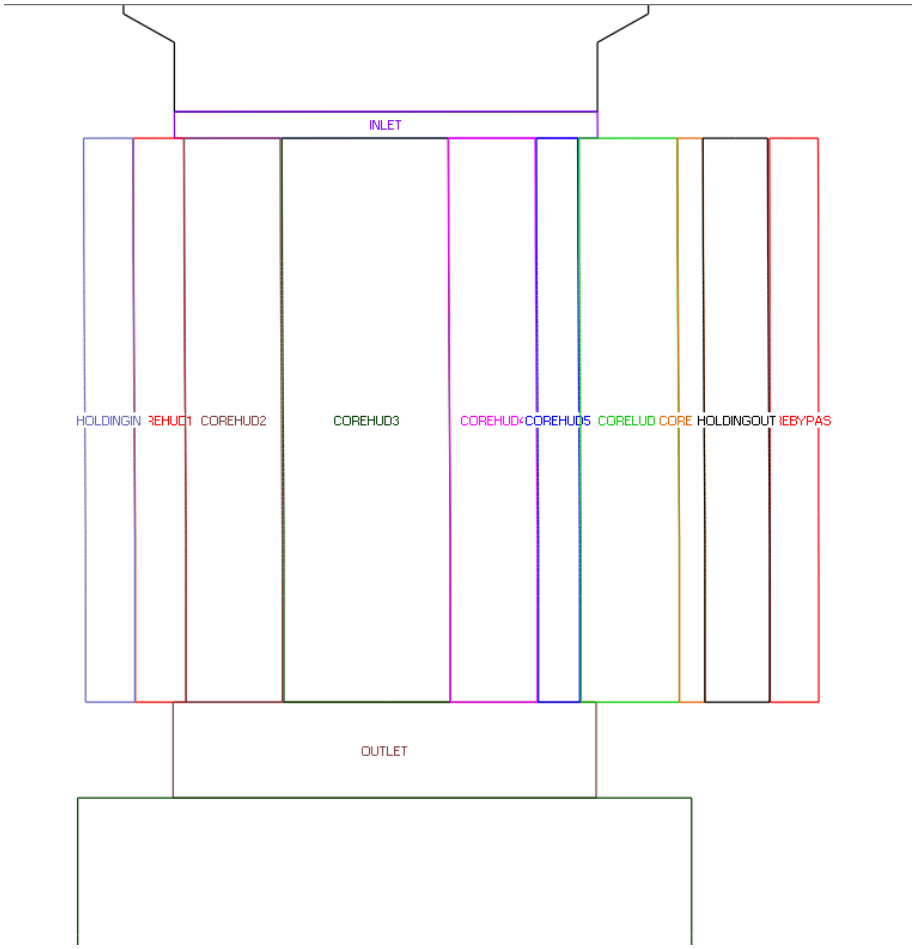

Figure 7.3: *Core model of* FRM II *modeled with ATHLET. From the inlet the cooling water is distributed to the various core channels. At the end of the active area the cooling water is gathered within the outlet.*

FRM II's fuel plates (see Figure 6.3) into account, the amount of simulated channels has been increased to a total of ten (see Figure 7.3).
In order to take into account every necessary aspect without generating unneeded excessive amounts of new channels, a new channel was created when the following criteria are fulfilled:

- The area is a known hot channel [10] or the power deposition changes significantly with respect to the local power deposition.
- Due to the coupling requirements of TORT-TD and ATHLET, a border of two mesh cells in the TORT-TD model is available.

The ten resulting channels are: Two un-cooled channels representing the holdings (HoldingIn, HoldingOut) of the fuel plates, five heated channels for the zone with high uranium density (COREHUD 1, COREHUD 2, COREHUD 3, COREHUD 4, COREHUD 5), two heated channels

for the zone with low uranium density (CORELUD 1, CORELUD 2) and one un-cooled core bypass.
The resulting piping scheme is shown in Figure 7.4 as overlay to the power deposition in the fuel plates. With this setup especially the most crucial areas, i.e. the hot channels at the edges

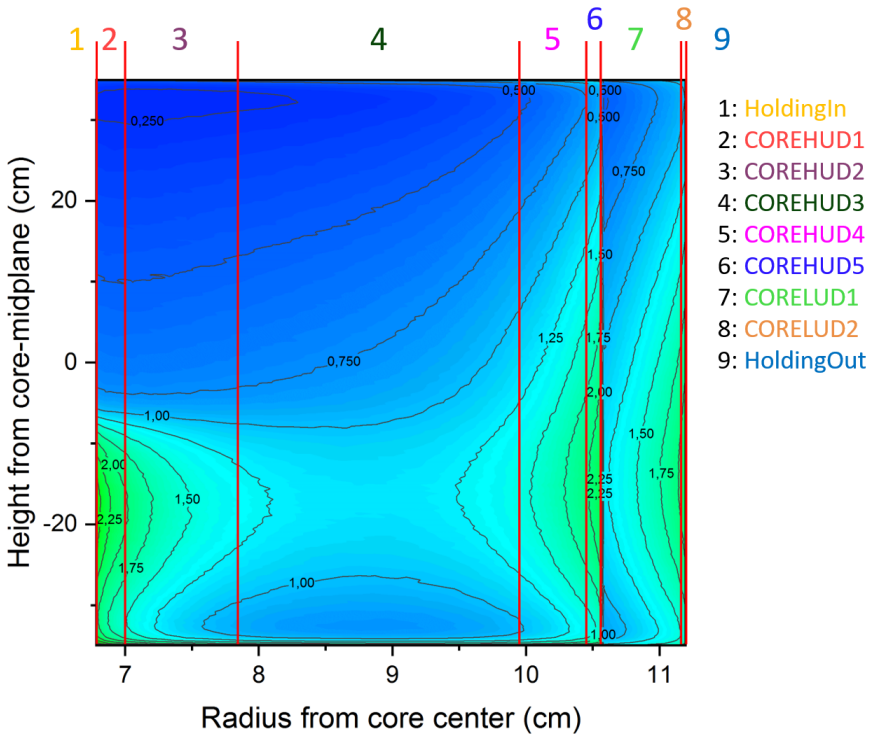

Figure 7.4: *Resulting piping scheme in ATHLET depicted as overlay over the power deposition in a representative fuel plate (see Fig. 6.3). The pipes HoldingIn and HoldingOut are connected left and right to COREHUD1 and CORELUD2, respectively.*

of the fuel plates and at the density jump are well represented. In axial direction, the pipes representing the core are divided in 100 sub-parts in order to have a sufficient resolution inside the active area. All core channels, except the bypass, are connected with cross connections, so that water and heat can be exchanged between neighboring channels.
For the correct distribution of the mass flow through the core channels, the area of each channel is provided in the inlet and outlet branch. With that data ATHLET can correctly distribute the incoming cooling water to each following tubing, so that the mass flows through each channel equals the results as calculated with CFX (see Chapter 5.1). Because ATHLET is a 1D code, small structures inside the fuel element like the combs (see [10]) of the fuel plates are not modeled, but their influence on the core behavior can be neglected.

7.2.2 Pipe friction

ATHLET calculates a pipe system serially, starting in one specified control volume (see Chapter 5.2) and propagating through the whole piping system. In order to let ATHLET reproduce the real conditions of FRM II's primary cooling circuit, the steady state flow parameters available

for all parts, like pumps, heat exchangers and especially the tubing of the primary circuit have to be provided. For pumps or heat exchangers data taken from their specifications are available (see Chap. 7.2.4, 7.2.5). Other data for installations like the sieve can be calculated using commercial CFD software like Cfx (see Chap. 7.2.3). For the pipe friction data there is no experimental data available, so a conservative assumption based on literature had to be made. As proposed by [62], a total wall roughness of 50 μm for the tubing and 2.2 μm for the heated core channels are utilized. The tubing of the primary cooling circuit of FRM II is assumed to be new and not crusted, so a roughness of 50 μm is reasonable [39]. Because the fuel element is made of aluminum and is exchanged after 60 days, the specified roughness of 2.2 μm is eligible, too [39]. The roughness for the cooling channel is slightly smaller than in [10].

7.2.3 Sieve

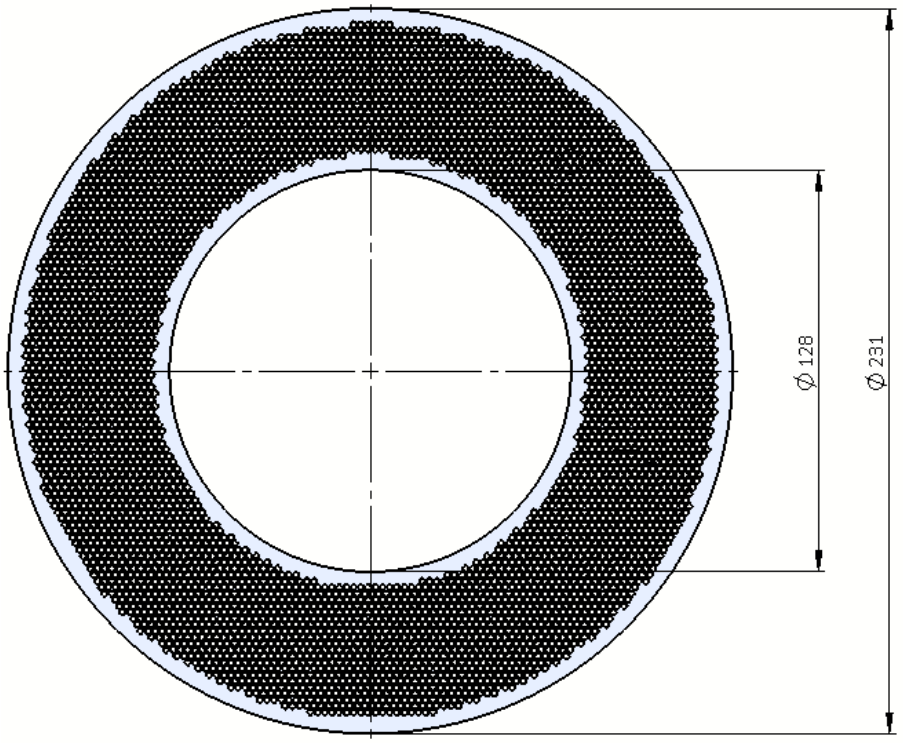

Figure 7.5: *Front view of the filter element*

As already described (see Chapter. 7.1), a sieve is installed at the top of the fuel element (see Figure 7.5) in order to prevent the fuel plates from damage. The sieve is 1.0 cm thick and has an outer diameter of 23.1 cm and an inner one of 12.8 cm. One single channel has a diameter of 1.8 mm, whereas the bevel angle to the channel axis is 20 °. In total, there are 5110 flow channels, with a horizontal x-distance of 2 mm and a horizontal y-distance of 2.3 mm. In Table 7.1 the relevant geometric data of the sieve is shown.

Table 7.1: *Geometric data of the sieve at the top of the fuel element.*

Geometry Parameter	**Value**
Outer sieve diameter	23.1 cm
Inner sieve diameter	12.8 cm
Thickness	1.0 cm
Number of channels	5110
Channel diameter	1.8 mm
Bevel angle to cylinder axis	20 °
Horizontal y - distance between channels	2 mm
Horizontal x - distance between channels	2.3 mm

In ATHLET an installation like the sieve cannot be modeled explicitly but rather has to be inserted as an additional friction loss. Including wall roughness, the pressure loss Δp has been calculated by G. Heidecker as 1.35 bar [31]. With

$$\zeta = \frac{2\,\Delta p}{\rho\,(v\,A)^2}, \tag{7.1}$$

whereas ζ is the pressure loss coefficient, ρ the fluid density, v the streaming velocity and A the area of the pipe, the corresponding pressure loss coefficient of the sieve can be calculated. With the values provided in [31] a resulting pressure loss coefficient of $\zeta = 2371.0\,{}^{1}/_{\mathrm{m}^4}$ has been obtained.

7.2.4 Pump model

The four main pumps are centrifugal pumps which are vertically installed. They are 6 m high, and their total weight is 4000 kg each. According to in the specification [86], one pump has a flow rate of $75\,{}^{\mathrm{kg}}/_{\mathrm{s}}$. During normal operation the impeller rotates at roughly 2950 rpm and delivers a pressure gradient of 11 bar. In case of a station blackout the moment of inertia of $4 \cdot 17\,{}^{\mathrm{kg}}/_{\mathrm{m}^2}$ of each main cooling pump helps to maintain the cooling of the core until other active emergency measures like emergency pumps or emergency power supply come online. Because the emergency pumps are buffered by batteries, in the case of a station blackout they would take over the reactor cooling almost immediately. The batteries can supply the emergency pumps for almost 3 h.

7.2.5 Heat exchangers

The main primary cooling circuit is connected to two U-tube heat exchangers, whereas one is specified for a power of 9.5 MW, according to their specification [86]. A third heat exchanger is installed in order to cool the remaining power which is deposited in the heavy water moderation tank or the reactor pool (see Figure 7.1). On primary side they run on purified pool water, and the secondary side is operated with purified water. Two main cooling pumps feed one of the heat exchangers, so the flow rate on the primary side is about $150\,{}^{\mathrm{kg}}/_{\mathrm{s}}$ each. The secondary side is fed

by roughly 227 kg/s. The total mass of one exchanger with cooling fill is 17550 kg. With a total length of roughly 6 m a heat transfer area of 445 m^2 can be provided, giving rise to an average temperature difference of 9.3 K.

7.3 Comparison of CFX and ATHLET

In order to validate the ATHLET model, steady state calculations have been performed to compare the results obtained with CFX. To simulate the heated core, the steady state power distribution of FRM II as calculated with MCNP6 (see Fig. 6.3) is used to heat the corresponding core pipes in the ATHLET model. The general CFX results for the fuel plates without the holding frames, e.g. for the segmentation of a cooling channel and the determination of the mass flows and temperatures, are described in a report by J. Becker [38].
In ATHLET, the integral power of one pipe and the corresponding axial distribution has to be provided. Therefore, C^2 has been used to generate an ATHLET input desk according to Figure 7.4 for the data for each core pipe (cf. Appendix D.10). The ATHLET model used for this comparison does not contain any time dependent events like leakages, pump trips or other excursions.
The CFX model used is based on the model developed within [10]. To compare ATHLET with CFX, the cooling channel in the CFX model has been divided into seven zones which represent the seven heated core pipes in ATHLET [38]. For the simulation with CFX the shear stress transport (SST) with automatic wall function has been used to model turbulence. With both models set up, they can be compared for the basic parameters like pressure drop over the fuel element, mass flows and coolant temperatures.

Pressure drop In [30] a pressure drop of 5.13 bar over the fuel plates is quoted. This value is in good agreement to the value of 5.20 bar calculated with CFX [10]. The pressure drop calculated with ATHLET of 5.65 bar is slightly higher. In ATHLET the whole primary cooling circuit is modeled and in order to reach numerical convergence for the whole system, ATHLET uses several correction methods like the adaption of the ζ values of each Thermo-Fluiddynamic Object (TFO) (see Chapter 5.2). Therefore, the pressure drop over the sieve is slightly smaller than the quoted 1.1 bar. Taking this fact into account, the pressure drop over the fuel plates has to be slightly higher in order to obtain the defined outlet pressure of 2.20 bar, which has been used as starting value.

Temperatures As shown in Table 7.2 and Figure 7.6, the temperature differences are rather high for the very thin hot channels but are fitting well for the other well streamed pipes. In the thin channels HUD 1, HUD 5 and LUD 2, the temperature differences are between 3.7 °C and 10.4 °C. As shown later in Table 7.3 and Figure 7.7 these three channels have a rather small mass flow. The higher coolant temperatures are explained by the missing lateral heat conduction in the fuel plates between the most outer channels HUD 1 and LUD 2 to the inner and outer holdings. Due to the high thermal conductivity of the aluminum cladding a non negligible amount of heat is stored in these two channels in the ATHLET model. CFX correctly distributes this heat to the holding frames leading to decreased temperature of the coolant. Taking CFX as reference, the results obtained with ATHLET are systematically higher in highly heated channels with a small mass flow. Taking the temperature differences in more streamed channels (see Table 7.2)

Table 7.2: *Temperatures of the different channels calculated with ATHLET and* Cfx *respectively. In the last column the absolute difference between both codes in the manner ATHLET − Cfx is written.*

Name	Temperature ATHLET [°C]	Temperature Cfx [°C]	Difference [°C]
HUD 1	54.753	50.939	3.814
HUD 2	51.013	51.952	-0.939
HUD 3	50.510	51.694	-1.184
HUD 4	57.264	57.437	-0.173
HUD 5	62.610	58.885	3.725
LUD 1	56.960	56.418	0.542
LUD 2	61.006	50.613	10.393

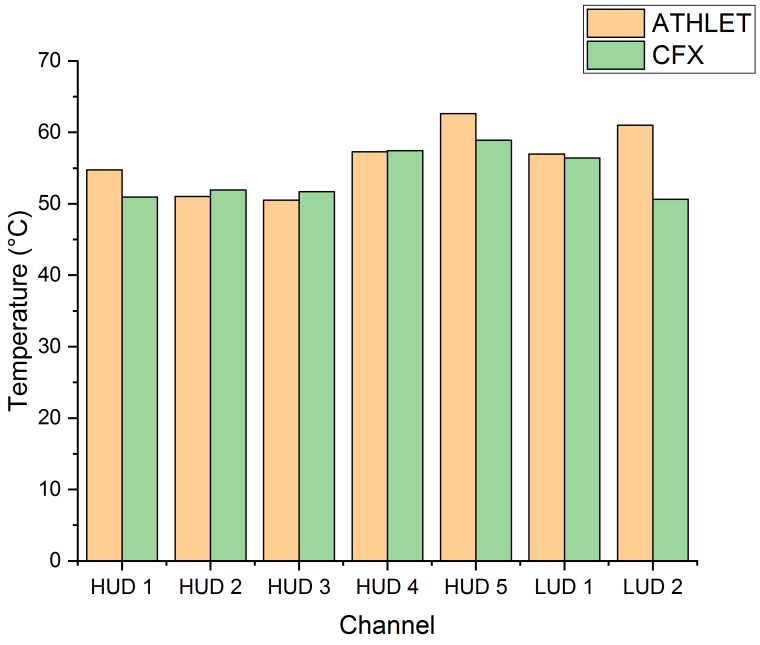

Figure 7.6: *Temperatures of the different channels calculated with ATHLET and* Cfx *respectively.*

the results match very well within ±1 °C. Due to increased heating of less streamed channels, ATHLET can be assumed as being conservative compared to Cfx.

Flow velocity In [10] an averaged coolant velocity of 15.91 m/s between the fuel plates is reported. With the ATHLET model used here a velocity of 15.85 m/s is calculated. Both values are in good

Table 7.3: *Mass flows of the different channels calculated with ATHLET and* Cfx *respectively. In the last column the absolute difference between both codes in the manner ATHLET − Cfx is written.*

Name	Mass Flow ATHLET [kg/s]	Mass Flow Cfx [kg/s]	Difference [%]
HUD 1	10.66	10.22	4.38
HUD 2	38.313	38.81	-1.29
HUD 3	114.60	114.13	0.42
HUD 4	31.33	33.24	-5.73
HUD 5	7.10	7.05	0.64
LUD 1	40.04	40.24	-0.49
LUD 2	2.73	2.70	1.04
Total	244.78	246.39	-0.65

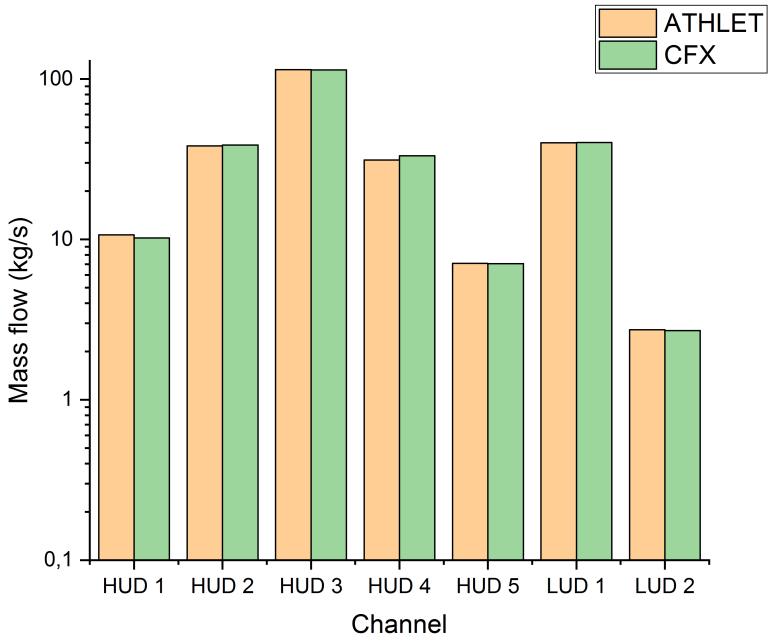

Figure 7.7: *Mass flows of the different channels calculated with ATHLET and* Cfx *respectively.*

agreement. In total, a mass flow $\dot{m}$ of 244.78 kg/s goes through the active heated area in the ATHLET model. This is smaller by 0.65 % than the 246.39 kg/s as calculated with Cfx. Adding the mass flow of the holding channels a total mass of 272.0 kg runs through the fuel element per second. Finally, the mass flow within each channel can be compared. As shown in Table 7.3 the

mass flows in each channel calculated with both codes match well within ±5 %. Especially in HUD 1 the higher temperature of the coolant leads to a repression effect and, therefore, to a smaller mass flow. This fact strengthens the heating effect further more.
The mass flow weighted outlet temperature of each channel can serve as a quality factor ξ of the ATHLET model. ξ is defined as:

$$\xi = \frac{\sum_i \dot{m}_\mathrm{i}\, T_\mathrm{i}}{\sum_i \dot{m}_\mathrm{i}}, \tag{7.2}$$

whereas $\dot{m}_\mathrm{i}$ is the mass flow of the i-th pipe and T_i the corresponding temperature. With Eq. 7.2 and the values given in Table 7.2 and 7.3, respectively a corresponding ξ_A and ξ_C can be calculated for the ATHLET and CFX model:

$$\xi_\mathrm{A} = 53.16\,^\circ\mathrm{C}, \tag{7.3}$$
$$\xi_\mathrm{C} = 52.75\,^\circ\mathrm{C}. \tag{7.4}$$

This results in a difference of 0.41 °C between the ATHLET and CFX model and means that the total energy balance in both models are in a good match. The very small temperature difference can be caused by the missing energy transport to the aluminum holding ducts in ATHLET. With these results shown the ATHLET model will be used for the following transient calculations (see Chapter 10).

CHAPTER 8

Coupling of TORT-TD and ATHLET

For the coupled transient calculation both codes, TORT-TD and ATHLET, respectively, will be used in coupled mode in which information about heat deposition, temperature and density is exchanged. Therefore, a link between the computing mesh of TORT-TD (see Chapter 6.4) and the piping scheme of ATHLET (see Chapter 7.2) has to be provided [78] (see Figure 8.1). However, the TORT-TD model contains details, like the exact design of the fuel element, the heavy water moderator tank or the control rod, which are not part of the ATHLET model. Because the coupling routine needs every mesh cell in TORT-TD linked to a Thermo-Fluiddynamic Object (TFO), these parts have to be assigned to an arbitrary object in ATHLET. In the ATHLET model, the reactor pool is modeled as so-called time-dependent volume whose thermal-hydraulical properties remain constant over time. During the transient calculations the cross sections of these structural parts are not modified. Therefore, there is no need of a temperature call-back and, hence, these parts can be linked to the reactor pool.
For all mesh cells of the active core zone, temperature dependent cross sections are available (see Chapter 4.2.1) and therefore the feedback from ATHLET is significant for TORT-TD. Also the whole thermal power is distributed within this volume and so the coolant is mainly heated there. Hence, the whole active core zone is represented within the TFOs HUD 1, HUD 2, HUD 3, HUD 4, HUD 5, LUD 1 and LUD 2, and all cells are linked to their corresponding TFOs. There are also counterparts in the ATHLET model regarding the holding structure of the fuel plates including the bypass which are assigned to each other. In total, 11 channels are used to link the TORT-TD model with its counterpart in ATHLET. The coupling scheme is shown in Figure 8.1. At the beginning of each coupled calculation, TORT-TD and ATHLET perform several steady state calculations to exchange data in order to reach a numerical convergence in both models. Information regarding power deposition, coolant density and temperature is transferred between both codes. In ATHLET several adjustment mechanisms try to ensure within certain limits convergence, e.g. the surface of the heat exchangers are automatically adjusted to balance the heat transfer.

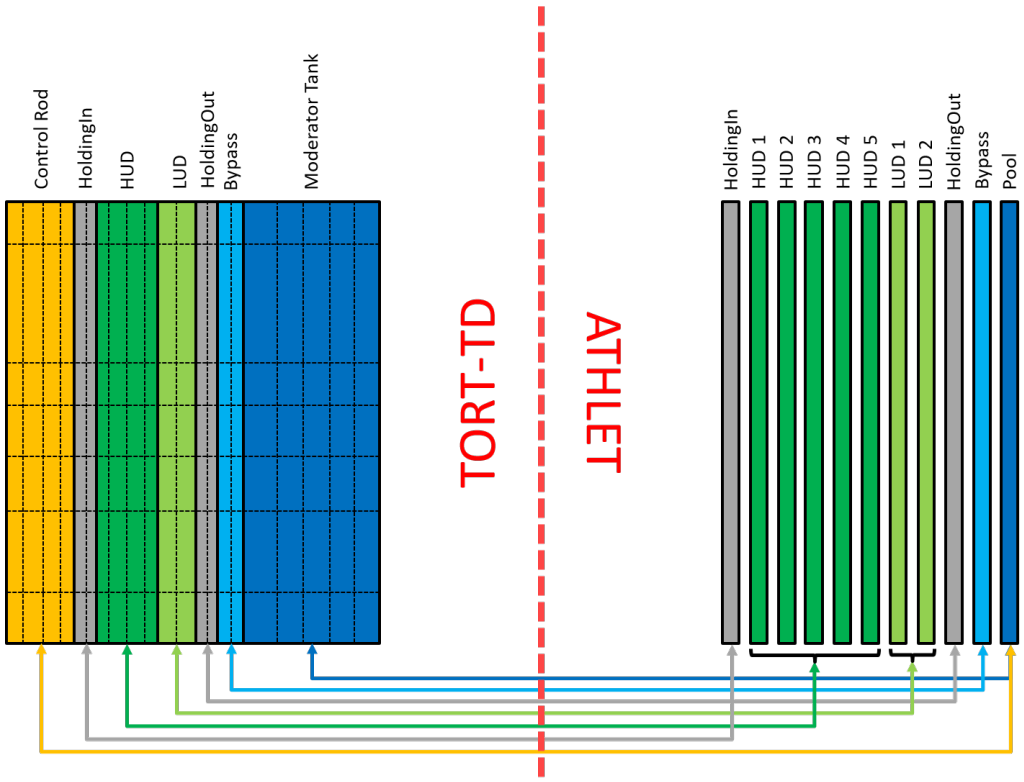

Figure 8.1: *General coupling scheme. On the left an excerpt of a simplified TORT-TD model is depicted (see Chapter 6.4). Here, the major components are combined and not every mesh cell is shown, so detailed spatial information is not available. On the right the piping scheme of the ATHLET model is depicted (see Chapter 7.2). The arrows show the coupling between the components in TORT-TD and the corresponding pipes in ATHLET.*

Part IV

Results

CHAPTER 9

Core study with Serpent 2

9.1 Study of the control rod

9.1.1 Reactivity worth of the control rod

With its complex geometry the control rod and the corresponding reactivity worth (see Chapter 2.1.5.3) plays a significant role in the time-dependent behavior of the reactor. Therefore, the multiplication factor was calculated in dependence of the position of the control rod. In [10] the reactivity worth of the control rod was studied with MCNP6, and the values obtained from this study can be compared with the Serpent 2 model developed within this thesis. Figure 9.1 shows the steady state multiplication factor and the corresponding reactivity for different control rod positions as calculated with Serpent 2. As in [10] the data is fitted with a parabola and yielding the following dependency:

$$k_{\text{eff}}(z) = \left[(-5.058 \pm 0.036) \cdot 10^{-5}\right] \cdot z^2 + \left[(0.446 \pm 0.001) \cdot 10^{-2}\right] \cdot z + (1.0328 \pm 0.0001). \quad (9.1)$$

The quality of the fit is $R^2_{\text{adj}} = 0.999$. The fitting curve given in Eq. 9.1 matches very well with the function found in [10], even if the multiplication factor calculated with Serpent 2 is slightly lower than in MCNP6. Due to the different handling of the S(α,β) of beryllium and the increasing influence of beryllium with a withdrawn control rod, this difference may occur. In summary, MCNP6 and Serpent 2 deliver well matching values for this study.

9.1.2 Influence of the control rod to the core key parameters

Due to the control rod movement the influence of the beryllium increases, and therefore, the fission rate, thermal and fast neutron flux distribution changes. As depicted in Figure 9.2, due to the withdrawal of the absorbing hafnium, there is a significant power deposition at the inner side of the fuel plates (compare Figure 6.3). At the outer side there are only marginal changes of the shape of the power deposition distribution, and the sharp density jump is still clearly visible. Figure 9.3 shows the thermal and fast neutron flux distribution with a fully withdrawn control rod. Compared to the critical position at BOL (compare Figure 6.4) the thermal flux distribution is expanded over the whole height of the fuel element. Also, the fast neutron flux distribution covers the whole fuel zone and is not limited to the lower region (compare Figure 6.5).

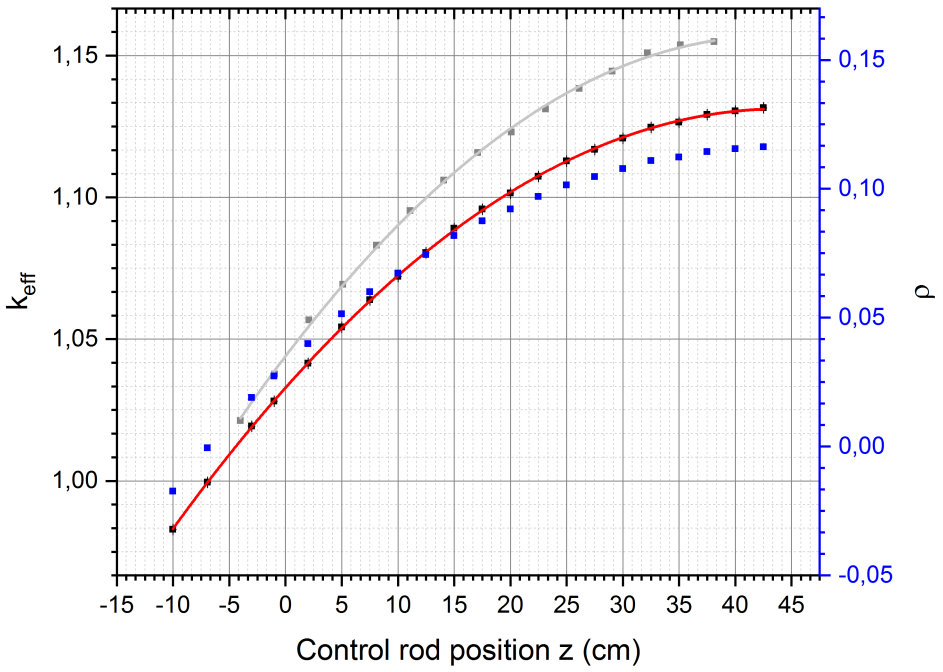

Figure 9.1: *The black points show the multiplication factor k_{eff} in dependence of the control rod position. In red the corresponding quadratic fit is depicted. The blue points show the resulting reactivity worth ρ. In grey the results of Breitkreutz [10] are shown.*

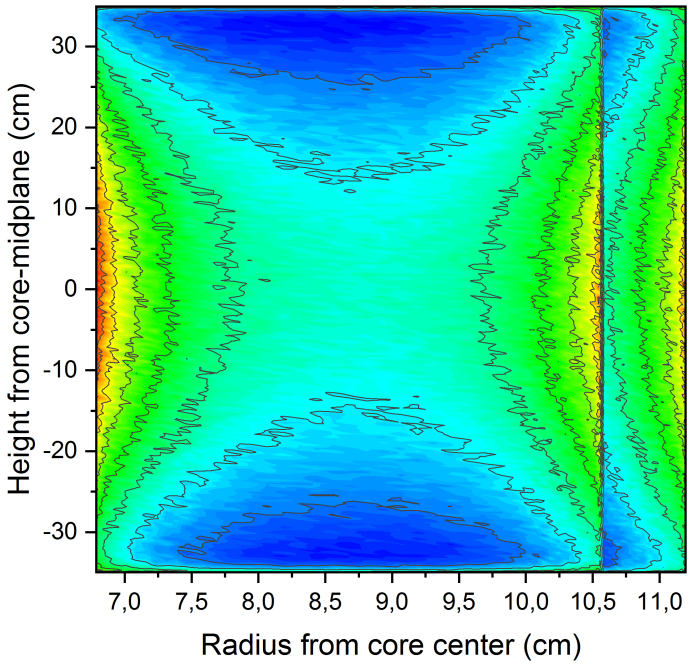

Figure 9.2: *Fission rate distribution of current fuel element with withdrawn control rod as calculated with Serpent 2.*

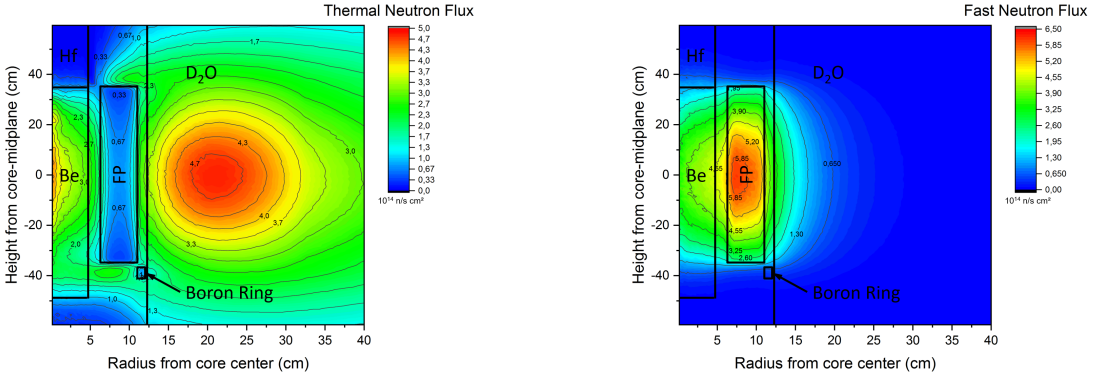

(a) Thermal neutron flux distribution of current fuel element with withdrawn control rod

(b) Fast neutron flux distribution of current fuel element with withdrawn control rod

Figure 9.3: *The left panel (a) shows the thermal neutron flux in* $10^{14}\,\mathrm{n/cm^2s}$ *of the current fuel element as calculated with Serpent 2 and fully withdrawn control rod. In the right panel (b) the fast neutron flux in* $10^{14}\,\mathrm{n/cm^2s}$ *of the current fuel element as calculated with Serpent 2 is shown.*

9.2 Burnup of a fresh fuel element

Serpent 2 has the inbuilt capability for burnup calculations. Using this feature allows to study the change of the multiplication factor in dependence on the burnup of the fuel element. In order to compare the results with [10] and [71], the same nuclide set was used for the Serpent 2 burnup calculations:
^{1}H, ^{2}H, ^{3}H, ^{3}He, ^{4}He, ^{7}Li, ^{9}Be, ^{10}B, ^{11}B, ^{12}C, ^{13}C, ^{27}Al, ^{28}Si, ^{29}Si, ^{30}Si, ^{83}Kr, ^{93}Zr, ^{95}Zr, ^{95}Nb, ^{92}Mo, ^{94}Mo, ^{95}Mo, ^{96}Mo, ^{97}Mo, ^{98}Mo, ^{100}Mo, ^{99}Tc, ^{101}Ru, ^{102}Ru, ^{103}Ru, ^{103}Rh, ^{105}Rh, ^{117}Rh, ^{105}Pd, ^{119}Pd, ^{109}Ag, ^{113}Cd, ^{129}I, ^{131}I, ^{135}I, ^{131}Xe, ^{133}Xe, ^{135}Xe, ^{133}Cs, ^{134}Cs, ^{135}Cs, ^{139}La, ^{141}Ce, ^{143}Ce, ^{141}Pr, ^{143}Pr, ^{143}Nd, ^{145}Nd, ^{146}Nd, ^{147}Nd, ^{148}Nd, ^{147}Pm, ^{148m}Pm, ^{149}Pm, ^{149}Sm, ^{150}Sm, ^{151}Sm, ^{152}Sm, ^{153}Sm, ^{153}Eu, ^{154}Eu, ^{155}Eu, ^{156}Eu, ^{157}Eu, ^{156}Gd, ^{234}U, ^{235}U, ^{236}U, ^{237}U, ^{238}U, ^{237}Np, ^{238}Np, ^{239}Np, ^{238}Pu, ^{239}Pu, ^{240}Pu, ^{241}Pu, ^{242}Pu.
This set includes a total of 83 nuclides. C^2 principally has the capability to move the control rod, and with the reactivity worth from Chapter 9.1.1, it would be possible to calculate the burnup of the fuel element by adjusting the control rod position. However, the necessary coupling interface between C^2 and Serpent 2 could not be fully tested in the context of this thesis, and will be implemented later. Hence, for the calculations in this chapter, the control rod stays fully withdrawn.

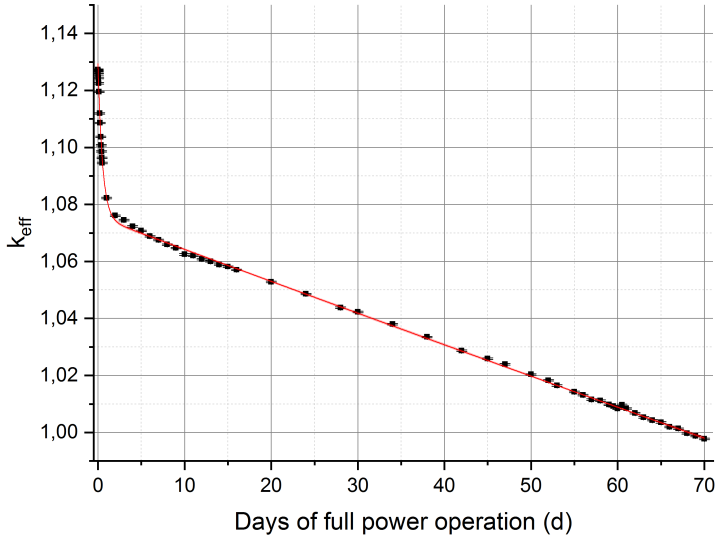

Figure 9.4: *Multiplication factor in dependence of the core burnup. In the first hours the multiplication factor decreases rapidly due to the build up of* ^{135}Xe. *The maximum days of full power operation is calculated as* 66 d.

Figure 9.4 shows the resulting multiplication factor depending upon the burnup. The steep incline of the curve at the beginning stems from the build-up of ^{135}Xe, a strong neutron absorbing poison, and later from additional fission products, especially ^{149}Sm.
In [10] a coupled system of MCNP6 and MonteBurns was used to calculate the burnup of the core. These values (see [10], Table 14.3) can be compared with the values calculated here using Serpent 2 (see Table 9.1). The average burnup after 60 d is 20.2 % which is identical to the

value calculated by Röhrmoser using MonteBurns [72], and very similar to 20.4 % calculated by Breitkreutz [10]. It has to be mentioned that both, Röhrmoser and Breitkreutz, included the movement of the control rod.
The total plutonium production during a cycle was estimated to be 11.91 g at End Of Life (EOL), of which are 10.48 g ^{239}Pu. Compared to [10], Serpent 2 estimates the total plutonium content 3.1 % lower and the amount of ^{239}Pu 1.3 % lower.
There are significant deviations between the two codes for very light isotopes like tritium (96 %), ^{4}He (−93 %) or ^{10}B (−100 %). Also the amount of the silicon isotopes are estimated much lower by Serpent 2. Due to a different or probably wrong handling of the (n,t)-reaction or ternary fission in MonteBurns these differences may occur. The results for all other Non-Actinides match well.

Table 9.1: *Nuclide inventory after* 60 d *full power operation divided into actinides and non-actinides.*

Isotope	**Quantity** [g]	**Isotope**	**Quantity** [g]	**Isotope**	**Quantity** [g]
Actinides					
^{234}U	6.097E+01	^{237}Np	4.636E+00	^{241}Pu	3.203E-01
^{235}U	6.005E+03	^{239}Np	8.227E-01	^{242}Pu	1.399E-02
^{236}U	2.931E+02	^{238}Pu	1.981E-01	^{241}Am	6.214E-04
^{237}U	1.680E+00	^{239}Pu	1.048E+01	^{244}Am	7.127E-08
^{238}U	5.010E+02	^{240}Pu	8.943E-01	^{245}Am	6.506E-11
Non-Actinides					
^{1}H	1.895E-03	^{98}Mo	2.965E+01	^{143}Ce	1.317E+00
^{2}H	9.880E-05	^{100}Mo	3.289E+01	^{141}Pr	1.922E+01
^{3}H	1.780E-03	^{99}Tc	2.920E+01	^{143}Pr	1.297E+01
^{3}He	4.949E-06	^{101}Ru	2.723E+01	^{143}Nd	2.852E+01
^{4}He	3.738E-02	^{102}Ru	2.328E+01	^{145}Nd	2.923E+01
^{7}Li	8.660E-05	^{103}Ru	1.017E+01	^{146}Nd	2.361E+01
^{9}Be	2.863E-05	^{103}Rh	6.255E+00	^{147}Nd	3.961E+00
^{10}B	1.452E-04	^{105}Rh	1.453E-01	^{148}Nd	1.378E+01
^{11}B	9.145E-08	^{105}Pd	4.356E+00	^{147}Pm	1.087E+01
^{12}C	1.542E-05	^{109}Ag	4.356E+00	^{149}Pm	4.547E-01
^{13}C	1.193E-11	^{113}Cd	8.505E-03	^{149}Sm,	3.653E-01
^{27}Al	5.970E+03	^{129}I	3.947E+00	^{150}Sm	7.806E+00
^{28}Si	5.655E-01	^{131}I	3.540E+00	^{151}Sm,	1.053E+00
^{29}Si	2.286E-05	^{135}I	2.637E-01	^{152}Sm,	3.725E+00
^{30}Si	4.562E-10	^{131}Xe	1.527E+01	^{153}Sm	1.235E-01
^{83}Kr	2.324E+00	^{133}Xe	5.258E+00	^{153}Eu,	1.663E+00
^{93}Zr	3.110E+01	^{135}Xe	4.678E-02	^{154}Eu	1.573E-01
^{95}Zr	2.355E+01	^{133}Cs	3.834E+01	^{155}Eu,	9.273E-02
^{95}Nb	6.019E+00	^{134}Cs	1.093E+00	^{156}Eu	1.171E-01
^{95}Mo	2.830E+00	^{135}Cs	5.703E+00	^{157}Eu	1.386E-03
^{96}Mo	3.930E-02	^{139}La	4.625E+01	^{157}Gd	2.184E-03
^{97}Mo	3.009E+01	^{141}Ce	2.355E+01		

9.3 Burnup of the Beryllium Follower in the Control Rod

The beryllium follower is exposed to a very high neutron flux. Hence, two main reactions cause the production of ^{6}Li and ^{3}He, which are both strong neutron absorbers:

$$\begin{aligned} {}^{9}\mathrm{Be} + n_{\mathrm{f}} &\longrightarrow {}^{4}\mathrm{He} + {}^{6}\mathrm{He}, \\ {}^{6}\mathrm{He} &\xrightarrow{\beta^-,806.7\,\mathrm{ms}} {}^{6}\mathrm{Li}, \\ {}^{6}\mathrm{Li} + n_{\mathrm{th}} &\longrightarrow {}^{4}\mathrm{He} + {}^{3}\mathrm{H}, \\ {}^{3}\mathrm{H} &\xrightarrow{\beta^-,12.3\,\mathrm{a}} {}^{3}\mathrm{He}. \end{aligned} \tag{9.2}$$

In Serpent 2 burnup calculations can be set up rather conveniently. In order to compare the results obtained from Serpent 2 with MCNP6 calculations performed within [10] a cycle length of 60 d followed by an average break of 30 d is assumed. Contrary to [10], the control rod is not moved for this Serpent 2 study. In Figure 9.5 the evolution of the atomic fraction inventory of

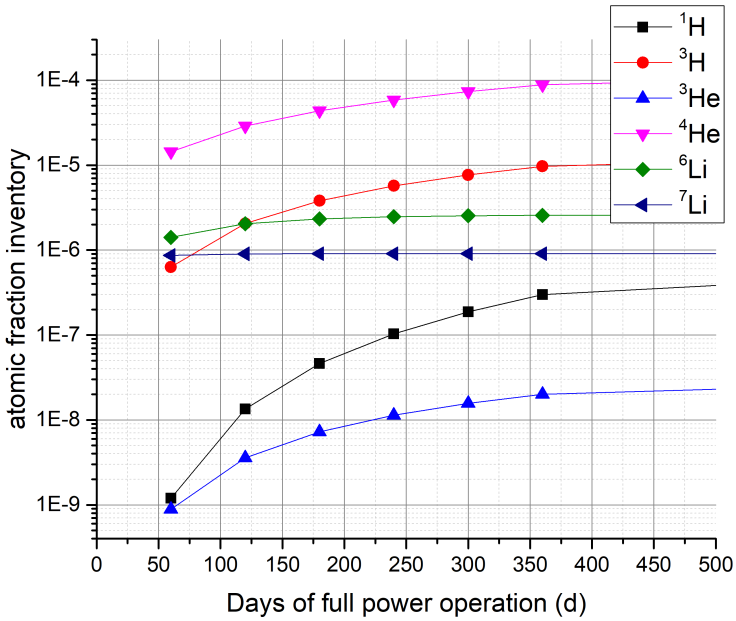

Figure 9.5: *Evolution of the atomic fraction inventory of different isotopes inside the beryllium follower, as calculated with Serpent 2. An average pause of* 30 *d is assumed between each* 60 *d cycle.*

^{1}H, ^{3}H, ^{3}He, ^{4}He, ^{6}Li, and ^{7}Li is shown. A comparison of the absolute atomic fraction inventory shows that Serpent 2 underestimates the absolute mass of the burnup products. In the Serpent 2 calculation the amount of ^{7}Li remains constant over time, while in [10] it follows the trend of ^{3}H. Nevertheless, the general trend of all isotopes except ^{7}Li is similar to that shown in [10]. Because of the missing control rod movement, the data in [10] has to be assumed as more realistic. More detailed comparisons of Serpent 2 and the code system used in [10] should use a moving control rod.

9.4 Influence of the (n,2n) reaction in the beryllium follower to the core

During the development of the Serpent 2 models it turned out that a different treatment of the (n,2n) reaction in the beryllium follower (^{9}Be $\longrightarrow$ ^{8}Be) in MCNP6 and Serpent 2 caused a notable mismatch of the resulting multiplication factors. This particular reaction was not supported by Serpent 2 in the ENDF/B V libraries. With a corresponding adjustment of the cross section libraries, the influence of this single reaction on total reactor performance can be isolated. In Serpent 2, this was achieved by directly turning off the reaction [48], while in MCNP6 it was achieved using first order perturbation theory with the kpert card [59]. Table 9.2

Table 9.2: *Comparison of the influence of the (n, 2n) reaction obtained with different codes. In the standard application of MCNP6 the (n,2n) reaction is included. For perturbation calculations MCNP6 does not provide an statistical uncertainty due to the inherent calculation method.*

Code	MCNP6 standard	MCNP6 kpert, no (n,2n)	Serpent 2 without (n,2n)
k_{eff}	0.99772± 0.00009	0.99538	0.99551± 0.00031

shows the impact of the (n,2n) reaction in beryllium on the multiplication factor for a fresh fuel element. If the (n,2n) reaction is neglected in the calculations, the multiplication factor k_{eff} decreases by about 0.002. Although this change is small, it is significant at the 1-σ level, and according to [10] it contributes nearly two days of cycle length. As before in the model comparison (see Chapter 6.3), both codes, MCNP6 and Serpent 2, are in agreement within the statistical uncertainty [64]. All other calculations presented in this work have been carried out using a correct (n,2n)-treatment.

CHAPTER 10

Transients

The main purpose for all of the models and methods developed within this thesis is the calculation of hypothetical transients for the FRM II. During the licensing process, before the first startup of the reactor, the general contractor Siemens performed numerous studies to cover all relevant emergency scenarios. The three most important cases include:

- reactivity accident, which is caused by an uncontrolled upwards movement of the control rod;
- Loss of coolant accident (LOCA), where a leakage of the main cooling circuit leads to an uncontrolled flow of coolant into the reactor pool;
- a loss of emergency power, in which all main cooling pump are turned off.

In the following, the system of models and methods developed within this thesis is used to calculate these transients, which will then be compared to the calculations performed by Siemens during the licensing process. This system has been created with the intention to explicitly model the actual core design and to reproduce the actual core behavior well. However, the time-dependent reactivity worth of the emergency shutdown rods the exact shutdown maneuver were not explicitly modeled by now. For this, the emergency shutdown rods would need to be implemented explicitly in the TORT-TD model. This is currently, not possible because the spiraled shaped channels of the emergency rods cannot be modeled exactly in TORT-TD due to the strict r-φ-z geometry. Hence, a substitutional geometry will need to be found and validated to be able to model transients involving the emergency shutdown rods in detail. This will be the topic of forthcoming studies.
The major outcome of the studies performed by Siemens are the timespans that pass after initiation of an event until the reactor safety system recognizes the different thresholds for shutting down the reactor. Therefore, these timespans will be compared to the corresponding periods obtained with the system developed within this thesis. If these periods of time can be reproduced within tolerable limits, the modeled dynamics of the reactor as well as the behavior of the core are practically identical to the licensed calculations. In Section 10.1 transients with the current fuel are considered, while in Section 10.2 the same cases are simulated using a potential UMo fuel candidate.
In the following only the uncertainties of the parameters of the fitting functions are presented. Because these parameters are highly correlated, the corresponding correlation matrix for each fit is also needed. Hence, all matrices are shown in the appendix (see Appendix F).

10.1 Results for transients with the current U_3Si_2 fuel

10.1.1 Reactivity accident

The first and most important transient is an uncontrolled reactivity insertion to the reactor. A malfunction of the control rod motor would cause such kind of scenario (see Figure 9.1). The control rod of the FRM II has a fast mode where it can be moved with 0.8 mm/s and a slow mode with 0.08 mm/s [43]. The fast mode is normally used during the early start-up phase, and the slow mode for power control when running with nominal power. The scenario discussed here is a combination of two different cases which Siemens has investigated during the licensing of FRM II [32]:

- Reactivity insertion during the early start-up phase. The control rod moves in the fast mode,
- Reactivity insertion during operation at nominal power. The control rod moves in the slow mode.

For this accident it is assumed that the reactor is operating at nominal power and the control rod starts moving at $t = 3\,\mathrm{s}$ from $-6.92\,\mathrm{cm}$ to the upper end position with the maximum possible speed of 0.8 mm/s. Modeling of the complex control rod has already been described in Chapter 6.4.1.4. In TORT-TD, only the power which is directly deposited in the fuel zone can be taken into account (see Chapter 6.4.1.2). The remaining portion mainly heats up the pool which is cooled directly via the secondary cooling circuit which is not modeled here (see Fig. 7.1). Therefore, the values for the absolute and relative reactor power refer to the thermal power deposited in the fuel zone. Conservatively, a fresh fuel element is used for this calculation.
After the steady state initialization calculations (see Chapter 8) the zero transient begins at $t = 0\,\mathrm{s}$ until $t = 3\,\mathrm{s}$. The geometry remains unchanged. However, Figure 10.1 shows an increasing trend of the reactor power even before the real transient starts: A steep change directly at at around $t = 0.7\,\mathrm{s}$ on the one hand and a slow increase of the reactor power afterwards on the other hand are notable. This is an effect caused by the coupling of TORT-TD and ATHLET. For comparison, Figure 10.2 shows a non coupled TORT-TD calculation with the same input parameters. As for the coupled calculation, the same trend is visible, but this time inverted; a steep decrease followed by a slowly decreasing reactor power. The change of the reactor power can be caused by uncertainties of the data for delayed neutrons and their inverse velocities which leads to a prompt jump phenomenon [85]. There is an influence of the coupling, too. First, the change is inverted and the absolute changes are smaller for the stand alone calculation of TORT-TD:

- In the non-coupled calculation the fast increase is about 500 kW. For the coupled calculation this increase is roughly 700 kW.
- The slow change of the reactor power is less than 300 kW in the stand alone TORT-TD calculation but 1 MW in the coupled one.

The whole zero transient is superimposed by the information transfer between TORT-TD and ATHLET. The different numerical behavior of both codes can lead to an increasing trend of the reactor power during the zero transient. A possible additional effect is the treatment of control rods in TORT-TD. Even if the control rods are not moved, TORT-TD performs a flux-volume-averaging at each of the mesh cell borders. For every time step, this could lead to a

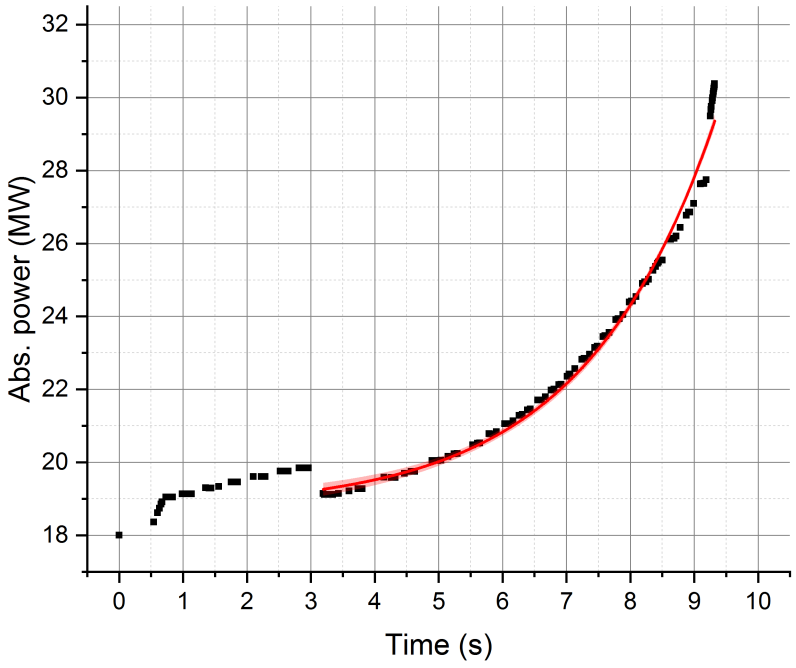

Figure 10.1: *Absolute reactor power as a function of time during the transient which starts at $t = 3\,\mathrm{s}$. Only the power deposited directly inside the fuel zone is plotted. The evolution of the reactor power after the beginning of the transient is fitted with an exponential function. The corresponding confidence bands are also plotted. For $t > 9\,\mathrm{s}$ the reactor period drops (see Figure 10.3) which causes the increase of the reactor power.*

numerical trend, even though there is no change of the actual geometry. Due to this observations, the trend of the reactor power after the beginning of the movement of the control rods are assumed to be correct within the limits given by the stand alone TORT-TD calculation.
After $t = 3\,\mathrm{s}$ the control rod begins to move and to add reactivity to the core. Due to the response of the delayed neutrons, this leads to an renormalization of the reactor power, so that 19.11 MW deposited inside the fuel zone are taken as starting value for the evaluations. As depicted in Figure 10.1, directly after the beginning of the movement the power jumps back to the level before the numerical drift, as already described before. Using Point Kinetics (PK) (see Chapter 2.1.5.3), the observable increase of reactor power $P(t)$ can be approximated with an exponential function:

$$P(t) = (0.112 \pm 0.020) \cdot \exp\left[t/(2.049 \pm 0.075)\right] + (18.732 \pm 0.143). \tag{10.1}$$

With a quality factor of $R^2_{\mathrm{adj}} = 0.986$ this function matches well the simulated evolution of the reactor power.
As described in [25], there are mainly three signals causing the reactor safety system to shutdown the reactor:

- The reactor period falls below 7 s,

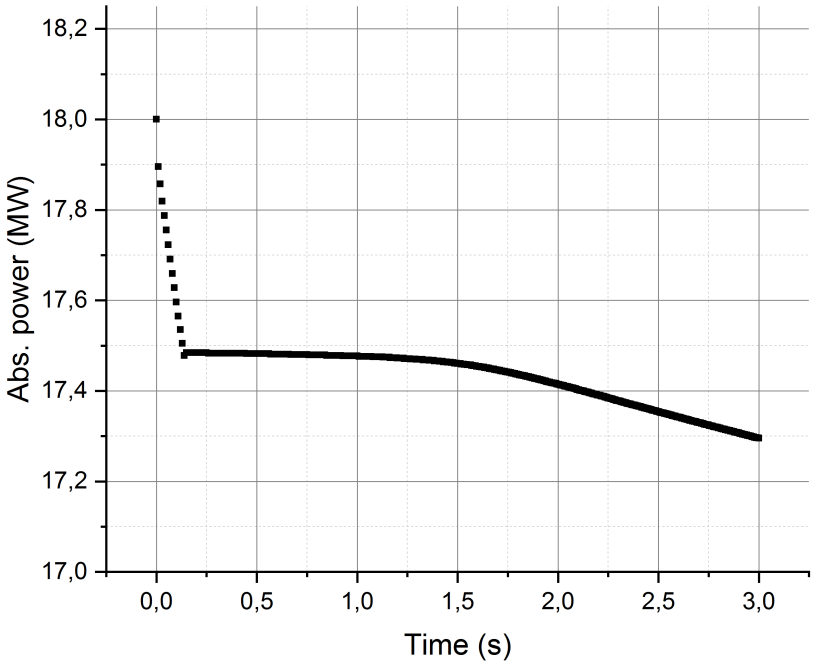

Figure 10.2: *Absolute reactor power during the zero transient as calculated with TORT-TD.*

- The reactor power exceeds 114 % nominal power ($\equiv 22.4\,\mathrm{MW}$),
- The coolant temperature at the outlet rises above 60.8 °C.

Reactor period The reactor period as calculated with TORT-TD was rather volatile. During the zero transient the reactor period is, expectedly, large and the reactor is running stable. After the beginning of the transient after $t = 3\,\mathrm{s}$ the reactor period decreases. Figure 10.3 shows the reactor period after the beginning of the transient. In order to take into account the volatile character of the reactor period, the reactor period $p(t)$ is linearly fitted and the time when the period falls below 7 s is calculated.

$$p(t) = (41.046 \pm 4.514) - (3.931 \pm 0.556) \cdot t \tag{10.2}$$

With Eq. 10.2 at 8.7 s, i.a. 5.7 s after the beginning of the control rod movement, the reactor safety system would safely shutdown the core. The volatility of the values is also expressed by a quality factor of the fit of $R^2_{\mathrm{adj}} = 0.511$ and comparably broad 1-σ confidence bands.

Reactor power As Figure 10.4 shows and with using

$$P_{\mathrm{rel}}(t) = (0.588 \pm 0.103) \cdot \exp\left[t/(2.049 \pm 0.075)\right] + (97.982 \pm 0.749), \tag{10.3}$$

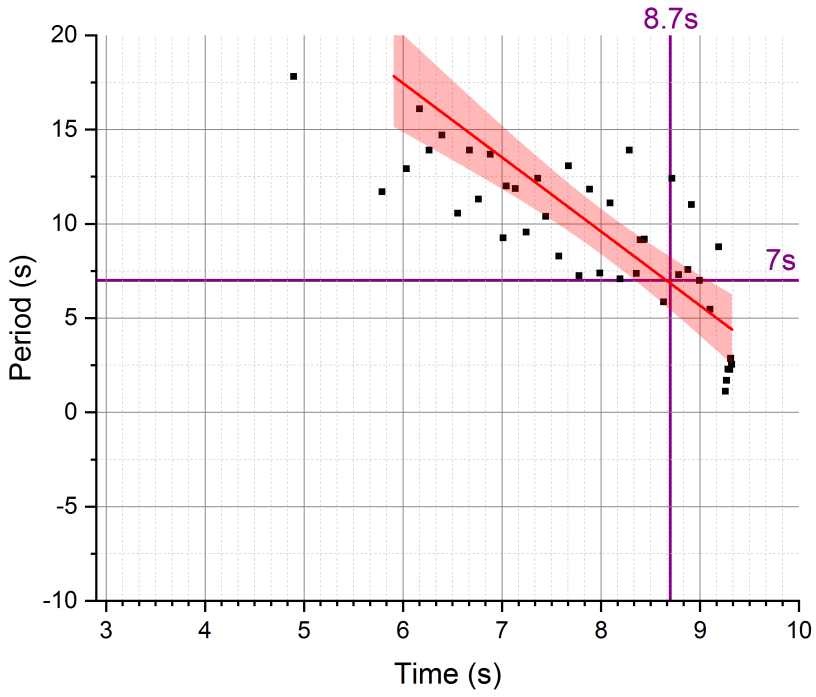

Figure 10.3: *Reactor period with corresponding fit including confidence bands as a function of time after the beginning of the transient. After* 8.7 s *the threshold of a period smaller than* 7 s *is reached.*

for the relative reactor power $P_{\mathrm{rel}}(t)$, the threshold of 114 % would be reached 3.7 s after the beginning of the transient.

Coolant temperature Figure 10.5 shows the outlet coolant temperature with an exponential fit and the corresponding confidence bands. The outlet coolant temperature $T(t)$ as a function of time after the beginning of the transient can be described with:

$$T(t) = (0.042 \pm 0.020) \cdot \exp\left[t/(1.766 \pm 0.153)\right] + (53.387 \pm 0.223). \tag{10.4}$$

With Eq. 10.4 the threshold for the temperature is reached after 9.13 s. In the outer hot channel (CORELUD 2, see Chapter 7.2) the temperature increase from 65.4 °C to 70.0 °C, in the channel at the density jump (COREHUD 5) from 50.4 °C to 55.7 °C and in the most inner channel (COREHUD 1) from 56.6 °C to 63.8 °C.

Conclusion The conditions simulated here are a combination of two separated scenarios calculated by Siemens; an uncontrolled control rod movement with the fast velocity of 0.8 mm/s at a nominal power of 20 MW. Due to the very different conditions, a direct comparison to the Siemens calculations cannot be done. Nevertheless, the results for the timespans that passes before the reactor safety system triggers the shutdown of the reactor obtained in this work are comparable

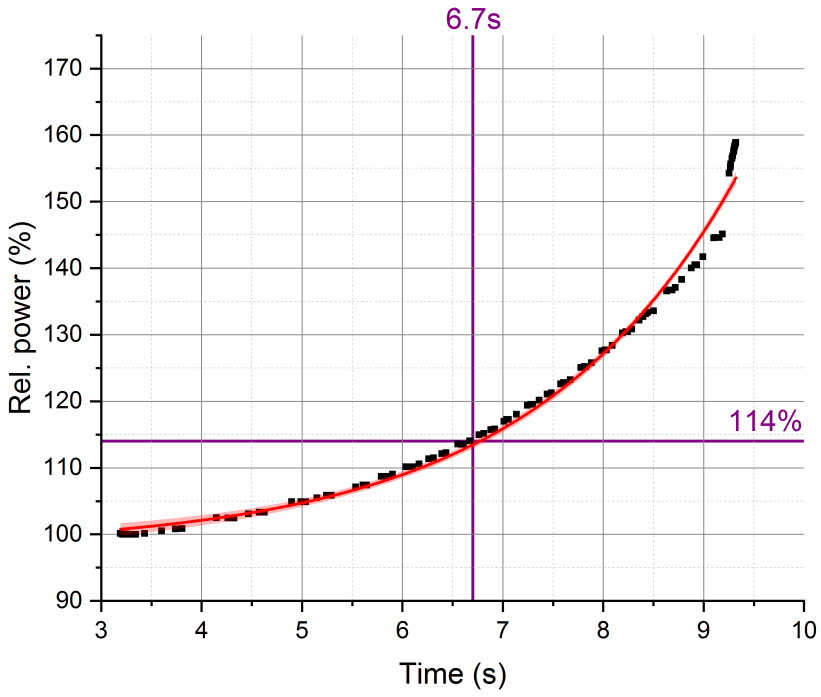

Figure 10.4: *Relative reactor power as a function of time after the beginning of the transient. The exponential fit with corresponding confidence bands are depicted in red. After* 6.7 s *the threshold for the relative reactor power of* 114 % *is reached. For* $t > 9$ s *the reactor period drops (see Figure 10.3) which causes the increase of the reactor power.*

to the values calculated by Siemens. Hence, the model system developed in this work is supposed to be able to reproduce both Siemens cases well.

10.1.2 Loss of coolant accident (LOCA)

The second important transient is the Loss of coolant accident (LOCA) scenario. The main cooling circuit of FRM II is designed fail-safe, so that a complete breach of the main tubing is considered to be impossible. Therefore, abnormal conditions caused by breaches of the biggest connections or other possible cracks are covered by investigating a leakage with a cross section of 25 cm^2 which is located directly above the inlet of the fuel element [42], i.e. within the part of the central channel which is located inside the heavy water moderator tank. Due to the double-walled construction, there will be no mixing of light and heavy water. This scenario was also investigated during the licensing process.
As described in [42], the hydraulical dimensioning of the FRM II must ensure that in case of such leakage the mass flow in the primary circuit does not fall below 188 kg/s. In 1997, Siemens performed the calculations using a program called *DUST* [40, 41]. In the Siemens calculations, a sharp-edged leakage geometry is assumed [42].
The ATHLET model developed within this thesis has been modified for this transient by introducing a discharge valve which is located directly above the inlet to the fuel element and

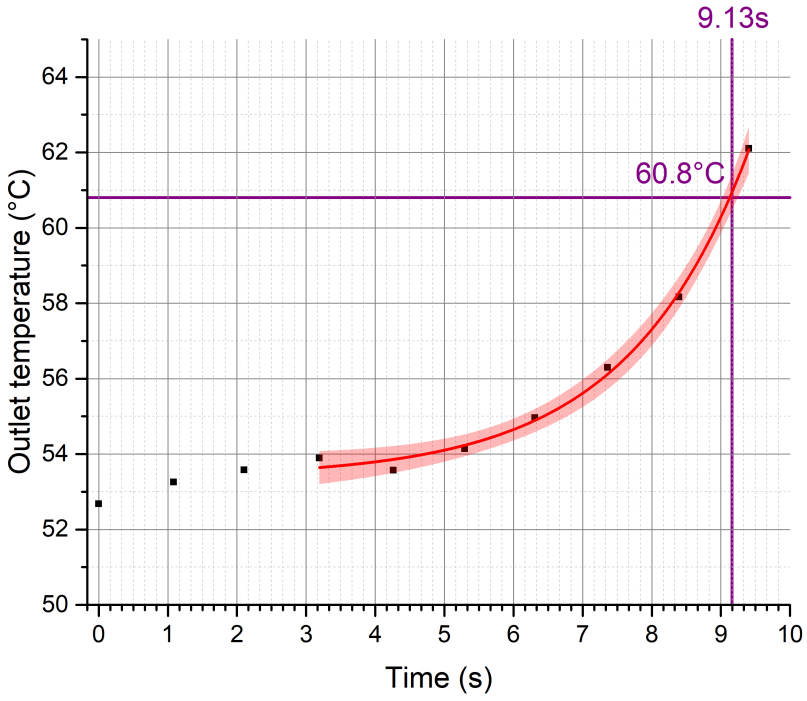

Figure 10.5: *Outlet coolant temperature as a function of time. The exponential fit with corresponding confidence bands are depicted in red. After* 9.13 s *the threshold for the coolant temperature of* 60.8 °C *is reached.*

connected to the reactor pool. ATHLET needs a pressure loss coefficient to simulate the valve properly. Therefore, with the geometry given in [42] and using Eq. 7.1 which can also be applied here, a pressure loss coefficient of $\zeta = 208000\,{}^{1}/_{m^4}$ is assumed [35]. During the simulation the valve is instantly opened at $t = 5\,s$ to start the transient. The calculation for this transient has been performed using TORT-TD and ATHLET in coupled mode.
As depicted in Figure 10.6, after a short period in which ATHLET performs some corrections to reach numerical convergence (see Chapter 7.2), the mass flow through the central channel stabilizes slightly above 280 kg/s. Directly after the opening of the discharge valve the mass flow instantly drops to 233.05 kg/s. After the first impact of the leakage the mass flow rises up to 259.32 kg/s and stabilizes at this level. As for the model system used by Siemens, the threshold for the minimal mass flow allowed is not undercut. In [42] a minimal mass flow of 222 kg/s is reported, 4.7 % lower than the value found here. Siemens calculated a stationary mass flow of 246 kg/s, also 5 % lower than the value found here. As Figure 10.7 shows, Siemens estimated the minimal mass flow with a spline. Due to the unknown shape and exact location of the leakage such differences may occur. Hence, the licensing calculations can be supposed to be conservative compared to the results obtained with the methods of this thesis.
Figure 10.8 shows the mass flow through the leakage. After the valve is opened at $t = 5\,s$ the coolant mass flow through the leakage rises to 86.10 kg/s. In [42], a mass flow through the leakage of 89 kg/s is reported. This means a 3 % higher leakage flow than calculated by Siemens.

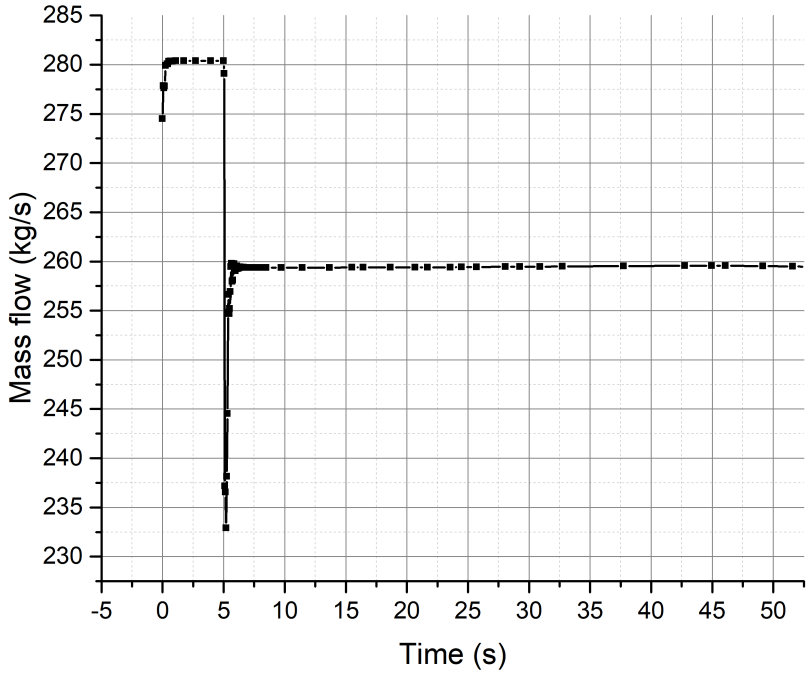

Figure 10.6: *Time dependent mass flow through the central channel during the transient.*

As depicted in Figure 10.9, the coolant temperature at the core outlet jumps to 51.9 °C and further increases to 53.2 °C after 37.7 s after the begin of the transient. Due to the pressure drop caused by the leakage, the primary pumps begin to suck water from the pool. Therefore, a backward flow of 89 kg/s from the pool to the central channel arises (see Figure 10.10) and nearly replaces the coolant loss. After going through the primary coolant pumps and the heat exchangers, the fresh, cold water from the pool cools down the outlet temperature back to 51.1 °C.
In general Siemens calculated all mass flows 3 % to 5 % smaller than the model system used here. Hence, the Siemens calculations can be assumed to be more conservative than the coupled model system of this thesis. The mass flow through the leakage is very close to the Siemens reports. The fitting leakage mass flow in both calculations give a strong hint that the modeling of the shape of the leakage fits. Also the dynamical behavior of the central channel is reproduced well with the here used models.
Because this scenario is also resulting in a decreased mass flow through the central channel, it is very comparable with the running on emergency power case. A more detailed discussion can be found in Chapter 10.1.3.

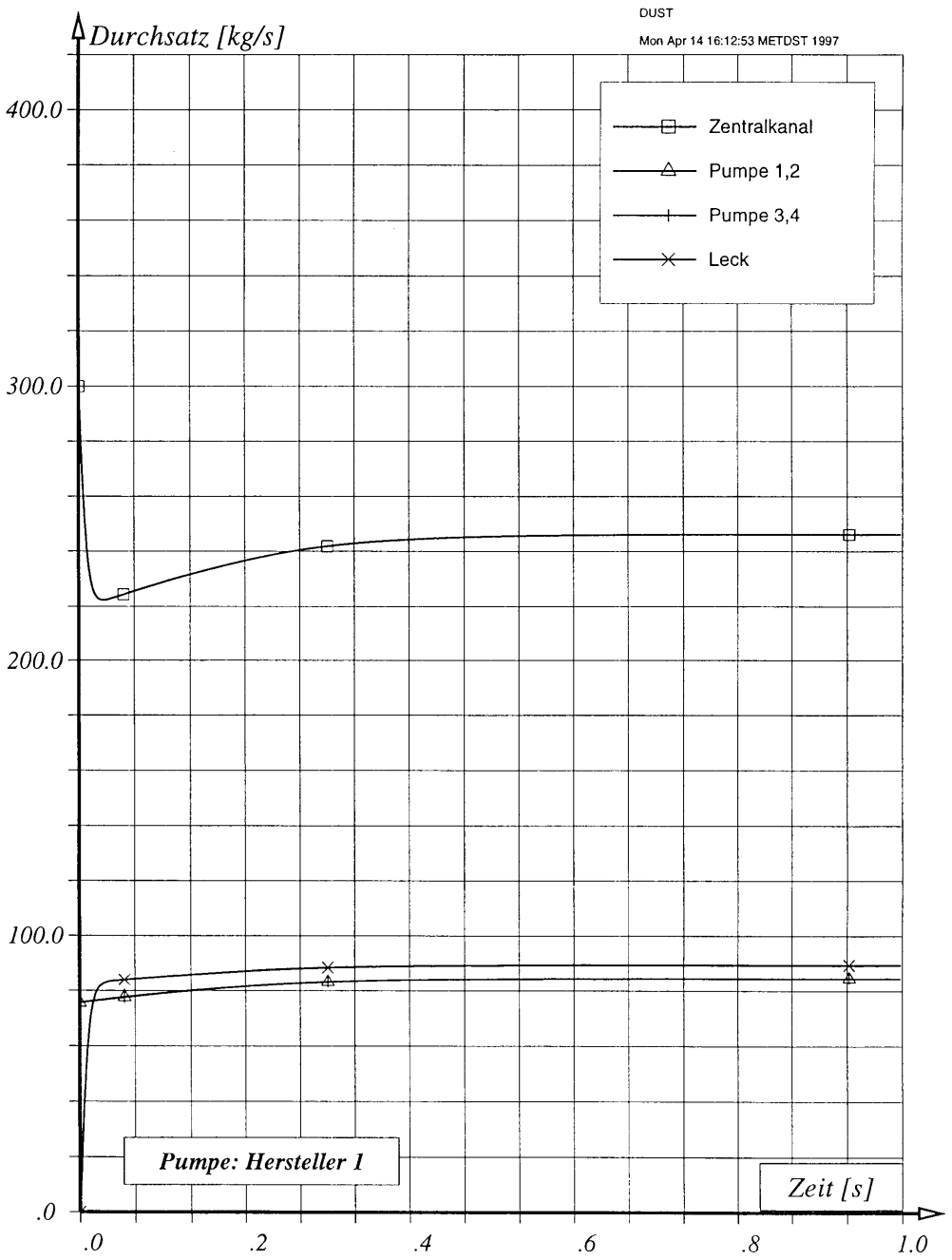

Figure 10.7: *Time dependent mass flow through the central channel during the transient calculated by Siemens [42].*

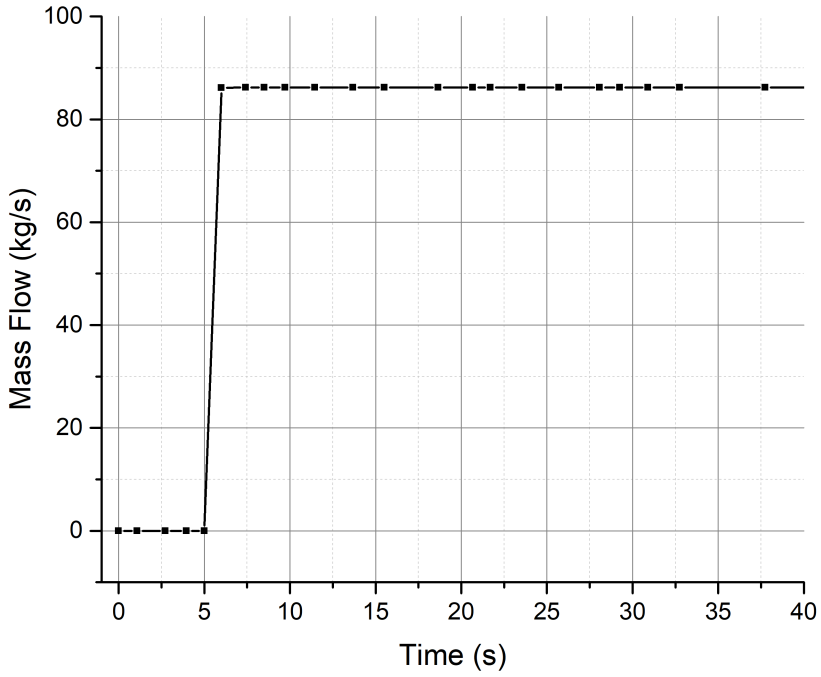

Figure 10.8: *Time dependent mass flow through the leakage during the transient.*

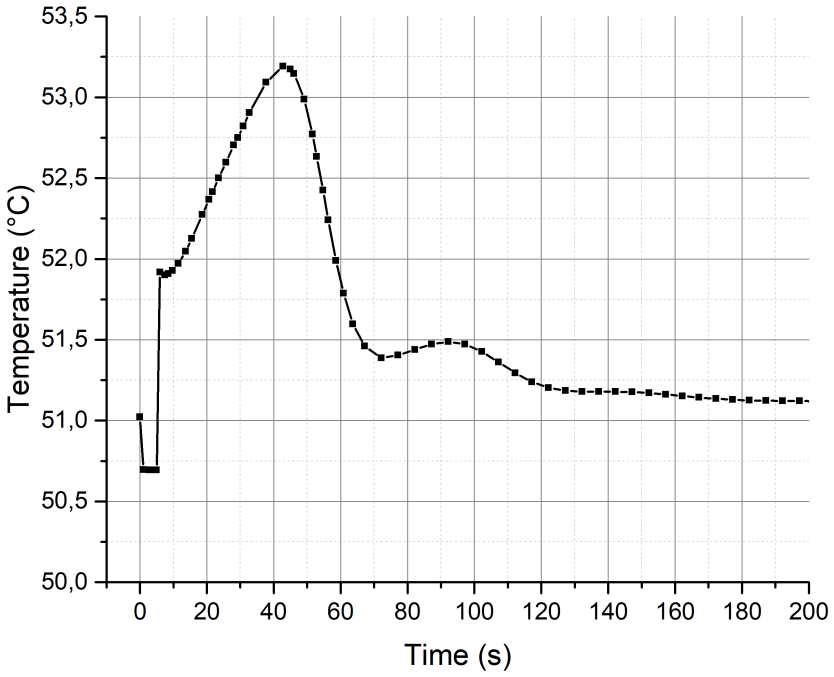

Figure 10.9: *Time dependent coolant temperature of the outlet during the transient.*

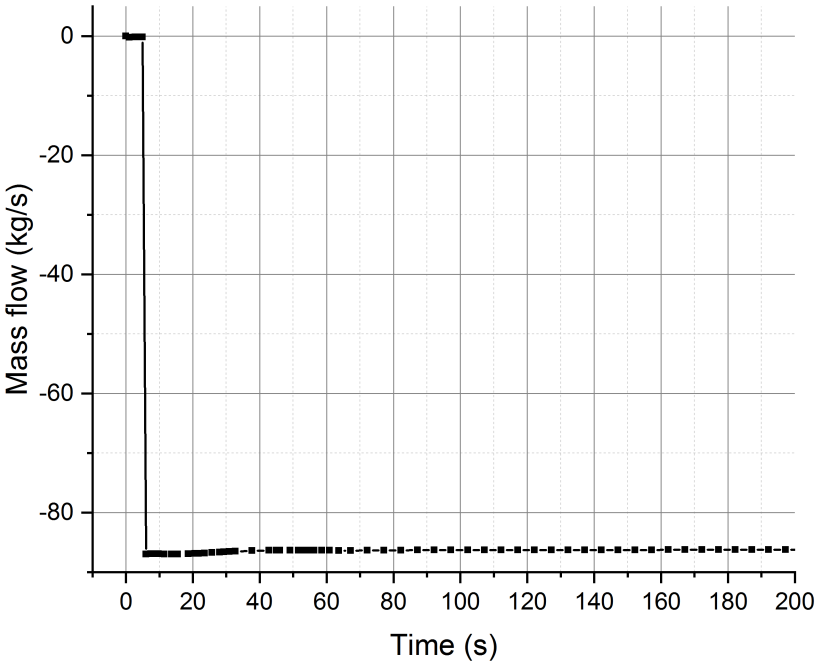

Figure 10.10: *Time dependent mass flow from the pool to the central channel during the transient.*

10.1.3 Emergency power

For every nuclear reactor it has to be shown that a failure of the main coolant pumps is manageable. In 1997, Siemens investigated such a scenario for the FRM II during the licensing process. Conservatively, Siemens used more severe starting parameters than normal operation condition, e.g. running on 22.8 MW. In [81] a detailed description and the order and type of triggers for the shutdown of the reactor can be found:

1. The pressure difference between the collector and the reactor pool is smaller than 1.1 bar with a maximum slope of 0.06 $^{\mathrm{bar}}/_{\mathrm{s}}$.
2. The total mass flow through the central channel falls below 85 % of the nominal flow, including all tolerances and uncertainties.
3. The temperature at the outlet rises above 60.8 °C.

After a threshold is triggered, it takes 0.46 s until the emergency shutdown rods begin to fall near the fuel element to safely shutdown the reactor. Conservatively, Siemens additionally assumed that the first trigger (pressure difference) fails. Therefore, the decreasing mass flow signal initiates the shutdown of the reactor.
In [81], the signal for a too low mass flow through the central channel is reached after 2.61 s. Due to technical constraints, however, this trigger is further delayed by 0.7 s. Hence, the emergency control rods begin to fall 3.07 s after the begin of the transient. As a third trigger, the coolant temperature at the outlet reaches the threshold after 5.91 s and would initiate the fall of the emergency shutdown rods 6.87 s after the transient has begun.
The ATHLET model used for this simulation has been adjusted in the way that all primary coolant pumps are shut down at $t = 10\,\mathrm{s}$ in order to begin the transient. In contrast to [81], due to the coupling of the ATHLET model and TORT-TD, there is a direct neutronic feedback to the thermal-hydraulical calculation. Siemens used the stand-alone code *DUST* [40, 41] with a special model to cover this explicit scenario. There, the starting parameters like reactor power, mass flow through the central channel or temperature at the inlet can be adjusted rather easily, because there is no neutronical feedback. The coupled models used in this thesis have been designed to be used and to work together and to cover all possible scenarios. Therefore, the starting values represent the current nominal reactor conditions.
Figure 10.11 shows the coolant mass flow directly below the outlet of the fuel element. In the first 10 s before the transient starts, the mass flow stays constant at 280.37 $^{\mathrm{kg}}/_{\mathrm{s}}$. At $t = 10\,\mathrm{s}$ a timed signal shuts down all four main coolant pumps and the mass flow inside the central channel begins to decrease rapidly. In order to evaluate the trend, the data points are fitted with an exponential decay:

$$M(t) = (377.36 \pm 12.69) \cdot \exp\left[-t/(10.99 \pm 0.59)\right] + (129.25 \pm 3.74), \tag{10.5}$$

whereas $M(t)$ is the time dependent mass flow in $^{\mathrm{kg}}/_{\mathrm{s}}$ and t is the total simulation time in s. With the quality factor $R^2_{\mathrm{adj}} = 0.998$ this functions fits the data well. The reactor safety is triggered after reaching 85 % of the nominal flow, i.e. a mass flow of 238.31 $^{\mathrm{kg}}/_{\mathrm{s}}$. With Eq. 10.5, this critical mass flow is reached 3.64 s after the shutdown of the primary pumps. A comparison of this result with the calculation performed by Siemens shows, that the model and code system used here reaches the threshold for the mass flow 1.03 s later. This difference between Siemens and this work can be caused by using different model handling of the pump performance after

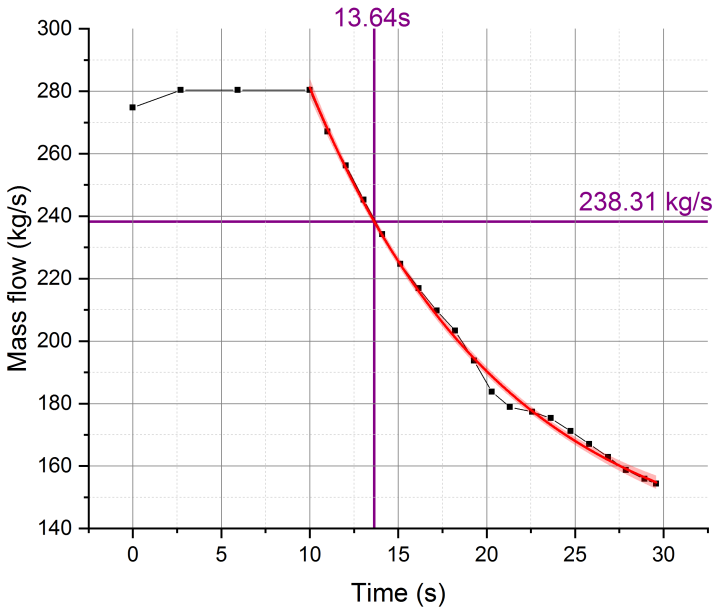

Figure 10.11: *Time dependent mass flow through the central channel during the transient. The corresponding fit with confidence bands are shown in red. After* 13.64 s *simulation time, the critical mass flow of* 238.31 $^{kg}/_{s}$ *triggers the reactor safety system.*

the shutdown. For example, a direct comparison betweeen *DUST* and ATHLET how both codes handle the the moment of inertia of the primary pumps hardly possible.
The same approach was chosen for the evolution of the coolant temperature. As depicted in Figure 10.12 the temperature of the coolant begins to increase after the transient was started at 10 s. The first data point with a temperature larger than 60.8 °C is supposed to trigger the reactor safety system. To describe the evolution of the temperature $T(t)$, an exponential growth function ($R^2_{\text{adj}} = 0.998$) was used, whereas the points after 22 s are not taken into account, because the temperature is already above the threshold and feedback of valves inside the central channels start to cause non linear effects. The temperature can be described with:

$$T(t) = (12.29 \pm 4.79) \cdot \exp\left[t/(28.80 \pm 7.22)\right] + (35.03 \pm 5.34). \tag{10.6}$$

Using the coupled system developed here and using the temperature function (Eq. 10.6), the reactor safety system would shut down the reactor after 11.33 s after the transient has started. It can be noted, that the critical temperature is reached 5.42 s later than in the Siemens calculations. Due to the inherent characteristics of the model system used within this thesis, the starting parameters cannot be chosen freely. The power deposition distribution is being calculated by TORT-TD and the data is exchanged with ATHLET. As described in Chapter 6.4, normal operation conditions are chosen as starting parameters for the coupled calculations. As already described, Siemens used 22.8 MW for the reactor power which is completely deposited in the central channel; this model system heated the cooling water inside the fuel zone with only 18.2 MW. Therefore, the power deposited inside the fuel plates is smaller than in the model

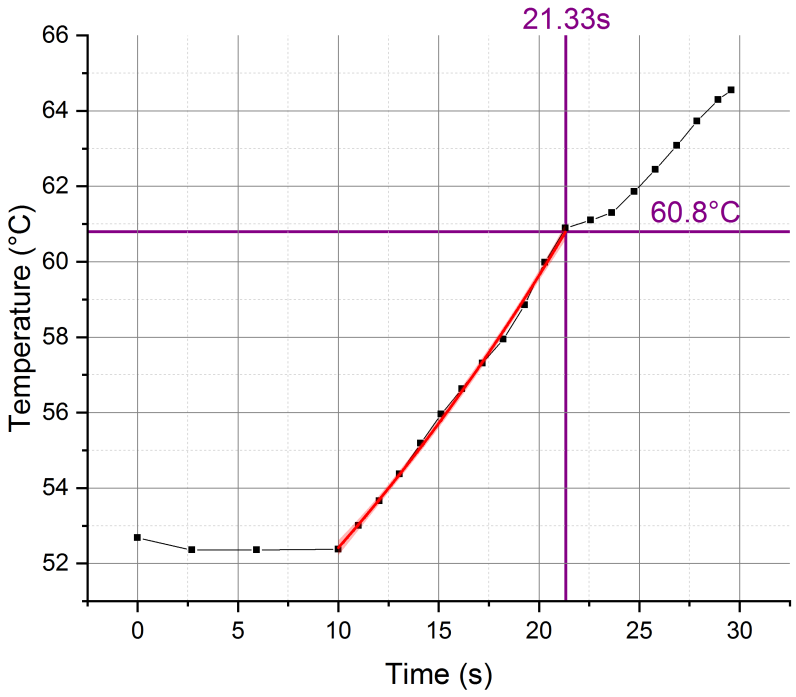

Figure 10.12: *Time dependent coolant outlet temperature during the transient. The corresponding fit with confidence bands are shown in red. After* 21.33 s *simulation time, the coolant temperature of* 60.8 ° *triggers the reactor safety system. The abrupt change of the coolant temperature at roughly* 21 °C *is not caused by triggering the reactor shutdown, but by some flow feedback of the primary circuit (see Figure 10.11).*

developed by Siemens. Hence, the coolant is heated slower and the threshold is reached later. Therefore, the results in this work do not inidcate that the calculations of Siemens were not conservative.

10.1.4 Summary

Comparing this three different transient scenarios, it could be shown that modeling the control rod leads to a prompt-jump like behavior of the coupled model system during the zero-transient. The behavior of TORT-TD and ATHLET is influenced if the codes are used in coupled mode or not. When no control rod is modeled the reactor power remains constant. Hence, the data of the delayed neutrons and the data exchange between TORT-TD and ATHLET plays a significant role for the simulation of reactivity transients. The model system developed within this thesis can reproduce the results obtained by the general contractor Siemens during the licensing process within tolerable deviations. The observed differences can be attributed to the use of different calculation approaches, and initial conditions. The calculations of Siemens are conservative.

10.2 Results for transients with a possible UMo fuel candidate

Finally, the performance of the FRM II using a possible UMo fuel candidate for the three cases discussed in Chapters 10.1.1 through 10.1.3 can be investigated. Because a final fuel candidate has not been selected yet, a draft core with an enrichment of 50 % and identical geometry is chosen for the study here. Similar to [10] and to the current fuel element the uranium densities in this model are 8.0 $\mathrm{gU/cm^3}$ and 4.0 $\mathrm{gU/cm^3}$, respectively. The remaining core layout stays unchanged. The cross sections needed for this model are generated with Serpent 2 by adjusting the material mixture of the fuel zone. For the simulations, thermal properties of the UMo fuel (density ρ, thermal conductivity λ and specific heat capacity c_p) are taken from [10] (Table 10.1). These values also agree with [34].

Table 10.1: *Data for UMo disperse fuel at BOL at room temperature.*

Quantity	Value 8.0 $\mathrm{g/cm^3}$	Value 4.0 $\mathrm{g/cm^3}$
λ [$\mathrm{W/m\,K}$]	82.1	142.1
c_p [$\mathrm{J/kg\,K}$]	236	394
ρ [$\mathrm{g/cm^3}$]	10.04	6.37

10.2.1 Reactivity accident

The model which has already been described in Chapter 10.1.1 has been used for the simulation of a reactivity insertion using the possible UMo fuel candidate described above. Also, the initial and computational parameters remains untouched by meaning that the control rod starts moving at 3 s with a velocity of 0.8 $\mathrm{mm/s}$. The coupled code system again needed 11 steady state initialization calculations until the zero transient begins. Figure 10.13 shows the evolution of the reactor power during this transient. In the first time step, the reactor power jumps to 18.66 MW due to the inserted data for delayed neutrons and the inverse velocities. Also, a slow trend is visible which is probably again caused by numerical issues and the data exchange between TORT-TD and ATHLET. After the movement of the control rod has started, the reactor power begins to rise. The calculated reactor power $P(t)$ can be described with:

$$P(t) = (0.072 \pm 0.012) \cdot \exp\left[t/(1.876 \pm 0.058)\right] + (18.670 \pm 0.124). \tag{10.7}$$

With a quality factor of $R^2_\mathrm{adj} = 0.990$ this function matches well the evolution of the reactor power.
Again, the times when the reactor safety system would shutdown the reactor are investigated.

Reactor period As for the current U_3Si_2 fuel the reactor period $p(t)$ is very volatile, as depicted in Figure 10.14. Hence, the same approach using a linear fit $R^2_\mathrm{adj} = 0.595$ was chosen:

$$p(t) = (33.126 \pm 2.517) - (3.017 \pm 0.296) \cdot t \tag{10.8}$$

Using Eq. 10.8, at 8.66 s, i.a. 5.66 s after the beginning of the control rod movement, the reactor period is being calculated smaller than 7 s and would trigger the shutdown maneuver. This would

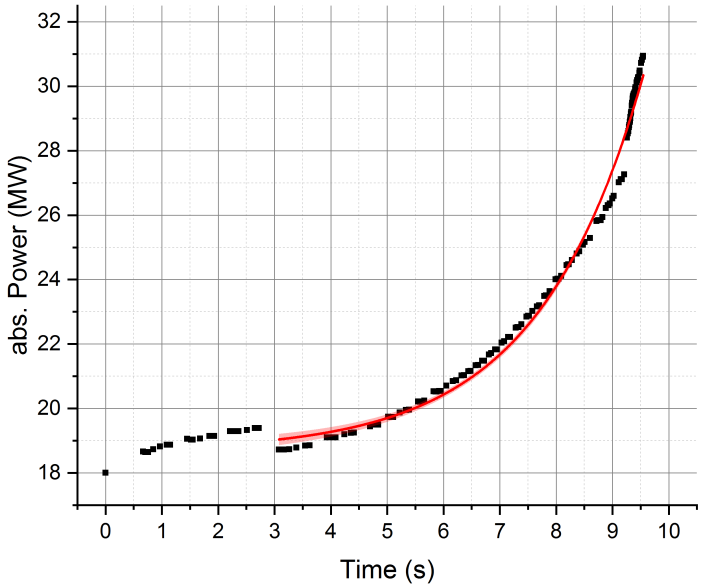

Figure 10.13: *Absolute reactor power as a function of time. The fit with corresponding confidence bands are depicted in red. For $t > 9.2\,\mathrm{s}$ the reactor period drops which causes the steep increase of the reactor power.*

be 0.04 s later than with the current fuel. This is well within the assumed uncertainties of the calculations and meets the expectation that the differences between both core designs are minor.

Reactor power In order to determine the time when the relative power threshold would be reached, the power is again normalized to the reactor power of the first time step (see Figure 10.15). The relative reactor power $P_{\mathrm{rel}}(t)$ can then be described with

$$P_{\mathrm{rel}}(t) = (0.384 \pm 0.062) \cdot \exp\left[t/(1.876 \pm 0.058)\right] + (99.714 \pm 0.663). \tag{10.9}$$

Using Eq. 10.9, then the threshold of 114 % would be reached after 3.8 s after the beginning of the transient. This means that the reactor while running with this possible UMo fuel candidate would be shutdown 0.1 s later than it would be now.

Coolant temperature The outlet coolant temperature with an exponential fit and corresponding confidence bands is shown in Figure 10.16. The outlet coolant temperature $T(t)$ as a function of time after the beginning of the transient can be described with:

$$T(t) = (0.078 \pm 0.026) \cdot \exp\left[t/(1.992 \pm 0.132)\right] + (52.664 \pm 0.196). \tag{10.10}$$

With Eq. 10.10 the threshold of 60.8 °C is reached after 9.25 s. This is 0.12 s later than with the current fuel. The temperatures in the hot channels, COREHUD 1 and CORELUD 2 increase from 57.29 °C to 70.50 °C and from 69.68 °C to 86.74 °C, respectively. Near the density jump

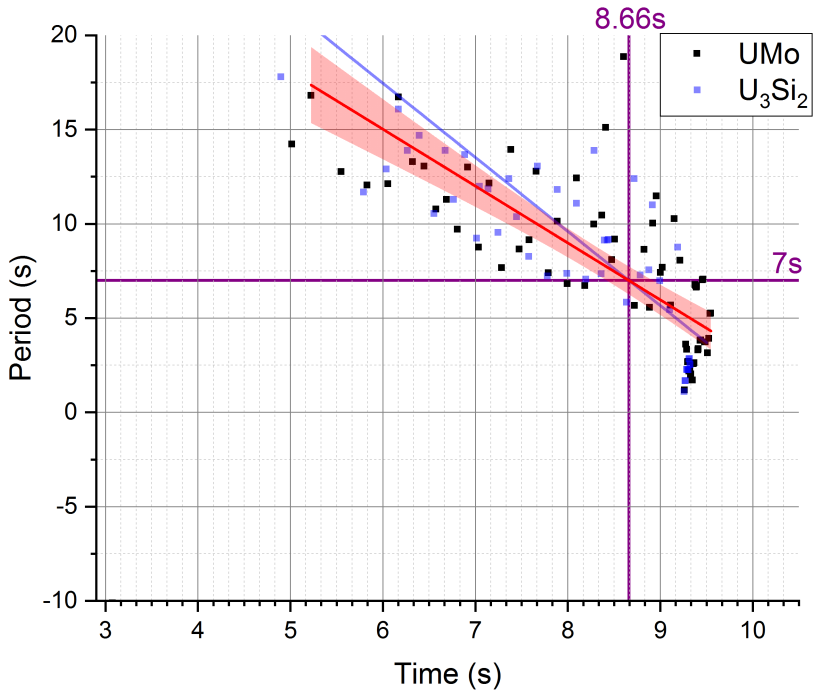

Figure 10.14: *Reactor period as a function of time after the beginning of the transient. The linear fit with corresponding confidence bands are shown in red. In blue the reactor period with corresponding fit as calculated for the current U_3Si_2 fuel is depicted. After* 8.66 s *the threshold of a period smaller than* 7 s *is reached.*

(COREHUD 5) the temperature rises from 50.25 °C to 59.09 °C. While there is almost no difference in the increase of temperature near the density jump, the two hot channels at the very outside for the fuel zone are heated up much more than with the current fuel. As depicted in Figure 10.17 the power deposition in the most inner and most outer channel is higher by more than 15 % for the UMo fuel. Due to the higher density of fissile material in these areas, such differences are reasonable. Hence, the coolant is heated more in these channels with such UMo fuel candidate.

10.2.2 Loss of coolant accident (LOCA)

For this calculation the same model which has already been described in Chapter 10.1.2 has been used, except that the thermal data for the fuel has been replaced. Because the LOCA mainly affects the primary circuit, no major differences compared to the current fuel are to be expected. Figure 10.18 shows the time dependent mass flow through the central channel. There are only marginal differences between the simulation using the current fuel and the UMo fuel candidate. Again, the threshold for the minimal mass flow allowed is not undercut.
Figure 10.19 shows the mass flow through the leakage. After the valve is opened at $t = 5$ s the coolant mass flow through the leakage rises up to 86.07 $^{kg}/_{s}$, i.e. as expected, there is almost no difference between the current fuel and a possible UMo fuel.

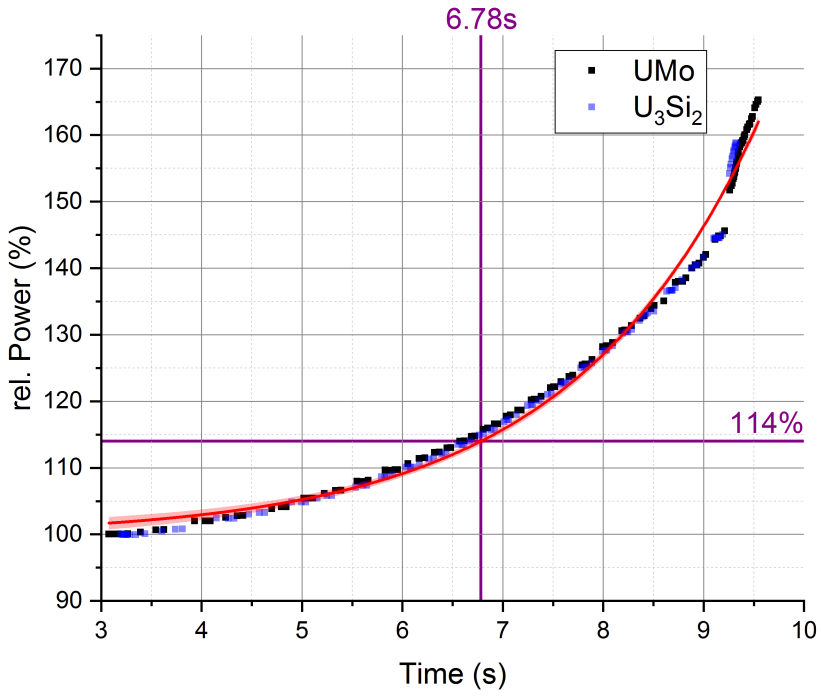

Figure 10.15: *Relative reactor power as a function of time after the beginning of the transient. The fit with corresponding confidence bands are shown in red. In blue the relative reactor power as calculated for the current U_3Si_2 fuel is depicted. After* 6.78 s *the threshold for the relative reactor power of* 114 % *is reached.*

Figure 10.20 shows the time dependent coolant temperature at the core outlet. After the beginning of the transient the coolant temperature jumps to nearly 52 °C and further increases to 53.3 °C after 48.4 s after the beginning of the transient. Compared to the current fuel (see Chapter 10.1.2) the time span for the temperature increase is very similar, even though the maximum coolant temperature is higher than with the U_3Si_2 fuel. The reason for this has already been described more in detail in Chapter 10.17. Due to the pressure drop caused by the leakage the primary pumps begin to suck water from the pool. Again, a backward flow of 89 kg/s from the pool to the central channel arises (see Figure 10.21) and nearly replaces the coolant loss. After going through the primary coolant pumps and the heat exchangers, the fresh cool water from the pool cools down the outlet temperature back.
As expected, only marginal differences in the mass flows are to be observed if the current fuel is replaced with a possible UMo fuel candidate. Due to a volatile reactor power during the zero-transient and a therefore reduced average heating, the outlet coolant temperature is systematically lower than for the current fuel.

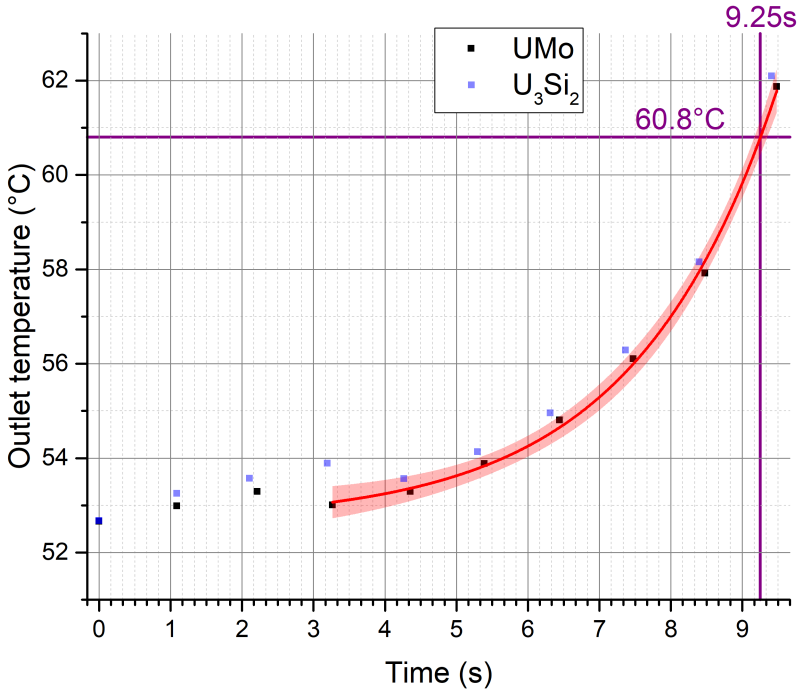

Figure 10.16: *Outlet coolant temperature as a function of time. The corresponding fit with confidence bands are shown in red. In blue the outlet coolant temperature as calculated for the current U_3Si_2 fuel is depicted. After* 9.25 s *the threshold for the coolant temperature of* 60.8 °C *is reached.*

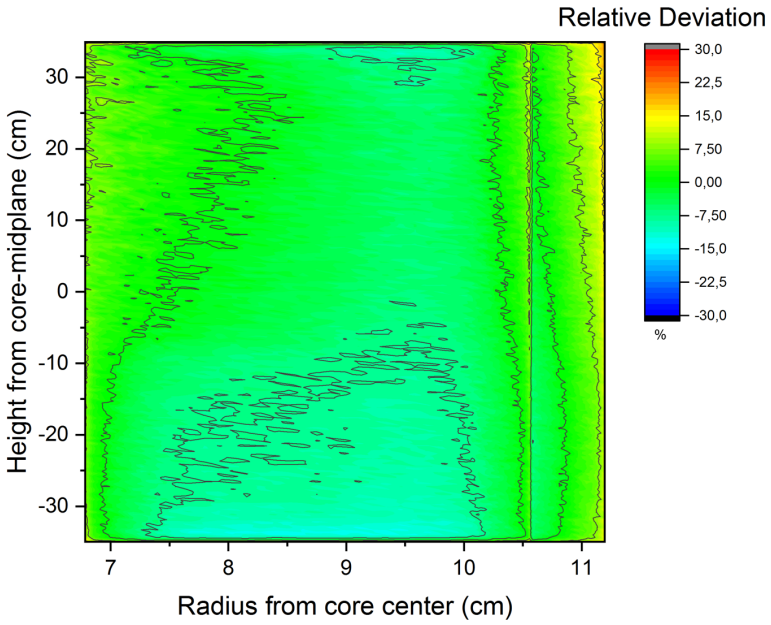

Figure 10.17: *Realative comparison of the power deposition between the current U_3Si_2 core and a possible UMo fuel candidate in the sense of $UMo - U_3Si_2$ as calculated with MCNP6.*

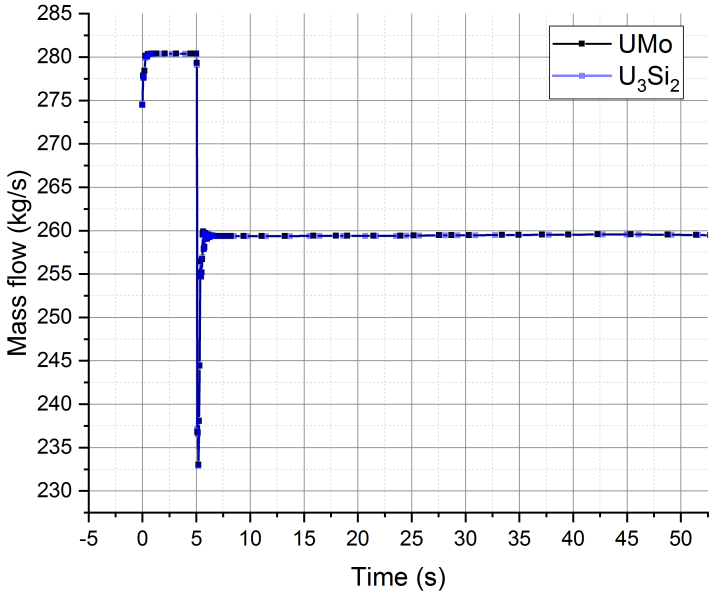

Figure 10.18: *Time dependent mass flow through the central channel during the transient. The mass flow through the central channel for the current U_3Si_2 fuel is shown in blue.*

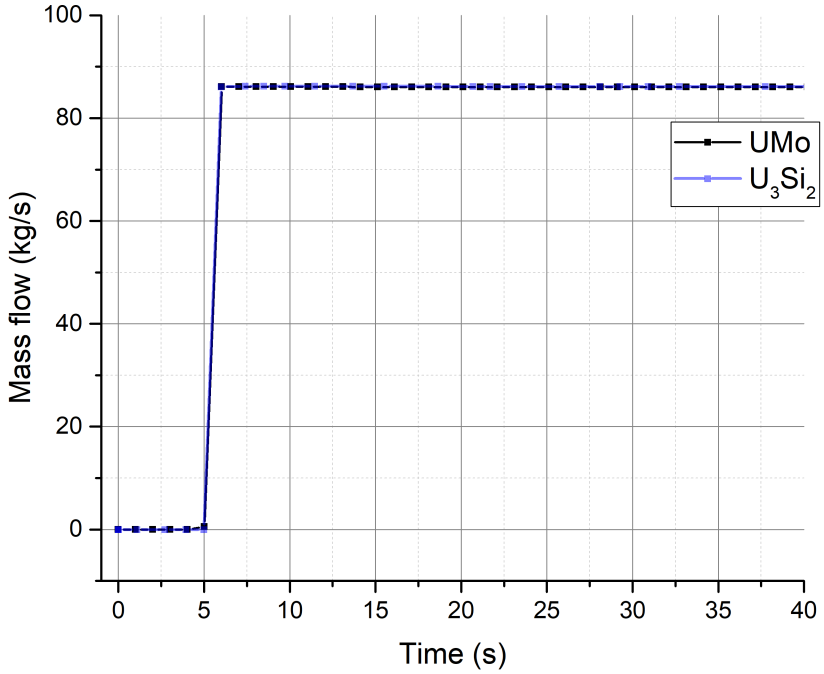

Figure 10.19: *Time dependent mass flow through the leakage during the transient. The mass flow through the leakage for the current U_3Si_2 fuel is shown in blue.*

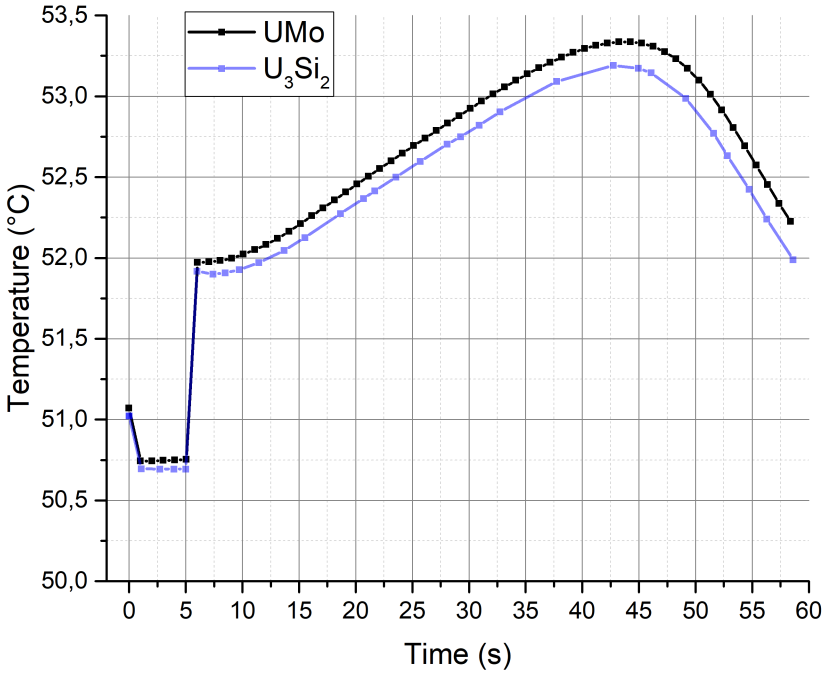

Figure 10.20: *Time dependent coolant temperature at the core outlet during the transient. The coolant temperature for the current U_3Si_2 fuel is shown in blue.*

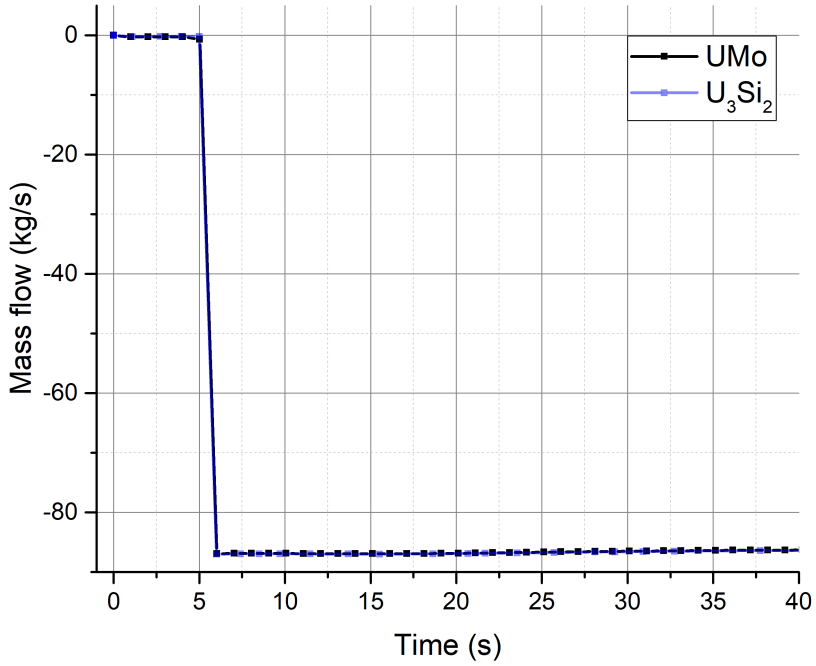

Figure 10.21: *Time dependent mass flow from the pool back into the central channel during the transient. The mass flow from the pool back into the central channel for the current fuel is shown in blue.*

10.2.3 Emergency power

To calculate the emergency power case with failure of the primary pumps, the four main cooling pumps are once again shut down after 10 s (compare Chapter 10.1.3). A coolant mass flow lower than 238.31 kg/s and outlet temperature higher 60.8 °C than are again used as shutdown criteria.

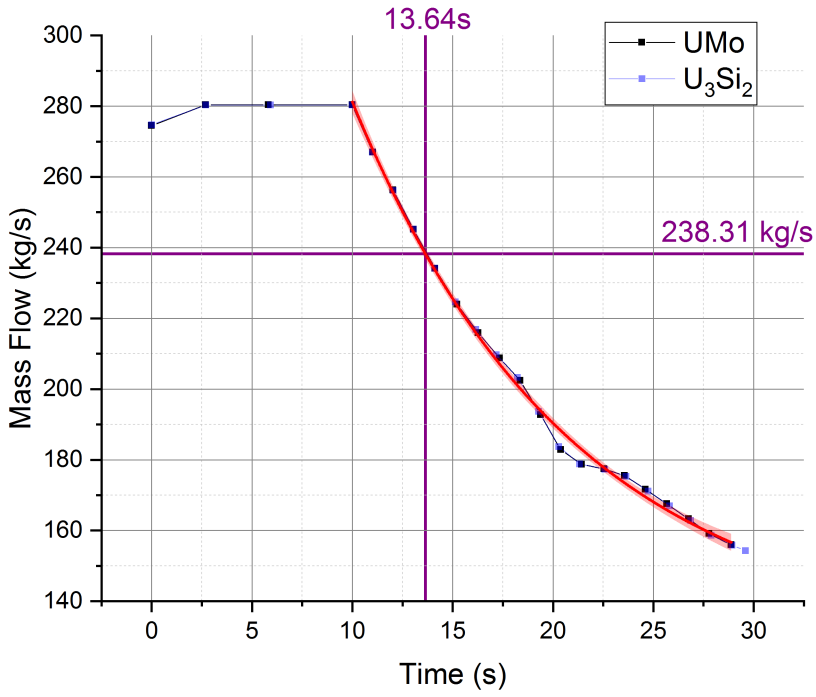

Figure 10.22: *Time dependent mass flow through the central channel during the transient using a possible UMo fuel candidate. The exponential fit and the corresponding confidence bands are shown in red and the mass flow through the central channel for the current fuel is shown in blue. After* 13.64 s *simulation time, the critical mass flow of* 238.31 kg/s *triggers the reactor safety system.*

Figure 10.22 shows the coolant mass flow through the central channel during the transient. Starting from 280.37 kg/s, the mass flow instantly begins to drop after the primary coolant pumps are shut down at $t = 10$ s simulation time. In order to calculate the exact time when the threshold flow is reached, an exponential fit ($R^2_{\text{adj}} = 0.997$) is once again used (see Chapter 10.1.3):

$$M_{\text{UMo}}(t) = (378.53 \pm 13.98) \cdot \exp\left[-t/(10.91 \pm 0.66)\right] + (129.84 \pm 4.36). \tag{10.11}$$

Using Eq. 10.11, the threshold mass flow is reached after 3.64 s after the start of the transient. Hence, there is no difference in this trigger of the reactor safety system between the UMo and the current U_3Si_2 fuel.
Figure 10.23 shows the time dependent outlet coolant temperature. Before the start of the transient, the coolant temperature reaches a stable value of 52.33 °C a the outlet.

$$T(t) = (15.61 \pm 7.19) \cdot \exp\left[t/(33.72 \pm 10.53)\right] + (31.41 \pm 7.80). \tag{10.12}$$

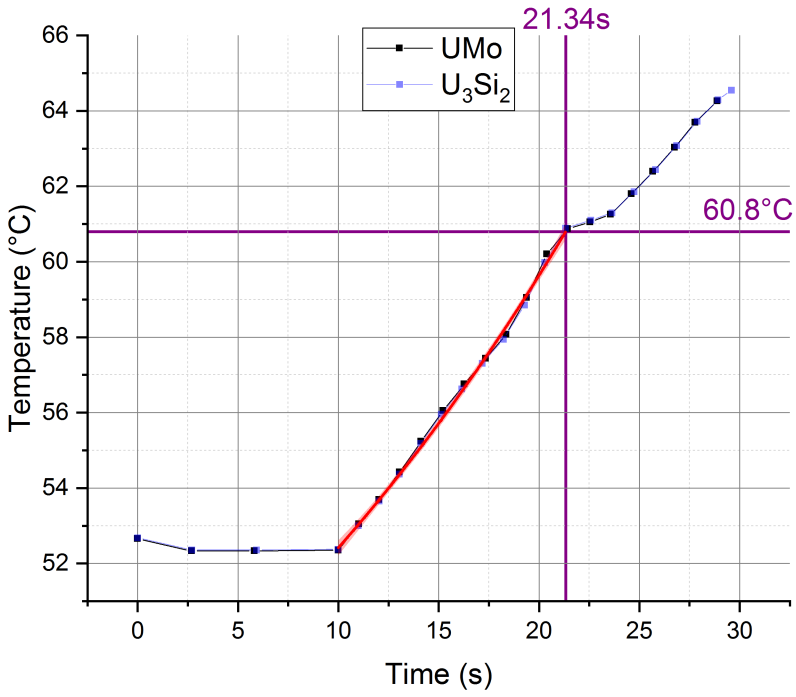

Figure 10.23: *Time dependent coolant outlet temperature during the transient using a possible UMo fuel candidate. The exponential fit and the corresponding confidence bands are shown in red and the coolant outlet temperature for the current fuel is shown in blue. After* 21.34 s *simulation time, the coolant temperature of* 60.8 ° *triggers the reactor safety system.*

The shutdown of the primary coolant pumps leads to an increase of the temperature and using an exponential fit ($R^2_{\text{adj}} = 0.998$) of the outlet coolant temperature (Eq. 10.12) after 11.34 s after the start of the transient the threshold of 60.8 °C is reached. Again, there is no difference in the triggering time between the current and this UMo fuel.
The time dependent temperature in the outer hot channel CORELUD 2 (see Chapter 7.2) is depicted in Figure 10.24. When the shutdown rods begin to fall in the core the temperature rose to 76.7 °. Due to the higher fissile material in this part of the fuel zone this hot channel is heated more than with the current U_3Si_2 fuel. For a possible UMo core, in this hot channel area, the heat load has to be reduced more than with the current fuel. This could be achieved e.g. with a steeper density gradient or by introducing burnable poisons into the outer fuel element [74].

10.2.4 Summary

The results for the shutdown conditions while using a possible UMo fuel candidate do not differ much from the one with the current fuel. It has to be noted, that it is possible that the thresholds will have to be adjusted during the conversion. The main goal of this thesis is the establishment of a coupled model system to calculate various transient scenarios for FRM II. Due to its complexity, a possible adaption of the shutdown criteria for a new fuel should be investigated, when a new fuel has finally been selected.

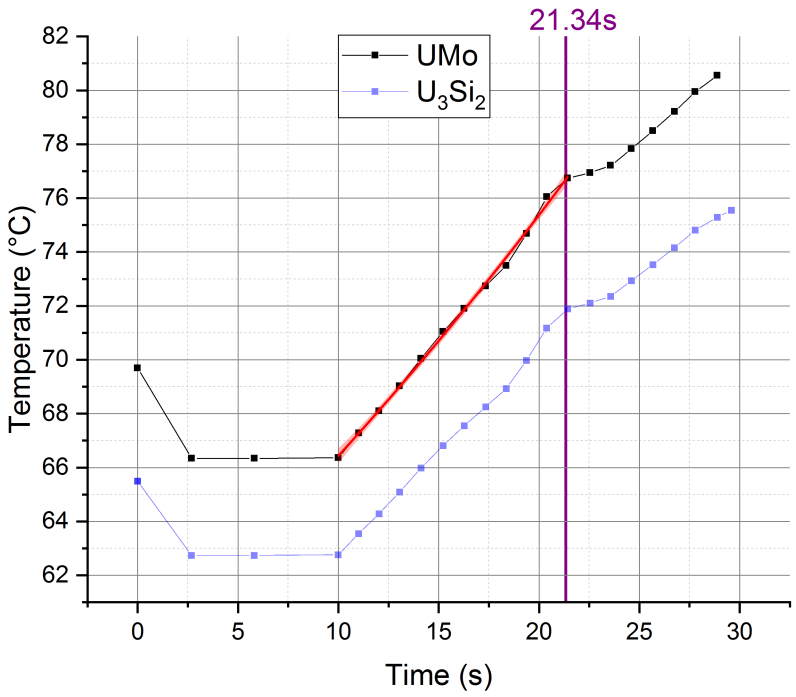

Figure 10.24: *Time dependent coolant outlet temperature in the outer hot channel CORELUD 2 during the transient using a possible UMo fuel candidate. When the shutdown rods begin to fall into the core the temperature rose to 76.7 °. In blue the corresponding temperature as calculated for the current U_3Si_2 fuel is depicted.*

Part V

Conclusions and Outlook

CHAPTER 11

Summary

The main purpose of this work was the development of a flexible system of models and methods that allows the calculation of various transient scenarios for FRM II. By using the coupled code system of the deterministic neutronic code TORT-TD and the system code ATHLET, a state of the art and well-proven reactor-physics calculation scheme was established. The Monte Carlo (MC) code Serpent 2 was used to calculate the multi-group cross sections used in TORT-TD. With the self-developed post processing tool C^2, a powerful tool is available to handle the models comfortably. An overview of all capabilities of C^2 can be found in the Appendix D.
The complex geometry and especially the involute shaped fuel plates cannot currently be explicitly modeled, neither by Serpent 2 nor by TORT-TD. Hence, a study of different approaches for a substitutional model with simplified geometry has been performed. All investigated models have been compared to the well-established full core MCNP model of FRM II (OISM) developed by Röhrmoser [71] regarding multiplication factor, power deposition, thermal and fast neutron flux distribution. By introducing a grading factor which includes all these characteristic parameters it could be shown that the vertical stack model with two reduced fuel plates at the top and bottom of the fuel zone VSM2 performed best (see Chapter 6.2.5). As already discussed in Chapter 6.2.3.3, the multiplication factor of this model matches perfectly with the multiplication factor obtained from the original model. Also, for all relevant parts of the reactor core the power deposition distribution of both models matches within $\pm 1.25\,\%$, and both the thermal and fast neutron flux distributions are also in very good agreement within $\pm 1\,\%$.
The selected substitutional model was translated into a geometrically equivalent Serpent 2 model which has been validated by comparing the reactor key parameters with the well-established full core MCNP model (see Chapter 6.3.1). The multiplication factor as calculated with Serpent 2 matches with the corresponding MCNP6 calculation. The calculation of the thermal and fast neutron flux calculated with both MC codes yielded matching results within $2\,\%$. Because Serpent 2 does not calculate the power deposition in the same manner as MCNP6, only the fission rate distribution could be compared. It was shown that for the whole geometry both codes deliver matching results within the statistical uncertainties. With the thereby validated Serpent 2 model, multi-group cross sections have been calculated using a bimodal approach: Serpent 2 can only calculate cross sections within universes (c.f. Chapter 2.2.1). Hence, the model was set up in the way that every single cell is defined in one corresponding universe. There are a few areas in the reactor core which suffer from poor neutron statistics: three aluminum parts at both ends of the control rod, the helium above the heavy water fill level, and the inner hafnium of the control rod. For these areas the external source mode of Serpent 2 (c.f. Chapter 6.3.2.2) has been used in order to obtain reasonable results for the cross sections even for these areas.

With this approach and together with C^2 it is possible to calculate very quickly multi-group cross sections for the whole reactor. For the subsequent TORT-TD calculations cross sections with 30 energy groups for different temperatures and densities have been calculated.
Finally, a TORT-TD model has been set up with the idea that the meshing in the TORT-TD-geometry is aligned to the material borders of the real geometry. For the validation calculation using MCNP6 the most accurate but still feasible computational parameters have been chosen: A quadrature order of 8, 30 energy groups, cross sections to the first Legendre order and a very fine computational mesh. The resulting multiplication factor calculated with TORT-TD matches sufficiently well with both the MCNP6 reference value and the Serpent 2 value. The results for the power deposition and neutron flux distributions agree also well and hence, the TORT-TD ($S8$) model can be considered to be able to reproduce FRM II's core behavior correctly and, therefore, as being validated. Because TORT-TD is not parallelized, the computational burden is comparably high. In order to calculate transients in an acceptable amount of time, the TORT-TD model was therefore optimized. The quadrature order could be reduced to $S4$, a partial usage of the diffusion approximation was employed, and the computational grid was optimized to a coarser structure. In total, all these measures resulted in a time saving of 81.8 % whereas the reactor parameters differ only marginally compared to the TORT-TD ($S8$) model.
A similar approach has been chosen for the validation of the thermal-hydraulical ATHLET model, where comparisons with steady-state calculations using CFX have been performed. Besides the fuel element, which is represented by ten channels, the whole primary circuit with the four primary cooling pumps and the two heat exchangers is represented in the ATHLET model. The sieve which is installed above the fuel plates has been modeled by introducing an additional pressure loss coefficient, the characteristics of the primary pumps have been taken into account and the pipe friction has also been updated. The comparison of this ATHLET model with the CFX calculations yielded matching pressure drops over the fuel zone, and also matching flow velocities inside the cooling channels. Due to the missing lateral heat conduction in the fuel plates between the most outer channels and the inner and outer holdings, ATHLET overestimated the coolant temperature in these channels. In the remaining channels the results match very well within $\pm 1\,^{\circ}\mathrm{C}$. Due to increased heating of less streamed channels, ATHLET can be assumed as being conservative compared to CFX. The mass flows through the fuel element differ only marginally, and the difference between both codes is just $-0.65\,\%$, in the sense ATHLET minus CFX. Taking the temperature, weighted by the mass flow as quality factor, ATHLET has proven to be able to reproduce the results obtained with CFX.
With the built-in burnup module of Serpent 2, the reactivity worth of the control rod, the burnup of a fuel element during a 60 d cycle, and the burnup of the beryllium follower could be compared with results obtained by MCNP6 and MonteBurns. No difference could be quantified for the reactivity worth of the control rod, and also the overall burnup of a fresh fuel element is almost the same. There are small differences for some isotopes which can be caused by the missing movement of the control rod during the burnup steps. This leads to a difference of the total plutonium content by 3.1 % and the amount of ^{239}Pu by 1.3 %. Hence, also the total average burnup after 60 d of 20.2 % is slightly below the value calculated in [10]. The general trend of the isotope evolution matches very well with the MCNP6 calculations. Nevertheless, Serpent 2 estimates a lower absolute mass of the burnup products of the control rod.
During this work, it was possible to quantify the influence of the (n,2n) reaction in the beryllium follower to the reactor. With a comparison of Serpent 2 and MCNP6 using first order perturbation theory, it could be shown that the (n,2n) reaction contributes nearly two days of cycle length.

As final step, the models developed during this work have been used to calculate the three most important transient scenarios: An uncontrolled reactivity insertion, a Loss of coolant accident (LOCA) and the emergency power scenario. First, the results for the current fuel have been compared to the studies of the general contractor Siemens that have been performed before start-up of FRM II. Even though the reactivity insertion simulated here is a combination of two separated cases during the licensing, the results obtained within this thesis matches well to the Siemens calculations. The study of the LOCA showed very well matching results within $\pm 5\,\%$ for the mass flows through the central channel and the leakage. Also, the resulting back-flow from the pool into the central channel has been calculated well. For the emergency power case the loss of mass flow through the central channel is reached 1.03 s later than in the Siemens calculations. Due to a different power deposited in the central channel the signal triggered by the outlet coolant temperature is reached 11.33 s later.
The study of all three scenarios for a possible UMo fuel candidate showed that the time for reaching the threshold won't change much. During a reactivity insertion with an uncontrolled control rod movement, the shutdown criteria would differ by less than 1 s. The mass flows during a LOCA are the same as for the current fuel, only certain areas of the outlet coolant stream differ significantly. For the emergency power scenario no significant differences have been found. With the models and tools developed within this work, a powerful framework for transient calculations is now available in order to support the efforts of FRM II to convert to a fuel element with lower enrichment.

11.1 Outlook

The field of computational reactor physics is rapidly growing, and so are the methods and approaches used. Serpent 2 is constantly being improved, and new capabilities are implemented. In the latest version that has been released after all calculations in this work had already been performed, user-defined surfaces can be employed which may allow to exactly model involute shaped fuel plates. Currently, a master thesis is ongoing to investigate such possibility. If a Serpent 2 model could be set up with involute shaped fuel plates, and after a validation process, this model could be used to calculate multi-group cross sections without using a substitutional geometry. As discussed in detail in Chapter 6.2, such an improved model will not affect the results of this work significantly, but it would eliminate an approximation.
A further improvement of a newer Serpent 2 version allows for time dependent transient calculations. This mode is still under development and has a very high demand for computational power. Nevertheless, the capabilities of this mode should be investigated and tested in a separate work. Probably, that new mode in combination with a coupling of Serpent 2 and a CFD code such as CFX or OpenFoam can complement the deterministic approach chosen in this work, and would allow transient calculations of highest fidelity.
The meshing of the TORT-TD model developed within this thesis is aligned to the material borders of the real geometry. This yields a high number of mesh cells and, therefore, increases the computational time needed. In order to have a more flexible model, simplifications like the reduction of energy groups or the extensive usage of homogenization could be investigated in addition to the optimization that has already been performed in this work. Also, the TORT-TD model does not include any core installations like the cold source or the emergency shutdown rods. If these parts could be included in an approximate of effective form into an r-φ-z–mesh, it would be possible to simulate the shutdown maneuver properly and take into account the asymmetric heat deposition due to the cold source. The cross sections used for the TORT-TD calculations have been calculated with a very small uncertainty[1]. In a future work, a complete sensitivity analysis of the multi-group cross sections should be done in order to speed up the calculations by allowing larger uncertainties for some cross sections.
Because ATHLET is a one-dimensional code, high fidelity studies like those with CFX are not possible. Therefore, it would be a significant improvement if the fuel element would be simulated with a modern CFD code while the remaining primary circuit is still modeled with ATHLET. This would combine very detailed results for the fuel element obtained by the CFD code and the response of the primary circuit calculated with ATHLET. In that case the TORT-TD model could be coupled to the CFD code by using the already existing coupling scheme of ATHLET and CFX [57].
The self-developed post processing tool C^2 can be extended such that it could be used as a "full service" reactor calculation suite. This could include the automated calculation of power and neutron flux distributions at BOL and EOL as well as burnup calculations. Because C^2 is mainly designed to be used with Serpent 2, a better implementation of an MCNP6 interface would be desirable, too.

[1] less than 0.01 ‰

11.2 Conclusion

The codes used during this work, TORT-TD and ATHLET, are widely used for very different scenarios, have a broad community, and a long development history. Hence, they can be assumed as state of the art for licensing calculations in the coming years. In combination with C^2, the models developed within this thesis can serve as a basis for the detailed study of different transient scenarios. These new calculation capabilities will ease the conversion of FRM II to a fuel with lower enriched fuel by providing a detailed and flexible framework to keep the high safety standard of the reactor.

Part VI

Appendix

APPENDIX A

Total cross section of hafnium

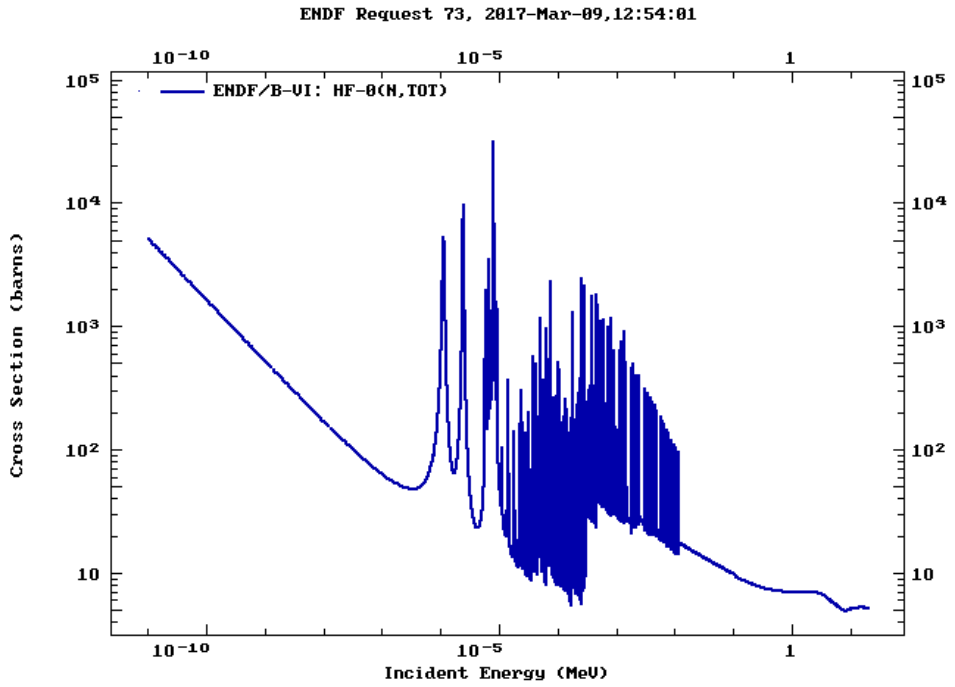

Figure A.1: *Energy dependence of the total cross-section for hafnium*

APPENDIX B

Subdivision of the heavy water moderator tank for Serpent 2

220	221	222	223	224	225	226	227	228	229	230	231	232
207	208	209	210	211	212	213	214	215	216	217	218	219
194	195	196	197	198	199	200	201	202	203	204	205	206
181	182	183	184	185	186	187	188	189	190	191	192	193
168	169	170	171	172	173	174	175	176	177	178	179	180
155	156	157	158	159	160	161	162	163	164	165	166	167

Figure A.1: *Universe structure of the fine subdivision of the heavy water moderation tank.*

APPENDIX C

Comparison of neutron fluxes for single energy groups (TORT-TD $S8$ vs. MCNP6)

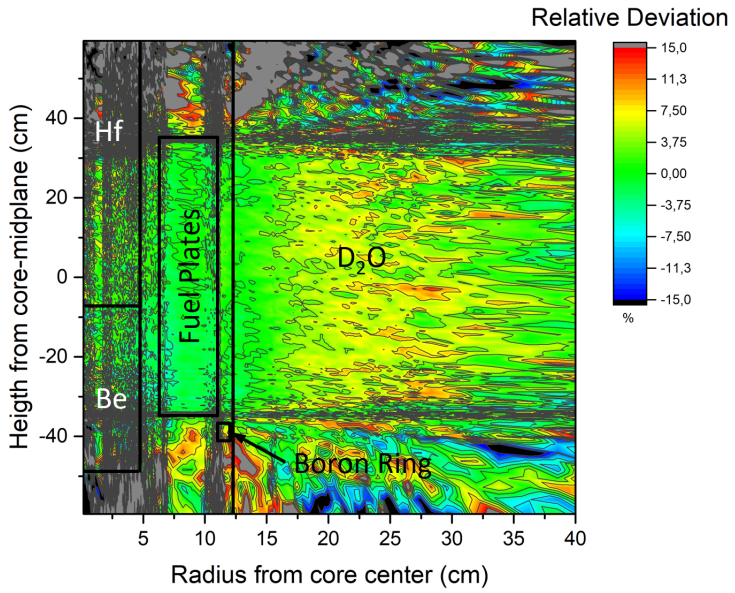

Figure A.1: *Relative deviation in % of the neutron flux of energy group 2 (see Table 6.9) between MCNP6 and TORT-TD.*

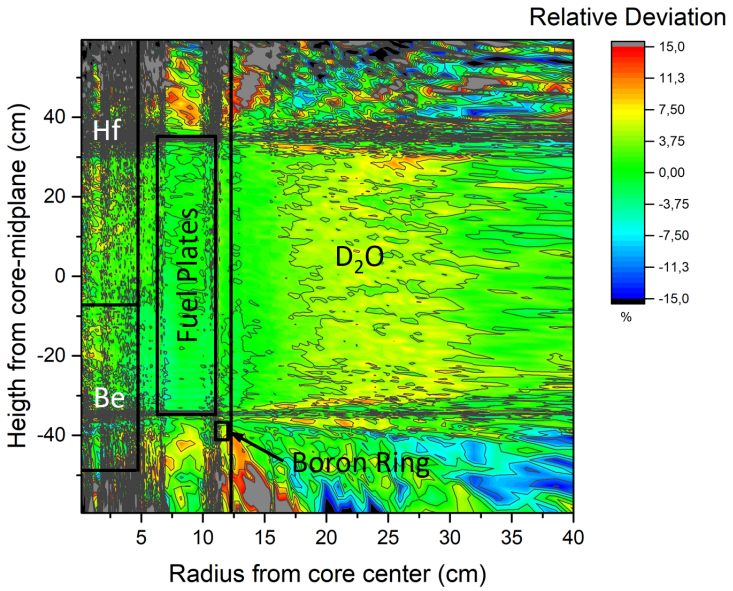

Figure A.2: *Relative deviation in % of the neutron flux of energy group 3 (see Table 6.9) between MCNP6 and TORT-TD.*

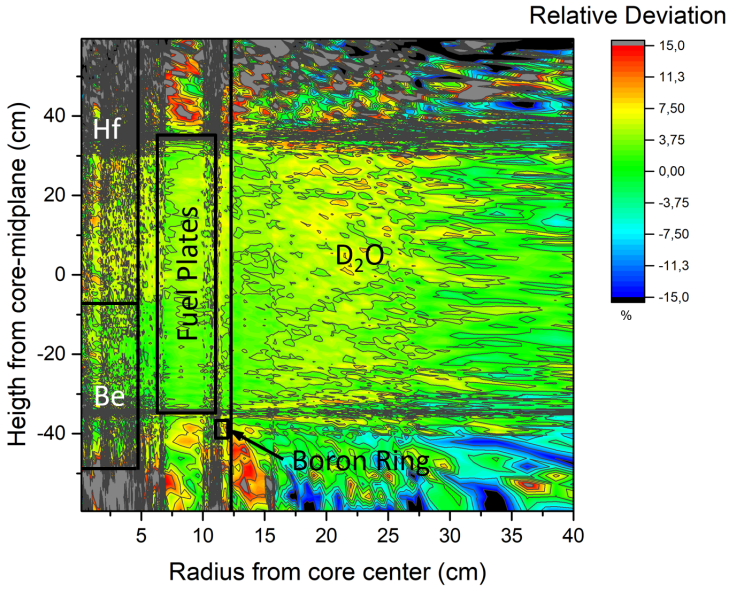

Figure A.3: *Relative deviation in % of the neutron flux of energy group 4 (see Table 6.9) between MCNP6 and TORT-TD.*

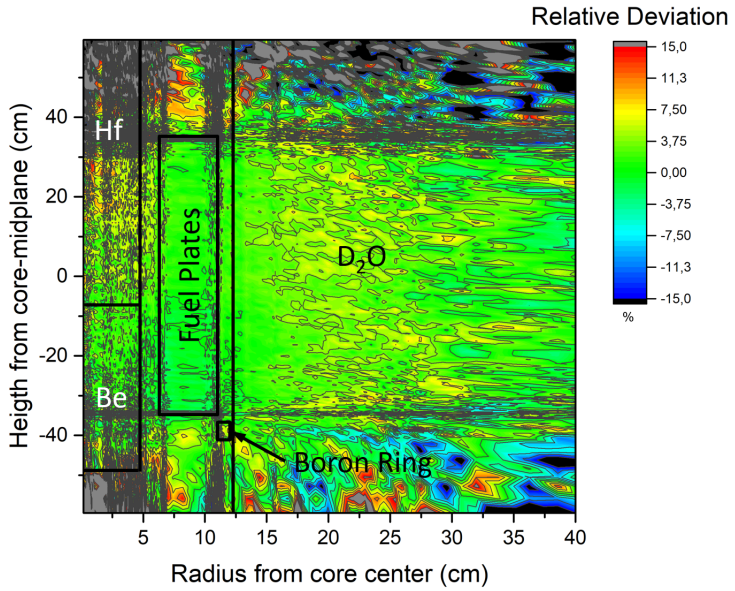

Figure A.4: *Relative deviation in % of the neutron flux of energy group 5 (see Table 6.9) between MCNP6 and TORT-TD.*

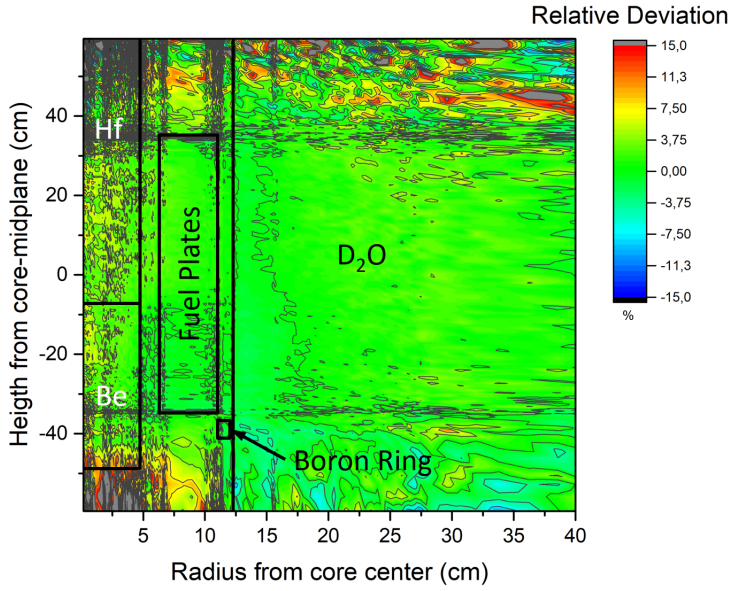

Figure A.5: *Relative deviation in % of the neutron flux of energy group 6 (see Table 6.9) between MCNP6 and TORT-TD.*

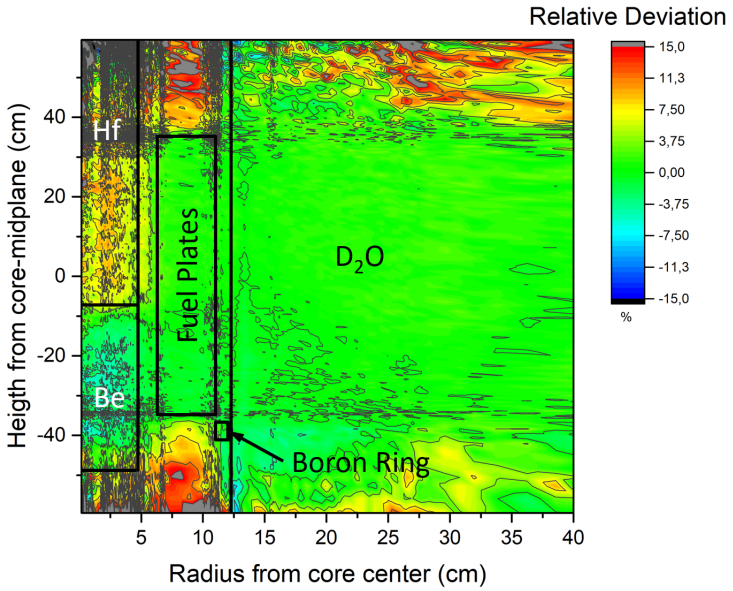

Figure A.6: *Relative deviation in % of the neutron flux of energy group 7 (see Table 6.9) between MCNP6 and TORT-TD.*

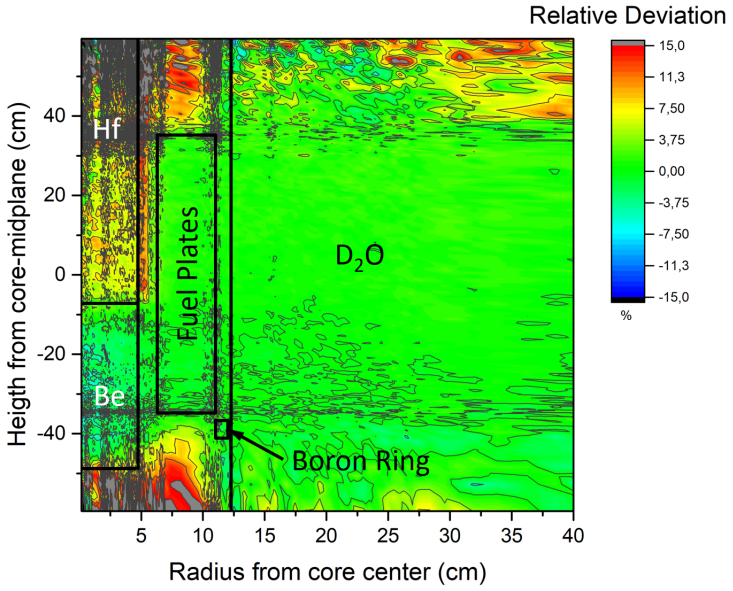

Figure A.7: *Relative deviation in % of the neutron flux of energy group 8 (see Table 6.9) between MCNP6 and TORT-TD.*

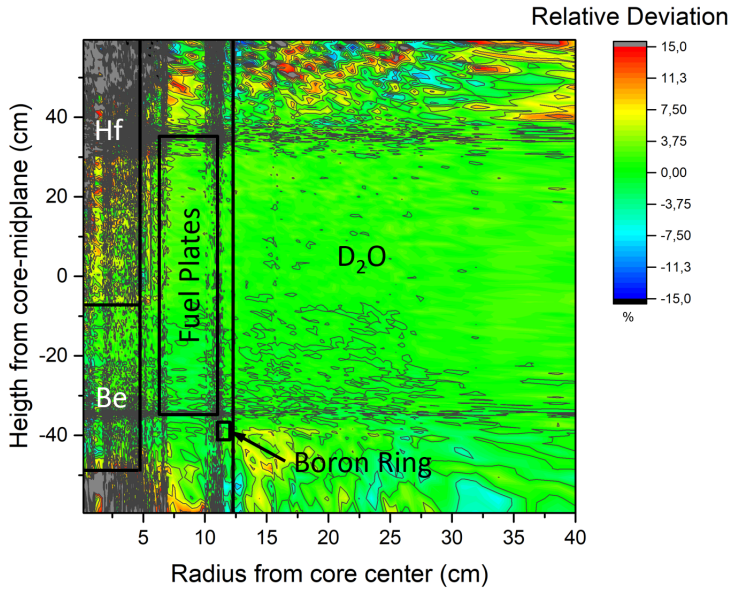

Figure A.8: *Relative deviation in % of the neutron flux of energy group 9 (see Table 6.9) between MCNP6 and TORT-TD.*

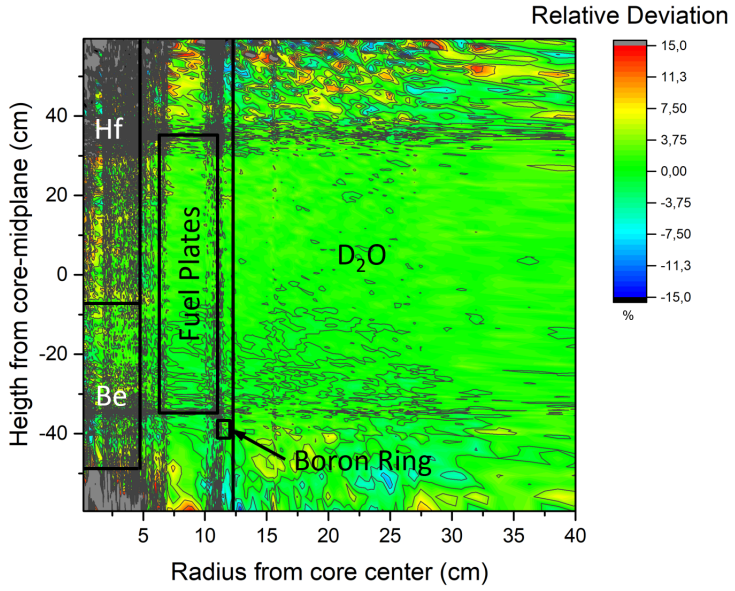

Figure A.9: *Relative deviation in % of the neutron flux of energy group 10 (see Table 6.9) between MCNP6 and TORT-TD.*

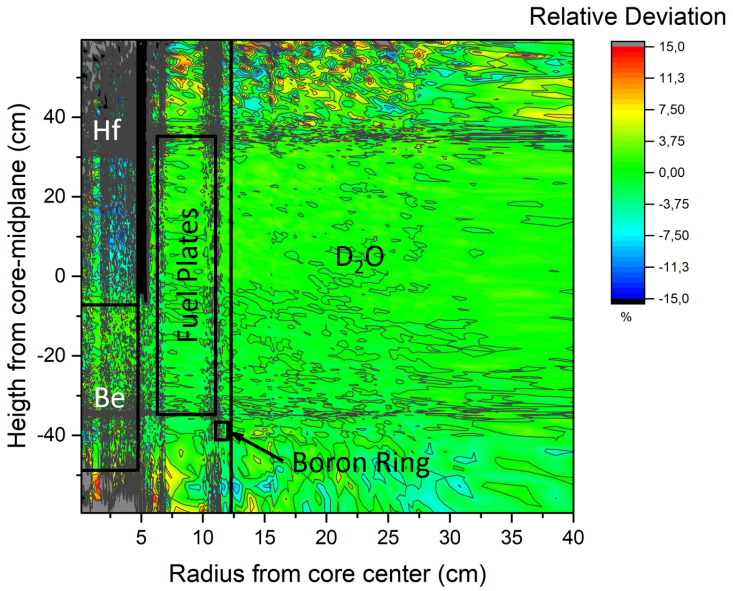

Figure A.10: *Relative deviation in % of the neutron flux of energy group 11 (see Table 6.9) between MCNP6 and TORT-TD.*

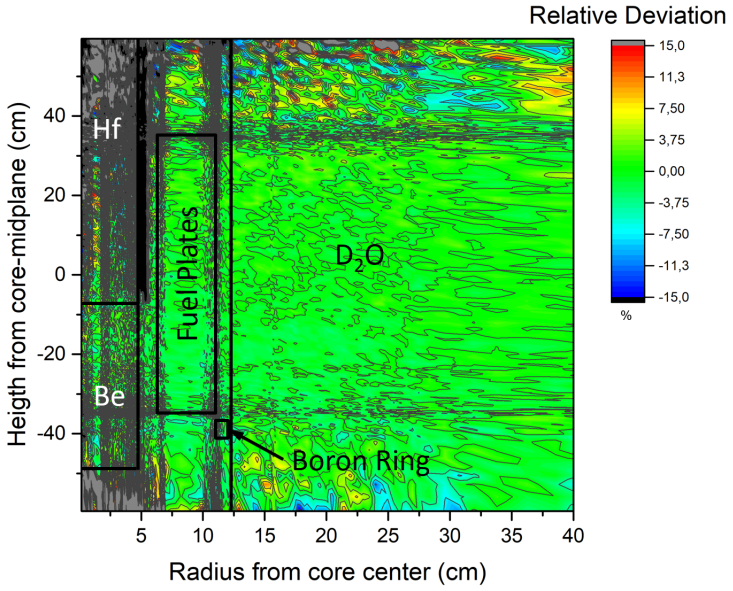

Figure A.11: *Relative deviation in % of the neutron flux of energy group 12 (see Table 6.9) between MCNP6 and TORT-TD.*

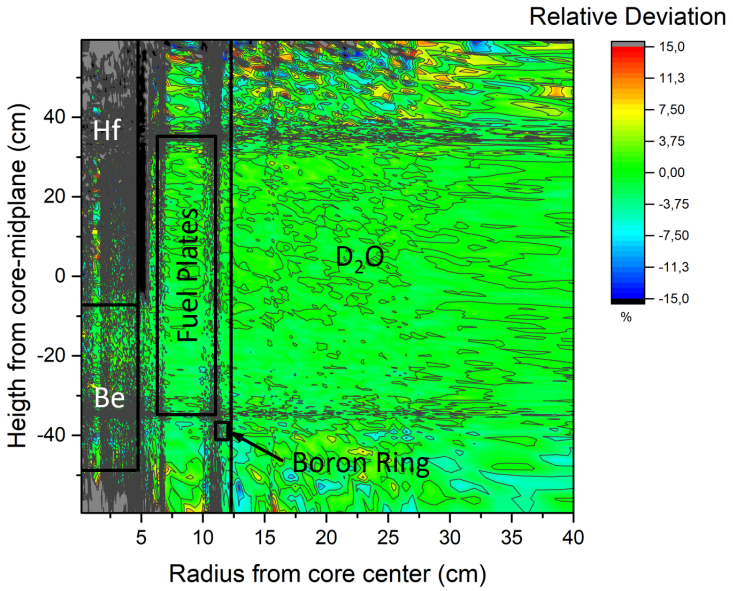

Figure A.12: *Relative deviation in % of the neutron flux of energy group 13 (see Table 6.9) between MCNP6 and TORT-TD.*

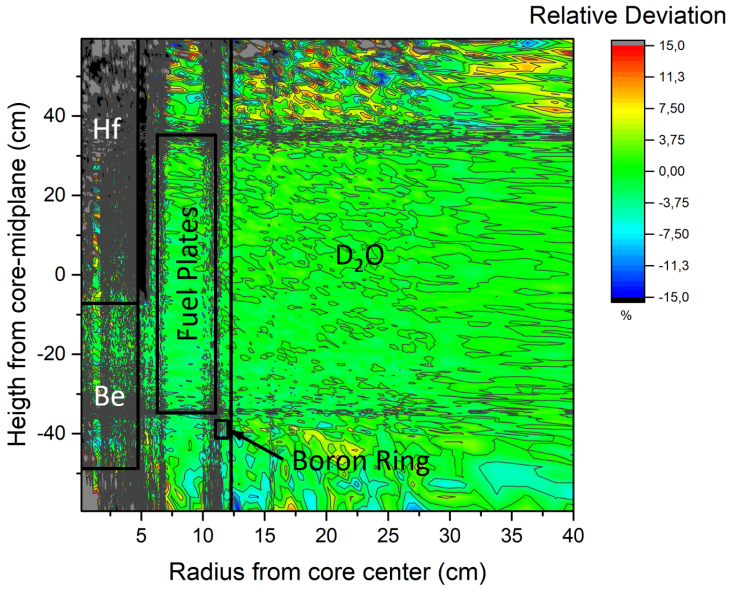

Figure A.13: *Relative deviation in % of the neutron flux of energy group 14 (see Table 6.9) between MCNP6 and TORT-TD.*

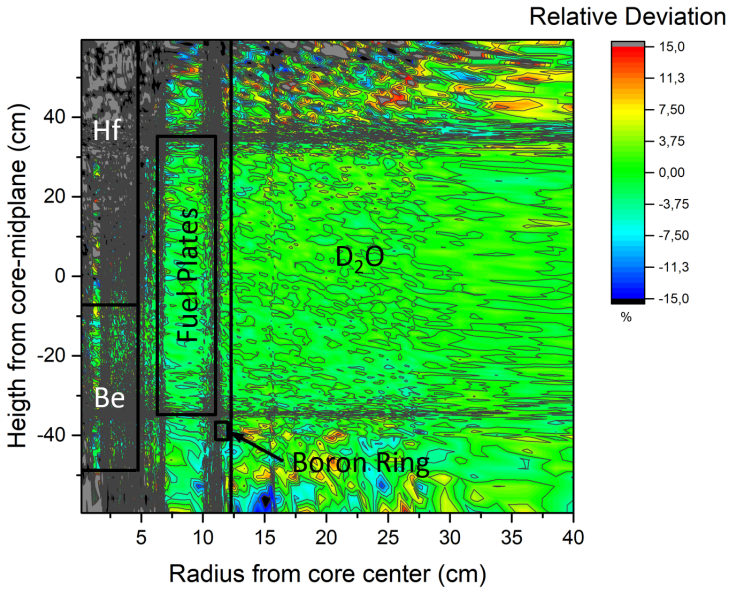

Figure A.14: *Relative deviation in % of the neutron flux of energy group 15 (see Table 6.9) between MCNP6 and TORT-TD.*

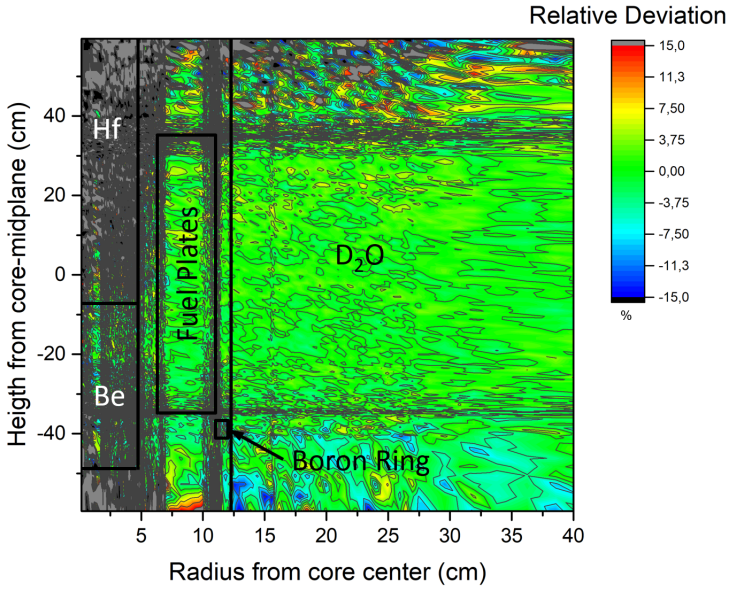

Figure A.15: *Relative deviation in % of the neutron flux of energy group 17 (see Table 6.9) between MCNP6 and TORT-TD.*

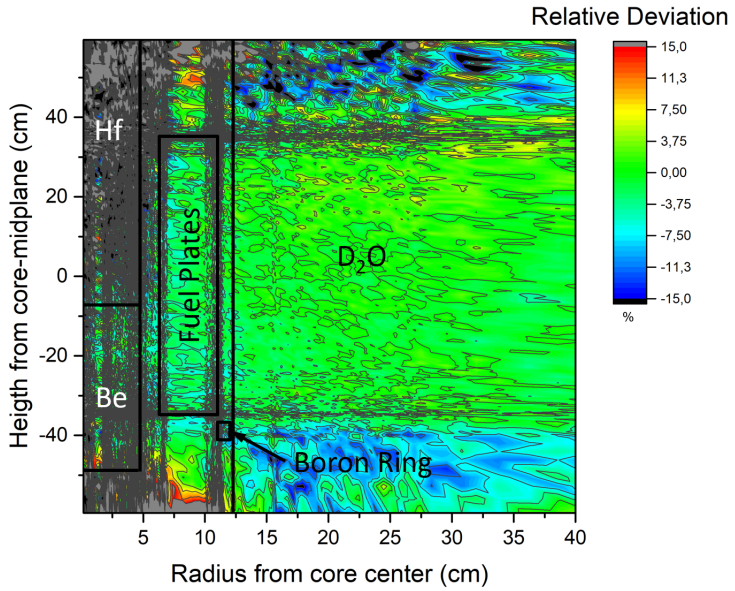

Figure A.16: *Relative deviation in % of the neutron flux of energy group 18 (see Table 6.9) between MCNP6 and TORT-TD.*

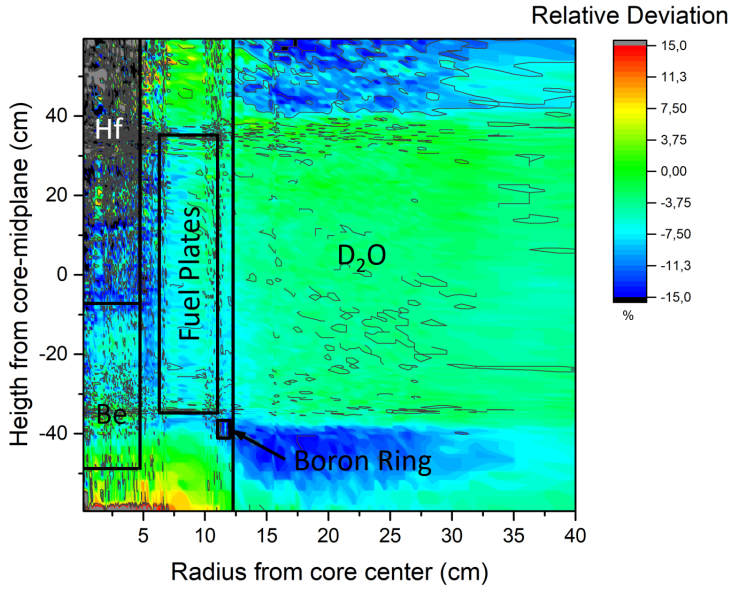

Figure A.17: *Relative deviation in % of the neutron flux of energy group 19 (see Table 6.9) between MCNP6 and TORT-TD.*

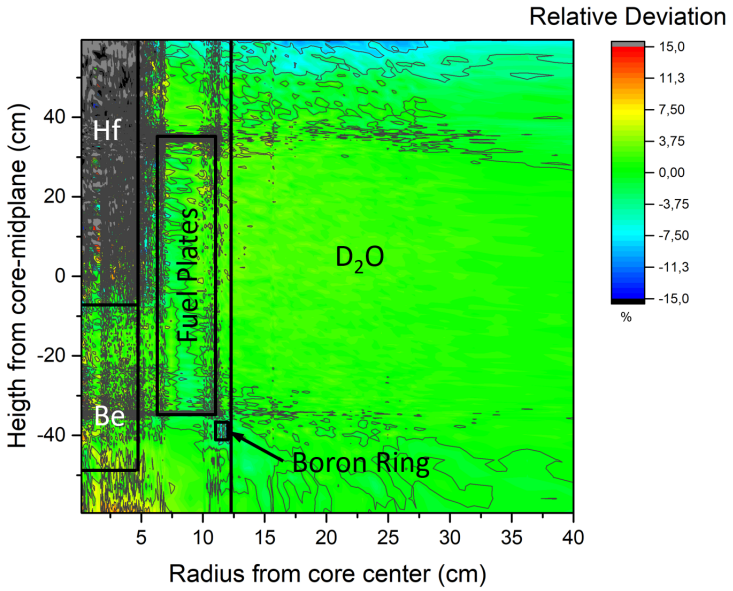

Figure A.18: *Relative deviation in % of the neutron flux of energy group 20 (see Table 6.9) between MCNP6 and TORT-TD.*

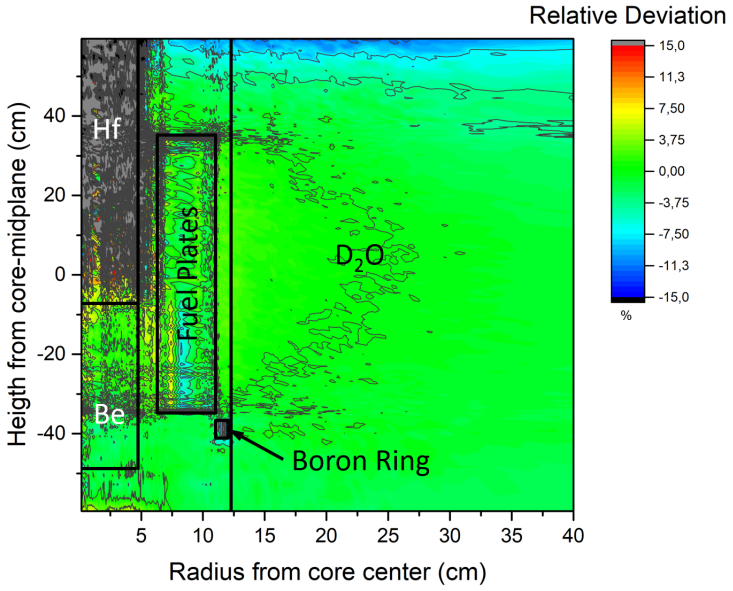

Figure A.19: *Relative deviation in % of the neutron flux of energy group 22 (see Table 6.9) between MCNP6 and TORT-TD.*

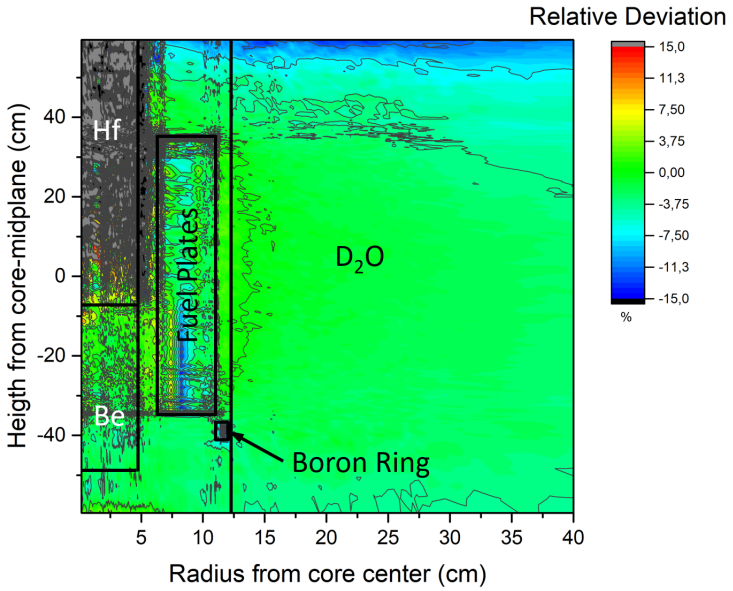

Figure A.20: *Relative deviation in % of the neutron flux of energy group 23 (see Table 6.9) between MCNP6 and TORT-TD.*

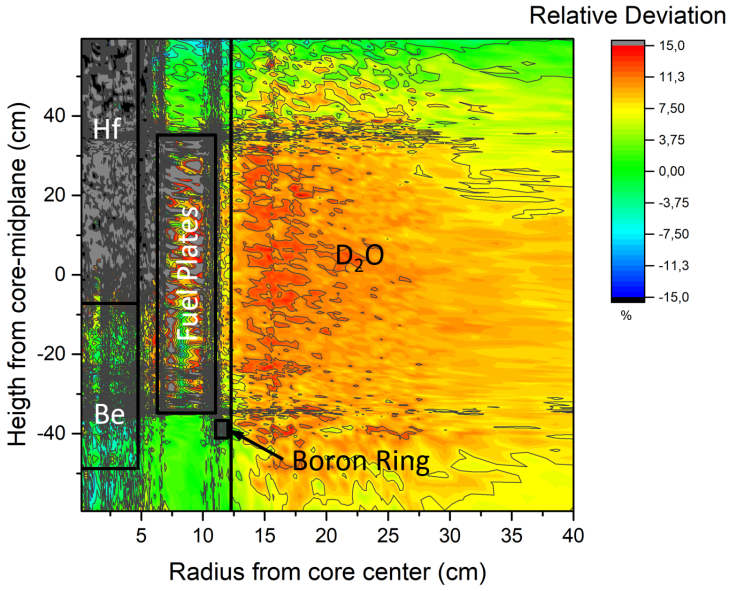

Figure A.21: *Relative deviation in % of the neutron flux of energy group 24 (see Table 6.9) between MCNP6 and TORT-TD.*

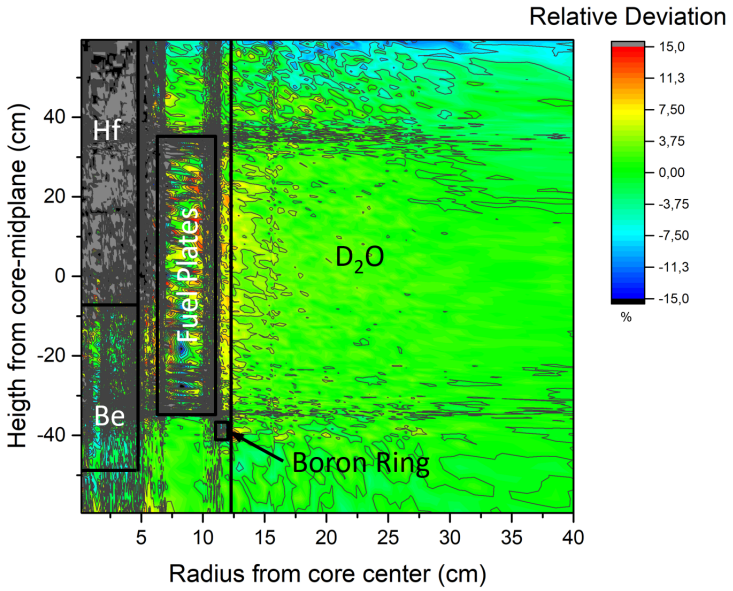

Figure A.22: *Relative deviation in % of the neutron flux of energy group 25 (see Table 6.9) between MCNP6 and TORT-TD.*

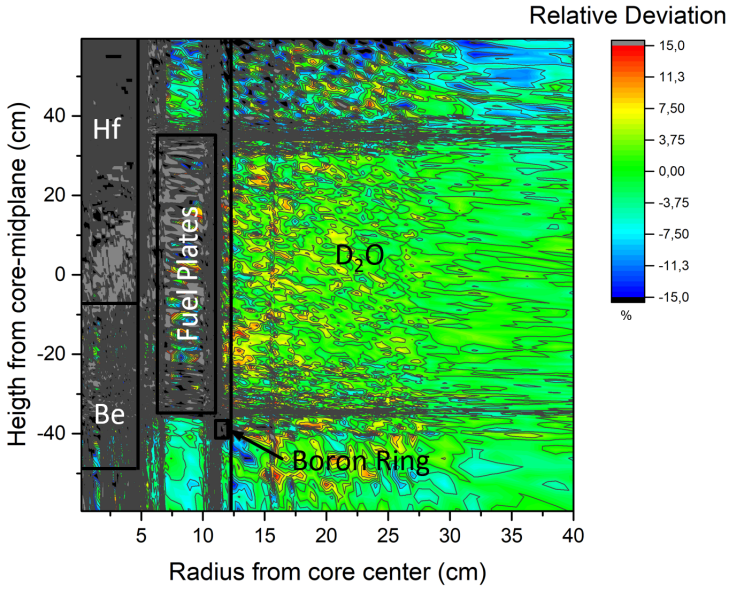

Figure A.23: *Relative deviation in % of the neutron flux of energy group 26 (see Table 6.9) between MCNP6 and TORT-TD.*

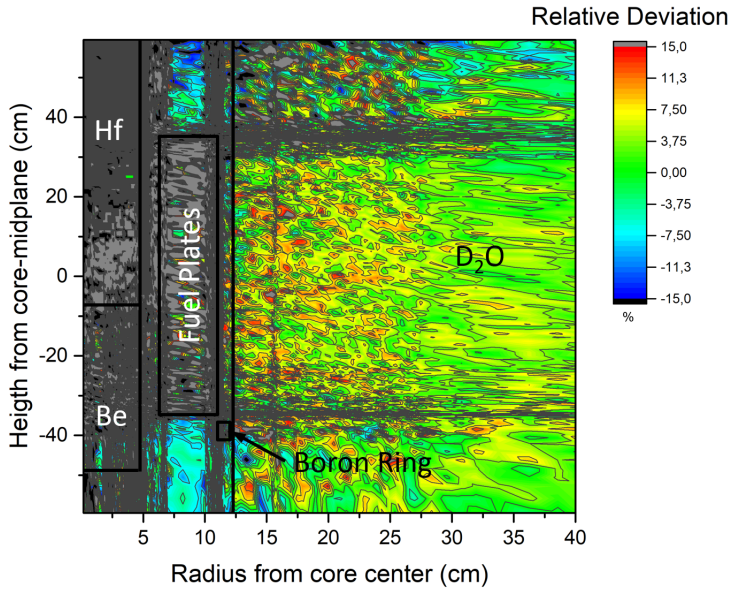

Figure A.24: *Relative deviation in % of the neutron flux of energy group 27 (see Table 6.9) between MCNP6 and TORT-TD.*

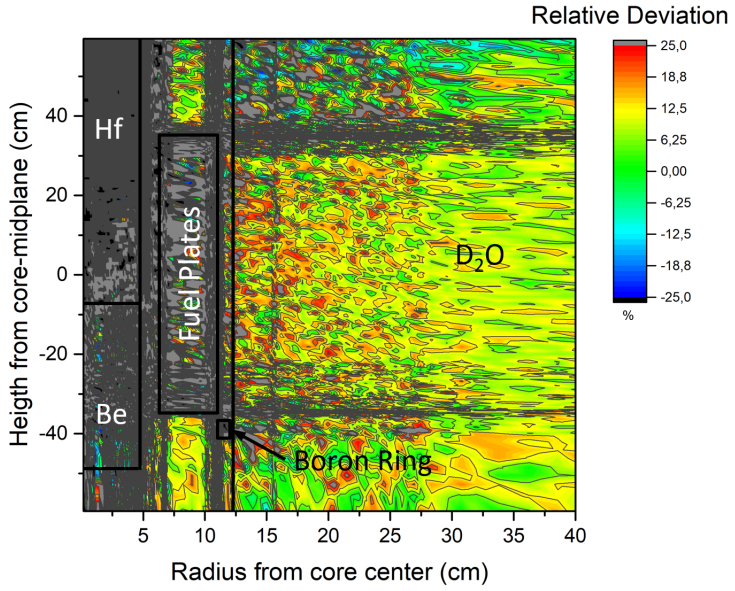

Figure A.25: *Relative deviation in % of the neutron flux of energy group 29 (see Table 6.9) between MCNP6 and TORT-TD.*

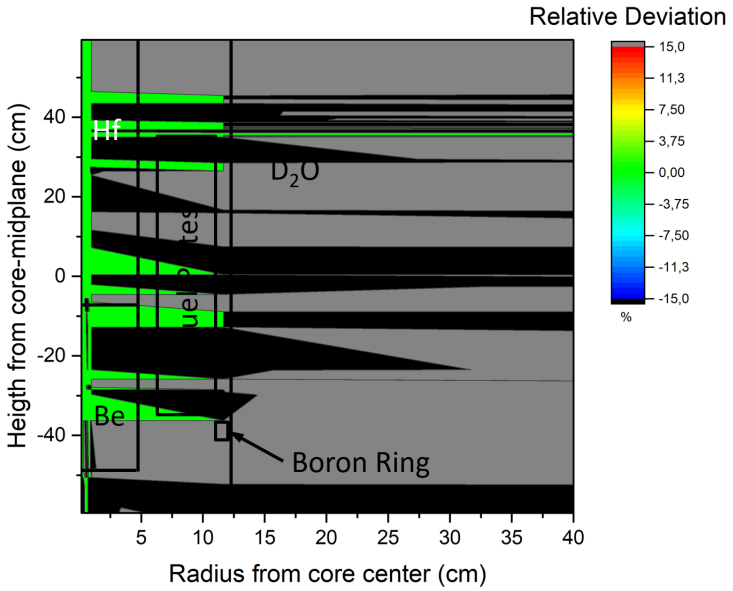

Figure A.26: *Relative deviation in % of the neutron flux of energy group 30 (see Table 6.9) between MCNP6 and TORT-TD.*

APPENDIX D

C^2

C^2 is a code framework which handles most of the calculations and data evaluations needed within this thesis. In Figure A.1, the main window of C^2 is depicted. From here, all the functionality is

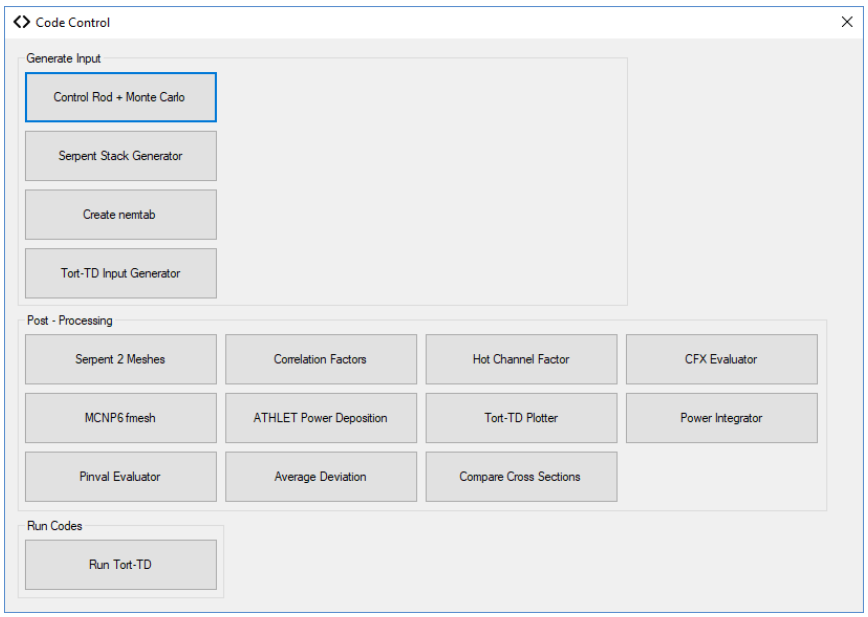

Figure A.1: *Main window of C^2. From here all available features are accessible.*

accessible. C^2 is written in C# and consists of several sub-parts. C^2 is still under envelopment, so there are some features which weren't used during this thesis but are already included to allow fully automated calculations with on-the-fly calculation of cross sections. Here, the mainly used features will be explained in the following.

D.1 Adjustments of MC models

With the MC control module the simulation parameters for MC calculations can be adjusted. As shown in Figure A.2, C^2 gives information for which code the model was written: MCNP6 (see Chapter 4.1) or Serpent 2 (see Chapter 4.2). This module also extracts and changes the position of the control rod, the number of neutrons simulated per cycle and the number of inactive and

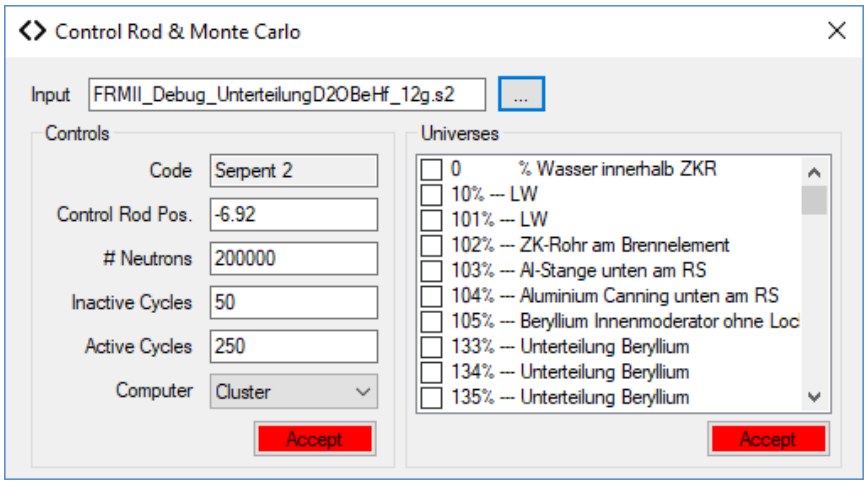

Figure A.2: *Feature of* C^2 *to manipulate the input desks for MC calculations. The control rod position, number of neutrons per cycle, number of active and inactive cycles and the computer to be used can be manipulated. For cross section calculations with Serpent 2 the universes which are taken into account are also selectable.*

active cycles, respectively. For a Serpent 2 model, the user has the possibility to change the computer the model is supposed to be used at. This means that the path of the cross sections used can be adjusted. The user has the possibility to create several pre-adjustments and to adjust the profiles. Also, for a Serpent 2 model, C^2 extracts the exact universe structure and provides the possibility to modify the model so that cross sections will be calculated for the selected universes (see Chapter 4.2.1).

D.2 Creation of Stacks for the VSM model

C^2 can create the Serpent 2 input desk for a VSM automatically. As Figure A.3 shows, the user

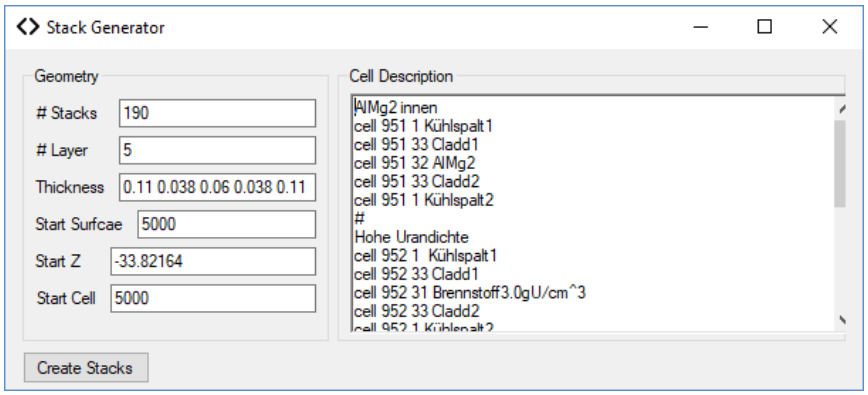

Figure A.3: *Feature of* C^2 *to generate the input desk for a VSM. In the left panel the needed geometrical data for the disks and some identifiers for the model have to be provided. In the right panel the exact horizontal and vertical division have to be provided by the user.*

has to provide the number of virtual discs, the number of vertical layers per disc, the thicknesses

of each disc, the z-position of the first disc and the numbers of free cell/surface identifiers. In a separate text box, the horizontal separation has to be provided by the user. Here the used universes, materials and comments have to be inserted.

D.3 Creation of cross sections in the NEMTAB format

For the deterministic calculations (see Chapter 4.3) group wise cross sections in the NEMTAB format have to be provided. The cross sections used for the calculations within this thesis have been calculated with Serpent 2 (see Chapter 4.2.1). Hence, the Serpent 2 output has to be converted to the NEMTAB format. In order to let C^2 write proper cross sections, the user has to

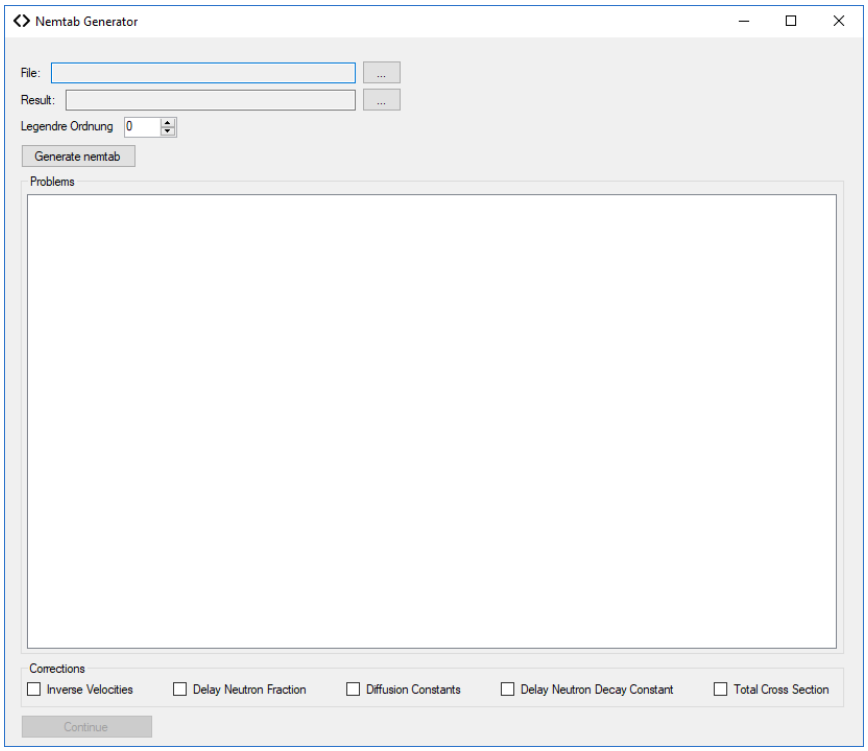

Figure A.4: *Window to create NEMTAB formatted cross sections libraries for calculations with TORT-TD. After providing a Serpent 2 output file and the Legendre order to be used,* C^2 *evaluates the Serpent 2 output and displays the data for all universes found in the lower panel. There the user has the possibility to force a correction of the corrupted data before all files are written to a specified folder.*

provide a Serpent 2 output file and a folder where the files will be written to. C^2 can extract the cross sections to a selectable Legendre order. In the case that the cross section data are corrupted, e.g. null entries of the inverse neutron velocities, delayed neutron fractions, diffusion constants, delayed neutron decay constant or the total cross section, C^2 will show the affected universe and what entry exactly caused the problems. The user has the possibility to set these corrupted entries to 10^{-15} for test case calculations. More sophisticated approaches are discussed in Chapter 6.3.2.2. Figure A.4 shows the window for the creation of the NEMTAB formatted cross section libraries.

D.4 Creation of geometry input for TORT-TD calculations

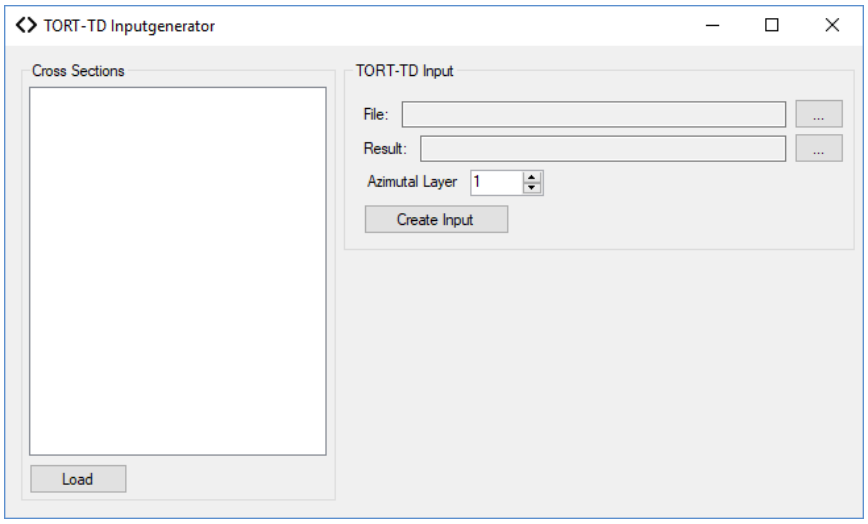

Figure A.5: *Feature of* C^2 *to generate an TORT-TD input desk. First, the file names of the cross sections to be used have to be inserted by the user. In the right panel the input matrix file and the number of azimuthal layers have to be provided by the user. When all data is given,* C^2 *writes the TORT-TD input desk to a specified folder.*

TORT-TD models are rather large files and a lot of pin cells have to be defined in the model. With C^2 the geometry input for TORT-TD can be generated automatically (see Figure A.5). The number of modeled azimuthal layers can be adjusted as well. The user has to write a so-called

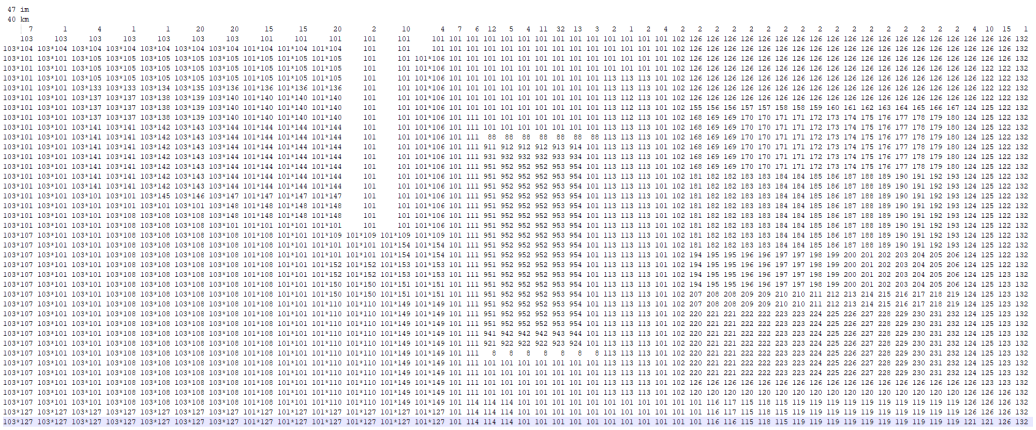

Figure A.6: *Exemplary input Matrix to be used by the TORT-TD input desk generator. If two numbers are provided for one node, a cross section for the controlled and uncontrolled case is defined (see Chapter 6.4.1.4).*

input matrix which links the cross sections to nodes of the computing mesh (see Figure A.6). Also, the horizontal subdivision and the control rods have to be provided. The output can directly be inserted into a TORT-TD model.

D.5 Evaluation of Serpent 2 detectors

The output of Serpent 2 detectors is written in a Matlab format. In order to use the results and to compare Serpent 2 with MCNP6, the data has to be post processed. C^2 first reads the Serpent 2 input desk and saves all defined detectors. After the first initialization step the detector result file is evaluated. With the definition of the mesh tally the volume of each cell can be calculated and together with the raw data, the actual neutron flux can be calculated. After all steps have been performed, the files are saved to a predefined folder. The window used for the evaluation of Serpent 2 detectors is depicted in Figure A.7.

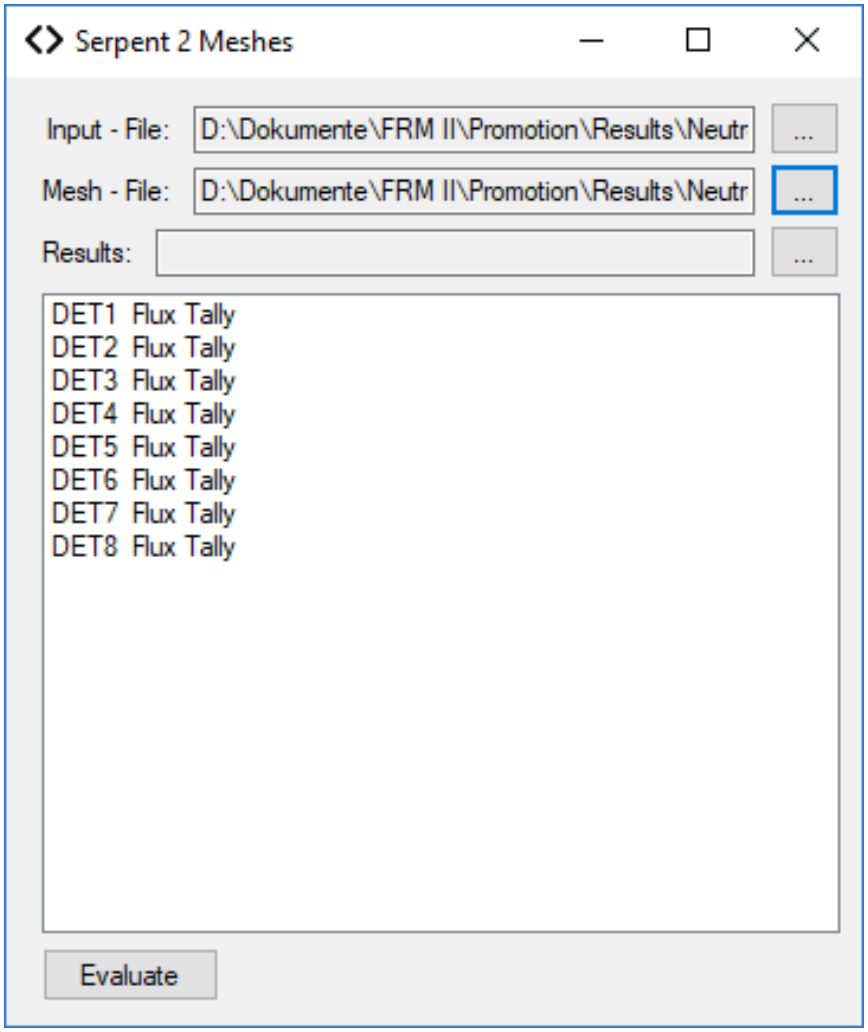

Figure A.7: *Window in C^2 to evaluate Serpent 2 detectors. After providing the Serpent 2 output file and the corresponding input desk C^2 will evaluate and display the stored mesh-tally geometry and data. Also all defined detectors in the input desk are shown to the user.*

D.6 Evaluation of MCNP6 FMESH tallies

Similar to Serpent 2 detectors, MCNP6 FMESH tallies can be evaluated as well (see Chapter D.5). After selecting an MCNP6 input desk and the corresponding output file, C^2 displays the boundary of the FMESH with the defined geometrical structure. C^2 then calculates all needed data of all cells and together with the raw data the values are written on the disc. The window used for the evaluation of MCNP6 FMESH tallies is depicted in Figure A.8.

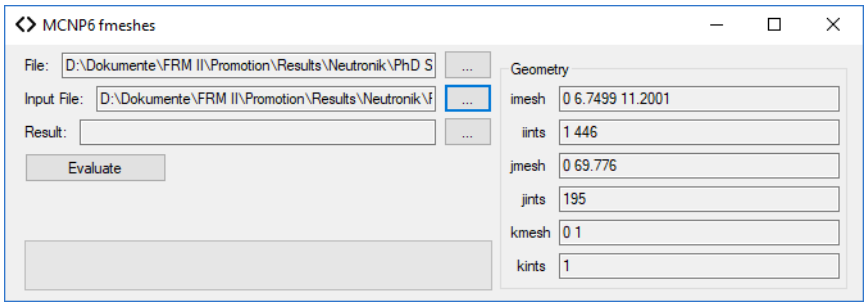

Figure A.8: *Window in C^2 to evaluate MCNP6 fmeshes. After providing the MCNP6 output file and the corresponding input desk C^2 will evaluate and display the stored mesh-tally geometry and data.*

D.7 Evaluation of TORT-TD pinval files

As for Serpent 2 (see Chapter D.5) and MCNP6 (see Chapter D.6), the calculation performed with TORT-TD also has to be evaluated. C^2 provides a module which is able to read the corresponding TORT-TD output files, calculates the geometry of the computational grid and converts all the data to actual real flux and power deposition values. The main control window for this application is shown in Figure A.9.

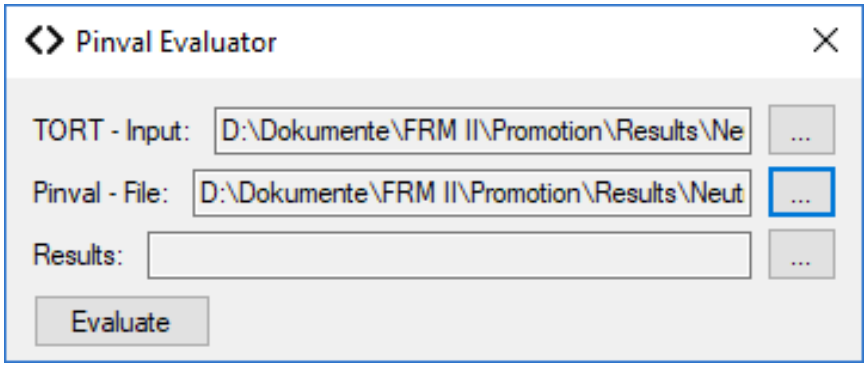

Figure A.9: *Feature of C^2 to evaluate TORT-TD pinval files. By providing a TORT-TD input and the corresponding output, C^2 will evaluate the mesh data for the neutron fluxes and power deposition and write the results to a specified folder.*

D.8 Calculation of the average deviation

C^2 provides a module which is able to calculate the average deviation of a quantity. After providing information regarding the computational mesh and areas which have to be excluded from the analysis, C^2 first visualizes the mesh and then calculates the average deviation and the corresponding standard deviation.The main control window for this application is shown in Figure A.10.

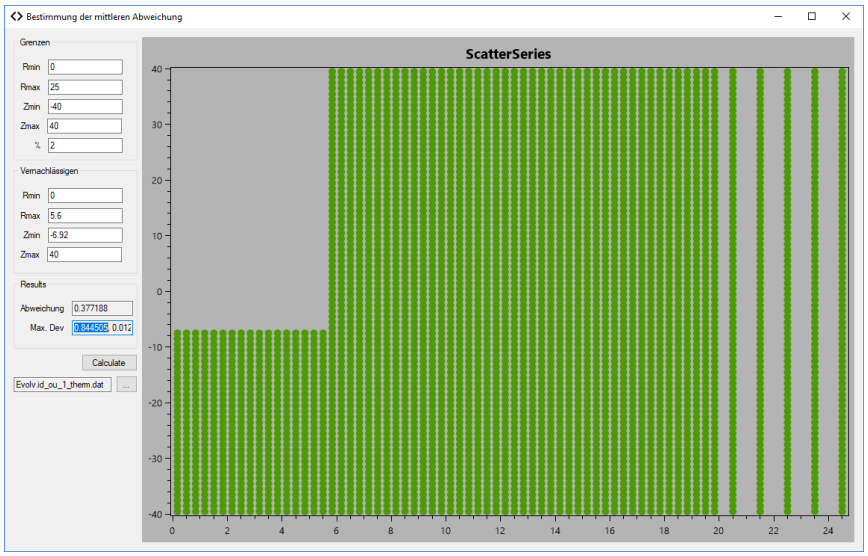

Figure A.10: *Feature of* C^2 *to calculate the average deviation of a distribution. Parts of the geometry can be excluded from the calculation.*

D.9 Calculation of the Pearson's correlation coefficient

In order to check two independent calculations for correlations between them, C^2 can calculate the Pearson's correlation coefficient. With that module one can, for example, check if the statistical error of a MC is correlated to the deviation of the neutron fluxes calculated with two different codes. For this example a .csv file which contains the geometry and both values, viz. flux and uncertainty thereof, have to be provided. For a given area, C^2 then calculates the Pearson's correlation coefficient according to

$$\Xi(\Pi,\Theta) = \frac{\sum_{i=1}^{n}(\Pi_i - \bar{\Pi})(\Theta_i - \bar{\Theta})}{\sqrt{\sum_{i=1}^{n}(\Pi_i - \bar{\Pi})^2 \cdot \sum_{i=1}^{n}(\Theta_i - \bar{\Theta})^2}}, \tag{D.1}$$

and displays the result in the main window. In Figure A.11, the corresponding window in C^2 is depicted.

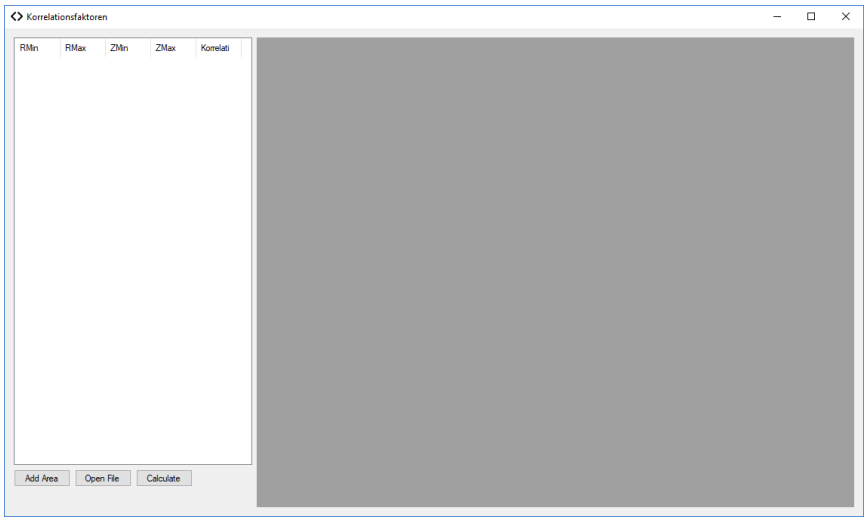

Figure A.11: *Window to calculate the Pearson's correlation coefficient. The user has to provide a .csv file with the geometrical data and both values to be compared. By giving a range of data* C^2 *then calculates the Pearson's correlation coefficient.*

D.10 Calculation of the Power Deposition Distribution for ATHLET

In ATHLET the axial power profile and total power has to be provided for each heated pipe. Therefore, C^2 can read a MCNP6 mesh-tally output and calculate both the power profile and the total power in a specified area. Figure A.12 shows the corresponding window of C^2 where the starting radial and axial coordinate and the area to be investigated has to be inserted.

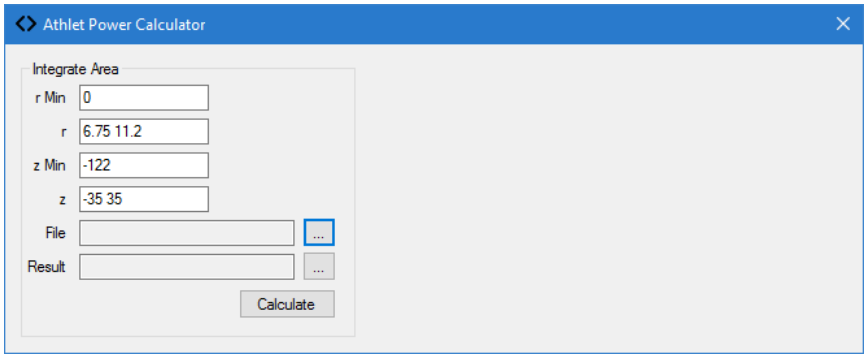

Figure A.12: *Feature of* C^2 *to calculate the needed heating data for an ATHLET input desk. The user has to provide a MCNP6 power deposition output and the area of interest.* C^2 *then calculated the axial power deposition distribution and the integral power deposited within this area.*

D.11 TORT-TD geometry plotter

For debugging of TORT-TD, models it can be useful to visualize the geometry. Hence, C^2 can read the .output.prot file of a TORT-TD calculation, extract the information regarding the geometry and show a simplified plot of the material assignment of the TORT-TD model used.

Figure A.13 shows the corresponding window of C^2 where an arbitrary plot of a TORT-TD geometry is depicted.

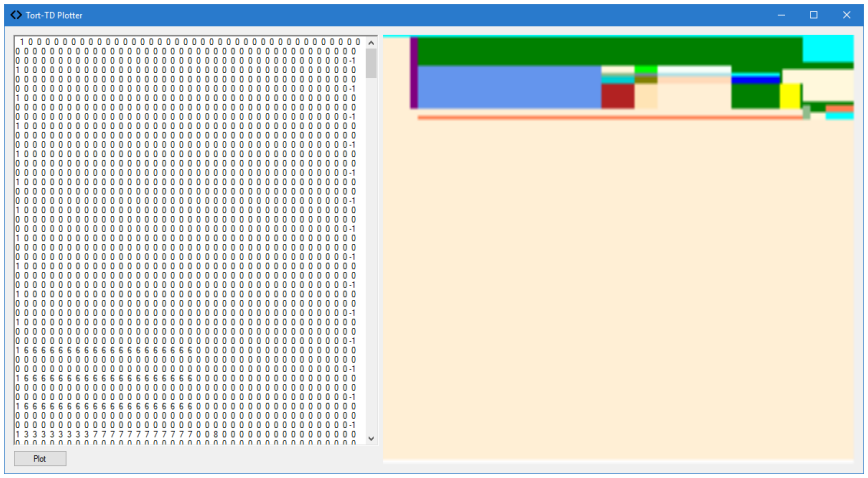

Figure A.13: *Window of the C^2 Tort geometry plotter. By pressing the button "Plot" the user has to provide a TORT-TD output file. Then, the geometry used by TORT-TD is depicted in the right PictureBox.*

D.12 Automated comparison of NEMTAB formatted cross sections

C^2 is able to compare several NEMTAB formatted cross sections. As Figure A.14 shows, the user has to select the files to be compared and C^2 then performs a pairwise alignment of the selected files and shows the result to the user.

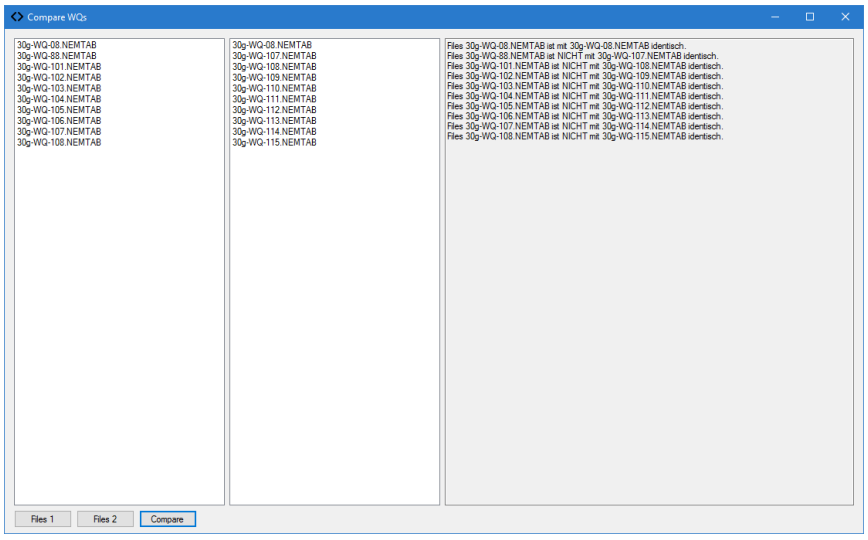

Figure A.14: *Window to compare several cross sections. The left and middle ListView shows the file names of the cross sections to be compared. In the right area the results of the comparison are shown.*

D.13 Automated run of TORT-TD

c^2 can run TORT-TD automatically. The executable and working folder can be adjusted by the user. This feature of c^2 has also the capability to be coupled to the evaluation of Serpent 2 outputs in order to provide an on-the-fly calculation of cross sections. This possibility has not been used within this thesis and needs further testing. As depicted in Figure A.15, the user has to provide an input desk for TORT-TD and a folder where the final results will be copied at the end. The output during the run is mirrored to c^2 as well.

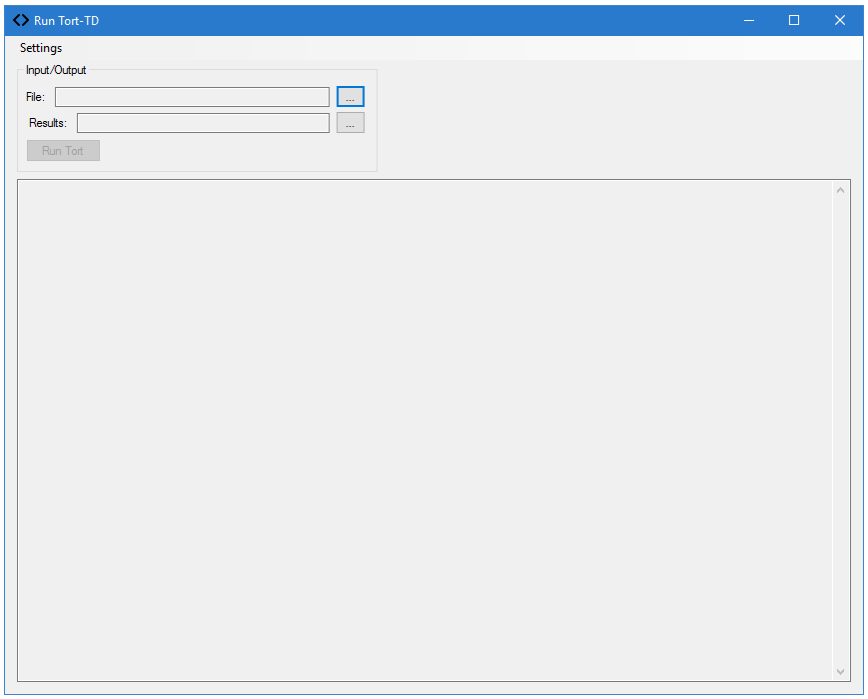

Figure A.15: *Window to run TORT-TD automatically. The user has to provide an input desk for TORT-TD and a folder for the results. All messages from TORT-TD are displayed within this window as well.*

APPENDIX E

Neutron fluxes in areas with poor neutron statistics

Table A.1: *Normalized 30-energy group neutron flux distribution for the four cells/universes, where the statistics using the standard calculation approach is too poor for meaningful results. The second column shows the relative flux normalized to the total neutron flux through the corresponding cell.*

Energy MeV	**Cell 3 (Univ 104)**		**Cell 1 (Univ 103)**		**Cell 17 (Univ 127)**		**Cell 590 (Univ 121)**	
	Absolute per starting particle	normalized	Absolute per starting particle	normalized	Absolute per starting particle	normalized	Absolute per starting particle	normalized
1.00E-10	0.00000E+00	0.00000E+00	3.94221E-12	2.13497E-06	0.00000E+00	0.00000E+00	3.97094E-12	5.02443E-06
1.00E-09	1.33463E-09	4.53314E-04	7.69685E-10	4.16837E-04	8.66186E-12	2.70837E-04	2.96101E-10	3.74657E-04
2.00E-09	4.71002E-09	1.59978E-03	2.90031E-09	1.57071E-03	4.34305E-11	1.35797E-03	9.74722E-10	1.23332E-03
2.50E-09	3.46857E-09	1.17812E-03	2.30979E-09	1.25091E-03	2.62024E-11	8.19289E-04	7.80623E-10	9.87722E-04
3.00E-09	4.38065E-09	1.48791E-03	2.28253E-09	1.23614E-03	3.37947E-11	1.05668E-03	1.30272E-09	1.64833E-03
6.50E-09	5.45413E-08	1.85253E-02	3.22664E-08	1.74744E-02	5.16488E-10	1.61494E-02	1.32427E-08	1.67560E-02
1.00E-08	8.37232E-08	2.84370E-02	5.13498E-08	2.78094E-02	9.67042E-10	3.02372E-02	1.99428E-08	2.52336E-02
3.00E-08	7.66053E-07	2.60194E-01	4.78568E-07	2.59177E-01	7.96927E-09	2.49181E-01	2.01328E-07	2.54740E-01
5.00E-08	7.52119E-07	2.55461E-01	4.72040E-07	2.55642E-01	8.19236E-09	2.56156E-01	2.01671E-07	2.55174E-01
1.00E-07	9.68126E-07	3.28829E-01	6.09769E-07	3.30231E-01	1.04972E-08	3.28223E-01	2.68097E-07	3.39223E-01
1.50E-07	2.41841E-07	8.21426E-02	1.53653E-07	8.32135E-02	2.85907E-09	8.93966E-02	6.66179E-08	8.42916E-02
2.75E-07	5.96718E-08	2.02679E-02	3.88928E-08	2.10631E-02	7.00930E-10	2.19165E-02	1.59650E-08	2.02005E-02
3.38E-07	3.60928E-10	1.22591E-04	2.38225E-10	1.29015E-04	5.80356E-12	1.81464E-04	9.62011E-11	1.21723E-04
4.00E-07	2.03675E-10	6.91793E-05	8.96413E-11	4.85468E-05	1.30208E-11	4.07131E-04	6.06366E-12	7.67235E-06
5.13E-07	2.79382E-11	9.48936E-06	0.00000E+00	0.00000E+00	0.00000E+00	0.00000E+00	5.84389E-13	7.39427E-07
6.25E-07	2.49216E-10	8.46476E-05	1.71430E-11	9.28410E-06	0.00000E+00	0.00000E+00	0.00000E+00	0.00000E+00
1.00E-06	1.43582E-11	4.87684E-06	6.89894E-11	3.73624E-05	0.00000E+00	0.00000E+00	0.00000E+00	0.00000E+00
1.77E-06	1.34346E-10	4.56314E-05	3.81304E-11	2.06502E-05	3.93199E-11	1.22944E-03	0.00000E+00	0.00000E+00
3.00E-06	1.41044E-10	4.79064E-05	2.50871E-11	1.35864E-05	6.13646E-13	1.91873E-05	0.00000E+00	0.00000E+00
1.00E-05	7.27975E-11	2.47261E-05	2.35917E-11	1.27765E-05	0.00000E+00	0.00000E+00	2.69124E-13	3.40523E-07
3.00E-05	7.63588E-11	2.59357E-05	7.31280E-11	3.96038E-05	4.06449E-12	1.27087E-04	0.00000E+00	0.00000E+00
1.00E-04	5.72E-11	1.94444E-05	7.70E-11	4.17020E-05	1.40E-11	4.36338E-04	0.00E+00	0.00000E+00
3.00E-03	4.87E-10	1.65261E-04	1.11E-10	6.00382E-05	1.14E-11	3.57768E-04	0.00E+00	0.00000E+00
1.00E-01	4.78E-10	1.62223E-04	1.90E-10	1.03029E-04	6.81E-11	2.12816E-03	0.00E+00	0.00000E+00
9.00E-01	8.79E-10	2.98531E-04	3.16E-10	1.71346E-04	2.37E-12	7.42236E-05	4.99E-13	6.30947E-07
1.35E+00	6.26E-11	2.12493E-05	2.73E-12	1.47836E-06	0.00E+00	0.00000E+00	3.05E-14	3.86283E-08
1.85E+00	2.24E-10	7.59235E-05	9.45E-11	5.11675E-05	0.00E+00	0.00000E+00	0.00E+00	0.00000E+00
3.00E+00	4.03E-10	1.37004E-04	1.10E-10	5.97848E-05	0.00E+00	0.00000E+00	0.00E+00	0.00000E+00
4.00E+00	5.37E-11	1.82504E-05	5.10E-11	2.76342E-05	8.76E-12	2.74042E-04	0.00E+00	0.00000E+00
2.00E+01	2.66E-10	9.03579E-05	1.59E-10	8.58943E-05	0.00E+00	0.00000E+00	3.72E-13	4.70821E-07

Table A.2: *Normalized 30-energy group neutron flux distribution for the four cells/universes, where the statistics using the standard calculation approach is too poor for meaningful results. The second column shows the relative flux normalized to the total neutron flux through the corresponding cell.*

Energy MeV	**Cell 15 (Univ 110)**		**Cell 616 (Univ 149)**		**Cell 617 (Univ 150)**		**Cell 618 (Univ 151)**	
	Absolute per starting particle	normalized	Absolute per starting particle	normalized	Absolute per starting particle	normalized	Absolute per starting particle	normalized
1.00E-10	0.00000E+00	0.00000E+00	1.05481E-13	2.20540E-09	1.67352E-16	4.16909E-13	4.42529E-13	1.05894E-09
1.00E-09	1.33152E-12	2.92323E-08	3.12280E-11	6.52917E-07	1.97188E-11	4.91237E-08	5.38450E-11	1.28847E-07
2.00E-09	7.73498E-12	1.69815E-07	1.75397E-10	3.66721E-06	1.15731E-10	2.88310E-07	2.65626E-10	6.35622E-07
2.50E-09	1.22120E-11	2.68103E-07	1.71050E-10	3.57632E-06	1.18856E-10	2.96095E-07	2.60240E-10	6.22734E-07
3.00E-09	1.12786E-11	2.47612E-07	2.19101E-10	4.58098E-06	1.65420E-10	4.12096E-07	3.69754E-10	8.84792E-07
6.50E-09	2.45117E-10	5.38132E-06	3.97073E-09	8.30202E-05	3.01531E-09	7.51177E-06	6.50904E-09	1.55756E-05
1.00E-08	5.06163E-10	1.11124E-05	7.99295E-09	1.67117E-04	5.64880E-09	1.40724E-05	1.24816E-08	2.98675E-05
3.00E-08	1.15570E-08	2.53724E-04	1.28775E-07	2.69243E-03	9.89704E-08	2.46556E-04	2.10415E-07	5.03506E-04
5.00E-08	2.51521E-08	5.52192E-04	1.95478E-07	4.08706E-03	1.64465E-07	4.09717E-04	3.48410E-07	8.33718E-04
1.00E-07	7.45550E-08	1.63679E-03	3.94498E-07	8.24818E-03	4.33528E-07	1.08001E-03	9.51100E-07	2.27591E-03
1.50E-07	5.11078E-08	1.12203E-03	1.84982E-07	3.86761E-03	3.29245E-07	8.20219E-04	7.36769E-07	1.76303E-03
2.75E-07	7.18482E-08	1.57736E-03	1.87923E-07	3.92910E-03	5.76380E-07	1.43588E-03	1.25205E-06	2.99606E-03
3.38E-07	2.57861E-08	5.66111E-04	5.91053E-08	1.23578E-03	2.20473E-07	5.49245E-04	4.63458E-07	1.10902E-03
4.00E-07	2.11631E-08	4.64617E-04	4.94484E-08	1.03387E-03	1.84048E-07	4.58502E-04	3.94945E-07	9.45072E-04
5.13E-07	3.08409E-08	6.77084E-04	7.36433E-08	1.53974E-03	2.70034E-07	6.72712E-04	5.94794E-07	1.42330E-03
6.25E-07	2.15514E-08	4.73142E-04	5.40433E-08	1.12994E-03	1.88410E-07	4.69369E-04	4.43281E-07	1.06074E-03
1.00E-06	2.23402E-08	4.90459E-04	6.95163E-08	1.45345E-03	1.99181E-07	4.96202E-04	5.64882E-07	1.35172E-03
1.77E-06	3.15871E-08	6.93466E-04	7.76468E-08	1.62344E-03	2.77349E-07	6.90935E-04	6.45561E-07	1.54478E-03
3.00E-06	2.96761E-08	6.51512E-04	6.74362E-08	1.40996E-03	2.60381E-07	6.48664E-04	5.65786E-07	1.35388E-03
1.00E-05	3.03809E-07	6.66985E-03	4.20027E-07	8.78195E-03	2.58226E-06	6.43295E-03	3.53154E-06	8.45070E-03
3.00E-05	1.02727E-06	2.25528E-02	1.13527E-06	2.37363E-02	8.76830E-06	2.18437E-02	9.70635E-06	2.32265E-02
1.00E-04	1.08455E-06	2.38103E-02	1.20211E-06	2.51338E-02	9.34772E-06	2.32871E-02	1.03865E-05	2.48541E-02
3.00E-03	4.51529E-06	9.91291E-02	4.86546E-06	1.01727E-01	3.92978E-05	9.78991E-02	4.27921E-05	1.02398E-01
1.00E-01	9.59851E-06	2.10727E-01	9.56647E-06	2.00016E-01	8.42646E-05	2.09921E-01	8.46441E-05	2.02547E-01
9.00E-01	1.53696E-05	3.37426E-01	1.53147E-05	3.20201E-01	1.36299E-04	3.39550E-01	1.36624E-04	3.26930E-01
1.35E+00	3.91103E-06	8.58631E-02	3.96311E-06	8.28609E-02	3.47510E-05	8.65721E-02	3.54321E-05	8.47862E-02
1.85E+00	2.85855E-06	6.27569E-02	2.95966E-06	6.18807E-02	2.55066E-05	6.35423E-02	2.64734E-05	6.33488E-02
3.00E+00	3.60296E-06	7.90997E-02	3.79735E-06	7.93952E-02	3.20796E-05	7.99170E-02	3.39859E-05	8.13256E-02
4.00E+00	1.40449E-06	3.08343E-02	1.49329E-06	3.12218E-02	1.24639E-05	3.10502E-02	1.33121E-05	3.18548E-02
2.00E+01	1.45557E-06	3.19557E-02	1.55596E-06	3.25321E-02	1.28389E-05	3.19844E-02	1.38198E-05	3.30697E-02

Table A.3: *Normalized 30-energy group neutron flux distribution for the three cells/universes, where the statistics using the standard calculation approach is too poor for meaningful results. The second column shows the relative flux normalized to the total neutron flux through the corresponding cell.*

Energy MeV	**Cell 619 (Univ 152)**		**Cell 620 (Univ 153)**		**Cell 621 (Univ 154)**	
	Absolute per starting particle	normalized	Absolute per starting particle	normalized	Absolute per starting particle	normalized
1.00E-10	0.00000E+00	0.00000E+00	7.76307E-14	1.42898E-10	6.41663E-08	1.00280E-09
1.00E-09	1.28808E-10	2.44304E-07	5.21106E-11	9.59222E-08	4.00329E-05	6.25637E-07
2.00E-09	5.60729E-10	1.06351E-06	3.32141E-10	6.11386E-07	2.14103E-04	3.34602E-06
2.50E-09	5.53098E-10	1.04904E-06	4.44149E-10	8.17564E-07	2.52173E-04	3.94098E-06
3.00E-09	7.30486E-10	1.38548E-06	4.84910E-10	8.92595E-07	3.04616E-04	4.76056E-06
6.50E-09	1.31943E-08	2.50250E-05	8.89188E-09	1.63677E-05	5.45511E-03	8.52528E-05
1.00E-08	2.65048E-08	5.02705E-05	1.68603E-08	3.10355E-05	1.01893E-02	1.59239E-04
3.00E-08	4.32206E-07	8.19746E-04	3.08726E-07	5.68285E-04	1.61698E-01	2.52703E-03
5.00E-08	6.67344E-07	1.26572E-03	5.20605E-07	9.58300E-04	2.41661E-01	3.77669E-03
1.00E-07	1.48266E-06	2.81210E-03	1.41821E-06	2.61056E-03	5.28484E-01	8.25918E-03
1.50E-07	8.93396E-07	1.69446E-03	1.08622E-06	1.99945E-03	3.11961E-01	4.87535E-03
2.75E-07	1.26585E-06	2.40088E-03	1.79319E-06	3.30080E-03	4.18761E-01	6.54442E-03
3.38E-07	4.49967E-07	8.53433E-04	6.58216E-07	1.21161E-03	1.42403E-01	2.22548E-03
4.00E-07	3.59977E-07	6.82753E-04	5.47566E-07	1.00793E-03	1.15743E-01	1.80884E-03
5.13E-07	5.31752E-07	1.00855E-03	8.42381E-07	1.55061E-03	1.72485E-01	2.69561E-03
6.25E-07	3.77614E-07	7.16204E-04	6.17978E-07	1.13754E-03	1.28477E-01	2.00785E-03
1.00E-06	4.19031E-07	7.94758E-04	7.68590E-07	1.41478E-03	1.67785E-01	2.62215E-03
1.77E-06	5.30737E-07	1.00663E-03	8.75285E-07	1.61118E-03	1.86208E-01	2.91007E-03
3.00E-06	4.91190E-07	9.31618E-04	7.64725E-07	1.40766E-03	1.66031E-01	2.59474E-03
1.00E-05	4.09897E-06	7.77434E-03	4.93739E-06	9.08847E-03	8.83058E-01	1.38005E-02
3.00E-05	1.26079E-05	2.39128E-02	1.34019E-05	2.46695E-02	1.89368E+00	2.95946E-02
1.00E-04	1.32866E-05	2.52001E-02	1.42346E-05	2.62022E-02	2.03630E+00	3.18234E-02
3.00E-03	5.39308E-05	1.02288E-01	5.71350E-05	1.05171E-01	7.74413E+00	1.21026E-01
1.00E-01	1.08553E-04	2.05888E-01	1.08720E-04	2.00126E-01	1.23383E+01	1.92824E-01
9.00E-01	1.73426E-04	3.28929E-01	1.74128E-04	3.20525E-01	1.83091E+01	2.86136E-01
1.35E+00	4.47314E-05	8.48401E-02	4.56990E-05	8.41201E-02	4.88402E+00	7.63278E-02
1.85E+00	3.33255E-05	6.32070E-02	3.46200E-05	6.37265E-02	3.88986E+00	6.07910E-02
3.00E+00	4.21471E-05	7.99385E-02	4.45708E-05	8.20434E-02	5.13002E+00	8.01723E-02
4.00E+00	1.63356E-05	3.09830E-02	1.74106E-05	3.20484E-02	2.01340E+00	3.14655E-02
2.00E+01	1.68575E-05	3.19729E-02	1.81727E-05	3.34513E-02	2.10743E+00	3.29351E-02

APPENDIX F

Fitting parameters

F.1 Fitting parameters U_3Si_2 reactivity accident

Table A.1: *Correlation matrix for U_3Si_2 reactivity accident: Absolute power (see Eq. 10.1).*

	y_0	A_1	t_1
y_0	1	-0.91035	-0.88802
A_1	-0.91035	1	0.99792
t_1	-0.88802	0.99792	1

Table A.2: *Correlation matrix for U_3Si_2 reactivity accident: Reactor period (see Eq. 10.2).*

	Intercept	Slope
Intercept	1	-0.99122
Slope	-0.99122	1

Table A.3: *Correlation matrix for U_3Si_2 reactivity accident: Relative power (see Eq. 10.3).*

	y_0	A_1	t_1
y_0	1	-0.91035	-0.88802
A_1	-0.91035	1	0.99792
t_1	-0.88802	0.99792	1

Table A.4: *Correlation matrix for U_3Si_2 reactivity accident: Outlet coolant temperature (see Eq. 10.4).*

	y_0	A_1	t_1
y_0	1	-0.86313	-0.84046
A_1	-0.86313	1	0.99792
t_1	-0.84046	0.99792	1

F.2 Fitting parameters U_3Si_2 emergency power

Table A.5: *Correlation matrix for U_3Si_2 emergency power case: Central channel mass flow (see Eq. 10.5).*

	y_0	A_1	t_1
y_0	1	0.81888	-0.96527
A_1	0.81888	1	-0.93379
t_1	-0.96527	-0.93379	1

Table A.6: *Correlation matrix for U_3Si_2 emergency power case: Outlet coolant temperature (see Eq. 10.6).*

	y_0	A_1	t_1
y_0	1	-0.99979	-0.9985
A_1	-0.99979	1	0.99939
t_1	-0.9985	0.99939	1

F.3 Fitting parameters UMo reactivity accident

Table A.7: *Correlation matrix for UMo reactivity accident: Absolute power (see Eq. 10.1).*

	y_0	A_1	t_1
y_0	1	-0.89644	-0.87604
A_1	-0.89644	1	0.99847
t_1	-0.87604	0.99847	1

Table A.8: *Correlation matrix for UMo reactivity accident: Reactor period (see Eq. 10.2).*

	Intercept	Slope
Intercept	1	-0.98954
Slope	-0.98954	1

Table A.9: *Correlation matrix for UMo reactivity accident: Relative power (see Eq. 10.3).*

	y_0	A_1	t_1
y_0	1	-0.89644	-0.87605
A_1	-0.89644	1	0.99847
t_1	-0.87605	0.99847	1

Table A.10: *Correlation matrix for UMo reactivity accident: Outlet coolant temperature (see Eq. 10.4).*

	y_0	A_1	t_1
y_0	1	-0.74283	-0.70923
A_1	-0.74283	1	0.99627
t_1	-0.70923	0.99627	1

F.4 Fitting parameters UMo emergency power

Table A.11: *Correlation matrix for UMo emergency power case: Central channel mass flow (see Eq. 10.11).*

	y_0	A_1	t_1
y_0	1	0.82578	-0.96858
A_1	0.82578	1	-0.93414
t_1	-0.96858	-0.93414	1

Table A.12: *Correlation matrix for UMo emergency case: Power outlet coolant temperature (see Eq. 10.12).*

	y_0	A_1	t_1
y_0	1	-0.99987	-0.9989
A_1	-0.99987	1	0.9995
t_1	-0.9989	0.9995	1

BOL Begin Of Life

BWR Boiling Water Reactor

CMM Cumulative Migration Method

CTM Concentric tubes model

ENDF/B Evaluated Nuclear Data File

EOL End Of Life

ERANOS European Reactor Analysis Optimized calculation System

FRM II Forschungs-Neutronenquelle Heinz Maier-Leibnitz

FRM Forschungsreaktor München

GET Generalized Equivalence Theory

GRS Gesellschaft für Anlagen- und Reaktorsicherheit gGmbH

HEU highly enriched uranium

HFR High Flux Reactor

HFIR High Flux Isotope Reactor

Institut Laue-Langevin Institut Laue-Langevin

IQS Improved Quasi-Static

LANL Los Alamos National Laboratory

LOCA Loss of coolant accident

MMFZ Material mixed fuel zone model

MC Monte Carlo

ODE Ordinary Differential Equation

OISM Original model with involute shaped fuel plates

ORNL Oak Ridge National Laboratory

PK Point Kinetics

PWR Pressurized Water Reactor

QS Quasi-Static

RBMK High Power Channel-type Reactor

TFO Thermo-Fluiddynamic Object

TMS Target Motion Sampling

TUM Technische Universität München

VSM Vertical stack model

VSM1 Vertical stack model with one explicit modeled, reduced fuel disc in the core–midplane

VSM2m Vertical stack model with two material mixed, reduced fuel disc at the top and bottom of the fuel zone

VSM2 Vertical stack model with two explicit modeled, reduced fuel disc at the top and bottom of the fuel zone

VTT Technical Research Center of Finland

List of Figures

List of Tables

Own Publications

The following own publications are related to this work:

- **First steps towards a coupled code system for transient calculations**
  Christian Reiter, Harald Breitkreutz, Anton Röhrmoser, Winfried Petry,
  presented at the Proceedings of the European Research Reactor Conference (RRFM), 2016, Berlin, Germany
- **First steps towards a coupled code system for transient calculations**
  Christian Reiter, Harald Breitkreutz, Anton Röhrmoser, Winfried Petry,
  Proceedings of Physics of Reactors (Physor), Vol 1, 2016, pp. 4009-40019, ISBN: 978-1-5108-2573-4
- **High precision neutronic calculations for transient simulations for FRM II**
  Christian Reiter, Harald Breitkreutz, Anton Röhrmoser, Armin Seubert, Winfried Petry,
  presented at the Proceedings of the European Research Reactor Conference (RRFM), 2017, Rotterdam, Netherlands
- **High precision neutronic calculations for transient simulations for FRM II**
  Christian Reiter, Harald Breitkreutz, Anton Röhrmoser, Armin Seubert, Winfried Petry,
  presented at the Proceedings of the Physics of Reactors (Physor), 2018, Cancun, Mexico
- **Deterministic neutronic calculations for transient simulations for FRM II**
  Christian Reiter, Harald Breitkreutz, Anton Röhrmoser, Armin Seubert, Winfried Petry,
  To be published in Nuclear Physics B

Acknowledgements

The completion of this thesis would not have been possible without the support and guidance of many people. They all contributed to this work, and I would like to show my gratitude in the following:

- Prof. Petry for providing me the opportunity to do this work, for his constant support, timely suggestions, and for giving me the confidence and freedom for my scientific work.
- Prof. Macián-Juan for his manifold advice and the discussions during my work.
- Dr. Harald Breitkreutz for being my mentor, for all his time, a lot of very good advice, very fruitful discussions, proofreading my thesis, becoming a good friend and just for everything.
- Dr. Armin Seubert for the supervision, all the lengthy discussions and for pointing out all the subtle mistakes that happened during this work and, most important, for his help with TORT-TD.
- Dr. Anton Röhrmoser for his kind interest on me at every stage of my research. His inspirations and enthusiasm have enabled me to complete my thesis.
- Thomas Voggenberger, Georg Lerchl and Dr. Fabian Weyermann for their help with ATHLET.
- Prof. Morkel for introducing me into reactor physics and for the awakening of my interest to work in this field.
- Tobias Chemnitz for supporting me, especially during the hard times, for all discussions during the coffee breaks and for being a friend.
- Wesley McCollough for proofreading my work, improving my English a lot and for becoming a friend.
- My colleagues Bruno Baumeister, Korbinian Faust, Thomas Kerschl, Andreas Ofner, Serhat Polat, Kaltrina Shehu, Christian Schwarz and Christian Steyer for the enjoyable time in the office.
- My very good friends Tobias Griesmeier, Florian Huber, Ludwig Schloder, Alexander Schnabl and Oliver Schug for supporting me over the years, no matter when and where.
- My family, Katharina Reiter, Waltraud Reiter and Dr. Johann Reiter for backing me up all the time. Without their constant help it would have been so much harder to complete this work. Especially, I want to thank my father for proofreading my work several times, and so many advices, ideas and discussions.
- My wife Lilly for her great support over the years, for patiently waiting until this work has been completed and for accepting to be without me on so many evenings. Thank you for everything!

Bibliography

[1] H. Anglart, editor. *Reactor Kinetics and Reactor Operation*, Lectures on Applied Reactor Technology and Nuclear Power Safety, Lecture No 5, 2005.

[2] Ansys CFX. Solver theory guide, Ansys Inc. *Release*, 15, 2013.

[3] H. Austregesilo and et al. *ATHLET 3.1A Models and Methods*, 2016. Gesellschaft für Anlagen- und Reaktorsicherheit (GRS) gGmbH.

[4] Y. Azmy and E. Sartori. *Nuclear Computational Science: A Century in Review*. Springer Netherlands, s.l., 1. aufl. edition, 2010.

[5] B. Becker, R. Dagan, and G. Lohnert. Proof and implementation of the stochastic formula for ideal gas, energy dependent scattering kernel. *Annals of Nuclear Energy*, 36(4):470–474, 2009.

[6] J. Becker. *Thermal-hydraulic influence of manufacturing tolerances of involute shaped fuel plates*. Master thesis, Technische Universität München, München, 2017.

[7] R. B. Bird, W. E. Stewart, and E. N. Lightfoot. *Transport phenomena*. Wiley, New York, 2007.

[8] C. Bogenberger. *Assessment of the Usability of TRACE for Compact Core Transient Simulations*. Semester work, Technische Universität München, München, 2009.

[9] H. Breitkreutz. Acceptable limits for the multiplication factor: oral, 10.06.2018.

[10] H. Breitkreutz. *Coupled Neutronic and Thermal Hydraulics of High Density Cores for FRM II*. Dissertation, Technische Universität München, München, 2011.

[11] H. Breitkreutz, editor. *Introduction to Monte Carlo in Particle Physics*, Reaktorphysik II - Reaktorberechnung und Reaktorkonzepte, 28.05., 2015.

[12] H. Breitkreutz, A. Röhrmoser, and W. Petry, editors. *Influence of depleted Molybdenum on monolithic UMo fuel plate designs for FRM II*, RRFM, Ljubljana, Slovenia, 2014.

[13] F. B. Brown and M. E. Rising, editors. *Verification of MCNP6.1, MCNP6.1.1, and MCNP6.2-pre for criticality safety applications*, ANS Winter Meeting, 2016.

[14] J. S. Bull. Mcnp: Current capabilities and future plans, 2005.

[15] B. G. Carlson and G. I. Bell, editors. *Solution of the Transport Equation by the S_N Method*, 1958.

[16] M. Däubler. *New Approach to Saftey Analysis of FRM˜II.* Diploma thesis, Technische Universität München, München, 2012.

[17] B. Davison and J. B. Sykes. *Neutron transport theory.* International series of monographs on physics. Clarendon Pr, Oxford, reprinted. edition, 1958.

[18] C. Dean, R. Perry, R. Neal, and A. Kyrieleis. Validation of run-time doppler broadening in monk with jeff3.1. *Journal of the Korean Physical Society*, 59(23):1162, 2011.

[19] C. Döderlein. *Untersuchungen zur Kühlbarkeit eines kompakten Reaktorkerns mit evolventenförmigen Brennstoffplatten.* Diploma thesis, Technische Universität München, München, 1989.

[20] C. Döderlein. *Kinetik und Dynamik eines Forschungsreaktors mit einem reflektierten Kompaktkern.* Dissertation, Technische Universität München, München, 1995.

[21] J. Doriath and et al., editors. *ERANOS1: the Advanced European System of Codes for Reactor Physics*, Mathematical Methods and Supercomputing in Nuclear Applications, Karlsruhe, Germany, 1993.

[22] T. Downar, D. Lee, Y. Xu, Kozlowski T., and Staudenmier J. Parcs v2.6 u.s. nrc core neutronics simulator - theory manual.

[23] J. J. Duderstadt and L. J. Hamilton. *Nuclear reactor analysis.* Wiley, New York, 1976.

[24] D. Emendörfer and K.-H. Höcker. *Theorie der Kernreaktoren: Band 1 Der stationäre Reaktor*, volume 1. B.I.-Wissenschaftsverlag, 2 edition, 1982.

[25] Feltes and Sperber. *Störfallverhalten bei langsam ablaufenden Reaktivitätstransienten: 2B 0520.0010.* Siemens AG - Bereich Energieerzeugung (KWU), 1997.

[26] J. E. Gentle. *Random number generation and Monte Carlo methods.* Statistics and computing. Springer, New York, 2. ed., corr. 2. print edition, 2005.

[27] Gesellschaft für Anlagen- und Reaktorsicherheit (GRS) gGmbH. Athlet - mod 3.1 cycle a - program overview.

[28] V. Gnielinski. Neue Gleichungen für den Wärme- und den Stoffübergang in turbulent durchströmten Rohren und Kanälen. *Forschung im Ingenieurwesen*, 41(1):8–16, 1975.

[29] P. Grechanuk, M. E. Rising, F. B. Brown, and T. S. Palmer. Semi-analytical benchmarks for mcnp6.

[30] Gysler, Sperber, and Ehrich, editors. *Thermohydraulische Kernauslegung 2B 0320.0007*, Siemens AG - Bereich Energieerzeugung (KWU), 1996.

[31] G. Heideker. *Investigation of Fluid Flow Behaviour at the Particle Filter Element of the FRM II Core.* Semesterarbeit, Technische Universität München, München, 2012.

[32] Heinecke and Sperber, editors. *Leistungsstörfall durch Regelstabfehlfahren*, Siemens AG - Bereich Energieerzeugung (KWU), 1997.

[33] D. L. Hetrick. *Dynamics of nuclear reactors.* American Nuclear Society, La Grange Park, 1993.

[34] T. K. Huber. *Thermal Conductivity of High-Density Uranium-Molybdenum Fuels for Research Reactors.* Dissertation, Technische Universität München, München, 2015.

[35] I. E. Idelčik. *Handbook of hydraulic resistance.* Jaico Publ. House, Mumbai, 3. ed., 6. jaico impression edition, 2008.

[36] P. Ihle, H. Politzky, and H. Mahlang. *Experimentelle und rechnerische Untersuchungen zum Betriebsverhalten des Brennelementes des HFR Grenoble.* Forschungsbericht, Kernforschungszentrum Karlsruhe, 1975.

[37] K. Ivanov, editor. *NucE 521 - Neutron Transport Theory*, 2010.

[38] Julian Becker. *Simulation der gesamten Platte mit Hinblick auf radiale Unterteilungen.* Forschungsbericht, FRM II, 2017.

[39] K. Kabus, B. Alber-Laukant, F. Weidermann, F. Rieg, G. Engelken, and R. Hackenschmidt. *Decker Maschinenelemente - Formeln.* Carl Hanser Verlag GmbH & Co. KG, München, 8., neu bearbeitete auflage edition, 2018.

[40] Karrasch, editor. *Beschreibung des Programms DUST, Version 1.0*, KWU NDS1/95/2524, 1995.

[41] Karrasch, editor. *Validation des Programms DUST, Version 1.0*, KWU NDS1/95/2528, 1995.

[42] Karrasch, editor. *Primärdurchsatzreduktion durch 25 cm^2 Leck*, KWU NDS1/97/2030, 1997.

[43] A. Kastenmüller. Regelstabgeschwindigkeit: E-Mail, 23.10.2018.

[44] L. D. Landau and E. M. Lifshitz. *Fluid Mechanics: Landau and Lifshitz: Course of Theoretical Physics, Volume 6.* Elsevier Reference Monographs, s.l., 2. aufl. edition, 2013.

[45] C. Lemieux. *Monte Carlo and quasi-Monte Carlo sampling.* Springer Series in Statistics. Springer, New York, NY, 2009.

[46] J. Leppänen. Serpent – a continuous-energy monte carlo reactor physics burnup calculation code: User manual.

[47] J. Leppänen. Energy Calculation with Serpent 2: E-Mail, 05.01.2016.

[48] J. Leppänen. Problem with Beryllium: E-Mail, 11.08.2015.

[49] J. Leppänen. *Development of a New Monte Carlo Monte Carlo Reactor Physics Code.* Dissertation, Helsinki University of Technology, 2007.

[50] J. Leppänen. Performance of woodcock delta-tracking in lattice physics applications using the serpent monte carlo reactor physics burnup calculation code. *Annals of Nuclear Energy*, 37(5):715–722, 2010.

[51] J. Leppänen, M. Pusa, and E. Fridman. Overview of methodology for spatial homogenization in the Serpent 2 Monte Carlo code. *Annals of Nuclear Energy*, 96:126–136, 2016.

[52] J. Leppänen, M. Pusa, T. Viitanen, V. Valtavirta, and T. Kaltiaisenaho. The serpent monte carlo code: Status, development and applications in 2013. *Annals of Nuclear Energy*, 82:142–150, 2015.

[53] Z. Liu, K. Smith, B. Forget, and J. Ortensi. Cumulative migration method for computing rigorous diffusion coefficients and transport cross sections from Monte Carlo. *Annals of Nuclear Energy*, 112:507–516, 2018.

[54] R. Mosteller and R. C. Little, editors. *Impact of MCNP Unresolved Resonance Probability TableTreatment on Uranium and Plutonium Benchmarks*, 1999.

[55] C. Nam Zin. Fundamentals and recent developments of reactor physics methods. *Nuclear Engineering and Technology*, 37:25–78, 2005.

[56] K. O. Ott and R. J. Neuhold. *Introductory nuclear reactor dynamics*. American Nuclear Society, La Grange Park - Ill, 1985.

[57] A. Papukchiev, G. Lerchl, C. Waata, and T. Frank, editors. *Extension of the Simulation Capabilities of the 1D System Code ATHLET by Coupling with the 3D CFD Software Package ANSYS CFX*, 2009.

[58] A. Pautz. *Rechenmodellentwicklung für die Analyse von Reaktivitätstransienten mit Neutronentransporttheorie und gekoppelter Thermofluiddynamik für Hochfluss-Forschungsreaktoren*. Dissertation, Technische Universität München, München, 2001.

[59] Pelowitz D.B. and et al. *MCNP6 User's Manual*. LANL, 2013.

[60] Y. V. Petrov, M. S. Onegin, K. Böning, and M. Nuding. *Heterogeneous Calculations of FRM II*. Forschungsbericht, Department of Theoretical Physics, Petersburg, 2001.

[61] B. S. Petukhov. Heat transfer and friction in turbulent pipe flow with variable physical properties. In J. P. Harnett and T. F. Irvine, editors, *Advances in heat transfer*, volume 6 of *Advances in Heat Transfer*, pages 503–564. Academic Press, New York and London, 1970.

[62] A. Pöpperl. *Erstellung eines ATHLET-Datensatzes für die Darstellung des Primärkühlsystems des FRM-II zur Beschreibung stationärer und transienter Betriebszustände*. Diplomarbeit, Technische Universität München, München, 2001.

[63] C. Rabiti. *Modeling of fast neutron transients in an accelerator driven system*. Dissertation, Universität Stuttgart, Stuttgart, 2006.

[64] C. Reiter, H. Breitkreutz, A. Röhrmoser, and W. Petry, editors. *First steps towards a coupled code system for transient calculations for FRM II*, Physor, Sun Valley, USA, 2016.

[65] P. Reuss. *Neutron physics*. Nuclear engineering. EDP Sciences, Les Ulis France, 2008.

[66] W. A. Rhoades and R. L. Childs. TORT: A Three-Dimensional Discrete Ordinates Neutron/Photon Transport Code. *Nuclear Science and Engineering*, 107(4):397–398, 1991.

[67] W. A. Rhoades and D. B. Simpson. The TORT three-dimensional discrete ordinates neutron/photon transport code.

[68] J. Rhodes, K. Smith, and D. Lee, editors. *CASMO-5 Development and Applications*, 2006.

[69] A. Rineiski and J. Doriath, editors. *KIN3D - A Module that Extends Capabilities of the TGV2 Code for Solving the Time-Dependent Diffusion and Transport Equation*, 1996.

[70] A. Röhrmoser. *Untersuchungen zur Kühlbarkeit eines neuartigen Kompaktkerns für Forschungsreaktoren.* Diploma thesis, Technische Universität München, München, 1984.

[71] A. Röhrmoser. *Neutronenphysikalische Optimierung und Auslegung eines Forschungsreaktors mittlerer Leistung mit Zielrichtung auf einen hohen Fluss für Strahlrohrexperimente.* Dissertation, Technische Universität München, München, 1991.

[72] A. Röhrmoser, editor. *New burnup balculations*, RERTR, Lisbon, Portugal, 2010.

[73] A. Röhrmoser, editor. *Flat reactivity operation course when converting FRM II*, RRFM, Berlin, Germany, 2016.

[74] A. Röhrmoser, editor. *Smallest thinkable LEU Elements for FRM II with most progressive and also most conservative fuel options*, RERTR, Edinburgh, Scotland, 2018.

[75] R. Y. Rubinstein. *Simulation and the Monte Carlo Method.* Wiley Series in Probability and Statistics. Wiley, Newark, 3rd ed. edition, 2016.

[76] A. Seubert, editor. *Pin cell discontinuity factors in the transient discrete ordinates code TORT-TD*, Physor, Pittsburgh, PA, USA, 2010.

[77] A. Seubert, A. Pautz, M. Becker, and R. Dagan. *Time-dependent anisotropic external sources in transient 3-D transport code TORT-TD.* Inforum Verlag, Germany, 2009.

[78] A. Seubert, K. Velkov, and K. Langenbuch, editors. *The time-dependent 3d discrete ordinates code TORT-TD with thermal-hydraulic feedback by ATHLET models*, International Conference on the Physics of Reactors "Nuclear Power: A Sustainable Resource", Casino-Kursaal Conference Center, Interlaken, Switzerland, September 14-19, 2008.

[79] Siemens AG - Bereich Energieerzeugung (KWU). Leistungsstörfall durch Regelstabfehlfahren, 1994.

[80] Siemens AG - Bereich Energieerzeugung (KWU). Nukleare Kernauslegung: Arbeitsbericht, 1996.

[81] Siemens AG - Bereich Energieerzeugung (KWU). Ausfall aller Primärpumpen (Notstromfall), 1997.

[82] Siemens AG - Bereich Energieerzeugung (KWU). Störfallverhalten bei langsam ablaufenden Reaktivitätstransienten, 1997.

[83] Siemens AG - Bereich Energieerzeugung (KWU). FRM II Brennelemente, 23.03.2003.

[84] A. W. Solbrig. Doppler effect in neutron absorption resonances. *American Journal of Physics*, 29(4):257–261, 1961.

[85] W. M. Stacey. *Nuclear reactor physics.* A Wiley-Interscience publication. Wiley, New York, 2001.

[86] W. Tischler. KWU NLS2/95/0024. *Siemens AG - Bereich Energieerzeugung (KWU)*, 1995.

[87] T. Trumbull. Treatment of nuclear data for transport problems containing detailed temperature distributions. *Nuclear Technology*, 156:75–86, 2006.

[88] U.S. Nuclear Regulatory Commission. Trace v5.0p2 user's manual.

[89] V. Valtavirta, V. Tulkki, J. Leppänen, and T. Viitanen, editors. *The universal fuel performance code interface in Serpent 2*, 2013.

[90] T. Viitanen. *Development of a stochastic temperature treatment technique for Monte Carlo neutron tracking.* Dissertation, Aalto University, Espoo, 2015.

[91] Z. Warsi. *Fluid dynamics.* CRC Press, Boca Raton, Florida, 1993.

[92] C. A. Wemple, H.-N. Gheorghiu, R. Stamm'ler, and E. A. Villarino, editors. *The HELIOS-2 lattice physics code.* Kiadja and KFKI Atomenergia Kutatointezet, 2008.

[93] E. R. Woodcock and et al. Techniques used in the gem code for monte carlo neutronics calculations in reactors and other systems of complex geometry. *Argonne National Laboratory*, 1965.

[94] X-5 Monte Carlo Team. *MCNP – A General Monte Carlo N-Particle Transport Code, Version 5.* Los Alamos National Laboratory, 2003.

[95] G. Yesilyurt, W. Martin, and F. B. Brown. On-the-fly doppler broadening for monte carlo codes. *Nuclear Science and Engineering*, 171, 2012.